Defect Mechanisms in Diode Lasers at High Optical Output Power: The Catastrophic Optical Damage

D I S S E R T A T I O N

zur Erlangung des akademischen Grades

Dr. rer. nat.
im Fach Physik

eingereicht an der
Mathematisch-Naturwissenschaftlichen Fakultät I
Humboldt-Universität zu Berlin

von
Dipl.-Phys. Martin Hempel

Präsident der Humboldt-Universität zu Berlin:
Prof. Dr. Jan-Hendrik Olbertz

Dekan der Mathematisch-Naturwissenschaftlichen Fakultät I:
Prof. Stefan Hecht, PhD

Gutachter:
1. Prof. Dr. Thomas Elsässer
2. Prof. Dr. William T. Masselink
3. Prof. Dr. Joachim Wagner

eingereicht am: 07.05.2013
Tag der mündlichen Prüfung: 23. Oktober 2013

Contents

Zusammenfassung **v**

1 Introduction **1**

2 Physical Background **3**
2.1 Semiconductor Diode Lasers . . . 3
2.1.1 Development of the Structure of the Semiconductor Diode Laser . . . 3
2.1.2 Laser Mechanisms . . . 5
2.1.3 High-Power Diode Lasers . . . 8
2.2 The Catastrophic Optical Damage (COD) . . . 9

3 Experimental **13**
3.1 Thermocamera Based Setups . . . 13
3.1.1 Thermocamera . . . 13
3.1.2 Specific Setups . . . 14
3.1.3 System Characterization . . . 16
3.1.4 Basic Image Processing . . . 20
3.2 Streak Camera Based Setups . . . 22
3.3 The Step Test Approach . . . 23
3.4 Further Analytical Techniques . . . 24
3.5 Samples . . . 26

4 First Phase of COD – Aging **29**
4.1 Experimental Results . . . 30
4.1.1 Spatially Integrated Transient Data and Thermography . . . 30
4.1.2 Spatially and Temporally Resolved Data . . . 32
4.1.3 Active Layer Temperature Transient . . . 35
4.1.4 Influence of the Material System . . . 38
4.2 Discussion of First Phase Results . . . 40
4.2.1 The Time to COD . . . 40
4.2.2 Beam Properties *en route* to COD . . . 42
4.2.3 Temperature Contributions . . . 43
4.2.4 Influence of the Material System . . . 45
4.2.5 Mechanisms Determining the First Phase . . . 47

5 Second Phase of COD – Thermal Runaway and Start of Defect Spread 49
5.1 Experimental Results . . . 49
5.1.1 Time Constants for Different Material Systems . . . 49
5.1.2 Spatial and Temporal Resolved Nearfield Dynamics . . . 51
5.1.3 Microscopic Study of Early Defect Stages . . . 60
5.1.4 Short-Time Thermography . . . 63
5.2 Discussion of Second Phase Results . . . 64
5.2.1 Spatially and Temporally Resolved Dynamics . . . 64
5.2.2 Energy Balance of COD . . . 68
5.2.3 Microscopic Defect Analysis . . . 76
5.2.4 Heat Dissipation . . . 81
5.2.5 Mechanisms Determining the Second Phase . . . 83

6 Third Phase of COD – Defect Spread 85
6.1 Experimental Results . . . 85
6.1.1 Defect Analysis Through the Top Contact . . . 85
6.1.2 Simultaneous Analysis of Both Facets and Cavity . . . 89
6.2 Discussion of Third Phase Results . . . 92
6.2.1 Data Obtained Through the Top-Contact Window . . . 92
6.2.2 Data Obtained From Both Facets and Cavity . . . 100
6.3 Modeling . . . 101
6.3.1 Introduction of the Model . . . 102
6.3.2 Influence of the Model Parameters . . . 105
6.3.3 Application of the Model . . . 107
6.3.4 Evaluation of the Model . . . 114
6.4 Mechanisms Determining the Third Phase . . . 114

7 Investigation of Special Structures 117
7.1 Laser Bars . . . 117
7.1.1 Experimental Results . . . 117
7.1.2 Discussion of the Results Obtained with Laser Bars . . . 118
7.2 Single-Spatial-Mode Ridge Waveguide Diode Lasers . . . 121
7.2.1 Experimental Results . . . 121
7.2.2 Discussion of the Ridge Waveguide Laser Dynamics . . . 125
7.2.3 Comparison to BA Diode Lasers . . . 128
7.3 Quantum Dot Devices . . . 129

8 Conclusions 133

List of Abbreviations and Symbols 135

Publications 139

Bibliography 143

Zusammenfassung

Halbleiter-Diodenlaser spielen eine wichtige Rolle in allen Bereichen des täglichen Lebens, wie Datenspeicherung, Beleuchtung, Sicherheitstechnik, Markierungs-, Mess- und Drucktechnik. Sie stellen heutzutage die wichtigste Quelle für Laserstrahlung dar, entweder als direkte Strahlungsemitter oder als Pumplaser in Laser-Systemen. Hochleistungs-Diodenlaser sind die effizienteste menschgemachte Struktur zur Umsetzung von elektrischer in Strahlungs-Energie. Sie erreichen eine Effizienz von $\leq 73\%$ bei Raumtemperatur. Dieser hohe Wirkungsgrad führt nicht nur zu Energieeinsparungen, sondern reduziert gleichzeitig die Erwärmung des Bauelements durch Verminderung der Verluste.

Das Erreichen hoher optischer Ausgangsleistungen ermöglicht die Verwendung der Diodenlaser in einem breiten Anwendungsfeld. Eine herausragende Bedeutung dabei nimmt die Verwendung als Pump-Lichtquelle für Festkörper-Laser ein. Bei dieser indirekten Anwendung führt das Erzielen einer höheren Leistung pro Pumplaser-Emitter direkt zu einer Kosten- und Größenreduzierung des Gesamtsystems aufgrund der verringerten Anzahl benötigter Pumplaser. Beispiele für eine direkte Nutzung der erzeugten Strahlung mit hoher optischer Leistung sind die Verwendung als Seed-Laser, Materialbearbeitung, wie das Plastik-Schweißen, sowie medizinische und kosmetische Anwendungen.

Die Mechanismen, welche die maximal erreichbaren optischen Ausgangsleistung begrenzen, können in zwei Gruppen unterteilt werden, solche, welche die optische Leistung reversibel reduzieren und diejenigen, die zu irreversiblen Degradation führen. Der *catastrophic optical damage* (COD) gehört zur letzteren Gruppe. Nachdem viele, die Bauelemente-Lebensdauer bei hohen optischen Leistungen begrenzenden Faktoren, wie die Materialqualität, überwunden worden sind, bleibt der COD als ein fundamentales Limit. Das Ziel der vorliegenden Arbeit besteht in der Analyse der mikroskopischen Ursachen des COD und des Verständnisses der damit einhergehenden physikalischen Gesetzmäßigkeiten. Dies soll zu wissensbasierten Lösungen zur Verbesserung der Bauelemente Effizienz, optischen Leistung und Zuverlässigkeit führen. Damit ließen sich Anwendungen erschließen, die entweder auf niedrigen Preisen beruhen, z.B. ein Produkt für den Massenmarkt wie laserbasierte Zündkerzen, oder Systeme, welche eine gewaltige Anzahl an Pump-Lasern benötigen, wie Einrichtungen zur lasergestützten Fusion (mehrere Millionen Laserarrays werden hierfür benötigt). Diese Einsatzfelder haben offenkundig das Potenzial tiefgreifender Auswirkungen auf die ganze Gesellschaft.

In dieser Arbeit wird der COD zeitaufgelöst untersucht um die beteiligten Mechanismen zu identifizieren. Zu diesem Zweck wird der COD mittels kurzen Pulsen bei hohen Strömen gezielt hervorgerufen. Die Annäherung an die COD-Schwelle des jeweiligen Bauelements wird durch aufeinanderfolgende kurze Einzelpulse mit sukzessiv steigenden Strömen realisiert. Dieses Verfahren wird Stufentest genannt. Der prinzipielle Vorteil dieses Verfahrens ist die Möglichkeit den Zeitpunkt des COD-Auftretens relativ genau vorherzubestimmen. Die Nutzung des Stufentests zielt dabei nicht nur auf die Erforschung des gepulsten Laserbetriebs ab. Es wird in der Arbeit gezeigt, dass der Stufentest eine besondere Form der beschleunigten Alterung darstellt und auf den gleichen Mechanismen beruht, welche auch im Dauerstrichbetrieb zum COD führen. Damit sind die erhaltenen Erkenntnisse auch für andere Betriebsregime relevant.

Der COD Prozess konnte zeitlich in drei Phasen unterteilt werden, die Alterung, der thermische Runaway (ein sich durch positive Rückkopplung selbst verstärkender Prozess) und das Sekundärschadenswachstum. Die erste Phase konnte durch den Stufentest auf den Nanosekunden-Bereich reduziert werden. Die Rolle des Laser-Lichtfelds als wichtigste Energiequelle des COD-Prozesses wurde experimentell bestätigt. Die genutzten thermographischen Techniken erlaubten eine *in-situ* Verfolgung des Defektwachstums, auch wenn das Bauelement nicht, z.B. durch Öffnungen in den Metallkontakten, speziell dafür präpariert wurde. Diese direkte Messung der Ausbreitung, die Modellierung des Wärmeflusses und eine kristallographische Materialanalyse zeigen, dass das Material, welches von der Defekt-Front passiert wurde, innerhalb von Nanosekunden zu substanziell tieferen Temperaturen zurückkehrt. Verschiedene experimentelle Ansätze bestätigen das Vorhandensein einer Temperatur im Bereich von $1200°C - 1500°C$ während des gesamten Degradationsprozesses. Dabei hat sich gezeigt, dass selbst wenn keine Laseremission mehr vorliegt, die verstärkte spontane Emission ausreicht, um den fortschreitenden Degradationsprozess mit Energie zu versorgen.

Für den Start des thermischen Runaway muss ein bestimmter Temperaturunterschied zwischen der späteren COD-Position und dem übrigen aktiven Lasermaterial erreicht werden. Die vorliegende Arbeit zeigt verschiedene Mechanismen auf, die zu einer solchen Situation führen können. Dabei spielen auch physikalische Eigenschaften der verwendeten Materialsysteme und Schichtstrukturen eine entscheidende Rolle. Die Positionen dieser COD-Startpunkte haben entscheidenden Einfluss auf das spätere vollentwickelte Schadensbild. Ein neu im Rahmen dieser Arbeit entwickeltes Modell zur Beschreibung der räumlichen Schadensausbreitung nutzt diesen Umstand, um die Defektkinetik *ex-post* zu rekonstruieren. Dies ermöglicht das Aufzeigen von Schwachstellen im Bauelement. Aus einer Analyse der Schadensausbreitung während der zweiten und dritten COD-Phase konnte der thermische Widerstand des Materials als bestimmender Parameter für die Schadens-Dynamik identifiziert werden.

Experimentelle Befunde weisen darauf hin, dass der COD nicht am Quantengraben selbst beginnt, sondern im Bereich des Wellenleiters und der Mantelschicht. Dies ist überraschend, da die höchste Lichtintensität am Quantengraben als Verstärkermedium zu erwarten ist.

Die vorliegende Arbeit stellt experimentelle Strategien zu Präparation sehr früher Defektstadien vor, welche zukünftig dazu genutzt werden können gezielt frühe Degradationsstufen zu untersuchen. Dabei sind vor allem Untersuchungen zur Alterung in Systemen mit externer optischer Rückkopplung ein interessantes Anwendungsfeld. Dies ist eine Fragestellung, welche aufgrund der heutzutage erzielbaren hohen optischen Leistungen für nahezu alle Diodenlaser-Systeme relevant ist, da eine Rückkopplung durch teilweise Strahlreflexion an Strahlkombinations- und Formungs-Optiken auftritt.

1 Introduction

Semiconductor diode lasers are present in almost all fields of our daily life, e.g., data storage, marking, measuring, printing, lighting, security etc. They are the main source of laser light today, either as direct source or as pump source in laser systems. High-power diode lasers are the most efficient man-made structures for conversion of electrical to optical energy. Their efficiencies reach values of $\geq 73\%$ [1, 2] at room temperature. This leads not only to energy savings, but reduces heating by avoiding losses.

Reaching high output power levels opens up a wide variety of application fields. An important example is the pumping of solid state lasers [3]. For this application, higher power from a pump laser emitter results in cost and size reduction of the entire system due to a reduced number of necessary pump lasers. Examples for the direct utilization of diode lasers with high optical output power are the use as seed lasers, the treatment of materials as plastic welding, as well as medical and cosmetic applications.

The limiting factors for reaching higher output powers can be separated into two groups: Mechanisms that reduce the output power in a reversible way and irreversible degradation [4, 5]. The catastrophic optical damage (COD) belongs to the second group. After having sorted out many other factors, e.g., material quality, that impairs device reliability at high power levels, the COD remains as one of the main limitations. This thesis aims at revealing the microscopic origins of the COD and understanding its physics. This should lead to knowledge-based solutions for increasing the efficiency, output power, and reliability. This could enable applications that either rely on low prices, e.g., a mass-market product like laser driven spark plugs [6], or systems that need an enormous amount of pump lasers, as laser induced fusion facilities (several million laser arrays are required) [7]. Obviously, these options could affect the entire society.

The strategy followed in this thesis is to time-resolve the COD in order to understand the mechanisms leading to and being involved in the process. The COD is provoked with individual short high-current pulses. This addresses directly the pulsed operation regime, but also allows conclusions, as will be shown, about the COD failure in continuous wave operation representing the primary operation mode. The main advantage of the single pulse test is the possibility to trigger the start of the COD event. This is important for all kinds of measurements with high temporal resolution.

The main benefits of the single pulse approach are a direct analysis of the defect growth kinetics as well as the temperature transients during COD. Moreover, it makes the preparation of extremely early defect stages possible. By stopping the degradation process at the end of the pulse, the pulse width determines the temporal resolution of the measurement but not the technique applied to analyze the defect. Furthermore, this approach allows to study the COD by analyzing the incorporated energies by the control over the external parameters.

This thesis is organized as follows: After an introduction of the semiconductor diode laser and a review of existing knowledge about the COD process in Ch. 2, the experimental techniques are presented in Ch. 3. The analysis of the mechanisms involved in COD follows its three phases which will be introduced at the beginning of Ch. 4. Chapter 4 is dedicated to the first phase, while Ch. 5 addressed the second, and Ch. 6 the third. The universality of the uncovered mechanisms is verified in Ch. 7, where special device structures are investigated. Chapter 8 gives conclusions and an outlook.

2 Physical Background

2.1 Semiconductor Diode Lasers

2.1.1 Development of the Structure of the Semiconductor Diode Laser

The first semiconductor diode lasers (DL) have been presented in 1962 [8–11]. These structures consisted of a pn-junction formed by zinc diffusion into n-type GaAs. As today's edge-emitters, they had a Fabry-Perot-type laser cavity. These lasers suffered from two major problems [12]: Insufficient carrier confinement and unacceptable high optical losses. The transversal extent of the pn-junction is governed by the sum of minority carrier diffusion lengths. Additionally the light experiences high losses when propagating outside this gain region. The optical confinement in lateral direction was defined by the width of the entire chip. These problems result in a high threshold current (I_{th}) and make continuous wave (cw) operation of this structure impossible at room temperature.

An improved transversal carrier confinement is achieved by introducing energy barriers in the band structure [13]. In this *double heterostructure* DL, a lower band gap material is surrounded by one with a wider band gap. Figure 2.1(a) shows a schematic of the conduction band edge for Al(GaAs)-material. This approach also avoids high optical losses by absorption by using wider band gap material, which is transparent for the laser light. The use of $\mathrm{Al_xGa_{1-x}As}$ material was favored by the almost matching lattice constants of AlAs and GaAs. This allows material growth with low defect densities due to an almost vanishing built-in strain. Room-temperature cw operation of DLs have been demonstrated employing this concept [14, 15].

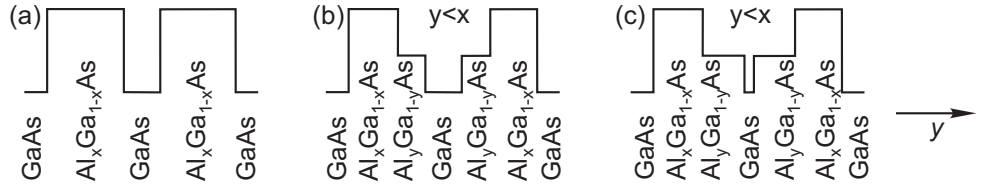

Figure 2.1: Schemes illustrating the various laser layer designs. The conduction band edge in transversal direction is given for: (a) Double heterostructure. (b) Separate confinement heterostructure. (c) QW heterostructure. As example, possible compositions of the AlGaAs-system are given. The idea for the graph is taken from [12, 16].

This idea was developed further in order to achieve separate control of carrier and optical confinement. Additional layers with even lower refractive index were added on both sides of the double heterostructure. These additional layers form an optical waveguide. The resulting structure is called *separate confinement heterostructure* [17]. Figure 2.1(b) schematically shows the conduction band edge for this case.

The use of molecular beam epitaxy and metalorganic chemical vapor deposition allowed for better

controllable and high quality growth of the DL structures. They allow to reduce the gain region thickness from $\approx 50\,\text{nm}$ to a *quantum well* (QW) of about $5-10\,\text{nm}$ [18]. A scheme of the conduction band edge of this structure is given in Fig. 2.1(c). Structures with multiple QWs forming the gain region are used, too.

Control of the lateral dimension was achieved by restricting the current (I) path to a narrow stripe [19]. This principle is called *gain-guiding*. The gain-guided lateral emitter width is influenced by the current spread under the contact stripe. The final width results from a gain-induced increase of the refractive index in lateral direction and is distorted by carrier-induced anti-guiding. The latter is a result of a decrease of the refractive index (n) in the material with increasing carrier density. This behavior is qualitatively discussed by Bennett *et al.* [20]; the authors identify the relevant mechanisms that affect n to be: (i) band-filling, resulting in the Burstein-Moss effect (detected as absorption decrease slightly above the band gap energy due to conduction band filling), (ii) band gap shrinkage which is an effect of the many-body interactions of electrons and holes at their band edges, and (iii) free-carrier absorption, which is, following the Drude theory, proportional to the density of electrons and holes and to the square of the wavelength.

These mechanisms, however, lead to an unstable lateral mode pattern in broad area (BA) emitters. A solution for this issue was the application of an built-in lateral refractive index step in the structure. Two methods became popular to achieve this: (i) the *buried heterostructure* laser, where after planar growth of the layers an emitter stripe is formed by completely removing the active layer outside and embedding the stripe thereafter in a material with lower n, and (ii) the *ridge waveguide* laser, where only the cladding layer outside the emitter stripe is thinned after growth. This results in an effective reduction of the refractive index in the region with thinned claddings due to compression of the optical mode in transversal direction there.

Other material systems have been used to build DLs for other wavelength than $\approx 800\,\text{nm}$. InGaAsP double heterostructure lasers emitting at 650 nm have been realized by Coleman *et al.* [21] and AlGaInP around 670 nm, also as double heterostructure, by Ikeda *et al.* [22]. Additionally, Yablonovitch *et al.* [23] and Adams [24] came up with the idea to use a strained QW by utilizing the lattice mismatch of the materials. Lattice mismatched materials allow a good, dislocation free growth as long as the strained layer does not exceed a critical layer thickness, as demonstrated by Matthews and Blakeslee [25]. In this growth regime, the lattice mismatched material accommodates to the host lattice constant and therefore builds up an intrinsic strain. This additional design freedom allows to reach the wavelength range from 980 nm to 1100 nm, e.g., demonstrated by Beernink *et al.* [26]. The blue and ultraviolet wavelength ranges have been accessed by the invention of DLs based on GaN by Nakamura *et al.* [27]. Wavelength of $1.3\,\mu\text{m}$ and the important wavelength of $1.55\,\mu\text{m}$ for fibre communication systems are realized in GaInAs on InP [28].

By further development and understanding of the growth mechanisms, other structures of the active region became possible. An approach, presented by Arakawa *et al.* [29], is to use quantum dots (QD) as the active material. Another approach is the quantum cascade laser (QCL) using intra-band transitions for lasing. A first successful experimental realization of it was reported by Faist *et al.* [30] in 1994. They realized coherent light amplification of the radiative relaxation of electrons from a higher to a lower state within the conduction band.

Typically, a fraction of $\approx 25\% - 50\%$ of the electrical power applied to a DL is converted into heat. Therefore, cooling of the active region is important. Especially BA lasers are packaged with their epi-

taxial layers close to the heat sink (also denoted as *sub-mount*). Due to the common use of n-doped substrates, the p-side of the diode is on top of the grown layer stack. If now placing the epitaxial layers as close as possible to the heat sink, the p-side is directly attached to it. Therefore this kind of mounting is called *p-down* (the vice versa situation is called *p-up mounting*). In case of p-down mounting, it is common to package the laser chip with an overhang of some $10\,\mu$m with respect to the heat sink. This is done to protect the front facet from solder material. Furthermore, the soldering techniques provide challenges, in particular for larger devices where a mismatch of the thermal expansion coefficients is crucial [31].

A photograph of a mounted DL is given in Fig. 2.2(a). There the GaAs/AlGaAs laser chip is mounted p-side down on a copper sub-mount. The front facet is directed towards the reader. The n-side metallization is connected by bond wires to a bond pad which is electrically insulated from the heat sink. This geometry is shown schematically in Fig. 2.2(b). The coordinate system used in the following chapters is also given – growth (transversal) direction: y, lateral direction: x, longitudinal direction/resonator axis: z. The layer scheme of the separate confinement heterostructure is shown on an enlarged scale on the right side. The epitaxial layers have a thickness of $\lesssim 4\,\mu$m in total, while the entire chip has a height of $\approx 120\,\mu\text{m} - 160\,\mu\text{m}$.

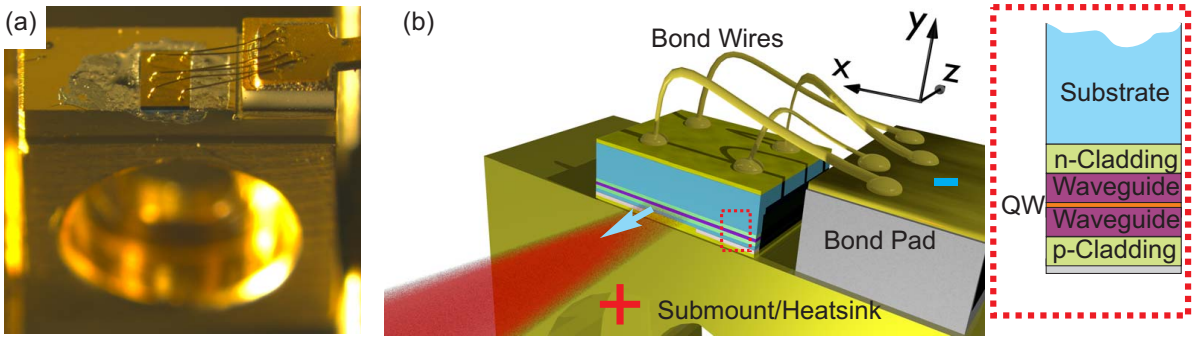

Figure 2.2: DL on sub-mount. (a) Photograph of a p-down packaged DL on a copper sub-mount. The bottom contact (p-side) is electrically connected by the sub-mount, while the top-(n)-contact is connected by bond wires to a bond pad. The front facet is directed towards the reader and appears dark. (b) Scheme of the p-down packaged laser (parts are labeled accordingly). The blue arrow indicates the direction of light emission. The layer scheme of the separate confinement heterostructure is given at the right side. Their position is indicated in the layer scheme by a dotted rectangle.

2.1.2 Laser Mechanisms

The majority of today's edge emitting semiconductor DLs are based on QWs as a gain medium. Therefore, it is worthwhile to discuss the physical properties of those structures with reduced dimensionality. The relevant case for semiconductor DLs is the so-called *type-I QW*, where a lower (confining) potential in the QW is experienced by both electrons and holes. For achieving a reduction in dimensionality from three dimensions in the bulk semiconductor to a two dimensional confined state in a QW, its thickness

must be on the order of the de Broglie wavelength $\lambda_B = h/\sqrt{2m_c^\star E}$ (with h: Planck's constant, $m_c^\star$: effective electron mass in the semiconductor; E: electron energy). This criterion is fulfilled by 5 nm to 10 nm thick QWs in DLs. The electrons in a QW can be treated as two-dimensional electron gas. In the envelope function approximation, the wave function for the electron in the QW can be separated into two contributions [32–34]:

$$\Psi(x,y,z) = \zeta(y)\ \mathrm{e}^{\mathrm{i}(k_x x + k_z z)}\ u(k=0,x,y,z) \tag{2.1.1}$$

with the lattice-periodic Bloch function u and the wave vector k and its components $k_x x$ and $k_z z$. In the $x-z$-plane the particle exhibits free dispersion as in the bulk case. The part of the wave function along growth direction $\zeta(y)$ equals the particle-in-a-box-problem for $k_x x = k_z z = 0$, and the energy states become quantized. With this wave function *ansatz* the possible energies of the system can be calculated [32]:

$$E_{c,\mathsf{n}} = E_{c0} + E_{y,\mathsf{n}} + \frac{\hbar^2\left(k_x^2+k_z^2\right)}{2m_c^\star} \quad \overset{\text{infinite high barriers}}{\Longrightarrow} \quad = E_{c0} + \left(\frac{\hbar^2}{2m_c^\star}\right)\left[\left(\frac{\mathsf{n}\,\pi}{L}\right)^2 + k_x^2 + k_z^2\right] \quad , \tag{2.1.2}$$

with the conduction band edge E_{c0}, the quantum-number $\mathsf{n} = 1,2,3,\ldots$ indicating the sub-band, the quantized energy in y-direction $E_{y,\mathsf{n}}$, and the thickness L of the QW. The quantum confinement increases the ground state energy by $\Delta E = (\hbar^2/(2m_c^\star))\cdot(\pi^2/L^2)$ compared to the bulk case, because the momentum is increased by a decrease in spatial uncertainty following the uncertainty relation. Moreover, the excited state energies become quantized. A similar relation holds for the holes in the valence band.

The reduction of dimensionality by the quantum confinement also impacts the density of states of the system by reducing the available space of possible wave vectors [35]. The densities of states (ρ_c) for the conduction band of bulk material, QWs, and QDs are (with the lowest energy $E_{c,\mathsf{n}}$ in sub-band n):

$$\begin{aligned}
&\text{bulk}: && \rho_c^{3D}(E) = \frac{\sqrt{2}m_c^{\star\,3/2}}{\pi^2\,\hbar^3}\sqrt{E-E_{c0}} \\
&\text{QW}: && \rho_c^{2D}(E) = \frac{m_c^\star}{\pi\,\hbar^2\,L} \quad \text{for} \quad E_{c,\mathsf{n}}\big|_{k=0} \le E \le E_{c,(\mathsf{n}+1)}\big|_{k=0} \quad \text{else} \quad \rho_c^{2D}(E) = 0 \\
&\text{QD}: && \rho_c^{0D}(E) = \delta(E - E_{c,\mathsf{n}})
\end{aligned} \tag{2.1.3}$$

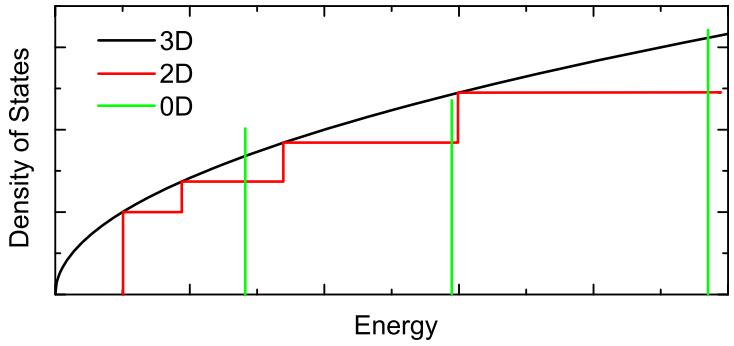

Figure 2.3: Density of states for bulk material (3D), QWs (2D), and QDs (0D).

Figure 2.3 depicts the density of states for bulk material (3D), QWs (2D), and QDs (0D) [33]. While for the bulk material ρ_c^{3D} gives a square root starting from E_{c0}, it is step like for the QWs with the bulk ρ_c^{3D} as limit. In case of the QDs ρ_c^{0D} is a Dirac-Delta function at the sub-band energies. Similar relations holds for the valence band density of states ρ_v. They can be combined to the joint density of states $\rho_j^{-1} = \rho_c^{-1} + \rho_v^{-1}$. This has been calculated for a single quasiparticle, an inclusion of Coulomb mediated many-body effects modifies the density of states, in particular at small electron energies [36].

When studying laser transitions only the first sub-bands in both conduction ($E_{c,1}$) and valence band ($E_{v,1}$) are of interest, caused by selection rules and occupation probability. The laser light frequency ν is determined by the transition energy between them, i.e., $h\nu = E_{c,1} - E_{v,1}$ which is the band gap E_g plus the confinement energies of the carriers. A quasi thermal equilibrium in the conduction and valence bands can be assumed, caused by the fast intraband thermalization ($\approx 100\,\mathrm{fs}$) compared to the interband relaxation ($\approx 1\,\mathrm{ns}$) [37]. Therefore, Fermi distributions are used to express the occupation probabilities in the conduction band (f_c) and valance band (f_v) [33]:

$$f_c = \frac{1}{\exp\left(\frac{E - E_{f,c}}{k_B T}\right) + 1} \qquad \text{and} \qquad f_v = \frac{1}{\exp\left(\frac{E_{f,v} - E}{k_B T}\right) + 1} \tag{2.1.4}$$

with the quasi Fermi energies for electrons $E_{f,c}$ and holes $E_{f,v}$, the Boltzmann constant k_B, and the Temperature T. The gain in the laser is [37]:

$$g(h\nu) \propto \frac{|M(h\nu)|^2}{h\nu} \rho_j(h\nu)\ (f_c - f_v) \tag{2.1.5}$$

The transition matrix element $|M(h\nu)|^2$ is almost constant for all III-V-compounds [38]. The quantum confinement affects the gain by ρ_j. The Fermi inversion factor $f_{inv} = f_c - f_v$ depends on the electrical pumping. It gives a sufficient condition for achieving positive optical gain:

$$\text{from} \quad f_{inv} \overset{!}{>} 0 \quad \text{follows} \quad E_{f,c} - E_{f,v} > E_{c,1} - E_{v,1} = h\nu \tag{2.1.6}$$

A second lasing condition arises from the losses in the Fabry-Perot cavity. The modal gain Γg has to compensate at least the internal (absorption) losses α_i and the mirror losses α_m:

$$\Gamma g \geq \alpha_i + \alpha_m = \alpha_i + \frac{1}{2L_{cav}} \ln\left(\frac{1}{R_1 R_2}\right) \tag{2.1.7}$$

with the confinement factor Γ which is the ratio between the volume of the gain medium and the volume of the optical mode (typically $\approx 1\%$ for DLs). Further parameters are the cavity length L_{cav} and the front and rear facet reflectivities R_1 and R_2, respectively.

The impact of ρ_j on the gain spectrum is shown in Fig. 2.4. The joint density of states for bulk material and QW are schematically shown in Fig. 2.4(a). The Fermi inversion factor on the same energy scale is given in Fig. 2.4(b), the zero-crossing of this curve is represents the sufficient lasing condition discussed above. Figure 2.4(c) gives a comparison of the gain curves for the bulk and QW case. There shapes are determined by the product of ρ_j and f_{inv}, as demonstrated in Eq. (2.1.5). The gain spectrum of the QW is narrower than in the bulk case and the peak gain is lower. In order to satisfy the second condition for lasing, the compensation of the losses $\alpha_i + \alpha_m$ the pumping has to be increased.

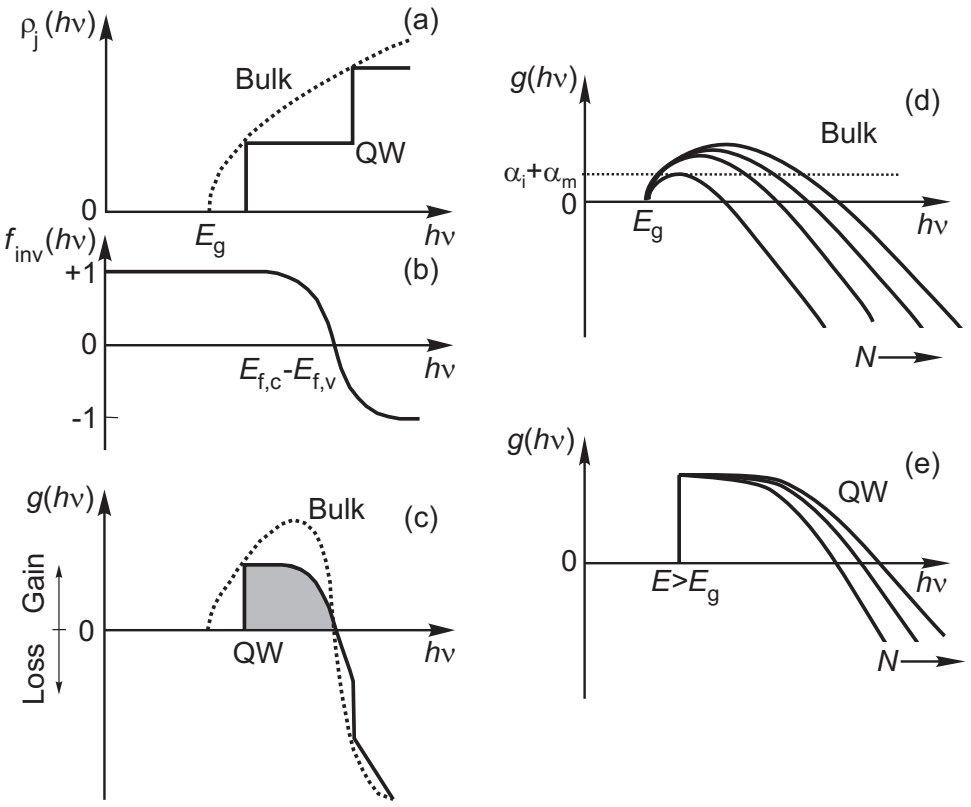

Figure 2.4: Comparison of gain spectra for bulk material and QW lasers. (a) Joint density of states. (b) Fermi inversion factor. (c) Gain. (d) Evolution of bulk material gain curve with varying carrier injection. (e) Gain curves of the QW with varying carrier injection. The idea for (a-c) is taken from [33].

Figures 2.4(d,e) show the evolution of the gain curves for bulk material and QW lasers with variation of the carrier injection N. The QW lasers satisfy the lasing threshold condition earlier, caused by the reduced density of states that has to be filled.

In QD lasers the lasing conditions are expected to be satisfied at even lower injection densities, because of the further reduced number of states to be populated. This is true, as long as the gain material contains only QDs of one size which have the same confinement energies. Otherwise, the Dirac-Delta peaks shown in Fig. 2.3 are distributed over a wider energy range negating the advantages of the strong quantum confinement.

2.1.3 High-Power Diode Lasers

In many fields of application, the optical output power of the DLs is a key parameter. Therefore, there is a permanent demand for further increasing emission powers. The internal power density of state-of-the-art devices amounts up to $10^{10}\,\mathrm{W/cm^3}$, which is higher than in the core region of the sun. Every success in pushing the extreme limits of technological feasibility further has an direct impact, e.g., on the size and

efficiency of laser systems that use DLs as pump source. Two standard applications in this field are the pumping of Nd:YAG at 808 nm and erbium-doped fiber amplifiers at 980 nm. For this reason, devices of these wavelengths cover the main part of the experimental work presented in the following.

Today's DLs are the most efficient man-made structures for converting electrical power to light with values exceeding 73% efficiency [1, 2]. Nevertheless, the remaining supplied electrical power remains in the device, leading to a heating of the semiconductor structure. Therefore, the achievable upper limits of high-power DLs operation are closely connected to cooling concepts. A common strategy is the p-down mounting to allow an efficient heat flow from the active region to the heat sink. The latter can be passively cooled, i.e., via heat conduction, but also actively cooled via a micro-channel water cooler.

Another difference compared to low-power DLs is the gain saturation at high current injection, which will be discussed in Sec. 3.5. Moreover, a way to extract more power from a single device is to increase the emitter width. BA DLs are a result of this powerful concept. The main drawback from this approach is the reduced beam quality by allowing the propagation of several lateral modes in the wide emitters. This leads to instabilities in the beam, known as *filamentation*. The characterization and control of it is still subject to on-going work. However, the maximal width of these structure has also an upper limit to allow sufficient beam guiding. In order, to achieve an higher output power in the kW-range from one monolithic device, arrays are formed by integrating several single emitters on one single chip. The most widespread concept is the parallel alignment of the emitter stripes, but also coupled waveguide structures have been tested.

Beside the decreased beam quality, high-power DLs face problems with the high internal optical load in the device. It is reduced by application of an efficient anti-reflective coating on the out-coupling facet. In order to maintain at the same time the high efficiency and output power level of the device, the cavity length is increased to compensate the elevated mirror losses and the epitaxial structure is optimized for low internal optical losses [39].

2.2 The Catastrophic Optical Damage (COD)

Failure mechanisms observed in DLs have been categorized by the time-evolution of the output power loss during operation with constant current, see Fig. 2.5(a). This leads to three main groups, as discussed by Jimenéz [40]:

(i) *Rapid* degradation is characterized by a quick decrease of the optical output power. This failure mode indicates significant defects, e.g., cracks or large dislocation networks, already present after device manufacturing.

(ii) *Gradual* degradation results in a slow output power decrease. This is a characteristic behavior for regular operation. It includes point defect creation and defect motion through the material, both on long time scales.

(iii) *Sudden* degradation, where the device shows regular operation and then experiences an almost instantaneous power drop. This kind of degradation gets activated when reaching a threshold condition that triggers the start of a fast degradation process.

The COD belongs to the third group. It is a sudden failure mechanism of edge-emitting DLs and occurs at elevated emission power levels. Together with a substantial power loss, structural damage is detectable.

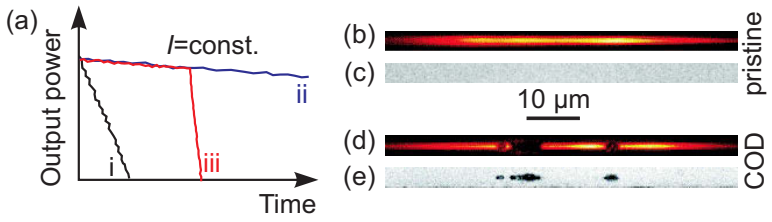

Figure 2.5: (a) Three different degradation mechanisms, categorized by the output power evolution during operation with constant current: (i) Rapid degradation, (ii) Gradual degradation, (iii) Sudden degradation. (b,c) The front facet of a pristine 808 nm emitting DL (device A_8) is shown. While (b) gives the lasing light emission, (c) is a micro-photograph of the surface. (d,e) The front facet is shown after COD occurred at the same device as in (b,c). (d) The laser light emission with COD damage taken under same conditions as (b). (e) Micro-photograph of the front facet impaired by COD.

An example is shown in Figs. 2.5(b-e). Figures 2.5(b,c) gives the situation for the pristine device – the emission pattern of the front facet (b) and the microscope image of the facet (c). In Figs. 2.5(d,e), the same is given for the device impaired by COD. The loss of optical power is clearly visible as dark areas in the emission pattern (d). Furthermore, the damage at the facet is obvious in Fig. 2.5(e). The main driving force of the COD is the optical light field, as shown by Chin *et al.* [41] and Bou Sanayeh [42]. They demonstrated that the defect growth during COD follows the optical mode direction and not, e.g., a crystal axis. Therefore, the COD is an optically driven degradation process and should not be confused with other types of sudden degradation mechanisms such as electrical failures like the electrostatic discharge etc.

The emission power at which COD starts is commonly called COD threshold power (P_{COD}). The optical output power is related to the current I via the DL characteristics. Therefore, a COD threshold current (I_{COD}) can be given. In this way, the term *COD threshold* is for both P_{COD} and I_{COD}.

Short after the first realization of the DL, reports were published addressing the observation of COD by Cooper *et al.* [43] in 1966 and Kressel *et al.* [44] in 1967. In 1973 Eliseev [45] characterized it as thermal micro-explosion. A comprehensive work, also addressing the origins of COD and its kinetics, has been published by Henry *et al.* in 1979 [46]. The main findings of this study are still valid for recent DLs: COD is jump-started by a fast *thermal runaway*. This process is initialized by reaching a certain temperature at the later COD site, named critical temperature (T_{crit}). The first direct experimental verification of this has been reported by Tang *et al.* [47]. In later studies [48–52], the influence of extrinsic effects was shown such as surface recombination and creation of structural defects.

The precondition for COD is an elevated local temperature. This can be caused by different heating mechanisms. At the facets, the dominating ones are surface recombination (as demonstrated by Ziegler *et al.* [53]) and surface currents (Tang *et al.* [54]). Moreover, the packaging with overhang, as discussed in Sec. 2.1.1, results in an elevated front facet temperature in comparison to the bulk. This is due to the lack of a good thermal coupling to the heat sink in this area. Yoo *et al.* [55] have found, that this temperature distribution is rather the 'normal' case. Furthermore, it explains why the facets are commonly affected by COD. Nevertheless, defects in the interior of the cavity can also lead to a local temperature rise resulting in a thermal runaway.

Higher operation currents or aging induced defect creation in long term operation[1] lead to a further increase of the temperature deviation between the later COD site and the remaining bulk material. This might be enough to reach T_{crit} and to start the thermal runaway by closing a positive feedback loop. This is characterized by a fast rise of the local temperature, which can be detected as a flash of Planck's radiation as shown by Ziegler *et al.* [56]. The feedback loops can be categorized as *intrinsic* or *extrinsic*, even combinations of both are feasible [57, 58]:

The intrinsic loop, as described by Henry *et al.* [46], works as follows: The elevated temperature causes a local shift of the band gap. Therefore, the re-absorption of laser light is increased in this region. The result is a higher density of non-equilibrium carriers. This leads to a further temperature increase by non-radiative recombination of these electron-hole-pairs, even if the recombination rate keeps constant. An elevated temperature increases the re-absorption further, as will be discussed in Sec. 4.2.3, and therefore closes the feedback loop. In the case of QW lasers, this remains still an issue, although the modal absorption is about two orders of magnitude smaller than for the double heterostructure devices (Tang *et al.* [59]). As shown by Chen *et al.* [49], the barrier and waveguide materials of the QW DLs are also involved in the process. Furthermore, free carrier absorption is an additional mechanism supporting this feedback loop.

The extrinsic feedback loop relies on the fact that an elevated temperature stimulates defect accumulation and creation. This leads to an absorption of laser light via defect-related optical transitions or to absorption by macroscopic defects. Non-radiative recombination transfers the energy from the light field to the semiconductor lattice. This acts as additional heat source making further defect creation increasingly likely. The relevance of this kind of feedback is supported by reports about a lowered COD threshold in aged DLs [60–63]. Another evidence for this is the *COD re-ignition* by subsequent current pulses, that will be discussed in detail in Secs. 5.1.2 and 6.1.1.

Much effort was invested to prevent degradation during high power operation. The facets were identified soon as one substantial bottleneck of the device structure. A major improvement was the application of facet coatings, allowing to adjust the reflectivities of front and rear facets (for as-cleaved facets it is about 30% determined by the refractive index change between semiconductor and air). Typically the rear is coated highly reflective ($\approx 99\%$ reflectivity), whereas the front facet has an anti-reflection coating ($\approx 1-5\%$ reflectivity). Common coating materials are dielectrics as Al_2O_3, applied in single or multilayers onto the facets, a comprehensive description is given by Macleod [64]. The mechanism that makes the as-cleaved facets susceptible to COD was found to be a temperature-activated surface-chemical reaction, as reported by Latta and Moser *et al.* [65–67].

In order to shift P_{COD} to even higher values, additional passivation of the as-cleaved facets became important. An example is the *E2*-technology, involving in-vacuum cleaving of the facets and low-energy deposition of silicon [68]. Approaches following a similar strategy use the deposition of germanium, aluminum, or antimony [69, 70] instead. An alternative approach is the cleaving of the facets in air and a subsequent cleaning, e.g., by ion-beam [71] or hydrogen-plasma [53] etching. This is followed by a passivation via nitridation [72] or sulphation [73–75]. Moreover, processes as InGaP or ZnSe epitaxy are used as well [76, 77].

[1] This results in an increased non-radiative recombination rate.

Beside the improvement of facet stability, a variety of additional methods have been developed to increase COD threshold:

- *Low optical confinement* structures: In this devices, the stripe width is widened in vicinity of the facet [78, 79]. This reduces the optical power density there.
- The *large optical cavity* concept: The transversal confinement, i.e., the waveguide thickness, is widened [80, 81]. The aim of this approach is the same – reduction of the optical power density at the facet.
- The use of alternative *material systems* help reaching higher P_{COD} [82, 83]: The sensitivity to COD varies between them, so that a proper choice, if possible at the desired wavelength, helps to increase COD threshold.
- The application of *non-injecting mirrors* where the current density is reduced at the facet [51, 84–87]: This reduces heating, e.g., by surface recombination. This structure is achieved by packaging the chip with overhang, cf. Sec. 2.1.1. Moreover, insulating layers can be applied close to the facet blocking the current flow there.
- In the *non-absorbing mirror* approach, the aim is a reduction of the modal absorption in vicinity of the facet [78, 88–95]. Therefore, two common techniques are applied to QW lasers: (i) Ion implantation or a thermal treatment is used to shift the laser transition to higher energies. (ii) A tensile strained QW is used. This strain relaxes at the facet and results in a blue shift of the QW absorption.

The result of such efforts is the state-of-the-art cw P_{COD} value per aperture width of $285\,\mathrm{mW}/\mu\mathrm{m}$ as reported by Petrescu-Prahova *et al.* [81]. This characterizes COD as a generic mechanism related to high power densities. After facet technology reached such a high level, COD starting at other locations, e.g., in the bulk, became more relevant.

Nevertheless, there is a lack of microscopic understanding of the mechanisms involved in COD. Therefore, the approaches to avoid COD are partly developed by trial-and-error. In order to achieve a deeper understanding of the physics on a microscopic level, the work presented in this thesis has been undertaken.

3 Experimental

In this chapter, the experimental techniques are presented that have been employed and in part introduced to study the COD. In the field of instrumentation, thermocamera- and streak camera-based setups are discussed in detail. Moreover, an overview is given of the in-house characterization techniques and of the external equipment.

3.1 Thermocamera Based Setups

The fact that COD is accompanied by a flash of Planck's radiation (often referred to as *thermal flash*) favors the use of a thermocamera. This has been demonstrated by Ziegler *et al.* [56]. Therefore a couple of experiments were designed incorporating such a camera into the measurement setup.

3.1.1 Thermocamera

A major advantage of using a thermocamera, compared to a single point detector, is the additional geometric information and the possibility to monitor different parts of the device in parallel. In the experiments, a Thermosensorik CMT384 thermocamera was used. It is based on a HgCdTe focal plane array with 384 pixel $\times$ 288 pixel of 20 μm size in square, with a pixel-pitch of 24 μm. The detector plane is cooled down to 80 K by a Stirling-cooler. The integration times can be chosen between 10 μs and 5.1 ms in steps of 10 μs. The noise equivalent temperature difference (NETD) is 20 mK. This is the temperature difference necessary to reach a signal-to-noise-ratio of one. The value given by the manufacturer is valid for a constant signal recorded with an integration time of 1 ms.

Two different objectives were used in the experiments. The *standard* one with a working distance of 0.1 m to infinity and the *microscope* objective with 2.5$\times$ magnification and a working distance of $\approx$ 20 mm. In order to get the highest geometric resolution, the latter one was used. The resolution obtained with the microscope objective is 8.8 μm $\times$ 8.8 μm per pixel. Notice, that the resolution in thermography is mainly limited by the longer light wavelength, e.g., in comparison to microscopy in the visible range. Therefore, a magnification of 2.5$\times$, in conjunction with the given detectors' pixel-size, is close to the theoretical resolution limit. The depth of focus while monitoring a DL is $\approx$ 40 μm, as will be shown in Sec. 6.1.2.

A second thermocamera was used for some of the experiments in collaboration with the Technical University of Denmark. The CEDIP Titanium 560M is based on a InSb focal plane array. It has 640 pixel $\times$ 512 pixel with a pixel-pitch of 15 μm. In conjunction with the 2.5$\times$ microscope objective this gives a resolution of 4.7 μm per pixel. The spectral sensitivity is in the range from 3.6 μm to 4.9 μm. The integration times are between 3 μs and 20 ms, and the NETD is 20 mK. The use of this camera was analogous to the Thermosensorik CMT384. Results obtained with the CEDIP camera will be indicated, otherwise the Thermosensorik camera was used.

3.1.2 Specific Setups

Figures 3.1 and 3.2 show an overview of the thermocamera-based setups. A frame synchronous output signal is given by the thermocamera, cf. Fig. 3.3. It triggered a Stanford Research DG535 delay generator which delivered a delayed trigger signal to the DL driver PicoLas LDP-V50-100 V3, Fig. 3.2. The DL was directly attached to the driver in order to guarantee fast current rise times of $\leq 10\,\text{ns}$. Excited by the current pulse, the DL emited laser radiation and thermal radiation, Fig. 3.2. A dichroic mirror, being transparent for thermal radiation and highly reflective for laser radiation, was used under 45° angle to separate this two signals. The laser emission was directed to a fast photo-diode (PD, ThorLABS DET10A/M, $\approx 1\,\text{ns}$ rise time); neutral-density filters (ND) were used to damp the signal if necessary. The PD signal was recorded by a fast oscilloscope (Agilent Infiniium, 2 GHz). The thermal radiation was detected by the thermocamera. Additionally, the current passing the diode was monitored and also recorded with the oscilloscope.

For mounting the DL, different configurations were used, as shown in Fig. 3.2(b-d). Figure 3.2(b) shows the typical situation for monitoring the front facet, the location where COD is most likely to start. The laser emission was pointed directly towards the thermocamera. The cooled background shield gives an uniform thermal background which is desirable in thermography. In sub-figure 3.2(c) a configuration is shown that allows for inspection of front facet and top side at the same time, e.g., if the device has a window in the top-contact materialization. In order to image front and rear facet and additionally the side of the laser cavity at once, an arrangement as shown in Fig. 3.2(d) was chosen. Here, the DL was placed in a 90° gold-coated corner-mirror.

If no spatial information is needed, the thermocamera can be replaced by a single-point MCT detector. In this case a configuration as in Fig. 3.1 was used. The laser emission and near-infrared (NIR)-signal coming from the front facet of the laser were directed via an off-axis parabolic mirror onto point detectors. Both contributions were separated by a dichroic beam-splitter. The emission power transient was monitored by the fast PD (ThorLABS DET10A/M). The NIR emission was detected by the fast infrared detector Judson J15D22-M204-S250U-60 that ensures together with a fast preamplifier a time resolution of better than 100 ns. Filters formed a bandpass that allows detecting the $1.5 - 2.5\,\mu\text{m}$ NIR spectral range. The thermocamera was used in parallel to analyze the thermal radiation along the cavity by looking at the side of the laser stripe.

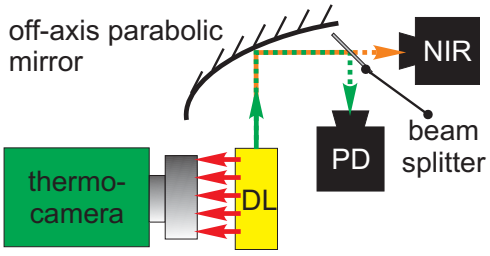

Figure 3.1: Scheme of setup with thermocamera for inspection of the side of the cavity and two point detectors analyzing the radiation coming from the front facet in different spectral ranges.

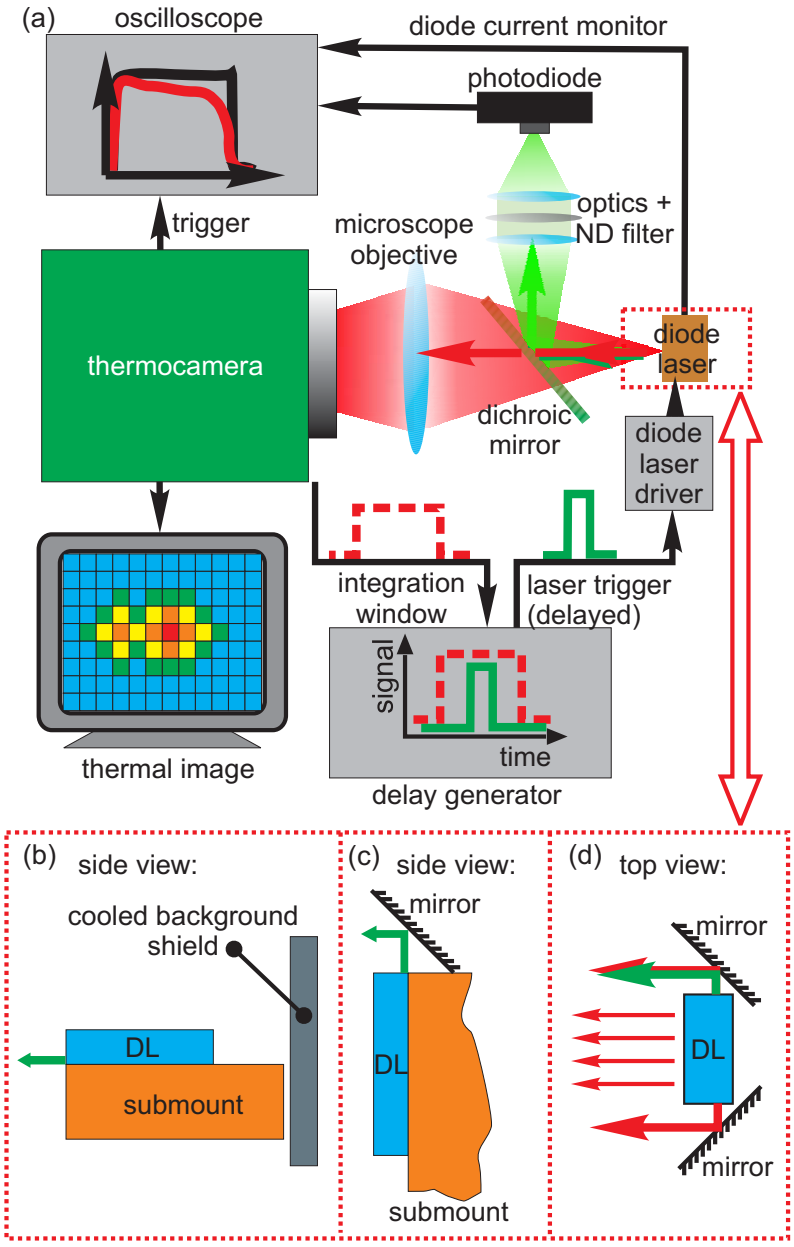

Figure 3.2: Thermocamera-based setups. (a) Overview of a typical experimental arrangement. The trigger hierarchy is indicated. The area around the DL is marked by a dotted line, here different configurations as shown in (b-d) are placed. (b) DL mounting for front facet inspection; green arrow indicates direction of laser emission. (c) Configuration that allows for measuring the top side of DL chip and the front facet simultaneously. (d) Placing the DL into 90° corner mirror allows imaging of front facet, rear facet and the side of the cavity in parallel; red arrows indicate thermal emission.

3.1.3 System Characterization

For use as thermal detector in COD experiments, the full sensitivity range of $1.5\,\mu\text{m} - 6\,\mu\text{m}$ of the thermocamera was limited by a filter to the $3.4\,\mu\text{m} - 5.5\,\mu\text{m}$ wavelength range. This prevented the recording of the GaAs-substrate-related emission below $2\,\mu\text{m}$ that has been characterized by Ziegler *et al.* [96].

Trigger Scheme

The camera is equipped with single-pulse trigger capability. It provides a camera frame synchronous output trigger signal, as schematically shown in Fig. 3.3(a). Due to the fact that neither the stability of this trigger nor its relation to the camera integration window were specified by the manufacturer, an additionally characterization was done. The details will be given in the following subsection. The frame synchronous output, provided by the thermocamera, is a square wave signal with negative amplitude, see Fig. 3.3(a). Its negative slope is used as time reference and set to $t = 0$, see dashed line in Fig. 3.3. The image integration time t_{int}, i.e., the time window in which the camera-sensor is sensitive to impinging photons, starts with a delay that is determined to be $129.04\,\mu\text{s}$, see Fig. 3.3(b). Details about the measurement of this delay will be given later. The delay generator DG535 is triggered by the signal at $t = 0$. It provides two trigger pulses, one as trigger for the laser pulse generator (c), and another one as reference signal (d) at $t = 0$ in order to trigger further devices, e.g., the oscilloscope. With the help of these trigger-logic-signals, Fig. 3.3(a-d), the pulse generator is triggered and provides a single current pulse (e) to the laser diode. The pulse width t_{PW} is defined by the length of this current pulse. The delay is chosen in a way that the laser pulse is centered in the image integration window of the thermocamera. It would be desirable, of cause, if t_{int} and t_{PW} match in length and temporal position. But, due to the fact, that the lowest given integration time of the thermocamera is $10\,\mu\text{s}$ and the preferred[1] pulse length for the used single pulses is around $1\,\mu\text{s}$, this alignment provided best results.

The output power was recorded by the PD. A typical result in case of COD is shown in Fig. 3.3(f). The time where COD occurs, i.e., the significant output power drop, is marked by a star and labeled accordingly. The time interval from the leading edge of the pulse to the point where the power drop starts, i.e., the COD ignition, is denoted *time to COD* (t_{COD}), see Fig. 3.3(f). The time-resolved temperature profile of the COD site, in conjunction with the scenario shown in (f), is given in Fig. 3.3(g). The shape of the profile will be discussed in Ch. 4. The expected temperature transient is faster as the time resolution of the thermocamera. The recorded thermal signal is an average. If we consider only the time in which an elevated temperature is present an effective integration time $t_{\text{int,eff}}$ can be given, see indicated interval in Fig. 3.3(g).

Image Integration Window of the Thermocamera

In order to determine the camera trigger-timing and the sensitivity during a single pulse experiment, a fast-switchable mid-infrared light-source was used, namely a quantum cascade laser (QCL). It was emitting around $4.1\,\mu\text{m}$ and provided, together with the PicoLas LDP-V 50-100 V3 pulse driver, pulses of $(18 \pm 1)\,\text{ns}$ width at $I = 5.6\,\text{A}$. Details about the device are given in Ref. [34]. This short pulse was shifted in time by the delay generator with respect to the zero time mark, cf. Fig. 3.3.

[1] Details will be given in Ch. 4.

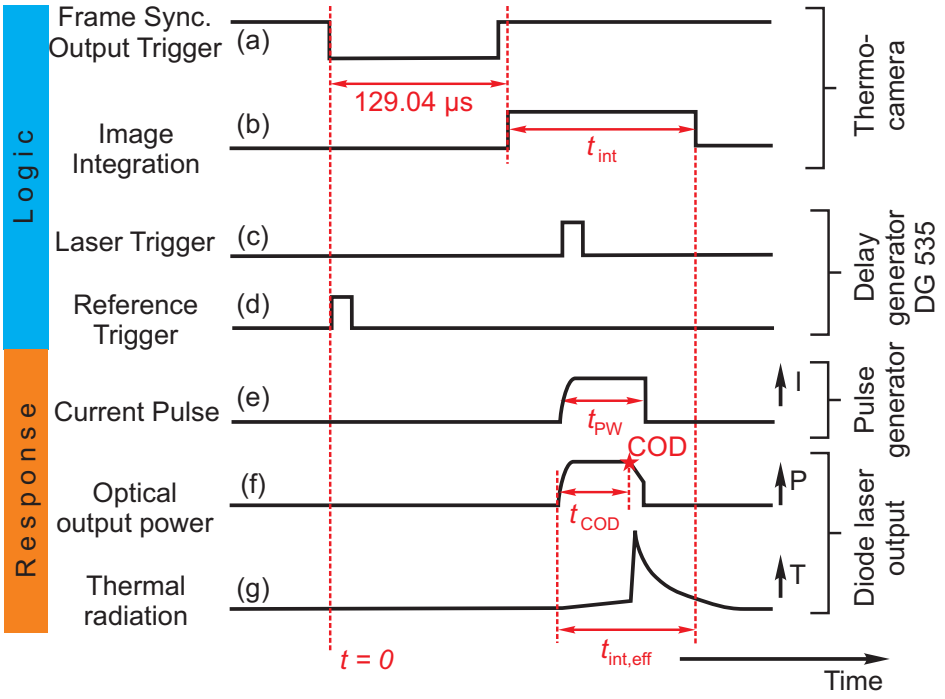

Figure 3.3: Thermocamera setup – basic timing diagram. The trigger signals (a-d) are given, labeled as 'Logic'. The ordinate represents a logic level, e.g., in case of (c,d) TTL signals. The frame synchronous output trigger (a) is provided from the thermocamera. It has a fixed relation to the leading edge of the image integration window (t_{int}) (b). The delay generator DG535 is triggered by the negative slope of (a) and provides a delayed laser trigger (c) and a delay-free reference trigger (d). The response to the trigger signal is shown in (e-g). (e) The current pulse delivered by the pulse generator; the ordinate gives the current. The length of the pulse defines the pulse width (t_{PW}). (f) The optical power output (ordinate) in case of COD occurrence (marked by the star; after time t_{COD}). (g) Temporal evolution of the thermal radiation; the ordinate gives the temperature at the COD site. The effective integration time ($t_{int,eff}$) starts with the leading edge of the current pulse. The indicated time intervals will be discussed in the text. All graphs are aligned in time, as indicated at the bottom. The corresponding devices are given at the right side.

For every delay interval, the single pulse emission was recorded with the thermocamera and integrated over all pixels. Due to the short duration of the laser pulse, compared to the integration window, a mathematical deconvolution of the data sets was proven to be unnecessary.

First, it was checked if the nominal integration times are in agreement with the real ones. The result for four different values is given in Fig. 3.4. Beside the nominal integration times of $t_{int,nom} = 10\,\mu$s, $40\,\mu$s, and $100\,\mu$s, the camera manufacturer provides a setting called '$0\,\mu$s'. Its meaning becomes clear in Fig. 3.4. The integration time can be set in steps of $10\,\mu$s, representing the interval between the leading and trailing edge of the integration window. In case of $t_{int,nom}$ ='$0\,\mu$s', the window consists only of leading and trailing edge without any delay in between.

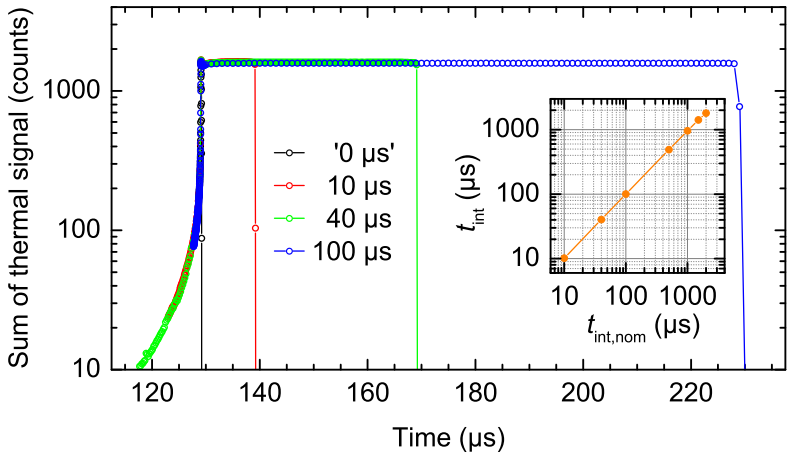

Figure 3.4: Thermocamera integration windows. Sum of thermal signal over time. The time reference is the negative slope of the signal shown in Fig. 3.3(a). The inset shows the relation between nominal integration time $t_{\mathrm{int,nom}}$ and measured integration time t_{int}.

By taking data for different integration times, the relation between the set value $t_{\mathrm{int,nom}}$ and the real window t_{int} was verified to be linear, see inset in Fig. 3.4.

It is obvious, that there is a deviation from a rectangular shape of the camera integration window around its leading edge, see Fig. 3.4 ($\approx 115\,\mu\mathrm{s} - 130\,\mu\mathrm{s}$). This deviation is negligible for integration times of $\geq 10\,\mu\mathrm{s}$. However, it is worth to take a closer look at this interval for two reasons:

- to check the temporal stability of the position of the beginning of the integration window, and
- to characterize the camera integration in case of $t_{\mathrm{int,nom}} =$'$0\,\mu$s'.

Figure 3.5 shows the leading edge of the integration window on an expanded scale. In order to check the trigger stability not only for different $t_{\mathrm{int,nom}}$ values, but also for independent runs, the measurements for $t_{\mathrm{int,nom}} =$'0' μs and $10\,\mu$s were repeated on another day. The curves of Fig. 3.5 are labeled with 'day 1' and 'day 2' (the remaining curves are taken on day 1).

The result is, that the leading edge of the integration window[2] is always at $(129.040 \pm 0.008)\,\mu$s. The jitter of the signal of 8 ns is thereby mainly caused by the laser current pulse generator. Moreover, the full width at half maximum (FWHM) of the '0' μs integration window has a value of 130 ns. Here, the leading tail of the curve ($< 129.04\,\mu$s) is relevant in contrast to the longer integration times. For practical measurements, a more realistic value of 460 ns is derived, considering the areas under the curve.

The problem with the use of such short integration times is the small number of photons contributing to the signal. As long as the NETD is dominated by thermal and shot noise, it scales in accordance with the integration time. Following this scaling, Tab. 3.1 gives an impression of the NETD-values (based on the given value for $t_{\mathrm{int}} = 1$ ms). However, these values are valid for the average temperature of the area that is detected by one camera pixel and has to be scaled accordingly if the heat source becomes smaller.

[2] It is the time, where the signal reaches the half of the value of the constant plateau that starts at $\approx 129.3\,\mu$s.

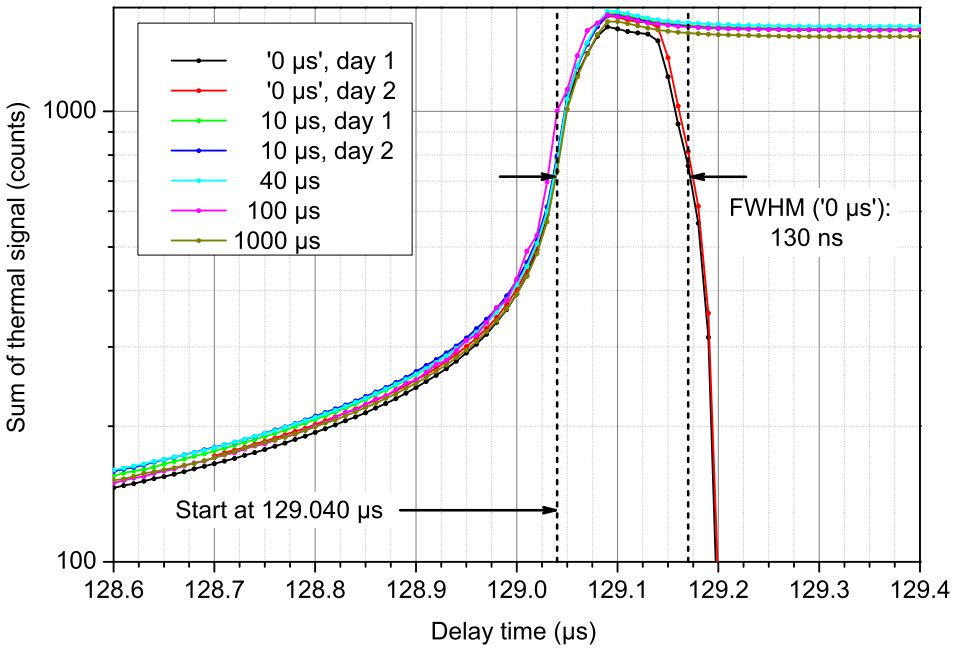

Figure 3.5: Leading pulse edge of data as shown in Fig. 3.4 on an enlarged scale.

t_{int} (μs)	0.46	10	40	100	1000	2000
NETD (K)	≈ 44.00	2.00	0.50	0.20	0.02	0.01

Table 3.1: NETD values for different t_{int}.

3.1.4 Basic Image Processing

In this subsection, two basic image processing steps for the thermal images will be introduced. An advantage of the Thermosensorik CMT384 camera is that it records the raw count rates for each pixel and, thus, gives complete control over the image processing. One has to take into account that the dark level of each pixel in the array differs. This is no problem as long as the count rate has the same linear slope independent of the zero level. However, this calls for taking a reference picture to correct for the offset.

During each measurement campaign an image with long integration time, i.e., in the millisecond range, is taken. This gives information about the geometry. During a long t_{int} a contrast between different emissivities of the materials can be detected, even if they have the same temperature. An example is given in Fig. 3.6(a-c). Figure 3.6(a) represents an image of the raw absolute pixel counts. Figure 3.6(b) is an image of an uniform area with constant temperature introduced between the object and the lens of the thermocamera, taken with the same t_{int} as used for (a). These two images were taken with a temporal delay of just seconds. By taking the difference of (a) and (b) one gets image (c), where the discussed individual pixel-offset is corrected. In Fig. 3.6(c) one can clearly identify the geometric structure of the device, with the bond wires (marked by 'A', one of the wires is additional indicated by a dashed line), the DL chip ('B') and the sub-mount ('C').

The flash of Planck's radiation that is indicative for a COD event is recorded with much shorter t_{int} of usually $10\,\mu$s. The detection of an emissivity contrast additional to the thermal flash is not possible under such conditions. However, the pixel-offset has to be taken into account, too. Therefore, an image of the unpowered device is taken immediately before the single pulse experiment. Both images were subtracted, Figs. 3.6(d) and (e). This leads to an image that reflects temperature differences, see Fig. 3.6(f). Notice, that also negative count rates around the zero line can appear, caused by this image subtraction.

In a last processing step, the two images, one giving the geometry [Fig. 3.6(e)], and one indicating the position of the COD event [Fig. 3.6(f)] can be composed, as long as the device is not moved between the image acquisitions. A threshold count-rate is chosen up to which the image (f) is set transparent, i.e., removing the parts of the image that have not changed its temperature during the single pulse. Afterwards, it is overlaid to the background image. In order to distinguish between the data recorded with different t_{int}, the background is given in grayscale, while the thermal flash is represented in colorscale, see Fig. 3.6(g).

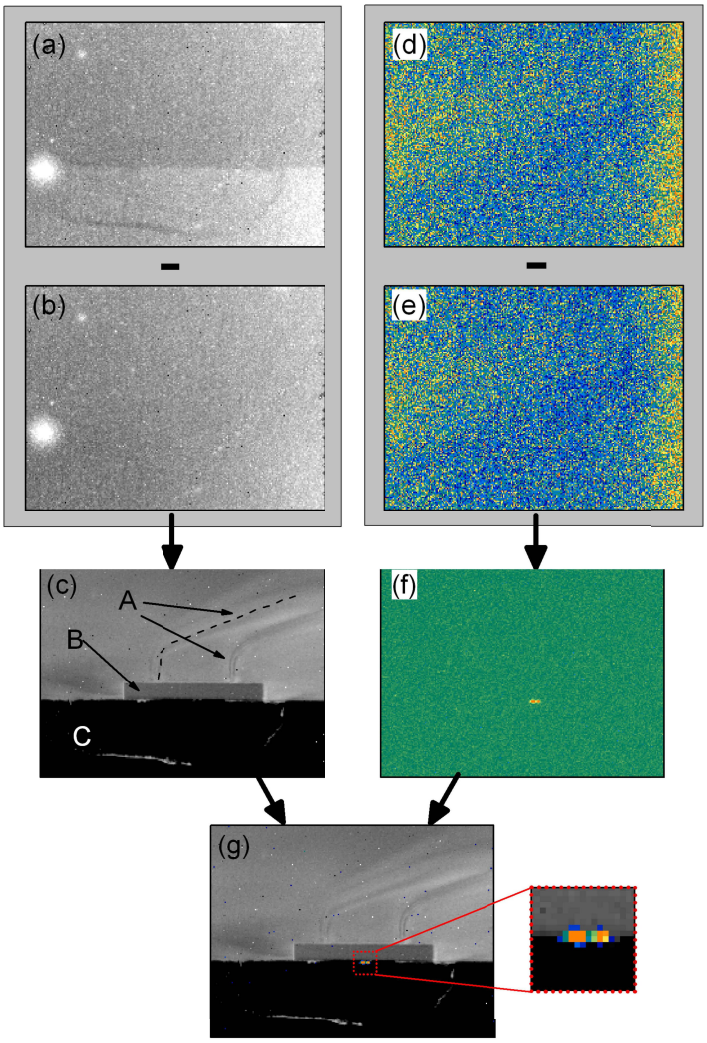

Figure 3.6: Basic image processing of thermal images. As an example the direct observation of a DLs' front facet is shown. (a) Raw image of absolute count rates of each pixel. The image is taken with $t_{\mathrm{int}} = 1\,\mathrm{ms}$. (b) Image of an uniform plane of constant temperature taken with $t_{\mathrm{int}} = 1\,\mathrm{ms}$. (c) Result of the subtraction of (b) from (a). The labeled objects are: bond wires (marked by 'A', one of the wires is additional indicated by a dashed line), the DL chip ('B') and the sub-mount ('C'). (d) Raw image taken during a COD event with $t_{\mathrm{int}} = 10\,\mu\mathrm{s}$. (e) Reference image taken of the un-powered device with $t_{\mathrm{int}} = 10\,\mu\mathrm{s}$. (f) Result of the subtraction of (e) from (d). (g) Composition of the images in (c) and (f). The area marked red is shown on an enlarged scale at the right side.

3.2 Streak Camera Based Setups

There are two reasons to use a streak camera for the present study:

- A temporal resolution of a line image in the picosecond time range, and
- continuous image-acquisition without any dead times.

The basic working principle of the camera is the following: Light enters the lateral entrance slit in front of the streak-tube. At the cathode, it is converted by the external photoelectric effect to a number of electrons according to light intensity. The electrons are accelerated in an electric field. They get deflected by a time-dependent electric field perpendicular to their flight direction and perpendicular to the lateral direction. This gives the temporal resolution while keeping the information about the lateral position at least in one dimension. Temporally dispensed this way, the electrons enter a multi-channel plate electron-multiplier. The resulting bunches of electrons hit a phosphor screen. The image visible on this screen is recorded by a CCD camera.

The experiments presented in this work used the Hamamatsu C1587 streak camera (with single sweep module M1953) to monitor the lateral intensity distribution of the lasing nearfield (NF) of the device. The DL was mounted on a heat sink and directly attached as close as possible to the used pulse driver Picolas LDP-V50-100 V3 to reduce the current rise time. In dependence on the width of the emitter, a microscope objective with appropriate magnification was chosen to image the NF onto the lateral entrance slit of the camera, see Fig. 3.7. In case of a multi-emitter device, e.g., an laser array, a simplified setup with a single lens was chosen. Two different streak-tubes were used, a S-1 tube which is infrared-enhanced (280 μm-1550 μm) and a S-20 one (200 μm-900 μm, higher sensitivity compared to S-1 in this range).

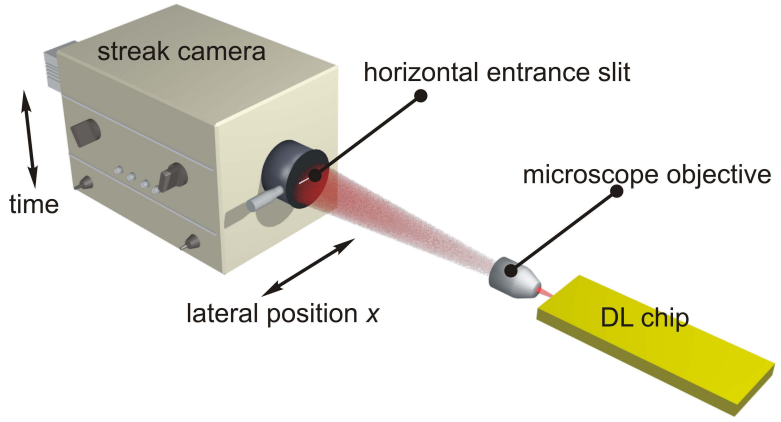

Figure 3.7: Scheme of the streak camera based setup.

3.3 The Step Test Approach

The concept of a step test, used in most of the presented experiments, is explained by the flow chart scheme shown in Fig. 3.8. The measurement is started by applying a short single pulse (in the range of $t_{PW} = 1\,\mu s$) with current I_0 to the device. This current is significantly below the COD threshold I_{COD} for the used pulse length. During this single pulse experiment, the desired device data are recorded, e.g., a thermal image, the lasing NF and/or the integrated optical output power, and additionally the current passing the laser is monitored. To check if there occurred any (even small) degradation, a *test pulse* with I_0 is applied and the data are compared to those recorded under same conditions at the beginning of the test cycle. If a clear sign for a COD event is detected, the test can either be stopped to apply further analysis in an early damage stage or the COD can be re-ignited by a subsequent current pulse. If no COD has been detected, the current is increased by a small step ΔI for the next single pulse.

It is important to clarify, if the step test approach is able to address the same degradation mechanisms as cw tests. It will be shown that this is indeed the case, based on the data analyzed in the following chapters. Therefore, the findings which are obtained with the step test, are of practical relevance for improving the device reliability in other operation regimes including cw. Moreover, the step test is considered a special type of accelerated aging. This issue will be addressed in Sec. 4.1.1.

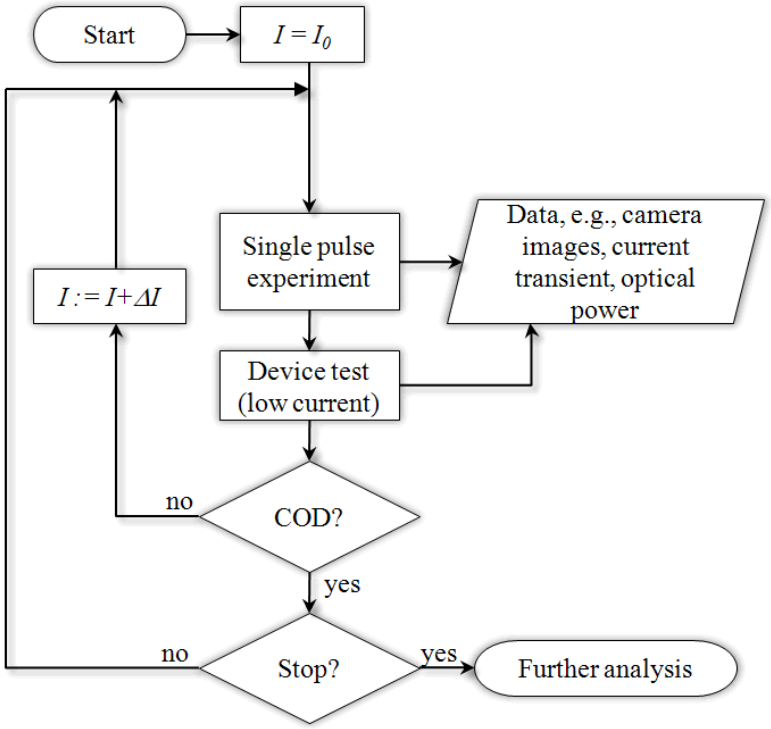

Figure 3.8: Scheme of device testing strategy denoted as *step test*.

3.4 Further Analytical Techniques

Complementary to the thermo- and streak camera measurements, the following methods were applied:

- The measurement of the L-I-V curve or L-I-V characteristic of the device gives the light output power and the voltage drop across the device in dependence on the applied current. The measurement is done in the cw regime with an integrating sphere.
- A fast inspection of the facet surface of the DL was performed by using a Leica DM4000 optical microscope. Moreover, the lasing NF (above I_{th}) and the electroluminescence (EL; below I_{th}) NF were imaged, while switching off the external illumination.
- Inspection of the geometry and surface morphology of the COD-related defects by scanning electron microscopy (SEM) using a JEOL JSM 8400F.
- The spectrum of the DL was measured with a SPEX 1250M monochromator using a 150 lines/mm grating which gives a spectral resolution of 0.2 nm. The system is equipped with a Princeton Instruments PIMAX-2: 1003 intensified CCD camera allowing an exposure time in the range down to 10 ns.

Moreover, the following in-house techniques were used:
The *photocurrent* (PC) *spectrum* of the unbiased device was obtained using a Bruker IFS66v Fourier-spectrometer equipped with a microscope at ambient temperature, as presented in Ref. [97]. PC generation involves two basic processes, namely absorption and electron-hole-pair generation on the one hand side, and carrier separation (transport) on the other hand. Thus, both mechanisms are probed in a PC measurement. This technique was used to analyze defect absorption and in this way the presence of defects.

For measuring the *laser beam-induced current* (LBIC), a laser beam was used to generate electron-hole-pairs. If they can be spatially separated by the pn-junction before they recombine, as necessary also in PC spectroscopy, one measures a current at the contacts of the device. The wavelength of the excitation laser can be chosen to be selective for a specific part of the device structure, e.g., the QW itself or defects, as demonstrated by Tien *et al.* [98]. Signals obtained with a wavelength in the band gap of bulk material or below the lowest quantum-confined transmission of the QW are defect related, as demonstrated by Ropers *et al.* [99]. In the presented experiments, this technique was used with a Nd:YAG laser emitting at 1064 nm providing 2 mW output power. The beam was focused to a spot with a full width at half maximum (FWHM) of $\approx 4\,\mu$m. The excitation was modulated with 454 Hz and the current response was detected by a lock-in amplifier. The sample was moved by a computer-controlled 2-axis stage, so that a 2-dimensional LBIC map was generated at a fixed focus plane, e.g., the QW plane.

Micro-Raman spectroscopy was used to determine the surface temperature of the front facet region. A SI TriVista TR 557 spectrometer was used. Typical measurement times for a single spectrum were on the order of 100 s. For excitation, a 442 nm HeCd laser was used, with $\approx 800\,\mu$W focused down to $\approx 1\,\mu$m. Due to the strong absorption at this wavelength in the material, the measurement depth was below 100 nm. The temperature was determined by two approaches from the resulting Raman-spectrum: (i) The intensity ratio of Stokes and anti-Stokes lines of the GaAs-like transverse optical phonon mode, as shown by Epperlein *et al.* [100]. The temperature dependence results from the fact that the envelope

for these peaks is given by the Bose-Einstein statistics. (ii) The phonon frequency is also determined by the temperature dependent lattice constant. The peak position of the Stokes or anti-Stokes lines is used as temperature measure. However, a temperature change may also result in strain of the semiconductor, which additionally changes the phonon energy. A cross check of both methods was made, because they rely on different mechanisms. In the presented experiments, the second approach was applied and cross-checked. Both methods need a calibration which was achieved by stabilizing the entire sample on different temperatures and taking Raman spectra.

In cooperation with external partners, the following measurement techniques were applied:
Measurements of *electron beam-induced currents* (EBIC) were carried out in collaboration with the *GdS Optronlab* at the *Universidad de Valladolid*, Spain. This method is similar to LBIC. Instead of a laser beam, an electron beam generates the electron-hole pairs here. EBIC was performed in a field emission scanning electron microscope (FESEM-Carl Zeiss LEO 1530), with a typical e-beam acceleration voltage of 30 kV, and the EBIC signal was collected with a low-noise current amplifier (FEMTO Messtechnik GmbH model DLPCA-200). This system was used in case of p-up mounted samples with a thin top-contact metallization of ≈ 400 nm. It allowed the electron beam to well penetrate across the metallization and the laser structure and allowed a sufficient electron-hole-generation at the position of the pn-junction to image the defective region. If the pn-junction is impaired, the carrier pair cannot be separated at this location. Therefore, no EBIC signal is obtained and the EBIC map shows a dark region at this location. The spatial resolution in the QW plane was analyzed with the help of the software CASINO (Version 2.4.8; Ref. [101]) and estimated to be 1.3 μm (width of Gaussian fit to distribution of deposed energy in QW plane).

In order to image defect regions, a number of samples were opened and investigated by plane view *cathodoluminescence* (CL). This work was done at the *Ferdinand-Braun-Institut für Höchstfrequenztechnik* Berlin, Germany. During the preparation, the top-contact of the p-down mounted samples and partly the GaAs substrate were removed by mechanical grinding. The remaining substrate was removed by selective etching. The prepared sample was introduced into a SEM system and cooled down to 80 K. The QW plane of the sample was mapped by an electron beam with an acceleration voltage of 20 kV and a beam current of 10 nA. The light that is produced by radiative recombination of electron-hole-pairs forms the detected CL signal. Areas of non-radiative recombination appear dark in the obtained CL map, indicating regions where the QW is damaged.

A similar sample preparation as used for CL was done at the *Fraunhofer Institut für Angewandte Festkörperphysik* Freiburg, Germany. These samples were inspected by *micro-photoluminescence* (μPL) mapping[3] while exciting the QW luminescence, details are given by Baeumler *et al.* [102]. The optical excitation energy was above the lowest QW transition. In the defect free case, radiative recombination is likely and the emitted light is detected. In case of the presence of defect levels (impaired QW), non-radiative recombination dominates and the detected photoluminescence-light-intensity at this positions is reduced.

[3] This means a pointwise measurement which eventually forms the image.

Defect analysis with *high resolution microscopy* was performed in collaboration with the *EMPA Swiss Federal Laboratories for Materials Science and Technology* in Dübendorf, Switzerland and the *Interdisziplinäres Zentrum für Materialwissenschaften* at the *Martin-Luther-Universität Halle-Wittenberg*, Germany. In order to allow defect inspection, the devices were prepared in cross section by *focused ion beam* (FIB) preparation. Details about this preparation technique are given by Wirth [103]. A FEI Strata 235 Dual Beam Ga-FIB was used. This system consists of a SEM operating at a maximum of 30 kV and a Ga-FIB operating at 30 kV. The two columns are combined in a cross angle of 52°. The SEM allows for non-destructive inspection during the FIB cut.

High resolution images were taken by an ORION Helium Ion Microscope from Carl Zeiss (henceforth referred to as 'He-microscope') at cross-sections prepared by FIB. The resolution improvement of this technique compared to SEM is discussed by Ramachandra *et al.* [104]. The imaging process is comparable to that in a SEM, the detected signal consists of secondary electrons excited from the material. The advantage of using ions to release the secondary electrons is the higher rate of energy transfer which results in the secondary electron generation close to the point where the ions hit the material. Moreover, the cleaning and inspection of the cross section is done *in-situ* during the image acquisition by the ions. The He-microscope used for the present study is based on a He FIB and was operated with a beam current of 0.5 pA at 30 kV.

For transmission electron microscopy (TEM), a lamella of the defective region was prepared and thinned by FIB. For investigations in diffraction contrast, a JEM 4000 FX was used at an acceleration voltage of 200 kV. As overview of the defect, bright field images in multiple-beam orientation were recorded. The high-resolution TEM investigations were carried out using a JEM 4010 at an acceleration voltage of 400 kV. Energy dispersive X-ray (EDX) analysis were performed on a JEM 2200FS operating at 200 kV in scanning TEM mode.

3.5 Samples

Basic properties of the DL samples studied are given in Tab. 3.2, such as the emission wavelength λ_c, the material system of the QW, the geometry of the emitter stripe, I_{th}, and the slope efficiency η_d.

The DLs of batches A,B,F,G,H, and K are packed p-down, the remaining batches are processed with p-up packaging. The emitters have an anti-reflective front facet coating ($\approx 1-5\%$ reflectivity) and a high-reflective rear-facet coating ($\approx 99\%$), except of batches F and K which are uncoated. The active region of batch D is formed by a double-QW, the remaining QW DLs are based on a single-QW.

A special sample set is formed by the devices of batches C, D, and E. Figure 3.9 depicts the epitaxial layer sequences. Two structures C and D have an Al-free active region with GaInAsP barriers. Structures C and E contain a symmetric GaInAsP single QW, whereas structure D has an asymmetric GaInAs double QW. In all devices the claddings are made of AlGaAs, in the case of the double QW the Al content on each side of the QW differs to push the mode apart from p-type material. The facets of all devices are treated in exactly the same manner and the same mounting technology is used to guarantee highest-possible comparability. Therefore, this sample set is suitable for comparing different device architectures of DLs lasing at the same wavelength.

Batch	λ_c (nm)	Material	Emitter stripe (μm) Width	Length	I_{th} (A)	η_d (W/A)	Ref.
A	808	GaAs/AlGaAs	50	1400	0.21 ± 0.01	1.19 ± 0.01	[105]
B	980	GaInAs/AlGaAs	100	1400	0.224 ± 0.003	1.16 ± 0.01	
C	975	GaInAs/GaInAsP	100	2000	0.29 ± 0.01	0.59 ± 0.01	[106]
D	975	GaInAs/GaInAsP	100	2000	0.56 ± 0.01	0.60 ± 0.01	[106]
E	975	GaInAs/AlGaAs	100	2000	0.26 ± 0.01	0.62 ± 0.01	[106]
F	780	GaAsP/GaInP	100	2000	0.88 ± 0.02	0.45 ± 0.02	
G	650	InGaP/AlGaInP	100	1200	0.42 ± 0.06	0.95 ± 0.05	[107]
H	808	InGaP/AlGaAs	$19 \times 100^*$	1500	5.6 ± 0.1	1.1 ± 0.1	[108]
J	980	InGaAs/AlGaAs	3 to 8^{**}	3900	0.075 ± 0.005	0.94 ± 0.01	[109]
K	724	InP/(Al)GaInP QD	100	1500	2.7 ± 0.5	–	[110]

Table 3.2: Basic properties of the used DLs (λ_c: emission wavelength; I_{th}: threshold current; η_d: slope efficiency). * Laser array with 19 emitters and a pitch of 500 μm. ** Tapered ridge waveguide, emitter width changes continuously from 3 μm at the rear facet to 8 μm at the front.

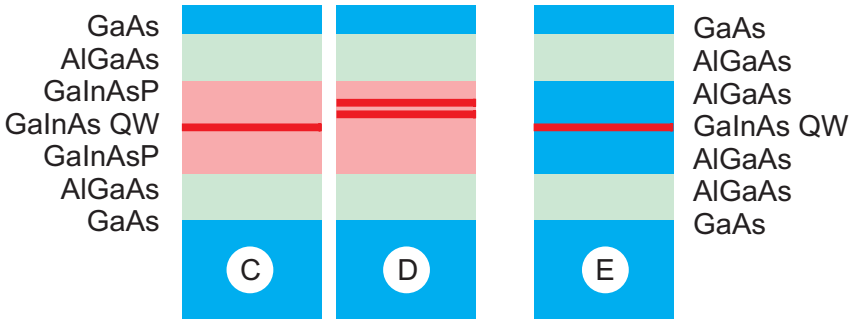

Figure 3.9: Layer schemes of the investigated structures C,D, and E.

All these devices were pre-characterized by measuring the L-I-V curves and inspecting the facets under the light microscope. During the step test, one additionally obtains the pulsed L-I curves describing the DL behavior at power levels reachable in pulse operation only. An example from batch A is shown in Fig. 3.10 (device A_{14}).

At this point it is worthwhile to address the mechanisms that lead to the output power saturation, which is typical for the pulsed L-I curves, such as the one in Fig. 3.10. A detailed discussion of the physical mechanisms is given by Wenzel *et al.* [5] and Wang *et al.* [111]. For cw operation, they identify the ohmic heating of the active region, which consumes about 25% (around I_{th}) up to more than 50% (for $I \gg I_{th}$) of the electric energy used to drive the device, as origin for the power saturation. Additionally, carrier leakage over the potential barrier formed by the hetero-structure is identified to be a limiting factor by Pietrzak *et al.* [112]. The ohmic heating is mostly excluded by operating the device with short current pulses in the nanosecond to microsecond range.

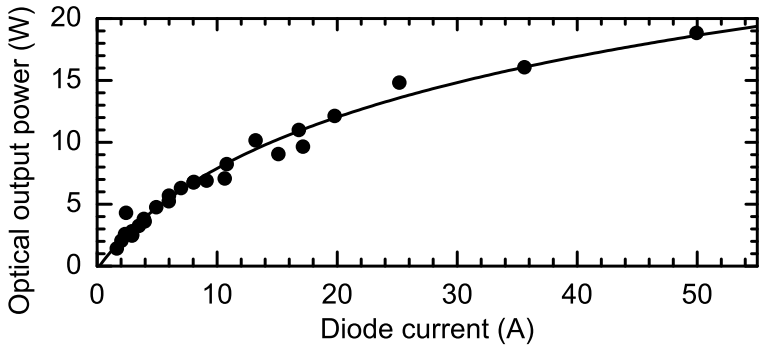

Figure 3.10: Pulsed L-I curve of batch A (device A_{14}); single pulses with $t_{PW} = 1\,\mu$s. The line represents a logarithmic fit to the data.

Under pulsed operation, saturation can be observed also at higher output powers compared to cw (Fig. 3.10). For this operation regime, a main limitation is given by the finite carrier capture time from waveguide to active region, according to Slipchenko *et al.* [113]. They have shown that this is mainly a problem of the finite intraband relaxation time. This leads to an accumulation of charge carriers at higher energies, making their escape from the hetero-barrier more likely. Furthermore, the longitudinal spatial hole-burning results in a reduced gain, which is a result of the standing wave in the resonator reducing the carrier concentration particularly around their maxima. As measured by Rinner *et al.* [114], the longitudinal spatial hole-burning affects also the carrier concentration in a way that it is reduced near the anti-reflective coated front facet and enhanced near the high-reflective rear facet. The effect of the inhomogeneous carrier concentration along the laser stripe will be discussed in Sec. 4.2.4. Moreover, at high bias operation, higher order transversal (y-direction) modes can appear leading to a higher absorption by shifting the intensity maxima towards the edge of the waveguide. Additionally, lateral anti-waveguiding effects due to the lateral carrier concentration profile [and therefore a change of the refractive index (n)] have influence on the optical output power, as discussed by Crump *et al.* [115].

4 First Phase of COD – Aging

In order to outline the COD kinetics, the process is sub-divided into three phases [58]:

(i) During the *first phase*, the future COD site heats up and eventually reaches T_{crit}. This is achieved by long time aging (on the time scale of up to years) or by an accelerated aging using high current single pulses. The latter reduces the duration of the first phase to a couple of nanoseconds.

(ii) The thermal runaway is the *second phase*. It involves the fast temperature rise by closing the positive feedback loops. A small volume is heated up to the materials' melting point. The further defect extension starts after this initial defect site has been created.

(iii) In the *third phase*, the defect site develops to macroscopic size. Its further growth is fed by energy from the light field.

The temperature dynamics are shown in Fig. 4.1 for these three phases. Furthermore, the typical duration of each phase is given. These phases will be discussed in detail in the following chapters. In this way, the analysis of COD follows its temporal dynamics.

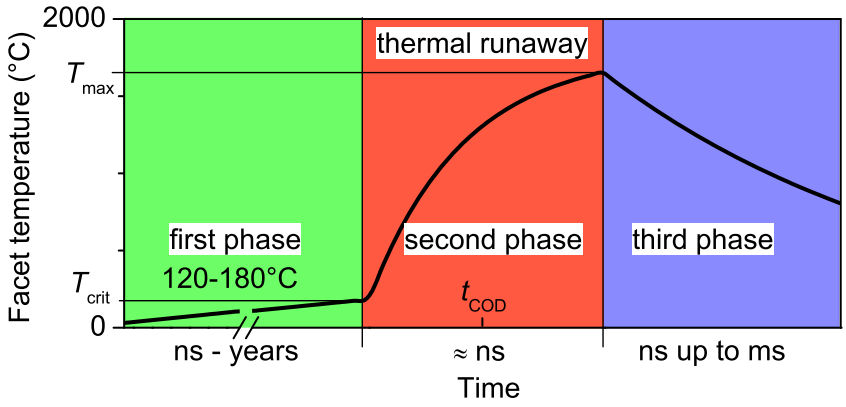

Figure 4.1: COD Phases. The temperature evolution is shown during the three COD phases. The typical duration of each phase is given. The values for T_{crit} and T_{max} will be discussed in the following chapters.

4.1 Experimental Results

4.1.1 Spatially Integrated Transient Data and Thermography

A crucial point in COD experiments is the detection of the event itself. Since COD is related to a drop in optical output power and a flash of Planck's radiation, a thermocamera and in parallel a fast PD monitoring the integrated output power are used to detect the COD event. Results are presented in Fig. 4.2. In these experiments, a simplified version of the step test approach was used [116, 117]. The current I_0 was above I_{COD} for the given t_{PW}, i.e., the step test scheme is reduced to a single pulse [116]. Results for devices A_{14}-A_{17} of batch A are shown. The first (left) column, sub-figures 4.2(a,e,i), gives the situation where no COD occurs, i.e., $I < I_{COD}$. The remaining columns represent cases where $I > I_{COD}$.

The first row, Figs. 4.2(a-d), gives current traces for the devices. They verify a sufficiently short current rise time, i.e., the current reached its designated level before COD sets in. Furthermore, the current keeps at this level without showing any features like dips or peaks.

The second row, Figs. 4.2(e-h), gives the transients of the PD during the pulse. While no power drop is visible in Fig. 4.2(e), clearly visible ones in (f)-(h) indicate the sudden device degradation by COD, additionally marked by arrows.

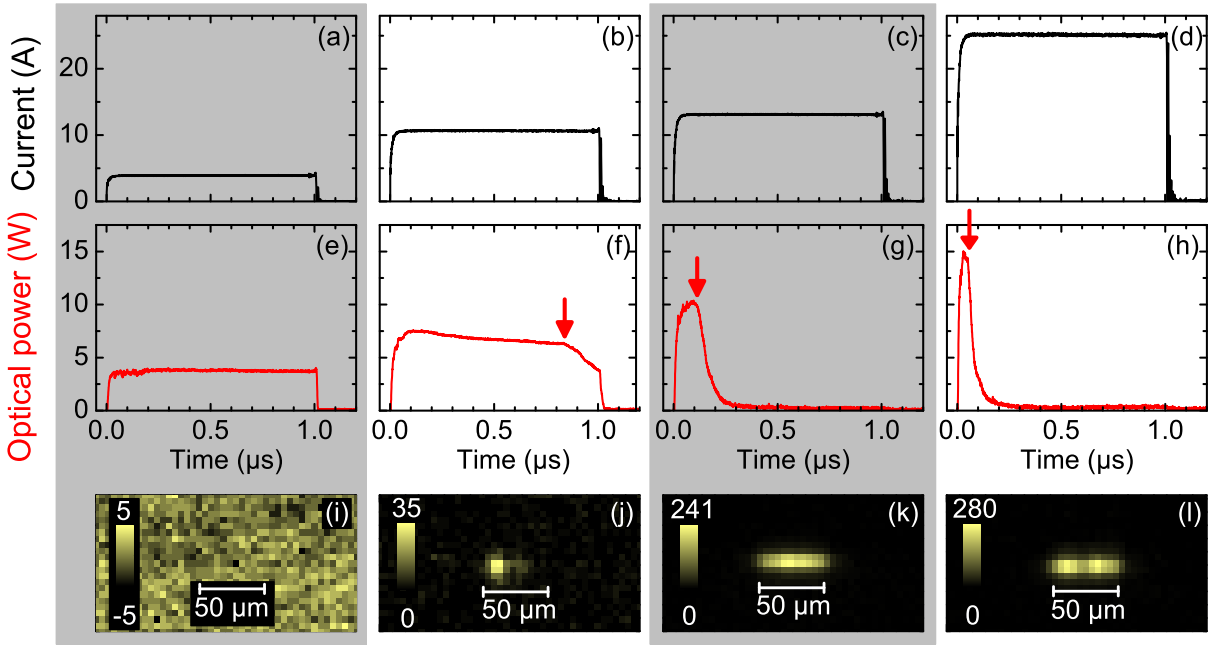

Figure 4.2: Results obtained in single pulse experiments with devices of batch A [A_{14}(a), A_{15}(b), A_{16}(c), A_{17}(d)]. (a)-(d) DL current as function of time. (e)-(h) Optical output power as function of time. The onset of COD at t_{COD} is marked by arrows. (i)-(l) Thermal images recorded during the single pulses. The magnitude of the thermal signal is given in counts. Notice, that the three figures in each column belong to the same single pulse experiment and device, e.g., (a)+(e)+(i). The heat sink temperature was always thermo-electrically stabilized to $(23.0 \pm 0.2)^{\circ}$C.

The third row, Figs. 4.2(i-l), gives thermal images (CEDIP thermocamera, $t_{\mathrm{int}} = 8\,\mu$s, $t_{\mathrm{int,eff}} \approx 4\,\mu$s) of the region around the front facet. Thermal backgrounds, recorded before the pulse was applied, have been subtracted. The detection of a thermal flash and the sudden drop in optical output power are correlated one-to-one. Furthermore, an inspection of the front facet by optical microscopy after these experiments confirms this behavior, by revealing surface damage typical for COD.

This approach allows to determine the time when the thermal runaway, the second phase of COD, starts and makes it possible to categorize experimental findings following the scheme of the three phases.

As discussed, the occurrence of COD is closely connected to the presence of a high temperature seen as signal detected by the thermocamera. Therefore, it is straightforward to investigate the dependence of the COD threshold on the heat sink temperature (T_{hs}). Devices from batch A were investigated using the step test approach with $t_{\mathrm{PW}} = 1\,\mu$s and $\Delta I = 0.5\,$A. The COD was detected by the power drop during the pulse and in the test pulse. Furthermore, a local drop of the lasing NF amplitude was detected with a streak camera based setup. T_{hs} is thermo-electrically stabilized to values between $(20.0 \pm 0.2)^{\circ}$C and $(101.6 \pm 0.2)^{\circ}$C (in particular: device A_{18} at 20.0°C, A_{19} at 40.5°C, A_{20} at 60.5°C, A_{21} at 101.6°C).

The result is shown in Fig. 4.3, where the average optical output power during the pulse is plotted versus the driving current. The one-by-one correlation of power drop and device degradation by COD is confirmed by the evaluation of the NF data. This data will be discussed in detail in Ch. 5. Here, however, the COD threshold is of interest for investigating the influence of T_{hs} during device aging. For clarity, the respective I_{COD} values are indicated by vertical dashed lines. Comparable results have been obtained for red emitting lasers ($\lambda_{\mathrm{c}} \approx 650\,$nm) under cw conditions by Bou Sanayeh *et al.* [107]. Obviously, the optical output power is significantly reduced for temperatures above ambient temperature at a fixed current and I_{COD} increases with the heat sink temperature.

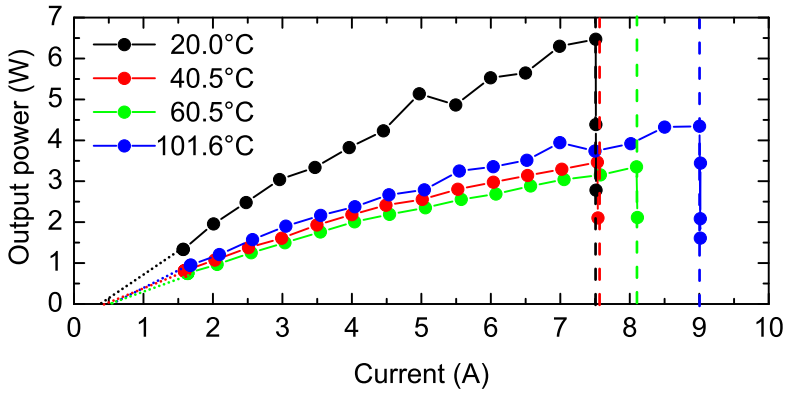

Figure 4.3: Optical output power evolution during step tests for different values of T_{hs} (device A_{18} at $T_{\mathrm{hs}} = 20.0^{\circ}$C, A_{19} at 40.5°C, A_{20} at 60.5°C, A_{21} at 101.6°C, and all with $t_{\mathrm{PW}} = 1\,\mu$s). The respective I_{COD} values are indicated by dashed vertical lines.

4.1.2 Spatially and Temporally Resolved Data

In order to temporally and spatially resolve the NF in the picosecond time range, the streak camera setup was chosen [118–120]. As an example for a typical gain-guided device structure, devices from batch A were used. The NF was imaged by a 25× microscope objective to the horizontal entrance slit of the streak camera system. In an updated version of the setup, an optical microscope with 50× objective was used. The experiments followed the step test approach. A t_{PW} value of either 300 ns or 1000 ns was used. The starting current was $I_0 = 2\,\mathrm{A}$ and the current step $\Delta I = 0.5\,\mathrm{A}$. The currents were kept below COD threshold. The situation where I_{COD} was reached will be addressed separately in Ch. 5.

Figure 4.4 shows the NF evolution during 300 ns long single pulses for device A_1. The behavior is typical for the investigated batch of devices and also found in reference samples which are purely gain-guided, but emit at $\lambda_c = 975\,\mathrm{nm}$. The data for three different driving currents are shown in the three rows of Fig. 4.4. These currents are $I = 6.0\,\mathrm{A}$ (representing approx. 29× the threshold current value), 7.5 A ($\approx 36 \times I_{th}$), and 8.5 A ($\approx 41 \times I_{th}$).

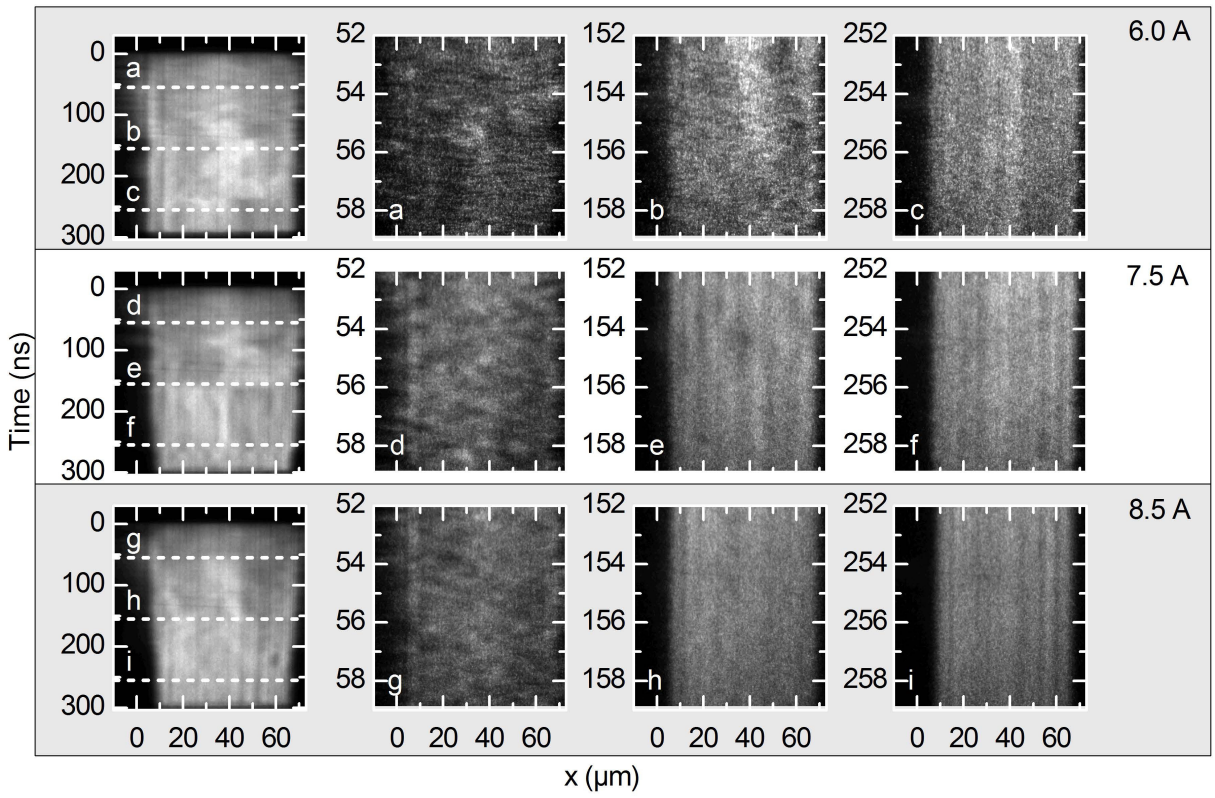

Figure 4.4: NF evolution of device A_1 during 300 ns long single pulses. The actual currents for each row are given at the right side. The left column gives overviews over the entire pulse, while the other images show the NF on an enlarged temporal scale at the positions indicated by dashed lines and letters. The heat sink temperature was always thermo-electrically stabilized to $(23.0 \pm 0.2)^\circ\mathrm{C}$. The NF intensity is represented in grayscale (dark $\widehat{=}$ low intensity; light $\widehat{=}$ high intensity).

The sub-figures in the left column give overviews over the entire 300 ns long single pulses with a temporal resolution of ≈ 680 ps per camera pixel. The behavior of subsequent pulses is well reproducible, so that images inside these pulses were taken on an expanded time scale. These images are shown in the remaining columns of Fig. 4.4. Their temporal resolution is ≈ 18 ps per camera pixel. The temporal position in the 300 ns pulses – shown as overview on the left side – is indicated by the dashed lines and the specific letters. The changes of the NF pattern and the decreasing overall NF width with increasing time and current are obvious. Closer to the leading pulse edge and especially for lower I, the NF patterns show distinctive spikes of higher intensity. In contrast, images recorded at later times and with higher current feature a stripe like pattern oriented along the time axis.

NFs of device A_1 at different times are shown in Fig. 4.5. Lateral cuts through the emission are given at $I = 8.5$ A, as shown in the bottom row of Fig. 4.4. The area under these curves is proportional to the optical output power of the DL. Results for this integration at different times along the pulse are summarized in the inset. The value stays almost constant although the NF pattern and width change significantly. If one compares this finding with spatially integrated measurements of the output power, the same result is obtained.

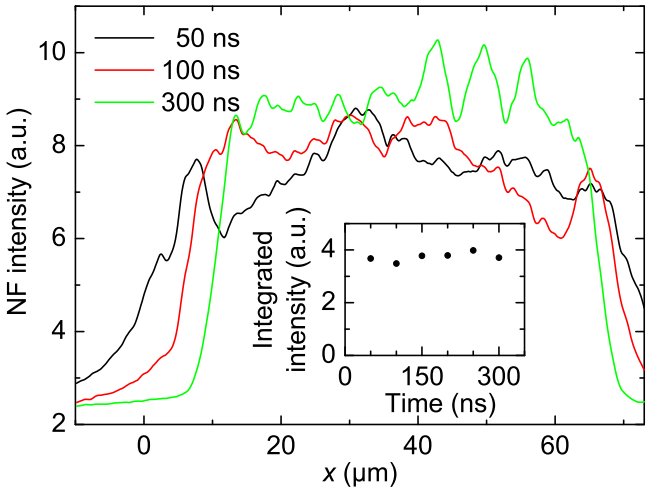

Figure 4.5: Lateral NF cuts of device A_1, averaged over ≈ 8 ns around the indicated time in a 300 ns pulse at $I = 8.5$ A. The inset gives the areas under the curves at different times. T_{hs} was thermo-electrically stabilized to (23.0 ± 0.2)°C.

A second example for this behavior is given in Fig. 4.6, showing data from device A_2. Figure 4.6(a) gives an overview of the NF of device A_2 during the entire 1 µs single pulse at $I = 4.5$ A. The decrease of the overall NF width saturates around 800 ns at a constant width, this approves the use of 300 ns long pulses in order to get a sufficient temporal resolution in the region of fastest NF dynamics. As for device A_1, cuts were taken along x at different times. They are presented in Fig. 4.6(b). This example is slightly different from the first one – which represents the majority of the batch. It shows a reduced intensity of laser emission at the left side (between 0 µm and 25 µm) during the first 300 ns of the pulse. Figure 4.6(c) verifies that the optical output power remains constant during the pulse in this case, too. The data points represent the area under the cuts, as in Fig. 4.5(inset). At this point, it is worthwhile to combine the main

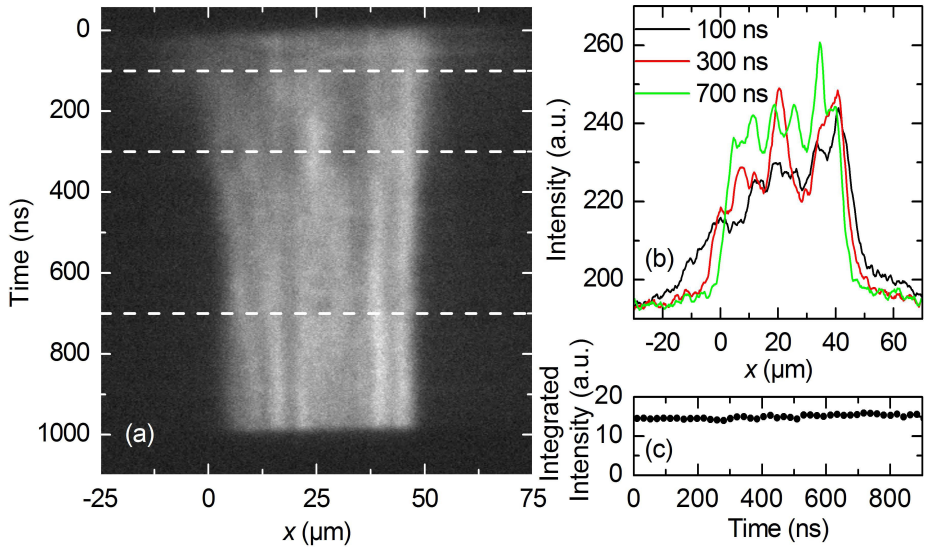

Figure 4.6: (a) NF evolution of device A_2 during a 1 μs long pulse at $I = 4.5$ A. (b) Cuts through the NF shown in sub-figure (a) at the given times (averaged over 8 ns). The temporal positions are additionally indicated in (a) by dashed lines. (c) Integrated area under curves as shown in sub-figure (b). T_{hs} was thermo-electrically stabilized to (23.0 ± 0.2)°C.

aspects of the preceding investigations. This means to address the question, how does T_{hs} influences the lasing NF. Therefore, the NF measurements with different currents were repeated, but additionally T_{hs} was varied. Figure 4.7 shows lasing NFs of the entire pulses of device A_{18} with $t_{PW} = 1\,\mu$s at currents between $I = 3.0$ A and 7.5 A and $T_{hs} = 20.0$°C. The NF for $I = 3.0$ A in Fig. 4.7(a) exhibits almost no decrease in its overall width. For higher currents as in Figs. 4.7(b-d) with 4.0 A, 5.0 A, and 7.5 A, respectively, the decrease of the NF width becomes obvious and also saturates at certain times; cf. also Fig. 4.6(a). The temporal position, where this period of constant width sets in, is marked by the dashed red line in Figs. 4.7(b-d) at $t \approx 980$ ns, 470 ns, and 260 ns, respectively.

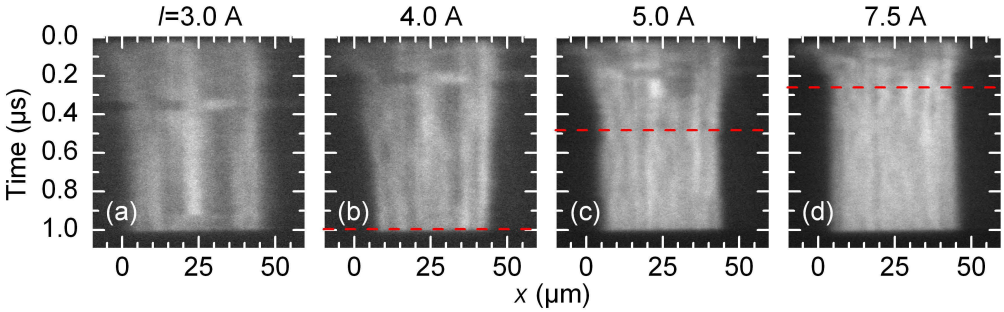

Figure 4.7: Lasing NFs of device A_{18} covering the entire pulse width of 1 μs length. The current is varied for the individual pulses, i.e., $I = 3.0$ A(a), $I = 4.0$ A(b), $I = 5.0$ A(c), and $I = 7.5$ A(d). The horizontal dashed red lines in (b-d) give the temporal position where the decrease of the NF width saturates. T_{hs} was thermo-electrically stabilized to (20.0 ± 0.2)°C.

Figure 4.8 shows the results obtained with the same setup for two different currents [$I = 5.0\,\mathrm{A}$ for (a-c) and $I = 7.5\,\mathrm{A}$ for (d-f)]. Furthermore, three different values for T_{hs} are applied, i.e., 20.0°C [device A_{18}; Figs. 4.8(a,d)], 60.5°C [device A_{20}; Figs. 4.8(b,e)], and 121.1°C [device A_{22}; Figs. 4.8(c,f)]. The details of the NF pattern differs slightly due to the fact that different devices were used. The dashed red lines, however, give the temporal position where the NF width saturates. The remarkable finding is that this time is almost independent from T_{hs}.

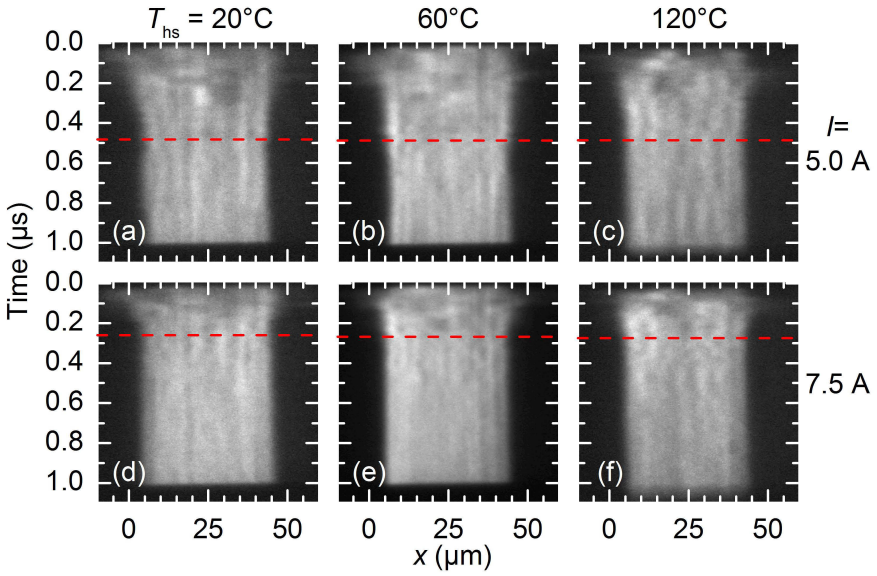

Figure 4.8: Lasing NFs are shown of devices A_{18} (a,d), A_{20} (b,e), and A_{22} (c,f) with $T_{\mathrm{hs}} = 20.0$°C, 60.5°C, and 121.1°C, respectively. The entire pulse width of $1\,\mu$s length is shown. The NFs at two different current settings are given, i.e., $I = 5.0\,\mathrm{A}$(a-c) and $I = 7.5\,\mathrm{A}$(d-f). The horizontal dashed red lines indicate the temporal position where the decrease of the NF width saturates.

4.1.3 Active Layer Temperature Transient

In order to determine the temperature transient of the active region during the current pulse, two independent methods were used. This allows for a cross-check of the results. The two temperature-dependent parameters that were monitored are:

- the spectral shift of the laser emission and
- the drop in optical output power.

The first method – the spectral shift – will be explained in the following. It is a result of the reduction of energy of the lowest QW confined transition due the band gap shrinkage with increasing temperatures. This behavior can be calculated following Allen and Cardona [121]. They take into account two main influences. One is the thermal expansion of the lattice which changes the lattice constant and therefore the energy gap. The second major contribution arises from electron-phonon interaction. The latter contribution consists of two effects which have typically opposite signs, i.e., a Debye-Waller term describing

the coherent electron scattering and a self energy term depending on atom displacement. Lourenço *et al.* [122] have shown that the consideration of these contributions is sufficient, even in the case of QWs. This is valid as long as the band gap shift in barrier and QW is almost similar, otherwise one has to consider the varied barrier height additionally, as discussed by Olkhovets *et al.* [123]. This *ansatz* is in need of fitting parameters from the experiment. In contrast, a first-principle study based on density functional theory calculation is possible as demonstrated by Liu *et al.* [124]. This approach, however, is only feasible for bulk material. The mean active region temperature transient can be determined by measuring the wavelength shift of the laser emission during a laser pulse. A calibration is, however, necessary to link both quantities.

Spectra of the laser emission of device A_3 each averaged over 10 ns were recorded along the 1 μs long laser pulse. The single spectra were recorded during successive pulses with a repetition rate of 1 Hz, to allow the DL to cool down to the heat sink temperature of $(23.0 \pm 0.2)^\circ$C. Each subsequent spectrum was recorded at a time shifted 10 ns towards the trailing edge of the pulse. Figure 4.9(a) shows the result in case of the pulse current fixed to $I = 7.0$ A.

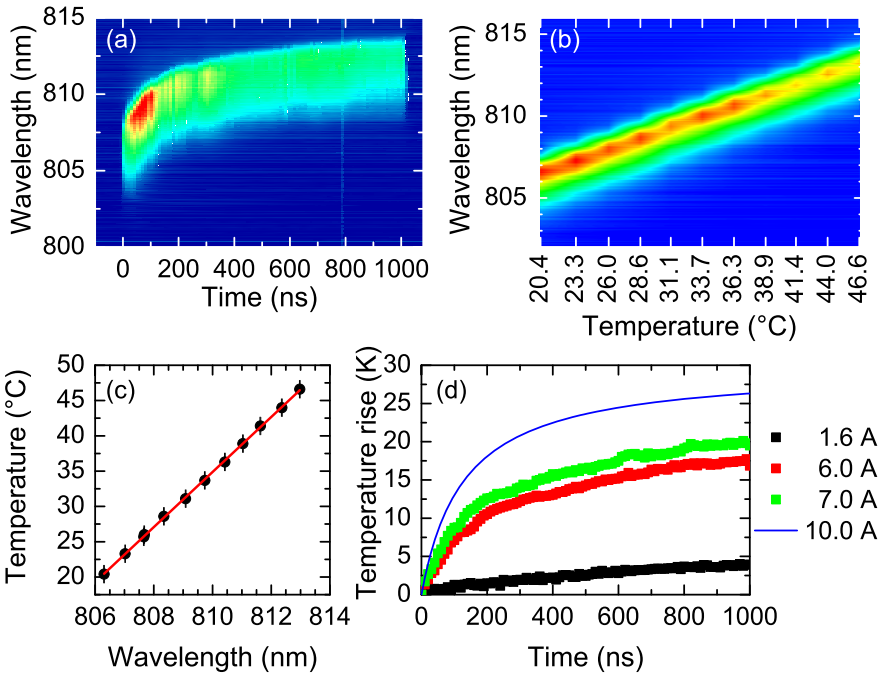

Figure 4.9: (a) Composition of measured spectra for device A_3 each averaged over 10 ns at $T_{hs} = 23.0^\circ$C. The spectra are recorded during successive pulses and each subsequent spectrum 10 ns later in the 1 μs long laser pulse, than the previous one. (b) Spectra for calibration, the entire laser structure is thermo-electrically heated to the given temperature. The emission intensity is color encoded in (a) and (b) from high intensity (red) to low intensity (blue). (c) The evaluation of the series of spectra shown in (b) gives an calibration between wavelength shift and average active region temperature. (d) Summarized results for the average active region temperature rise at $T_{hs} = 23.0^\circ$C as the result of the evaluation of measurements as shown in (a) for different currents. The curve for $I = 10$ A is extrapolated.

In order to extract the average active region temperature from this measured shift of the emission wavelength, a calibration is necessary. It was done by heating the entire structure to a specific temperature and recording a spectrum as close as possible to the leading edge of the laser pulse. This avoids active region heating additional to the one applied externally. In the actual case, the spectra were taken 20 ns after the leading pulse edge with an exposure time of 20 ns. An overview of the calibration spectra is given in Fig. 4.9(b). The extracted relation between wavelength of the emission peak and temperature is shown in Fig. 4.9(c). A linear fit of the data leads to a temperature rise per wavelength shift of (3.89 ± 0.03) K/nm. Using this and data as shown in Fig. 4.9(a), the time-resolved average active region temperature rise for different currents can be determined. The result of such an analysis is shown in Fig. 4.9(d), for $I = 1.6$ A, 6.0 A, and 7.0 A. The curve for 10 A is extrapolated. This current represents the typical I_{COD} value of batch A for the used t_{PW}.

The second method to determine the average active region temperature is related to the decrease of optical output power with increasing temperature. The L-I curves, as given in Fig. 4.10(a), show a decrease of the output power with time. A comparison of this power loss with L-I curves measured at different temperatures between 20°C and 50°C [Fig. 4.10(b)] allows for an estimate of the average temperature increase of the active region. The power drop in case of the investigated laser batch is rather small, cf. inset in Fig. 4.5 and Fig. 4.6(c). However, the collection of power traces recorded during the step tests, e.g., Fig. 4.10(a), allows an analysis by being sensitive to small deviations in the signal. The resulting average active region temperature increase in dependence on the drop in optical output power is given in Fig. 4.10(c).

Evaluating this for a pulse of $I = 10$ A after 1 μs, the result is a temperature increase of $\Delta T = (27 \pm 6)$ K. Comparing this with Fig. 4.9(d), which reveals $\Delta T \approx 26$ K for the same current and time, gives a good agreement of the results of both independent methods and verifies the identified temperatures.

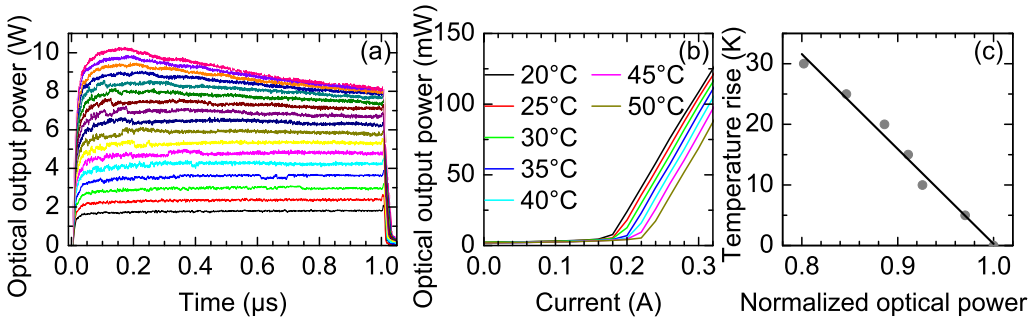

Figure 4.10: Determination of the average active region temperature from the change in optical output power during the single pulses for device batch A. (a) The temporal evolution of optical output power of successive single pulses during a step test (device A_{23}). The used currents ranging from $I = 1.6$ A in $\Delta I = 0.5$ A steps to $I = 9.6$ A from bottom to top trace. The power reduction with ongoing time is visible for higher currents. (b) Temperature dependent L-I curve measurement (device A_{24}). (c) Result of evaluation of the power drop shown in (a) with help of temperature dependent L-I curve (b). The curve gives the average active region temperature rise in dependence of the normalized drop in optical output power (compared to the peak power value that equals 1.0) for an ambient temperature of 23°C.

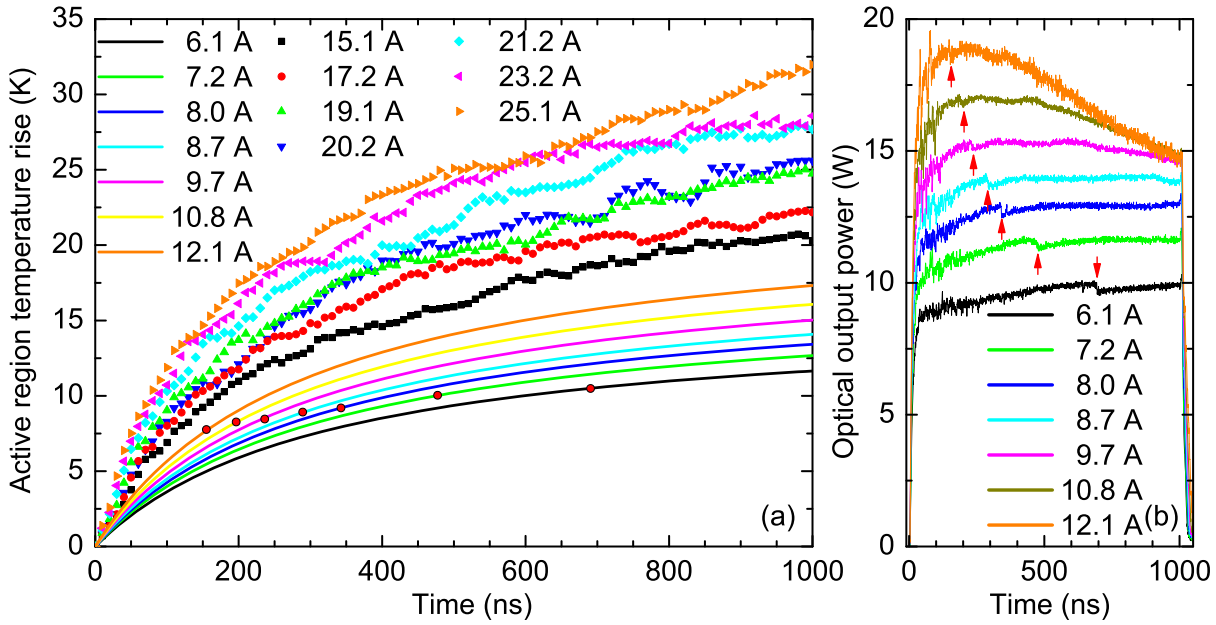

Figure 4.11: (a) Summarized results for the average active region temperature rise at $T_{\mathrm{hs}} = (23.0 \pm 0.2)^{\circ}\mathrm{C}$ as the result of spectral shift measurements as shown in Fig. 4.9 for different currents for device batch B (measured at device B_1). The curves for $I \leq 12.1\,\mathrm{A}$ are extrapolated. The red dots show the positions where the peculiarities, indicated in (b), took place. (b) Optical output power transients measured for device B_2 for different currents. The pulse length was $t_{\mathrm{PW}} = 1\,\mu\mathrm{s}$. The red arrows indicate the presence of kinks in the transients.

After having verified the applicability of both methods, the first – spectral shift analysis – was chosen for further investigation of devices with another emission wavelength. Figure 4.11(a) shows the active region temperature rise measured for devices of batch B ($\lambda_{\mathrm{c}} = 980\,\mathrm{nm}$) for a pulse of $1\,\mu\mathrm{s}$ length at different currents. The transients for 6.1 A to 12.1 A are extrapolated from the measured data (15.1 A to 25.1 A). Figure 4.11(b) gives the integral optical output power transients for device B_2 for different currents [color scheme is the same as for the extrapolated curves in Fig. 4.11(a)]. These transients show a clearly visible kink, indicated by the red arrows in Fig. 4.11(b). This temporal position shifts towards shorter times with increasing current. Taking into account the current and time at which the kink occurs, the temperature can be estimated at which this peculiarity appears from Fig. 4.11(a). There, the respective values are indicated by red dots. Obviously, the identified temperature rises are all around 9 K.

4.1.4 Influence of the Material System

Up to now, all samples experienced a COD that starts exclusively from the front facet. However, scenarios with a COD starting at other location are likely, too. Here, three batches of DLs (C,D,E) with different active regions, but the same emission wavelength, coating and mounting – produced at the same facility – are compared [106, 125]. A brief summary is given in Tab. 4.1, including average values for I_{th}, η_{d}, and calculated optical mode widths (in growth direction).

Device batch	C	D	E
Waveguide material	Al-free	Al-free	Al-containing
Number of QWs	1	2	1
Effective mode width (μm)	0.82	1.47	0.66
I_{th} (mA)	380	720	310
η (W/A)	0.93	0.98	0.92
P_{COD} (W)	25	45	20
Front facet COD (quantity)	0	1	2
COD at both sides (quantity)	0	1	2
Rear facet COD (quantity)	3	2	0
No COD at any facet (quantity)	1	0	0

Table 4.1: Average data describing performance and COD behavior of 12 devices from 3 batches.

For a study of the influence of the device architecture on COD, 12 devices out of a total of 27 are subjected to step tests. The thermocamera-based setup with the device in a corner mirror was used. This makes the inspection of both laser facets in parallel possible and allows detecting a COD event by recording its thermal signature. The step test was started at $I_0 = 2\,\mathrm{A}$ and continued with current steps of $\Delta I = 1\,\mathrm{A}$, t_{PW} was fixed to $1\,\mu\mathrm{s}$.

Table 4.1 compiles P_{COD} values and damage locations for the 12 devices tested. The devices of batch C are demaged, in the cases where the COD site have been located, exclusively at the rear facet. The other Al-free structure D shows COD starting sites at front and rear facet and additionally combinations, i.e., COD at both facets. The only DLs that exhibit no exclusive rear facet COD in this study stem from batch E, the Al-containing structure.

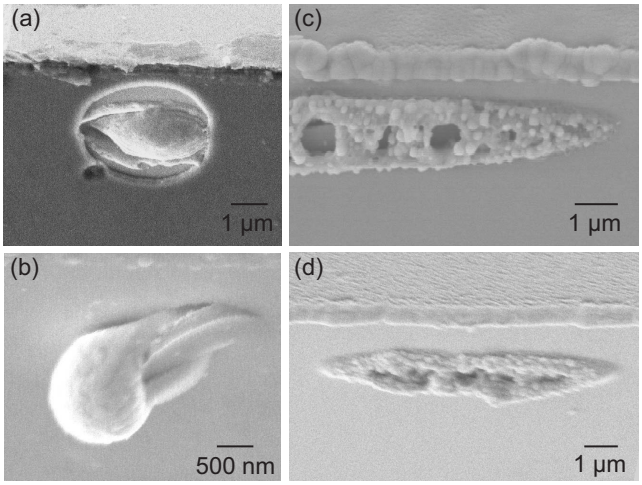

Figure 4.12: Scanning electron micrographs of typical front (a,b) and rear (c,d) facet damages. Device E_2 is shown in (a), device E_3 in (b), device D_1 in (c), and device D_2 in (d). Notice that the appearance of the damage pattern do not dependent on the device batch.

The appearance of the damage pattern at front and rear is very much different, but does not differ for the three batches. A front facet COD creates an extrusion underneath the almost *undamaged facet* coating; see Figs. 4.12(a) and (b). In contrast, rear facet COD leaves obviously thermally *damaged facet* coating material; see Figs. 4.12(c) and (d).

4.2 Discussion of First Phase Results

4.2.1 The Time to COD

The recorded optical output power transients allow for determination of t_{COD} by the presence of a significant drop, see Figs. 4.2(f-h). Moreover, the smooth current characteristics indicate that there is no change in the electrical properties during COD. The latter is reported, e.g., for single pulse COD experiments by Elliott *et al.* [126], who found kinks in the current traces of uncoated devices when COD sets in.

The detection of a thermal signal, as shown in Figs. 4.2(j-l), serves as a proof of COD occurrence. It has been checked that there is a one-to-one correspondence between a high thermal signal, clearly distinguishable from the background, and a fast output power drop. The relation of the external damage pattern to the data in Fig. 4.2, will be addressed in Sec. 5.1.2. Furthermore, the determination of the temperature of the process from images like Figs. 4.2(j-l) is discussed in Sec. 5.2.2.

In the following the time prior to COD, i.e., the aging phase, is discussed. It is obvious that for higher I_{COD} the values for t_{COD} become smaller, cf. Fig. 4.2. Figure 4.13 gives the experimental relation between the two. In this diagram, the data of provoked COD events (full circles) are complimented by data where no COD occurs (open circles), i.e., $I < I_{\mathrm{COD}}$ or $P < P_{\mathrm{COD}}$. In the latter case, the pulse width t_{PW} is taken instead of t_{COD}. The two abscissas, current and average optical power before COD, are connected via the L-I curve for the pulsed high-current regime of this laser batch. Two regions, with and without COD occurrence, can be identified [116]. The border line between the two is somewhat blurred, because of the fluctuations of device properties (coating homogeneity, growth-related point defects, deviations in the mounting process etc.), even within the batch. That is why, the COD threshold is not sharp but follows a certain distribution. The 'square root law' empirically discovered by Eliseev [45] and Kappeler *et al.* [127] for devices with lower emission powers is indicated as dashed line in Fig. 4.13. They took the solution for the three-dimensional heat conduction equation of a point heat source [128] and integrated it over the facet area. The heat spread is calculated for a semi-infinite solid, its thermal properties depend only on temperature. They yield a relation between the maximal heat flux q_{max} necessary to melt a portion of the laser facet and the needed time t_{COD}. For short pulses, i.e., when the heat dissipation is small compared to the size of the heat source, they found a square-root-like behavior $q_{\mathrm{max}} \propto 1/\sqrt{t_{\mathrm{COD}}}$ and demonstrated that the calculated heat flow linearly depends on the optical output power, i.e, $q_{\mathrm{max}} \propto P_{\mathrm{COD}}$ at COD ignition. This characteristic is confirmed by the data obtained for batch A in the short-pulse-length region, i.e., where heat dissipation from the defect site is indeed negligible. The graph clarifies that the specification of an I_{COD} value for a device requires information about the corresponding t_{PW}. Figure 4.13 gives the maximal achievable optical output power for a given t_{PW}. It demonstrates, that the limits can be pushed to higher currents in pulsed mode operation, while the border line approaches the cw case on the left side (lower output power).

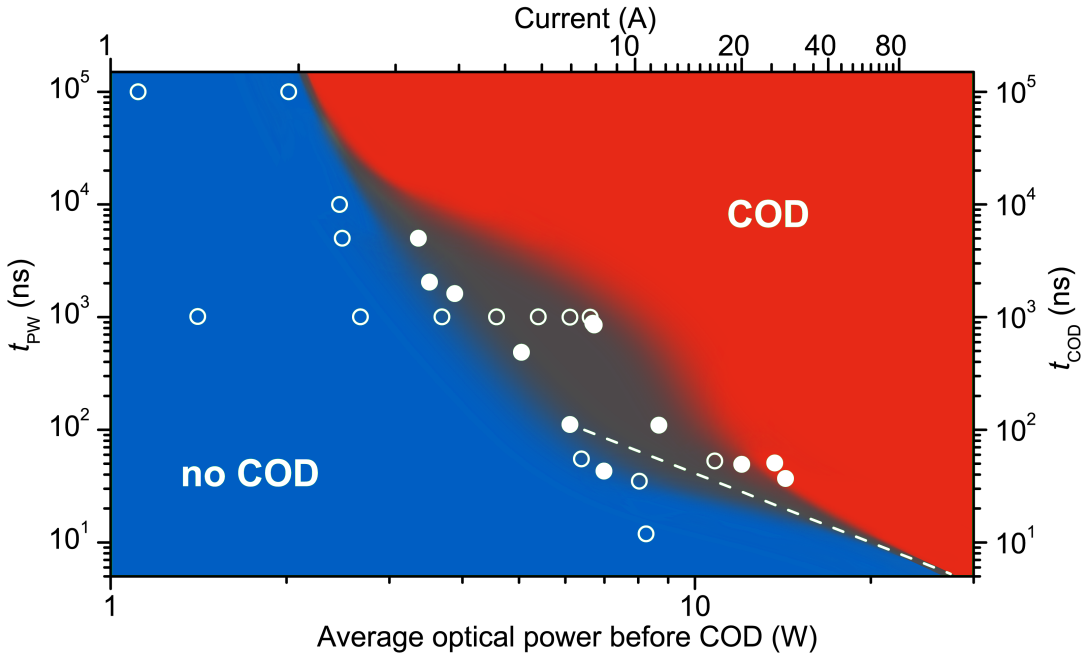

Figure 4.13: Pulse width t_{PW} (in case of no COD detection, open circles) or t_{COD} (if COD occurred, full circles) plotted versus the average optical output power in the pulse or before COD, respectively. The diagram shows the regions of COD (red background) and no COD (blue) for device batch A. The gray borderline is blurred because of the scatter in devices properties. The dashed line represents the 'square-root law' that has been reported for devices with lower emission powers [45, 127].

This allows to perform experiments focused on a particular point in the temporal evolution of COD and therefore to address a phase of COD explicitly. Shorter t_{COD} values at higher emission power levels indicate an optically induced defect process. Moreover, knowledge about this functional relationship enables analysis where the heating of the active region can be adjusted by varying t_{PW} and I along the border line. The aspect of temperature contributions, however, will be discussed in detail in Sec. 4.2.3.

The data presented in Fig. 4.13 can also be displayed in an Arrhenius plot, Fig. 4.14. This is possible, if the temperature for activating the thermal runaway is assumed to be proportional to the actual optical power when it starts. Moser and Latta [67] proved that this is valid for the investigation of DLs. Therefore, the value of P_{COD} per facet width (P_{COD}/μm) is used as equivalent to temperature. A straight line in an Arrhenius plot is typical for thermally activated mechanisms [129]. A similar dependence has been found by Moser *et al.* [65–67] in long term cw experiments. This indicates that both processes, single pulse high-current excitation and long term cw tests, are thermally activated. This is one experimental argument, why the step test approach is considered as special type of accelerated aging without changing the principal degradation mode.

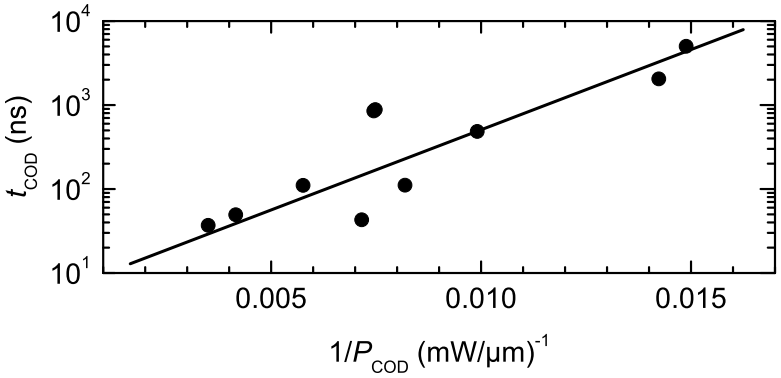

Figure 4.14: Arrhenius plot of data from batch A.

4.2.2 Beam Properties *en route* to COD

The lasing NF of a DL is influenced by different mechanisms. Following an analysis by Crump *et al.* [115], the most important are: (i) Lateral waveguiding structures introduced during the device processing, e.g., the processing of ridge structures by introducing a step in the lateral refractive index (n) profile in the material. (ii) The current flow through the device builds up a non-uniform temperature profile by ohmic losses. This causes a temperature-induced change of n. The heat diffusion forms a lens-like $n(x)$-profile. Therefore, this effect, as described for example by Nash [130], Andrews [131], and Bawamia *et al.* [132], is widely known as *thermal lensing*. (iii) Current spreading can result in a lateral gain profile that can lead to stable guided lateral modes. Eventually, this effect or a combination of all lead to filamentation of the mode pattern, e.g., reported by Nash [130].

A striking feature considering the NF evolution during a high-current pulse is the decrease of the overall NF width. This is especially visible in the NF images covering an entire pulse of 300 ns to 1000 ns length, as in Figs. 4.4 (left column), 4.6(a), and 4.7(b-d). This behavior is closely connected to the temperature of the active region, as reported by Lang *et al.* [133]. The authors report, that lasing in higher order lateral modes can be favored by a temperature-induced change of the refractive index profile along x-direction. The impact on degradation, however, results from the fact, that the output power keeps constant, Figs. 4.5(inset) and 4.6(c), while the NF width decreases. This leads to higher optical power densities at the facet, favoring degradation mechanisms that depend on high light intensities, as the COD.

In addition to the decreasing width of the NF addressed above, Figs. 4.4 and 4.6(a) show fundamental changes in the spatio-temporal structure of the NF. For lower currents and times closer to the leading pulse edge, a zig-zag motion of spots of higher intensity is visible, see Fig. 4.4, while for higher currents and later times a stripe-like pattern (stripes along the temporal direction) can be observed. This is due to an increase of the frequency of main filament motion caused by the rise of the active region temperature as discussed by Fischer *et al.* [134] and Adachihara *et al.* [135]. Eventually, the spots of high intensity become imperceptible according to the limited temporal resolution of the setup.

4.2.3 Temperature Contributions

The temperature is an important parameter for understanding the COD ignition mechanisms. Therefore, a first approach is to study the effect of T_{hs}-variation. The two main findings from Fig. 4.3 are:

- The optical output power at a given current is significantly reduced for higher temperatures,
- I_{COD} increases with heat sink temperature.

The explanation for the first is the temperature dependence of the gain curve. The peak gain value is reduced with increasing temperature. An example for a DL structure lasing around 830 nm is given in Fig. 4.15. Gity *et al.* [136] calculated the temperature-dependent gain curves starting from Fermi's golden rule including the optical transition matrix element, density of states, and Fermi-Dirac distributions for conduction and valence band. A Lorentzian-shaped broadening function accounts for the homogeneous spectral broadening in their model. The resulting equations have been solved numerically.

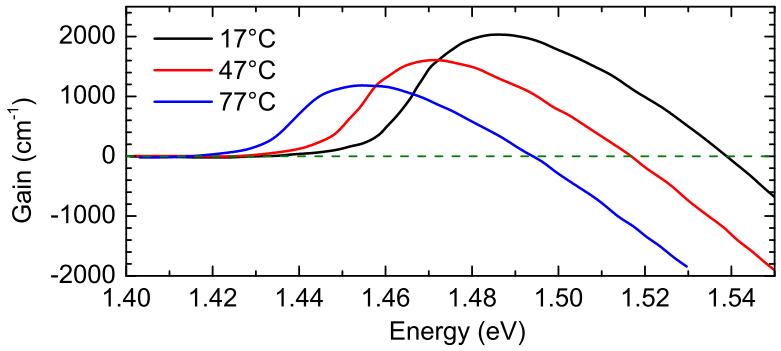

Figure 4.15: Example for the temperature dependence of material gain curves for a laser emitting at $\lambda_c \approx 830$ nm. The data were taken from Gity *et al.* [136].

In order to understand the second point, the effects of several temperature contributions have to be considered. As introduced in Sec. 2.2, the crucial factor for COD ignition is the heating of the later defect site up to T_{crit}. The temperature of the facet (T_{facet}), can be sub-divided into two parts:

$$T_{facet} = T_{bulk} + \Delta T_{facet} \tag{4.2.1}$$

with the bulk heating (T_{bulk}) of the active material in the cavity and the additional temperature increase (ΔT_{facet}) of the facet region with respect to the active region bulk. T_{bulk} contains T_{hs}.

An uniform heating of the entire active material, i.e., an increase of T_{hs}, only shifts the gain curve, see Fig. 4.15. This means that also the energy region of absorption, i.e., negative gain, is shifted the same way. In contrast to that, a local temperature difference leads to the situation, where the gain region of the active bulk material coincide with the absorption region of, e.g., the warmer front facet. Even if this overlap is small, it leads to a positive feedback loop increasing the overlap and therefore T_{facet}. During the first COD phase this temperature keeps far below the melting point of the material. During

the second COD phase this rate of temperature increase becomes explosion-like, i.e.,$\gg 100\,\mathrm{K/ns}$ as modeled by Nakwaski [137], this is what is called the *thermal runaway*. Notice, that this is just one possible mechanism closing the intrinsic feedback loop. In case of a lower device temperature the optical output power is increased which also favours the closing of the intrinsic feedback loop.

However, the I_{COD} value does not decrease for higher temperatures, as one might expect. The homogeneous temperature increase by T_{hs} of the entire material leads to a higher I_{COD} value by reducing the output power, cf. Fig. 4.3.

This calls for a determination of the active region temperature transient. As shown in Sec. 4.1.3 two methods have been successfully applied to address this. Taking into account the temperature dependent shift of the semiconductor band structure [32], the change of the refractive index (n) can be determined in the heated region. Since classical [138] and quantum-mechanical treatment [32] reveal a dip in the n-curve above the band gap, the laser emission is in the range of normal dispersion. A reduction of the band gap with increasing temperature, as discussed in Sec. 4.1.3, shifts this curve to higher n-values at the emission wavelength. For $Ga_{1-x}Al_xAs$ ($x = 0.315$), Aspnes *et al.*[139] found a relation of $\mathrm{d}n/\mathrm{d}T = 3.1 \cdot 10^{-4}\,\mathrm{K}^{-1}$ between refractive index and temperature. The temperature rise of $\approx 21\,\mathrm{K}$ after 300 ns and 26 K after 1000 ns, both at $I = 10\,\mathrm{A}$, leads to an increase of the refractive index of $\Delta n|_{300\,\mathrm{ns}} = 6.5 \cdot 10^{-3}$ and $\Delta n|_{1000\,\mathrm{ns}} = 8.1 \cdot 10^{-3}$. This change of n is comparable to the index step introduced in a ridge waveguide laser for lateral optical mode confinement [140]. This introduces a thermally-induced index step in the active region and transforms the intrinsic pure gain-guided system into a thermally-induced index-guided one, as theoretically shown in Ref. [141]. The fact, that the NF in case of device A_2 becomes more symmetric after 300 ns (see Fig. 4.6) indicates that the effect of the thermally-induced index step exceeds the influence of the inhomogeneity responsible for the NF at the leading edge of the pulse. Such a thermally-induced index step can be also created by externally applied heating of a limited zone of the active region, as demonstrated by Hadley *et al.* [142]. This result is additionally confirmed by NF measurements done at devices from batch F. They have a built-in index step that overcompensates the influence of the active region heating and therefore do not exhibit a noticeable reduction of NF width.

Further evidence for the presence of the thermally-induced index step comes from the measurements at devices from batch B (also a gain-guided structure); see Fig. 4.11. The output power traces of device B_2, cf. Fig. 4.11(b), show a kink (indicated by the red arrows). This indicates a sudden change in the lateral mode pattern, verified, e.g., by comparison of the NF data in Figs. 4.7(a,b). There, a peculiarity is obvious at ≈ 350 ns [Fig. 4.7(a)] and ≈ 200 ns (b) in the respective integrated power traces. The latter show similar kinks as found for device B_2 in Fig. 4.11(b). As discussed in Sec. 4.1.3 the kinks visible in Fig. 4.11(b) can be related to active region temperatures via the data shown in Fig. 4.11(a). The average active region temperature rise, with respect to the surrounding bulk material, is found to be in all cases around 9 K. Therefore, it strongly indicates that the mode pattern change occurs, when the thermally-induced index step starts to dominate the lateral waveguiding.

Figures 4.7 and 4.8 indicate the different nature of the two discussed heating mechanisms. The saturation of the NF width decrease (indicated by the dash red lines) is a consequence of the active region temperature rise with respect to the surrounding material. In contrast, a variation of T_{hs} does not cause any temperature differences and therefore no refractive index step. That is why the temporal positions of the red lines are independent of T_{hs}.

Moreover, a T_{hs}-variation does not affect the temperature difference $\Delta T_{\mathrm{facet}}$ that is crucial for closing the feedback loop leading to the thermal runaway. The removal of the heat created during operation is

changed due to the changed heat sink temperature level. Even if the idea to learn something about the physical background of COD by adjusting T_{hs} seems plausible, it cannot establish a thermal situation comparable to the result of active region heating during laser operation. More appropriate to analyze the temperature impact on COD is the utilization of the border line identified in Fig. 4.13. It can be used to adjust the effect of active stripe, facet and bulk heating.

4.2.4 Influence of the Material System

From the preceding section, the question arises how the material system influences the temperature difference at the facet. For asymmetrically coated DLs, i.e. the standard configuration with low reflectivity at the front and high reflectivity at the rear facet, COD is expected to occur at the outcoupling front facet where the photon density is highest, see 4.16(a). In contrast, practical failure analysis revealed COD also at rear facets, often in combination with extrinsic origins such as macroscopic defects or cleavage steps. Menzel [143] modeled the temperature rise that leads to the thermal runaway and therefore COD for these asymmetrically coated structures. He found a higher surface temperature of the rear than the front facet for surface recombination velocities (v_{surf}) below $2 \cdot 10^5\,\mathrm{cm/s}$, see Fig. 4.16(b). This behavior was verified by modeling work of Miftakhutdinov *et al.* [144, 145]. It pinpoints a tendency that devices with facets featuring low v_{surf} preferable tend to rear facet COD, even without any extrinsic origin. In practice, P_{COD} depends on the material system and the emission wavelength [146]. Record P_{COD} values are achieved mainly with the so-called $9XX\,\mathrm{nm}$ emitting devices [147]. The optical power density at COD threshold of the samples from batches C, D, and E has a value of $\approx 30\,\mathrm{MW/cm^2}$, see Tab. 4.1. This represents the present standard of device technology [81].

The investigated Al-containing devices display COD at the front facet, while Al-free structures tend to rear facet COD. This difference points to a different balance of heating processes by which the local critical temperature of the material for igniting the thermal runaway is reached. The main heat sources in a DL are:

- Joule losses,
- re-absorption of laser light inside waveguide and within the entire laser structure,
- Auger recombination in the active region,
- surface recombination at the facets.

Resistive and re-absorption heating are similar in the three investigated batches because of their similar electrical and optical configuration provided by the same manufacturing steps. While Joule heating is expected to be spatially homogeneous, the reabsorption of laser light favors a higher temperature close to the front facet where the intracavity photon flux is higher than at the rear facet, see Fig. 4.16(a). Additional heating by the comparably strong surface recombination leads to front-facet COD in case of the Al-containing devices (batch E). For Al-free devices (batches C and D) the situation is different, with their lower surface recombination rate [148–150] the carrier concentration N is higher close to the facets [143, 151], cf. Fig. 4.16(b).

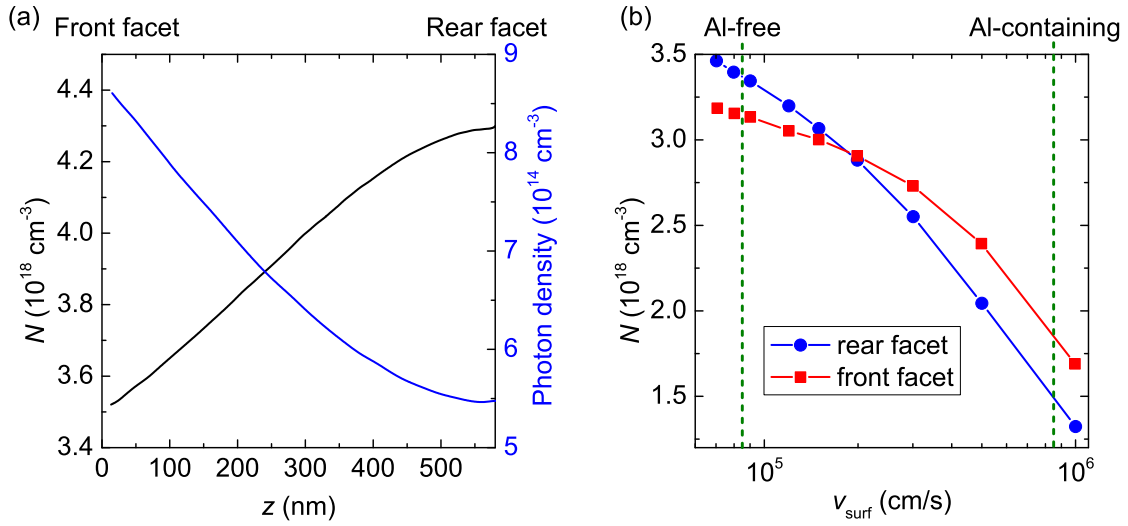

Figure 4.16: Graphs that illustrate the underlying physics as modeled by Menzel [143] (curves and data points extracted from there) for AlGaAs double-heterostructure DLs. (a) Characteristic carrier concentration (N) and photon density along the cavity. The positions of front and rear facet are indicated. Notice that the regions close to the facets are not included in case of N caused by a significant and rapid change near them. Details about N at the facets are given in (b). (b) N at the front and rear facet for different values of v_{surf}. The values for Al-free and Al-containing material are marked by dashed lines, the values are taken from [148].

As has been discussed by Menzel [143], heating by Auger recombination comes into play at such elevated carrier densities. The total recombination rate $R(N)$ can be expressed as [152]:

$$R(N) = \frac{N}{\tau} = A_{\mathrm{nr}} \cdot N + R_{\mathrm{sp}} \cdot N^2 + C_{\mathrm{Auger}} \cdot N^3 \quad , \tag{4.2.2}$$

with the effective carrier lifetime τ, the Shockley-Read-Hall coefficient A_{nr}, the radiative recombination coefficient R_{sp}, and the Auger coefficient C_{Auger}. For a high v_{surf}, the density N is smaller and the Auger effect does not dominate the heating mechanisms, cf. Fig. 4.16(b). For a low v_{surf} value, the surface recombination is reduced leading to higher N values, favoring Auger recombination since it is proportional to N^3 in the relevant density range of several $10^{18}\,\mathrm{cm}^{-3}$. This leads to a pronounced Auger-related temperature increase and, thus, the starting of COD at the rear facet of Al-free devices is more likely. Furthermore, the relation between N values at front and rear facet changes its sign considering Al-free and Al-containing case, see Fig. 4.16(b). The dashed lines indicating both cases. The data are in favor for a more pronounced Auger heating at the rear facet. In line with the above argument, the different primary damage patterns found at front and rear facet, see Fig. 4.12, indicate different scenarios *en route* to reach T_{crit} and therefore to start the thermal runaway.

This comparison of different material systems, while keeping other parameters (coating, mounting, etc.) constant, demonstrates the influence on the heating mechanisms in DLs that enable the later COD

staring site to reach T_{crit},[1] which is not very high compared to the temperatures reached during the subsequent thermal runaway phase.

The discussed mechanisms clearly indicate that the temperature along the cavity is influenced in many different ways. A reduced value of v_{surf} is found to protect the front facet by decreasing the influence of one heating mechanism. This, however, leads to the occurrence of a new bottleneck at higher (further increased) power levels, by favoring a different heating mechanism. This also describes why the problem of COD in high power DLs cannot be solved by just fixing one particular problem, but only by understanding the mechanisms and considering all bottlenecks of a device design.

4.2.5 Mechanisms Determining the First Phase

The first phase of COD relies on reaching T_{crit} at a limited region of the active material. There are many ways to achieve this by completing the intrinsic or extrinsic feedback loops. In long term cw tests, the first phase of COD is most likely dominated by a mixture of both. The intrinsic loop accounts for higher temperatures at the future COD location by a temperature-induced band gap shift. This elevated temperature enhances the diffusion of point defect towards this region. This leads to a further increased temperature there, giving a positive feedback in both loops. This process starts with small temperature differences and the point defect kinetics take place on long time scales, explaining the occurrence of COD after a few hundred to several thousand hours. The use of high currents in the step test favors rather the intrinsic loop, because the time of tenth of nanoseconds is too short for point defect accumulation at the defect site as long as the temperature is below several hundred degree Celsius. However, the location where this takes place is most likely the same as would be affected in a cw test, because the sufficient condition is the same. The future COD site has to have intrinsically a slightly higher temperature than the remaining active region. If T_{crit} has been reached the thermal runaway and the defect propagation probably take place the same way in both test regimes, dominated by the fast energy redistribution via the extrinsic loop.

It has been shown, that the material system used for the active region has an impact on the approach of T_{crit}. A good heat extraction from the active region leads to an increase of the COD threshold. Moreover, other heating mechanisms, as the surface recombination velocity and Auger recombination, have to be taken into account. Especially if the device is of high quality, these kinds of temperature contributions are essential for setting the positive feedback loops into action. Eventually, all mechanisms point to the fact that T_{crit} has to be reached somehow. Furthermore, the results of this chapter verifies that a specification of a temperature for T_{crit}, as done widely in the literature [47, 54, 59, 67, 153, 154], is problematic. In fact, the temperature *difference* ΔT_{facet} is important for closing the feedback loop not the absolute value, as demonstrated by variation of T_{hs}. The term T_{crit}, however, as used in this thesis indicates the discussed concept of the different temperature contributions that eventually results in a situation where a feedback loop of heating and absorption is closed.

[1] more precisely a critical temperature difference between the volume of the active material and the region near the facet

5 Second Phase of COD – Thermal Runaway and Start of Defect Spread

5.1 Experimental Results

5.1.1 Time Constants for Different Material Systems

The COD-related drop in optical output power does occur not instantaneously, but has a short decay time during the thermal runaway [116, 155]. Figure 5.1 shows results of step tests with devices of batches G, A, and, D having emission wavelengths of $\lambda_c = 650\,\text{nm}$, 808 nm, and 975 nm, respectively. Figures 5.1(a,b) show the pulses where COD occurred for the first time to the particular device. Figures 5.1(c-e) give the situation for one device before, at, and after the first COD event, respectively. In order to characterize the decay times, the power drops are fitted by exponential functions, e.g., indicated in Figs. 5.1(a,b). This gives characteristic $(1/\text{e})$-decay times (τ_{drop}), as given in Figs. 5.1(a,b).

While the COD event is clearly visible in case of Fig. 5.1(a) and (b), it is harder to identify in (d). In this situation, the data obtained during the step test are helpful. The data shown in Fig. 5.1(c) represent the last current step before COD occurred. In Fig. 5.1(d), the current is $\Delta I = 1\,\text{A}$ higher and COD takes place, while it is re-ignited in (e). In order to detect the degradation, the output power loss during the entire pulse, which is a result of bulk heating, is fitted with a linear function for all pulses *en route* to COD. Therefore, it becomes possible to predict the drop in the subsequent pulse – assuming that no degradation takes place. These linear fits are given as green dotted lines in Figs. 5.1(c-e). The COD manifests as deviation from this predicted line, starting at $\approx 800\,\text{ns}$ in (d). In case of the re-ignition in (e), the increased power loss caused by COD is evident.

The thermocamera provides an additional tool to detect COD events via the recording of the thermal flash. Therefore, the thermocamera is pointed directly to the front facet of the DL ($t_{\text{int}} = 10\,\mu\text{s}$, $t_{\text{int,eff}} = 4.5\,\mu\text{s}$). The insets of Figs. 5.1(c-d) give the thermal images for the respective pulses. The thermal background, measured before the pulse was applied, has been subtracted. While in case of Fig. 5.1(c) the inset gives just noise around zero, a signal is visible in (d) coming from a hot spot, indicated by the white arrow. During the COD re-ignition, shown in Fig. 5.1(e), a clear thermal signal appears at exactly this position, again verifying the identification of the initial COD in (d).

However, although the COD has been detected the drop is insufficient to be fitted by an exponential. Therefore, a further experiment was performed with a 975 nm device. Since the drop seems to be slower, the pulse length was extended from $t_{\text{PW}} = 1\,\mu\text{s}$ in case of Fig. 5.1 to $t_{\text{PW}} = 10\,\mu\text{s}$. Moreover, a current substantially above I_{COD} was chosen. This helps to provoke COD in a single pulse and to get a situation where $t_{\text{COD}} \ll t_{\text{PW}}$, which makes it possible to observe a pronounced drop during the pulse. The result is shown in Fig. 5.2. The thermal image taken during this pulse is given as inset. The exponential fit is given as dashed blue line. In this particular case, a value of $\tau_{\text{drop}} = 400\,\text{ns}$ was achieved.

Figure 5.3 shows the collected τ_{drop}-results for a number of experiments such as shown in Figs. 5.1 and 5.2. In order to compare devices with different aperture widths, P_{COD} is normalized to that value.

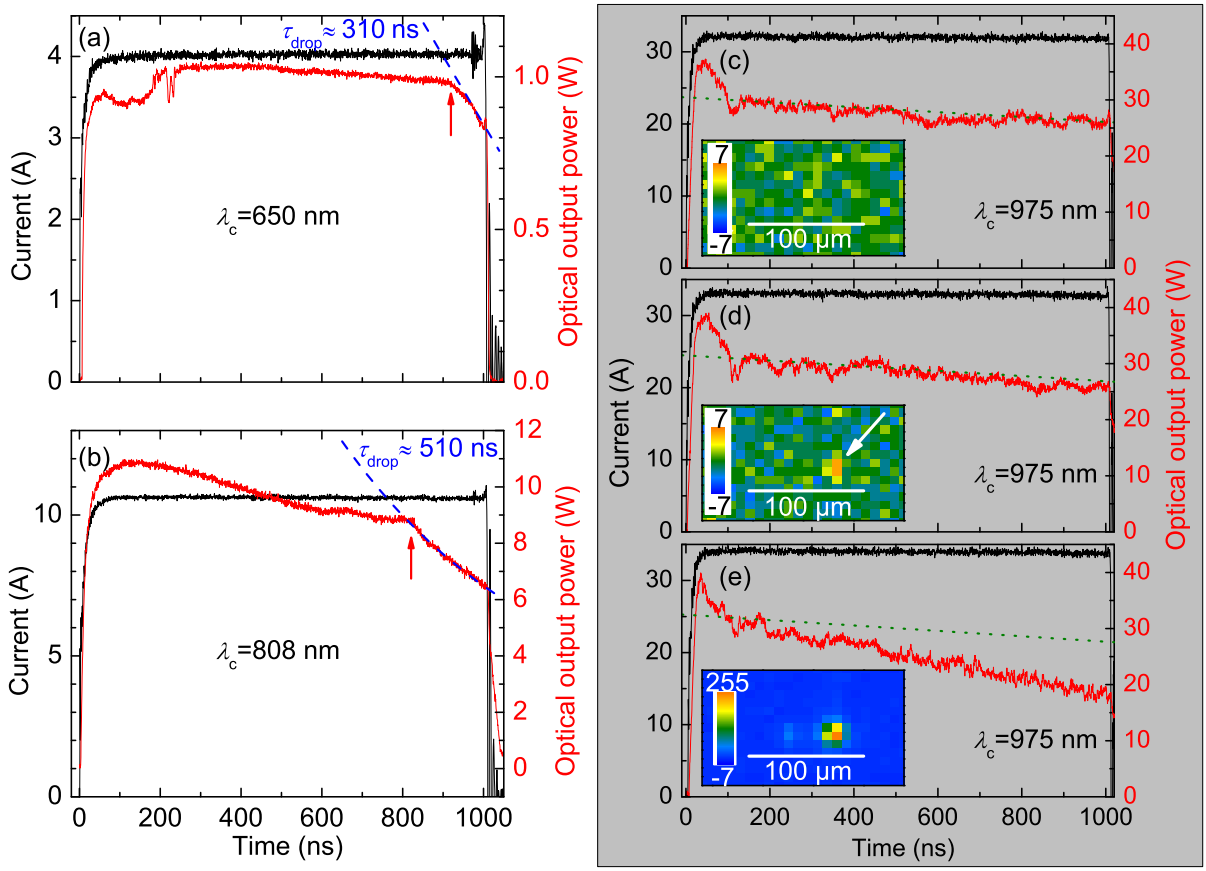

Figure 5.1: (a,b) Data from step tests; the pulses are shown where COD occurs first. Current pulse (left ordinate) and emission power (right ordinate) are displayed. The points where COD occurs are indicated by red arrows. Typical examples are given for lasers with $\lambda_c = 650\,\text{nm}$ (a) (device G_1) and $\lambda_c = 808\,\text{nm}$ (b) (device A_{23}). The dashed blue lines show exponential fits which give the characteristic decay times τ_{drop}. (c-e) Data from a step test *en route* to COD ($\lambda_c = 975\,\text{nm}$, device D_2); current pulse (left ordinate), emission power (right ordinate), and thermal image (inset, in counts) are given for the last step before COD occurs (c), the first COD ignition (d), and the COD re-ignition (e). The dotted green line in (c) represents a linear fit of the bulk temperature related power drop. In (d) and (e), the same type of line represents the expected power drop as extrapolated from transients taken between 2 A and 32 A.

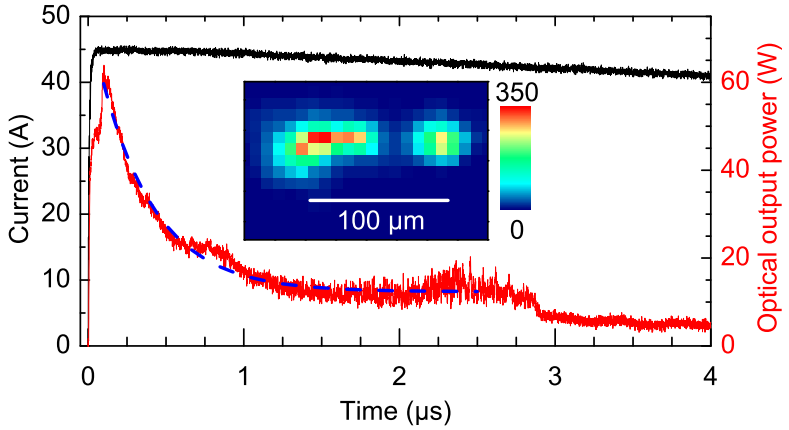

Figure 5.2: Data measured during a single pulse COD test with device E_1 from batch E: current pulse (left ordinate) and emission power (right ordinate) are displayed. The thermal image is given as inset in counts. The dashed blue line represents an exponential fit of the power decay.

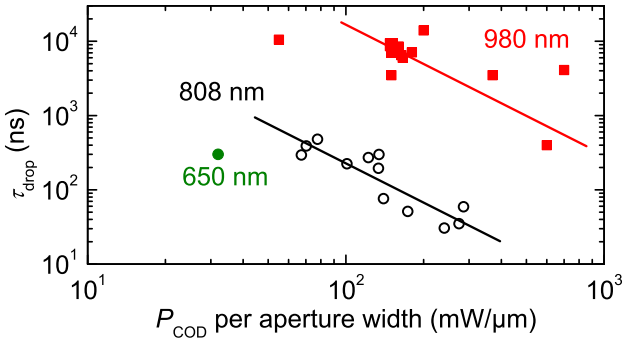

Figure 5.3: Power decay times τ_{drop} versus actual COD threshold P_{COD} per aperture width. The red square symbols mark data form batches B,C,D, and E emitting around 975 nm to 980 nm. Open black circles refer to devices from batch A (808 nm), whereas the green full circle describes the behavior of a typical 650 nm device from batch G. The lines are guides to the eye only.

5.1.2 Spatial and Temporal Resolved Nearfield Dynamics

In the preceding subsection the spatially integrated optical output power evolution was measured. In the following, experiments are shown that add spatial resolution of the laser emision.

Spatially Resolved Defect Kinetics

Due to its temporal resolution in the picosecond time range it is straightforward to use the streak camera for measurements of the thermal runaway – the COD-phase with the fastest kinetics. Furthermore, it provides the desired spatial resolution, necessary to analyze the defect kinetics.

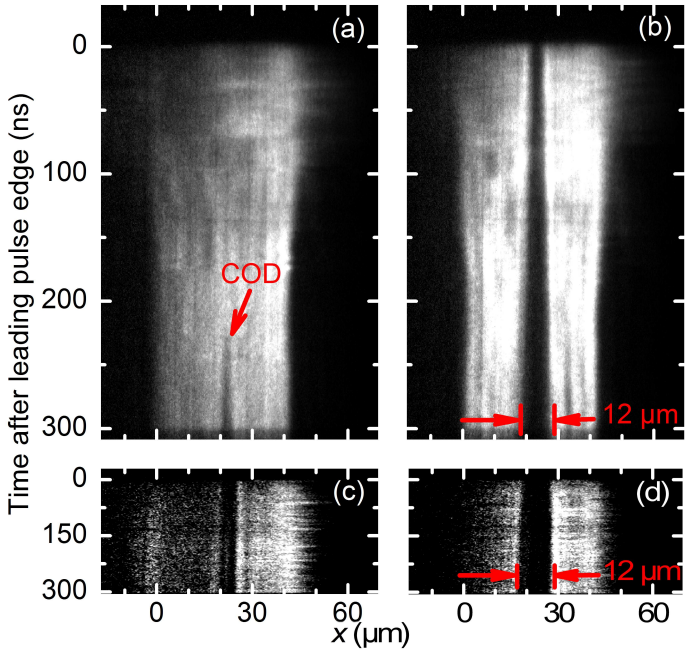

Figure 5.4: (a) NF of laser emission of device A_4 during a pulse, where COD occurs for the first time in the step test, $I = I_{COD} = 10\,A$. The onset of COD is marked by an arrow. (b) NF evolution during the following high current pulse including COD re-ignition. (c) NF evolution during test pulse ($I_0 = 1.6\,A$) after the first COD event. (d) NF evolution during test pulse (I_0) after the subsequent high current pulse with COD re-ignition.

Figure 5.4 shows an example of the NF evolution during COD at the end of a step test. The NF of sample A_4 (device batch A) is shown during COD in Fig. 5.4(a) at $I = 10\,A$. The NF during the subsequent current pulse of the same amplitude is given in (b). The low current test pulses ($I_0 = 1.6\,A$) following directly (a) and (b) are given in Figs. 5.4(c) and (d), respectively.

The point in time where COD starts to affect the NF is marked by a red arrow in Fig. 5.4(a). Starting from there a region of reduced intensity in the NF begins to broaden. The width of this *NF gap* is also visible in the test pulse, cf. Fig. 5.4(c). This NF broadening is revived in the subsequent high current pulse, Fig. 5.4(b). The final width of the gap is well visible in the following test pulse (d).

Internal Damage Width

In order to understand, how the detected NF gap is related to the damage, device A_4 was opened after the measurements shown in Fig. 5.4. A μPL map of the QW was recorded. The result is shown in Fig. 5.5(a). The dark area gives the region of non-radiative recombination, i.e., the damage. Figure 5.5(b) gives a cut through the lasing NF at $I = 0.5\,A$ taken with the optical microscope. Figure 5.5(c) gives a cut through the lasing NF at $I = 10\,A$, taken from the trailing pulse edge of the streak camera image in Fig. 5.4(b). The comparison of Figs. 5.5(b) and (c) verifies the results discussed in the preceding chapter – the decrease of the NF width and the formation of clearly visible filaments.

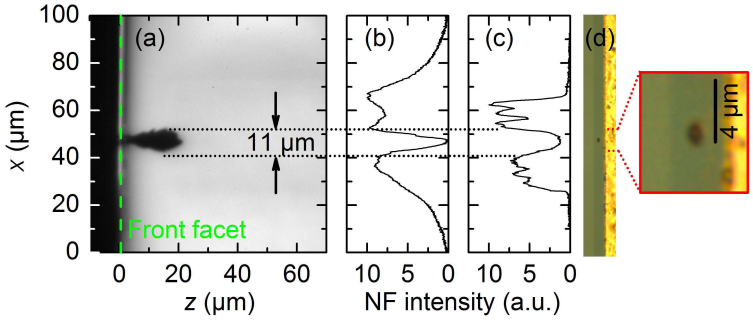

Figure 5.5: (a) μPL image of the QW plane of device A_4, opened after COD and one COD re-ignition. The position of the front facet is indicated by the dashed green line. (b) Cut through lasing NF at $I = 0.5\,\mathrm{A}$, seen with optical microscope after COD re-ignition, before device was opened. (c) Cut through lasing NF at the trailing edge of the streak camera image shown in Fig. 5.4(b). The width of the internal damage of $11\,\mu\mathrm{m}$ visible in (a) is indicated by the dotted lines in (b) and (c). (d) Image of the front facet taken with an optical microscope. On the right side, a part of the gold coated heat sink is visible. The lateral position scale is the same in (a-d). The front facet defect is shown on an enlarged scale at the right side. The position in image (d) is indicated.

Nevertheless, the width of the NF gap is the same in both cases and reflects the total damage width of the internal defect pattern, as indicated by the dotted lines. Moreover, Fig. 5.5(d) shows the external visible damage. The time during which the NF gap grows in both consecutive pulses is $\approx 270\,\mathrm{ns}$.

The NF maps presented in Fig. 5.4 indicate that the concept of time slicing by the use of short pulses also allows to build-up the internal damage structure step-wise. With this technique, it becomes possible to prepare different stages of defect extension. Utilizing this, another sample with more extended damage than in A_4 was prepared. The comparison between the internal defect pattern and external available data is shown in Fig. 5.6. Device A_6 experienced a single COD event at the end of a step test at $I_{\mathrm{COD}} = 10\,\mathrm{A}$ with $t_{\mathrm{PW}} = 1\,\mu\mathrm{s}$ and $t_{\mathrm{COD}} = 101\,\mathrm{ns}$. Therefore, this damage had $\approx 900\,\mathrm{ns}$ to develop after onset of COD which is more than three times the value that was available for the damage shown in Fig. 5.5. The CL map of the QW plane in Fig. 5.6(a) shows a significant larger defect area. Figure 5.6(b) gives the comparison between the lasing NF before (red line) and after (black line) the COD. The green arrows in Fig. 5.6(b) indicates redistribution of the lateral modes due to the presence of damage. Figure 5.6(c) gives the EL NF that shows just a local change around the defect. In sub-figure 5.6(d), the external damage as seen in the optical microscope is shown. The defect width is, again, represented well by the NF gaps in lasing and EL case and provides a better information about the internal defect width as the facet damage.

The data shown in Fig. 5.6 may suggest that the lasing and EL NFs provide equivalent information about the internal damage width. In order to check this, a comparison of the NF data and the internal damage pattern of sample A_7 is shown in Fig. 5.7. In the framework of a step test the device reached I_{COD} at $10.5\,\mathrm{A}$ with $t_{\mathrm{PW}} = 1\,\mu\mathrm{s}$. For the following $1\,\mu\mathrm{s}$ pulses, the current was kept constant at this level and the single pulse experiments went on until every sign of lasing vanishes. Including the first COD pulse, this needs 35 pulses. The NF cuts, taken with the optical microscope, are shown in Figs. 5.7(a) and (b). In these graphs the comparison of the state before the step test (red curves) and after the last pulse of the step test (black curve) are shown. While the lasing signal vanishes completely after the step test, the EL signal is still present [black curve in (b)], except for a narrow gap.

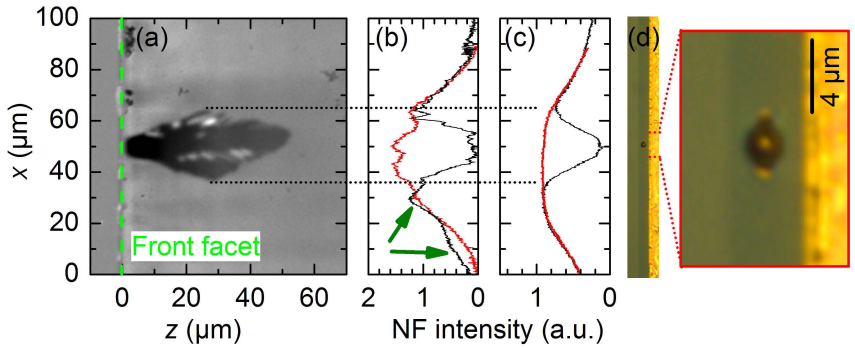

Figure 5.6: (a) CL map of the QW plane of device A_6 after a single COD event. The position of the front facet is indicated by the dashed green line. (b,c) Cuts through lasing (b) and EL (c) NFs before (red lines) and after COD (black lines). (d) Image of the front facet taken with an optical microscope, lateral aligned with (a-c). The front facet defect is shown on an enlarged scale at the right side. The position in image (d) is indicated.

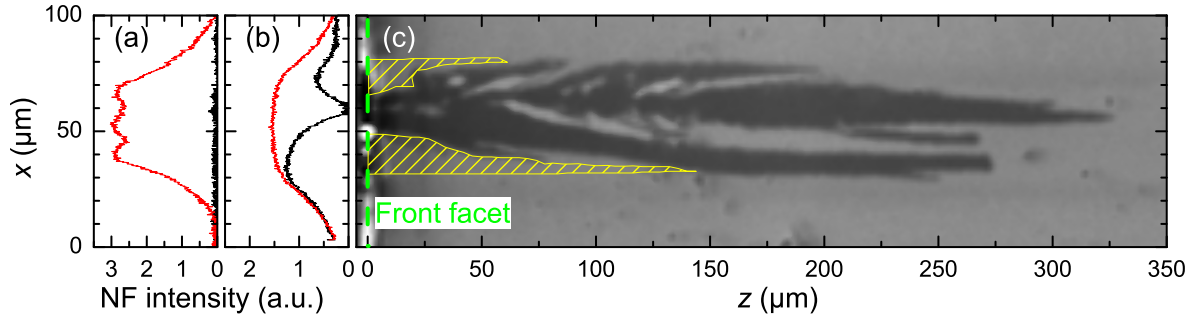

Figure 5.7: Device A_7 experienced a COD and 34 COD re-ignitions under identical current pulses. The cuts shown are through the lasing NF (a) and EL NF (b). While the red curves give the situation before COD, the black ones are taken after the last provoked re-ignition. (c) CL map of the QW plane after device opening after all other measurements have been finished. The position of the front facet is indicated by the dashed green line. The meaning of the yellow shaded areas will be discussed in Sec. 5.2.1.

Internal Damage Width Compared to NF Gap and Thermal Images

Now, the relation between the defect and the thermal signals recorded by the thermocamera will be analyzed. Data sets for two devices of batch A are shown in Figs. 5.8(a-j). The pulse length for both was $t_{PW} = 1\,\mu$s. The data of device A_8 are presented in Figs. 5.8(a)-(e). This diode experienced COD at $I_{COD} = 10.6\,$A after $t_{COD} = 853\,$ns. In contrast, COD in device A_9, Figs. 5.8(f)-(j), occurred at $I_{COD} = 25.2\,$A after $t_{COD} = 50\,$ns. Sub-figures 5.8(a,b) and (f,g) give the spatial distribution of the lasing NF at the front facet with $I = 0.5\,$A for device A_8 and A_9, respectively [before (a,f) and after (b,g) COD]. Lateral cuts through this images are given in (e) and (j), with black lines giving the NF before and blue lines after COD. The external COD damage pattern at the front facet are inspected by optical microscopy.

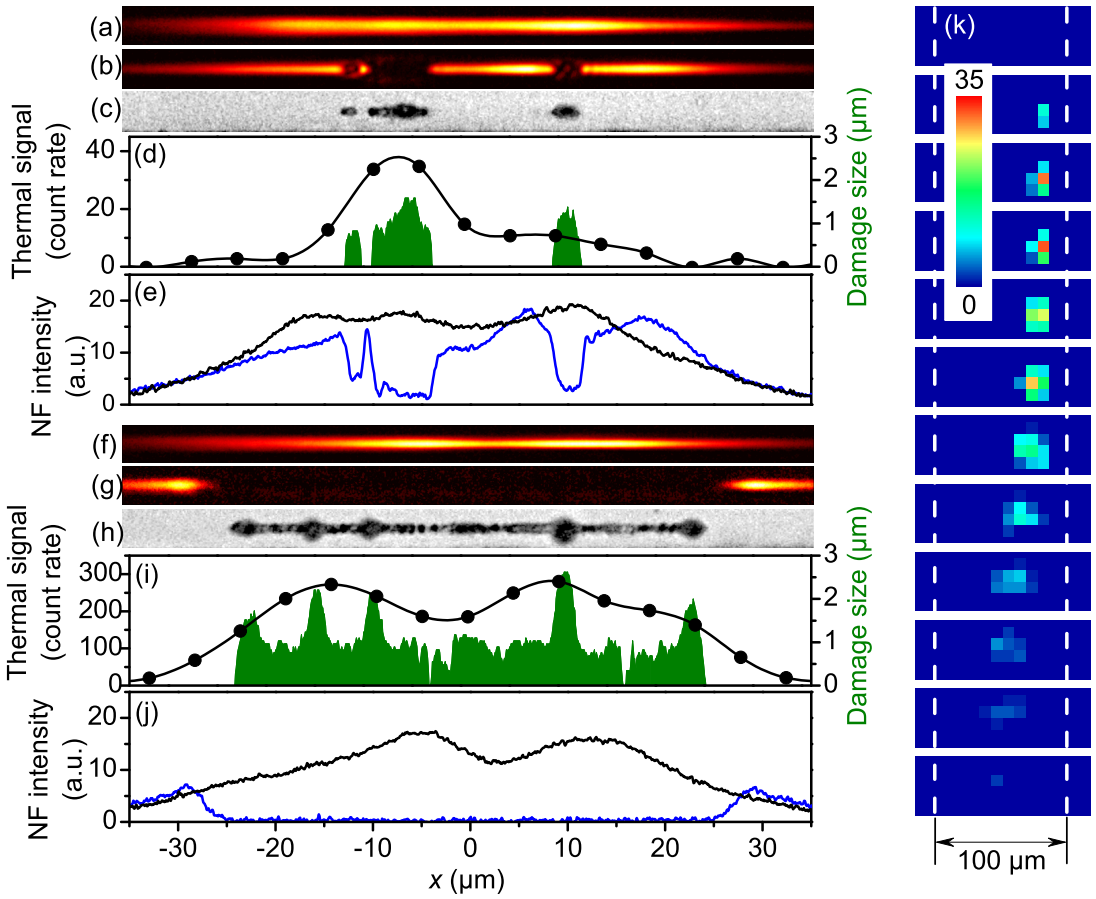

Figure 5.8: (a-j) Data sets from two devices of batch A, each experienced COD during a 1 μs long single pulse. (a)-(e) device A_8 with $I_{COD} = 10.6$ A and $t_{COD} = 853$ ns; (f)-(j) device A_9, with values of $I_{COD} = 25.2$ A and $t_{PW} = 50$ ns. (a,b,f,and g) Spatial distribution of the lasing NF at the front facet, measured with $I = 0.5$ A. Sub-figures (b,c,g,h) were recorded after COD. (c,h) Microscope images of the front facets acquired after COD showing the external damage as dark features. (d,i) Spatial profiles of the emitted thermal power (solid lines and symbols) and external damage size as derived from (c) and (h) represented by green areas. (e,j) Lateral cuts through the lasing NF before (black lines) and after COD (blue lines). (k) Thermal images showing the front facet of device E_4 from batch E. The images are taken during subsequent pulses between $I = 24$ A to 35 A (from top to bottom, the thermal signal is given in counts). The emitter stripe width of 100 μm is indicated.

The obtained images are shown in Figs. 5.8(c,h). Cuts through the thermal images measured during the COD pulses are given in Figs. 5.8(d) and (i). These sub-figures also include the size of the externally visible damage area, extracted from (c) and (h). Therefore, the green areas are identical with the areas of the external defect pattern A_{def}. It is obvious, that front facet damage width and the NF gap matches well for these devices. Furthermore, the thermal signal verifies the defect positions visible by NF gap position and external defect location.

Therefore, thermography can be used to detect the position of the COD-related defect creation. An example for tracing the COD-related hot spot is given in Fig. 5.8(k) showing thermal images of the front facet from device E_4 of batch E. They were recorded in subsequent pulses during a step test with $t_{PW} = 1\,\mu s$ and $\Delta I = 1\,A$. The images are obtained during the pulses from $I = 24\,A$ [sub-figure on top of Fig. 5.8(k)] to $I = 35\,A$ (bottom). The width of the emitter stripe is indicated by the dashed white lines. A clear motion of the hot spot from the right side to the left is visible.

Up to now the thermal signal was discussed as an indicator for the position of the thermal runaway only. The signal strength, however, provides additional information. Figure 5.9 shows data from device A_{10} which experienced a single COD event at $I_{COD} = 9.0\,A$ after $t_{COD} = 142\,ns$ in an 800 ns long pulse. Figure 5.9(a) gives a μPL map of the QW. The defect patterns are visible as two dark areas starting at the front facet. The thermal image recorded during the pulse is shown in Fig. 5.9(b) (with $t_{int} = 10\,\mu s$, $t_{int,eff} = 4.5\,\mu s$, corrected for the thermal background). In sub-figure 5.9(c), a cut through the thermal image in (b) is given by the black dots. The red and blue lines give Gaussian fits to the two peaks. Figure 5.9(d) shows an image of the defect at the front facet as seen through an optical microscope. The larger defect area, see Fig. 5.9(a) around $x \approx -18\,\mu m$, accounts for a higher thermal signal.

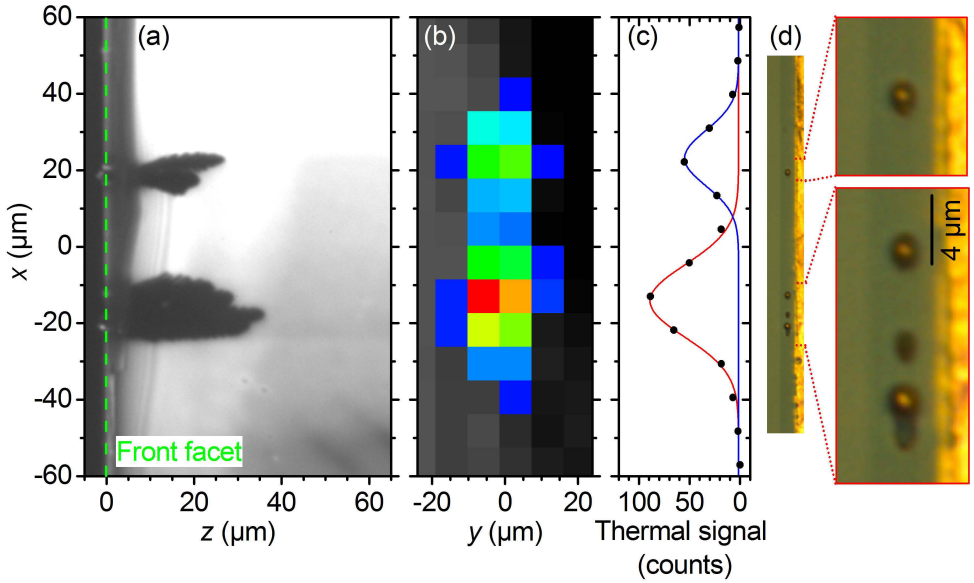

Figure 5.9: Device A_{10} inspected after a single COD event. (a) μPL map of the QW plane after COD failure. The position of the front facet is indicated by the dashed green line. (b) Thermal image of the front facet, recorded during the pulse in which COD occurs, the colorscale give the signal height (blue to red $\widehat{=}$ low to high). (c) The black dots give the cut through the image in (b), the two columns with highest signal are summed up. The blue and red lines give Gaussian fits to the two signal peaks. (d) Image of external part of the defect taken with an optical microscope. The front facet defect is shown on an enlarged scale at the right side. The position in image (d) is indicated. Sub-figures (a-d) are aligned in lateral direction.

Kinetics of the Thermal Runaway

By using the streak camera system focusing on high temporal resolution, it is straightforward to extract time depended information from the NF evolution. In the following, the presentation of the data is limited to two devices. As mentioned in the preceding chapter when discussing the blurring of the borderline in Fig. 4.13, the COD threshold follows a certain distribution depending on small device inhomogeneities. In case of batch A, Fig. 5.10 shows such a histogram of the frequency of COD events during step tests (with $\Delta I = 0.5\,\mathrm{A}$, $t_{\mathrm{PW}} \approx 300\,\mathrm{ns}$). While device A_4 comes right from the middle of the distribution, device A_{11} is rather an outlier on the high current side. This is also the reason why these two devices have been chosen for comparison in this section.

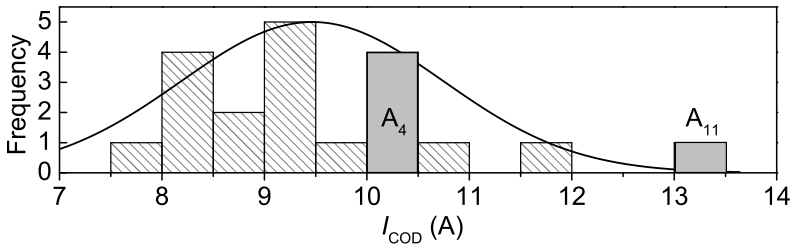

Figure 5.10: Distribution of COD events for device batch A with respect to I_{COD}. The bins containing devices A_4 and A_{11} are labeled accordingly.

Device A_4 has been already introduced in Sec. 5.1.2, especially with Figs. 5.4 and 5.5. This device experienced the first COD in a step test at $I_{\mathrm{COD}} = 10.0\,\mathrm{A}$ with $t_{\mathrm{COD}} = 220\,\mathrm{ns}$ in a $t_{\mathrm{PW}} = 300\,\mathrm{ns}$ pulse. Additionally, a COD re-ignition is provoked by the subsequent identical current pulse.

Figure 5.11(a) shows the NF evolution of device A_{11} recorded with the streak camera during the final step of a step test in which the COD occurs with $I_{\mathrm{COD}} = 13.0\,\mathrm{A}$. The spatio-temporal position is marked by an arrow. Figure 5.11(b) shows the mean NF taken from (a) before (red curve) and after (black curve) COD sets in. In sub-figures 5.11(c) and (d) cuts through the lasing and EL NF are shown, respectively. They are taken with the optical microscope. Figure 5.11(e) gives an image of the front facet affected by COD as seen by the microscope. The data clearly indicates the position of COD. Furthermore, in this case the internal damage width (from lasing NF) matches the external visible damage width [Fig. 5.11(e)].

From the streak camera images of the NF evolution, Figs. 5.4 and 5.11, two temporally resolved quantities are extracted and compared:

- The *width* of the NF gap, Fig. 5.12(a), is extracted in case of COD and COD re-ignition of device A_4 and COD of device A_{11}.

- Additionally, the *reduction of the NF intensity* at the COD site is evaluated, i.e. in the middle of the NF gap; Fig. 5.12(b).

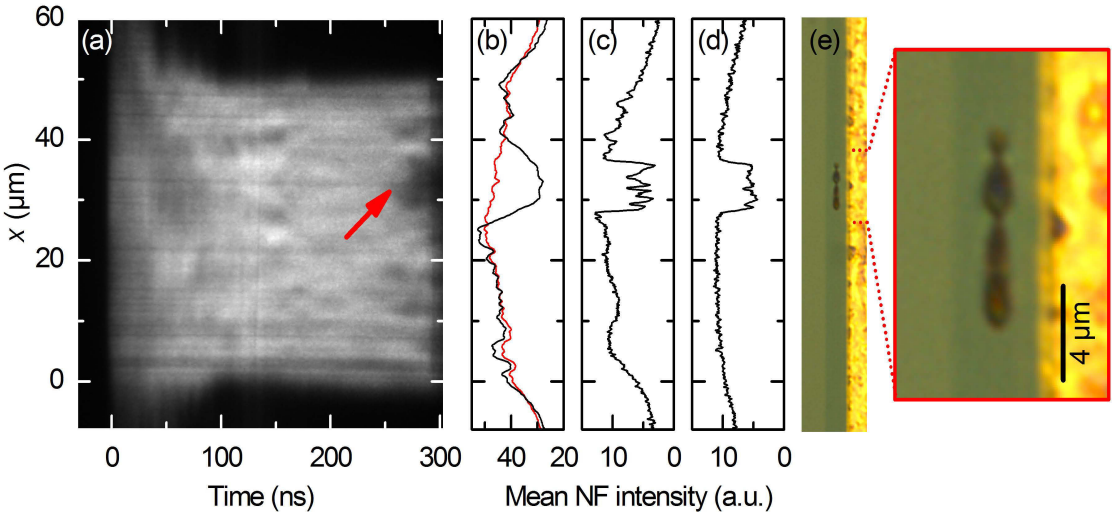

Figure 5.11: NF evolution of the COD event of sample A_{11}. (a) Streak camera image of the NF within the pulse where COD occurs, $I_{COD} = 13.0\,A$. The spatial and temporal position of the first degradation sign is indicated by the arrow. (b) Mean NF intensity taken from (a) before (red curve) and after (black curve) the COD event, which takes place at $\approx 230\,ns$. (c) Cut through mean NF intensity taken from optical microscope while applying $I = 0.5\,A$ (above lasing threshold). (d) Cut through mean NF intensity taken from optical microscopy under EL conditions at $I = 0.1\,A$. (e) COD defects at front facet seen with the optical microscope.

Linear fits to the data in Fig. 5.12(a) give velocities for the NF gap spread. The values obtained for device A_4 are almost the same for the first COD pulse $[(30 \pm 3)\,m/s]$ and COD re-ignition $[(28 \pm 1)\,m/s]$. In contrast the velocity determined for the NF gap of device A_{11} is much faster $[(190 \pm 10)\,m/s)]$. The data for the intensity drop at the COD ignition site in Fig. 5.12(b) are normalized to the intensity at this site before COD. Moreover, the origin of the time axis is set to t_{COD} in both cases. Exponential fits of these curves give characteristic decay times τ_p. The intensity drop during the first $\approx 70\,ns$ is faster in case of device A_4 ($\tau_p = 33\,ns$) compared to device A_{11} ($\tau_p = 77\,ns$).

Optical Mode Induced Defect Spread

Sometimes after device degradation, the optical output power increases at certain locations well separated from the COD ignition site, e.g., indicated by green arrows in Fig. 5.6(b). The presence of an elevated power level can trigger further degradation [156]. The data presented in the following give an example for a second COD ignition site triggered by the change of the lateral mode pattern which is cause by the first COD ignition site. The lasing NF of device F_1 from batch F was monitored during a step test ($t_{PW} = 1\,\mu s$ and $\Delta I = 1\,A$) *en route* to COD. While Fig. 5.13(a) gives the NF during the last single pulse before COD with $I = 29\,A$, (b) shows the pulse in which COD occurs at $I_{COD} = 30\,A$. In order to illustrate the change in the NF amplitude, Fig. 5.13(c) gives a difference image, i.e., (b) minus (a), where blue means a reduced NF amplitude, while red indicates an increase. The NF gaps are separated $\approx 15\,\mu m$ in x-direction. The delay in their occurrence is $\approx 50\,ns$. Higher NF intensities, i.e., red areas, are visible before the NF gaps start to grow.

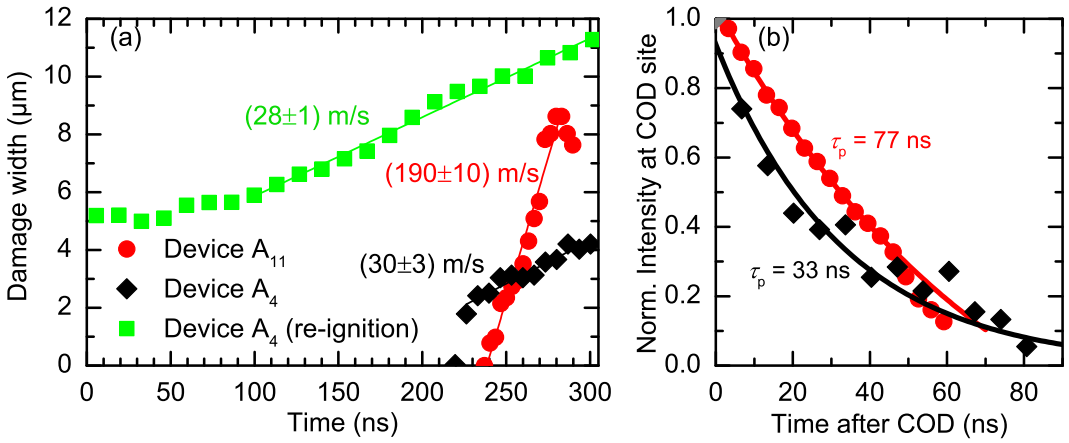

Figure 5.12: (a) Temporal evolution of the damage width (= width of the NF gap) during COD and, in case of device A_4, also during COD re-ignition. The solid lines indicate linear fits to the data and the growth velocities determined this way are given next to them. (b) Comparison of the intensity drops in the middle of COD defect site after onset of degradation. The solid lines indicate exponential fits, their characteristic decay times τ_p are given next to the data.

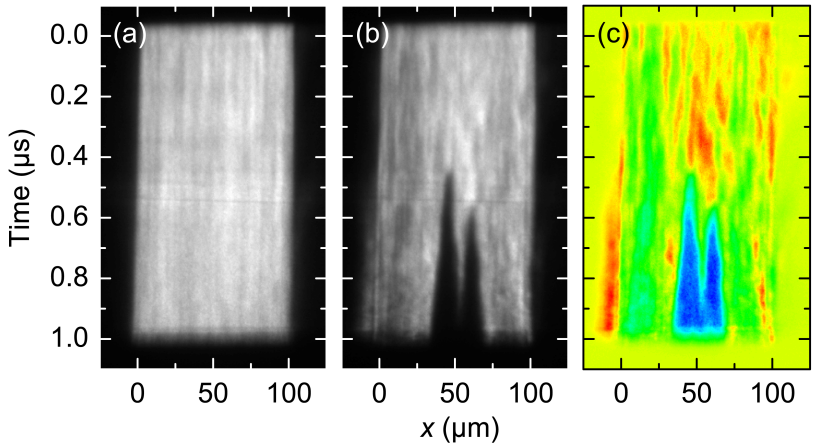

Figure 5.13: Lasing NF of device F_1 from batch F during COD with two separated starting points at the facet. (a) Last single pulse at $I = 29$ A before COD in the framework of a step test. (b) Single pulse with COD occurrence at $I_{COD} = 30$ A. The two initial defect sites are clearly visible as the start points of the two NF gaps. (c) The difference image [(b) minus (a)] illustrates the change in NF amplitude, blue means decrease, while red indicates an increase.

5.1.3 Microscopic Study of Early Defect Stages

In order to gain microscopic understanding of the mechanisms which result in COD, it is straightforward to open damaged devices and image the defect area with high resolution microscopy. Therefore, it is not surprising that work in this field have been done in the past by several authors, see Refs. [52, 157–166]. However, the step test approach introduced in Sec. 3.3 adds a method to prepare devices in very early defect stages, as demonstrated in the preceding section. Furthermore, the amount of energy W_{def} incorporated into the damage and the time of defect growth ($t_{\mathrm{PW}} - t_{\mathrm{COD}}$) are known. As a result, a new quality of samples is available for microscopic investigations [167].

Sample Preparation & External Inspection

In the following, the discussion is focused on two devices from sample batch A: A_{12} and A_4. These samples were chosen, because a large data set characterizing the COD is available for them, e.g., shown in the preceding sections. Table 5.1 summarizes the damage preparation parameters.

Sample	t_{PW} (ns)	I_{COD} (A)	t_{COD} (ns)	W_{def} (nJ)
A_{12}	1500	9	1320	155
A_4 (1$^{\mathrm{st}}$ COD)	300	10	225	45
A_4 (re-ignition)	300	10	≈100	246

Table 5.1: COD parameters of TEM samples. The value for t_{COD} in case of re-ignition is the time at which the NF gap starts to increase again, cf. Fig. 5.12(a).

In order to inspect the samples with microscope systems as introduced in Sec. 3.4, they were prepared by FIB, also described there. The FIB cuts are made perpendicular to the QW plane along the resonator axis, i.e., in the y-z-plane, as indicated by the semi-transparent reddish plane in Fig. 5.14(a).

Figure 5.14(b) shows the COD signature at the front facet of device A_{12} seen with the help of the optical microscope. The region marked as 'epitaxy' contains the QW, cladding, and waveguide layers; as shown in the inset of 5.14(a). Additionally, the location of the defect is visible as gap in the lasing NF (Fig. 5.14(c); $I = 0.5\,\mathrm{A}$), as discussed in Sec. 5.1.2. Sub-figures 5.14(b) and (c) are aligned in their horizontal position, as indicated by the dotted lines between them. A SEM image of the external front facet defect from device A_{12} is given in Fig. 5.14(d). It clearly identifies this structure as material extrusion. The labeling of the visible layers is in accordance with Figs. 5.14(a) and (b). In contrast to the optical micrograph, the n- and p-doped sides may be distinguished in the SEM image, while between waveguide and cladding no contrast is observed. Furthermore, small dark features on both sides, top and bottom, of the extrusion are visible. A similar data set is available for device A_4.

Single COD Event

First, the microscopic analysis of device A_{12} will be presented [167]. Figure 5.15(a) gives an overview image taken with the He-microscope. A cross section is imaged, which is obtained by a cut through the center of the defect pre-characterized in Figs. 5.14(b-d). Under the front facet coating, one clearly sees holes. During the FIB preparation of the samples, it became clear that these hollow spaces are identical with the dark features visible in SEM images of the external damage, see Fig. 5.14(d). The defect under

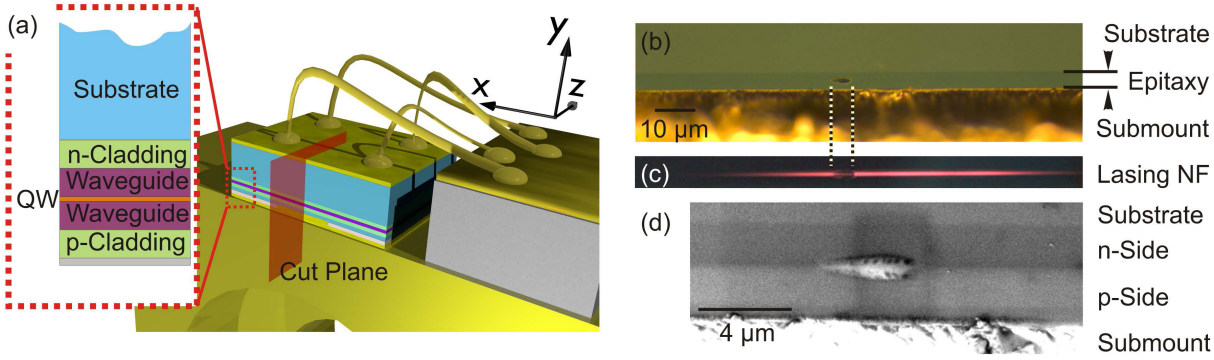

Figure 5.14: (a) Scheme of the mounted DL. The orientation of the sample cross sections is marked as semi-transparent reddish y-z-plane. The inset gives the layer scheme of the epitaxy. (b) Photograph taken with the optical microscope from the front facet of device A_{12} after COD. The surface part of the defect is visible as a spot in the epitaxial layer. (c) Lasing NF of the damaged laser taken at the same position as (b), but without external illumination at $I = 0.5\,\mathrm{A}$. (d) SEM image of the same defect as shown in (b,c).

the surface consists of modified material surrounded by a thin sharp line appearing bright in the used contrast mode. Therefore it will be referred to as 'white line' in the following, although its gray value depends only on the used measurement mode. The 'white line' stays around the damage, even when it becomes narrower in transversal direction with increasing distance from the front facet.

After the inspection by He-microscopy, a $\approx 100\,\mathrm{nm}$ thick TEM lamella was prepared by applying an additional FIB cut from the opposite side. Figures 5.15(b,c) show the region highlighted in Fig. 5.15(a) by a red dashed square on an enlarged scale. They are obtained at the JEM 2200FS TEM in elastic scattering TEM mode with a bright field detector Fig. 5.15(b) and inelastic scattering mode with a high-annular dark field detector Fig. 5.15(c), also known as chemical contrast. The contrast inversion between both images proves the presence of different element concentrations. In order to analyze this, EDX measurements are performed at the positions marked by the numbered red symbols in Fig. 5.15(c). The region denoted 'I' represents the material outside the main defect region. Location 'II' is at the 'white line' and 'III' is between the position where the QW was in the undamaged device, appearing dark in Fig. 5.15(b) and bright in Fig. 5.15(c), and the 'white line' which surrounds the main defect volume. The resulting EDX spectra are shown in Fig. 5.15(d), the respective transitions and elements are given at their peaks. Figures 5.15(e-g) summarize the changes in the element concentrations normalized to the outer region I. The same result is obtained by selecting equivalent measurement points at the opposite side, in y-direction, of the former QW. The EDX analysis reveals that the 'white line' is a region with reduced Ga and increased Al and As content. Additional EDX measurements were made at comparably located undamaged regions. This have been done to verify that the found composition change is a unique feature of the damaged region and not present in the pristine device already, caused, e.g., by composition grading in the structure. Absolutely no composition change has been detected at the pristine reference region, within the error limits of EDX.

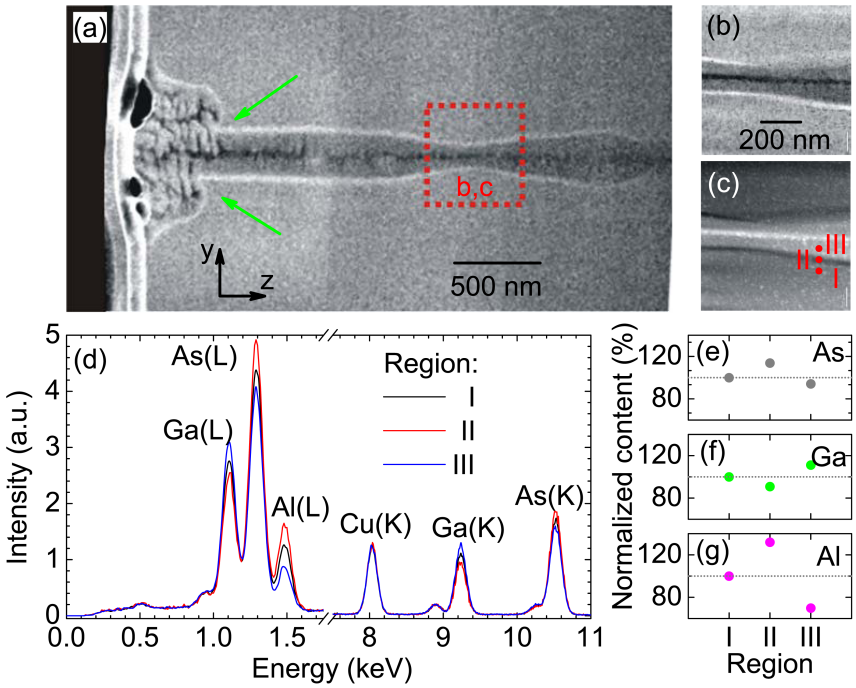

Figure 5.15: Cross section He-microscope image of device A_{12} in the y-z-plane. The abrupt contrast change at about 1.3 μm right from the front facet along z is a result of earlier imaging. Features that are highlighted by green arrows are discussed in Sec. 5.2.3. (b,c) TEM images of the part of the cross section marked by the dotted red line in (a). Bright-field contrast mode was used in (b), while dark-field contrast mode was used in (c). (d) EDX analysis at the three regions indicated in (c), the elements and respective core-shells are labeled. (e-g) The relative change of element concentration is given for the indicated elements with region 'I' taken as reference.

COD Re-ignition

After having analyzed a defect created by a single pulse, the question raises what happens on this scale in case of COD re-ignition. Device A_4 was prepared in order to study the location where this takes place [167]. Figure 5.16(a) shows a SEM image of the external defect part before preparing cross sections of the sample. The dotted line indicates the position of the ≈ 200 nm thick TEM lamella analyzed in the following. The cross section is investigated by the JEM 4000 FX and the JEM 4010 TEM; results are shown in Fig. 5.16(b) and Figs. 5.16(c-f), respectively. The region around the front facet is shown in Fig. 5.16(b). A hollow space, see arrow in Fig. 5.16(b), as seen in Fig. 5.15(a), is also visible under the coating, which has been removed in this preparation step. Furthermore, a defect region is visible around the former position of the QW. The positions where images (c-e) have been taken are highlighted by dotted rectangles in Fig. 5.16(b). Figure 5.16(f) is located right from (e) along the QW. Figures 5.16(c-f) show the region around the former QW on an enlarged scale. As in the He-microscope investigation, cf. Fig. 5.15, a 'white line' surrounds the damage region. While the thickness of the defect is nearly the same in (c) and (f), it is abruptly reduced in (d) and then slowly retrieves its former extent (e) to (f).

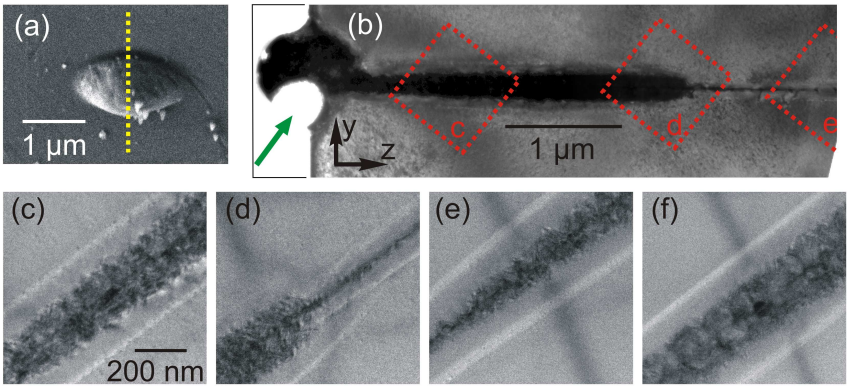

Figure 5.16: Results obtained from the analysis of device A_4: (a) SEM image of the external part of the COD-related damage. (b) TEM overview image of the front part of the cross section in y-z-plane. The arrow points to the hollow space under the front facet coating. (c-f) TEM images on an expended scale taken at the positions marked in (b) and in case of (f) from a position right of 'e' in (b).

5.1.4 Short-Time Thermography

As discussed in Sec. 3.1.3, the thermocamera has the ability to use a short integration time of $t_{\mathrm{int}} = 460\,\mathrm{ns}$. However, with such a short t_{int} only very high temperatures are detectable. This is caused by the high NETD value for short t_{int} ($\approx 44\,\mathrm{K}$ for $t_{\mathrm{int}} = 460\,\mathrm{ns}$). A further limitation is given, if the heat source size is smaller than the area monitored by one pixel, due to monitoring averaged values in this case only. COD represents, however, an ideal application for this approach, since a high temperature is reached for a short time.

Short-time thermography is used to address the question if the COD process stops when the optical power output of the device vanishes. Therefore, a single pulse of $I_{\mathrm{COD}} = 30.5\,\mathrm{A}$ and $t_{\mathrm{PW}} = 500\,\mathrm{ns}$ is applied to device A_{13}. This high current pulse provoked the COD after $t_{\mathrm{COD}} = 46\,\mathrm{ns}$ [red arrow in Fig. 5.17(a)]. The associated current and power curves are shown in Fig. 5.17(a). Thereafter, a subsequent pulse with $I = 30.5\,\mathrm{A}$ was applied to re-ignite the COD. During this pulse a thermal image is acquired with the mentioned short t_{int}. This integration window is placed around the trailing edge of the pulse in order to detect if there is still a significant heating after the optical output power has vanished. The COD re-ignition takes place at about $t_{\mathrm{COD}} = 26\,\mathrm{ns}$ and after $\approx 200\,\mathrm{ns}$ the detected power has dropped to noise level, see Fig. 5.17(b). Nevertheless, the thermal image, see inset of Fig. 5.17(b), shows a clear signal from the front facet (verified by the geometric background image taken at exactly the same position).

The front facet of the device has been inspected by optical microscopy before and after the second high-current pulse. Figures 5.17(c,d) show the external defect pattern after the first COD ignition (c) and after the re-ignition (d). No difference can be observed which indicates that no further damage was added to the facet in the second pulse. Nevertheless, the device degraded further, visible in the output power characteristic [Fig. 5.17(b)].

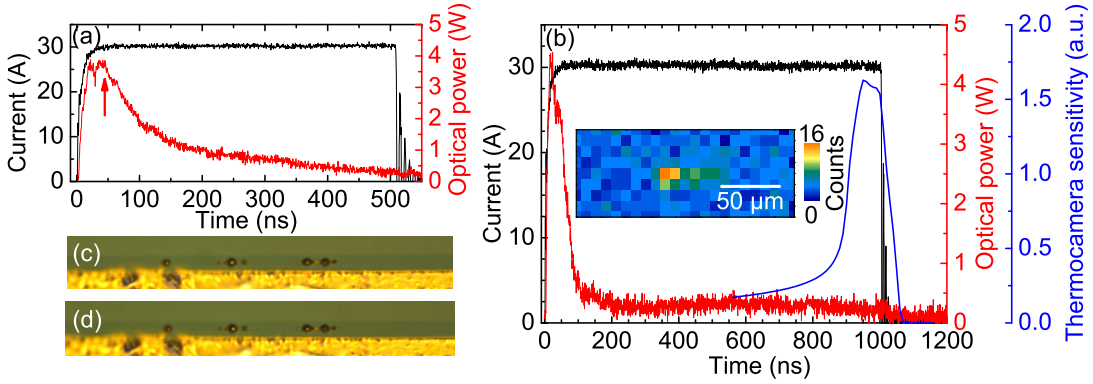

Figure 5.17: Results on device A_{13}. (a) Current and optical output power during the initial COD event. The point at which COD occures is marked by an arrow. (b) COD re-ignition. The current and optical power traces are given. Additionally, the temporal characteristic of the image integration window of the thermocamera is shown. The inset gives the thermal image of the front facet region recorded during the single pulse. (c,d) Images of the front facet taken with the optical microscope: (c) after the initial COD event, (d) after COD re-ignition.

5.2 Discussion of Second Phase Results

5.2.1 Spatially and Temporally Resolved Dynamics

Figure 5.3 relates the characteristic power decay times τ_{drop} to the optical power at the facet which initiated the COD. Three clearly separated groups are visible. The distribution of the data for each wavelength along a line, as indicated in the graph, is caused by the distinct relation between t_{COD} and P_{COD}, see Fig. 4.13 as an example for batch A. Nevertheless, there is a clear deviation between the behavior of different material systems. The power drop time of the long-wavelength devices is approximately an order of magnitude longer than for the shorter-wavelength ones. This is one reason why the record COD thresholds are achieved with devices in the so-called 9XX nm wavelength range, e.g., demonstrated by Petrescu-Prahova *et al.* [81]. A deeper understanding of the mechanisms that cause the different τ_{drop} values and the connection to material parameters requires extended knowledge about the damage expansion. This will be addressed in the following by evaluating spatially resolved data.

Time-Resolved Nearfield Analysis

Figures 5.5, 5.6, 5.7, 5.9 and 5.11 give comparisons of external defect patterns, internal defect patterns and the recorded NFs. The results verifies that the NF gap gives more accurate information about the lateral defect extension than the external visible front facet damage, e.g., Fig. 5.5(d). This verifies the assignment of the width of the NF gap, e.g., visible in Fig. 5.4, with the width of the internal damage pattern. Therefore, the lateral damage expansion can be observed on the picosecond time scale with the streak camera.

There is a difference, however, if one considers the EL or lasing NF, as shown for the well extended defect in Fig. 5.7. The different behavior of both signals is caused by their different origins. Lasing requires undamaged active material on a straight line between the mirrors, while this is not the case for EL. Therefore, no lasing action is left in case that the full width of the emitter stripe is damaged as in Fig. 5.7(c). In contrast to that, the EL results from spontaneous emission from the undamaged material next to the facet, indicated as yellow shaded area in (c). That is why the yellow shaded areas in Fig. 5.7(c) fit in their extend to the signals seen in (b).

This shows, that lasing and EL NFs provide different information, particularly if the damage is rather extended. The EL NF provides information about the defect spread at or under the front facet surface. The streak camera, while monitoring the lasing NF, gives direct information about the entire internal damage extension in lateral direction on the picosecond time scale.

Thermal Signal Analysis

It is obvious, that the thermal signal is also a good indicator for the position of COD, within the limits of achievable spatial resolution, see Fig. 5.8. In case of the two data sets shown in Fig. 5.8(a-j), NF monitoring, light-microscopic inspection of the external damage, and thermography give similar lateral damage widths. The major difference between these devices (A_8 and A_9) and the ones shown prior to them is, that there was no slow approach to the I_{COD} value with small ΔI. A high current is applied in the single pulse, resulting in a situation where $t_{COD} \ll t_{PW}$. A result of the high current is that the starting conditions needed for COD have been met at several places along the facet in a short time interval. This leads to a situation, where the external visible damage width is the same as the internal, proofed by the lasing NF gap, in Figs. 5.8(b) and (g). In contrast, the typical situation provoked in step tests with small ΔI, i.e., slowly approaching COD threshold, results in a single small external defect, see Figs. 5.5(d) and 5.6(d). Due to the step wise increased optical load on the facet, COD starts at the weakest point[1]. After creation of the initial damage, the defect spread proceeds in the interior, leading to the discrepancy between the external visible defect width and the real existing internal one. This means, that the external visible defect area A_{def} is only meaningful for further considerations, if a high I_{COD} value is chosen, so that $t_{COD} \ll t_{PW}$.

The approach to COD threshold in a step test is found to result in the same defect pattern as cw tests. This gives further evidence that the step test addresses the same degradation mechanisms as cw device tests, i.e. represents a special type of accelerated aging.

As demonstrated, thermography gives information about the position of COD occurrence. Nevertheless, the time-resolved NF measurement provides more accurate information about the COD defect site, due to the higher optical and temporal resolution. However, there is another difference between the two methods. The NF gap imaged by the streak camera gives the total width of the defect region. The kinetic of the defect is only visible at the edges of the existing gap. In contrast, the thermal signal shows the motion of the hot spot, i.e., the location where the thermal runaway takes place and damage is added to the existing defect pattern. Figure 5.8(k) shows a measurement illustrating this. The clear motion of the hot spot from the right to the left side of the emitter stripe reveals that not the entire existing defect is

[1]The term 'weakest point' stands here for the combination of optical intensity and material quality. Even if the material quality is homogeneous the NF intensity normally is not. Therefore, 'weakest' is here used as a system description and not necessarily as indicator for lower material quality.

heated up again during COD re-ignition in the subsequent pulses.

Not only the position of the thermal signal can be evaluated, its amplitude is meaningful, too. Figure 5.9(a) gives the internal defect pattern created in device A_{10}. It is within the focal depth of the thermocamera of $\approx 40\,\mu$m (this value is determined experimentally, cf. Sec. 6.1.2). Therefore, the entire process leading to the final defect pattern contributes to the thermal signal. This can be verified by comparing the areas of the two well separated defect regions with the areas under the two thermal peaks, each fitted by a Gaussian curve. The area of the more extended defect pattern is $486\,\mu\text{m}^2$, whereas the smaller one has $185\,\mu\text{m}^2$. The fits shown in Fig. 5.9(c) give areas of 2079 a.u. (red curve) and 971 a.u. (blue curve). This gives ratios between the thermal signal and the defect area in the QW plane of ≈ 2.2 for the defect centered around $x = -18\,\mu$m in lateral direction, and ≈ 2.6 for the one at $20\,\mu$m. Both ratios show a good agreement[2] so that the thermal signal height is indeed an indicator for the extension of the defect. In comparison to the streak camera approach, this is not limited to the lateral dimension.

This can be used to study the damage growth during COD re-ignition. In particular, the short-time thermography measurement shown in Sec. 5.1.4 is used to clarify if the process stops if the entire width of the laser stripe is affected by COD. The detected thermal signal in Fig. 5.17(b) is small but meaningful, taking into account the short integration time, i.e., short time to collect photons of Planck's radiation. In Sec. 6.1, it will be shown that the detection limit in case of this single pulses is about $400°\text{C} - 500°\text{C}$ for a COD site. Therefore, this signal is indicative for these high temperatures. It shows, that, even if nearly no more (laser and EL) light leaves the device, there is still enough energy transferred into the damage site to create such high temperatures. Therefore, it is highly likely that the damage growth goes on, although one mirror of the cavity – in this case the front facet – is destroyed. There, the high loop gain of the DLs comes into play. The amplified spontaneous emission from the remaining undamaged active material is sufficient to provide enough light energy. This light cannot be detected outside the laser, because it is absorbed by the damaged region close to the front facet. This finding will be used in energy balance considrations in Sec. 5.2.2. The COD re-ignition has not affected the front facet, but continued the defect growth in the facet near region into the interior. Exactly this has been verified by the thermocamera and the unchanged external defect, cf. Figs. 5.17(c,d). The short-time thermography measurement confirmed, that the defect growth process is not necessarily stopped when the detected optical output power vanishes. Moreover, the unchanged external defect pattern after the re-ignition admonishes of being cautious with predictions about the internal damage based on the external defect pattern.

Variation of τ_{drop} with Wavelength

With the knowledge about the internal damage expansion discussed in Sec. 5.1.2, it is worthwhile to discuss the resulting τ_{drop} values for different material systems presented in Sec. 5.1.1. As shown, the remaining lasing intensity leaving the DL, which is what the PD monitors, depends on the total internal defect width. This means if the entire stripe width is covered in lateral direction by damaged regions the lasing signal will vanish. At early stages the damage growth is almost isotropic. By taking into account that the emitter stripes are $\approx 50 - 200\,\mu$m wide but $\approx 1000 - 2000\,\mu$m long, the effect on the lateral direction is indeed stronger. Therefore, the characteristic time τ_{drop} is mainly determined by the

[2] The remaining difference is mainly caused by the lower sensitivity of the thermocamera for events close to the limits set by the focal depth.

lateral spread of the defect, while the extension along the cavity is of minor relevance at early stages of defect propagation. The key to understand the different lateral defect velocities are the different specific thermal resistances (R_λ) of the active region designs for different wavelengths. Materials with lower R_λ show lower lateral defect spread (discussed in detail in Sec. 6.3.3). The material that has to be considered here is the waveguide material. It removes the main thermal load, because the QW itself is thin (it can be seen as two-dimensional). The main heat flux goes into the surrounding region, i.e., the waveguide. On the other hand, a better heat removal from the active region allows to reach higher P_{COD} values, as demonstrated by Fujii *et al.* [168]. This explains the arrangement of the data points along lines for different wavelength in Fig. 5.3. There, the material with the lowest thermal resistance ($\lambda_\mathrm{c} = 980\,\mathrm{nm}$,$\mathrm{Al}_{0.085}\mathrm{Ga}_{0.915}\mathrm{As}$, with $R_\lambda = 4.5\,\mathrm{K\cdot cm/W}$) is in the upper right corner, i.e., higher maximal optical powers and longer drop times. The materials with higher thermal resistance have smaller values on both axis ($\lambda_\mathrm{c} = 808\,\mathrm{nm}$, $\mathrm{Al}_{0.3}\mathrm{Ga}_{0.7}\mathrm{As}$, with $R_\lambda = 8\,\mathrm{K\cdot cm/W}$ and $\lambda_\mathrm{c} = 650\,\mathrm{nm}$, InGaAlP, with $R_\lambda = 13\,\mathrm{K\cdot cm/W}$)

Initial Defect Growth Kinetics

Figure 5.12 shows two quantities extracted from lasing NF images. There, similar data sets are compared for two devices representing different positions in the I_{COD}-distribution of the batch, see the indicated columns in the histogram Fig. 5.10. As discussed, the width of the lasing NF gap gives the total internal damage width. Furthermore, the signal intensity can be interpreted as an information about the defect extension, too. Its value at the COD site monitors the defect growth in z-direction, i.e., the depth of the defect along the resonator axis. This is caused by the travel of the defect front, preventing more and more light passing the defect above or below, in y-direction, the COD site.

For both devices, the onset of damage creation lies between 220 ns and 240 ns, Fig. 5.12(a). The degradation starts with a jump-like creation of a defect with a width of $\leq 2\,\mu\mathrm{m}$ in less than 700 ps and $\leq 1\,\mu\mathrm{m}$ in $\leq 400\,\mathrm{ps}$ in case of device A_4 and A_{11}, respectively. These values result from data, e.g., presented in Fig. 5.4. There the NF gap emerges this fast that a continuous expansion for the very first moment cannot be detected. This is why only upper limits for this dynamics can be given. This fast onset represents most likely the initial thermal runaway event. The measured time ranges are in good agreement with the modeling work by Henry *et al.* [46] and Nakwaski [137, 169]. They calculated times in the nanosecond range and below.

After this fast onset, the lateral damage expansion continues with an almost constant velocity of $(30 \pm 3)\,\mathrm{m/s}$ in case of device A_4 and $(190 \pm 10)\,\mathrm{m/s}$ for device A_{11}. Device A_4 has been subjected to a subsequent current pulse of same length and magnitude as used for the first COD ignition. The evolution of the damage width in case of re-ignition, Fig. 5.12(a), proceeds with a velocity of $(28 \pm 1)\,\mathrm{m/s}$. It is almost the same value as in the previous pulse. This is a clear evidence for an almost constant energy feeding of the growth process. Furthermore, the constant growth velocity in both pulses accounts for the absence of significant material inhomogeneities. The much higher, but also constant, velocity in case of device A_{11}, indicates a constant energy feed of the process at a higher level than in device A_4. This is not surprising due to a 3 A higher current, resulting in an elevated optical power (confirmed by the L-I curve).

The drop of the intensity after the first COD event in both devices is given in Fig. 5.12(b). The time τ_p introduced here is not to be confused with the power decay time τ_{drop}. The value for τ_{drop} can also be obtained by considering the decrease of the integral output power, e.g., in case of device A_4 this gives

$\tau_{drop} = 180\,ns$, which matches the values shown in Fig. 5.3.

Taking both data sets into account, the NF gap giving the width of the damage and the intensity drop giving the depth of the damage, the defect expansion for devices A_4 is more pronounced in z-direction compared to device A_{11}. However, this is only valid for a short period of time after the onset of COD, see intersection of both curves after $\approx 70\,ns$ in Fig. 5.12(b). For later times the defect kinetics of both devices becomes similar. If a device shows faster lateral defect expansion, than it experiences an accelerated optical power drop. This slows down the damage growth automatically, resulting in the described convergence.

The kinetics at different positions in the COD threshold distribution for one device batch indicates that the value of I_{COD} is crucial for the dynamics of the first COD occurrence. This means, the available optical energy is of importance, verifying the concepts of a fast energy redeposition by re-absorption of the laser light.

Optical Mode Induced Defect Spread

The lasing NF is not only a passive probe for the COD damage as discussed in the preceding sections. The COD-related change in the mode pattern can lead to further degradation. Figure 5.13(c) shows the NF evolution of device F_1 were two COD ignition sites in a single current pulse are present.

The first COD site appears after $t = 0.45\,\mu s$ in the pulse at $46.5\,\mu m$ after a filament of high NF intensity was present at this place. This confirms COD ignition to be related to high light intensities. Then the mode pattern start to redistribute which is a dynamic process, because the NF gap and therefore the defect width increases with time. This leads to a high amplitude filament that moves in lateral direction due to thermal lensing [115]. Eventually, this local high intensity causes the occurrence of a second COD site after $t = 0.56\,\mu s$ at $60.8\,\mu m$, see Fig. 5.13(c). It is most likely that this filament hits a region of the front facet that has a slightly lower COD threshold during its lateral motion. This means that the distance between the COD sites is an indicator for facet quality and homogeneity. The results show that the optical mode redistribution can act as fast defect spread mechanism by causing an additional COD ignition site well separated from the first one.

5.2.2 Energy Balance of COD

Energy Re-Distribution Indicated by Power Drop

An advantage of the step test approach is the knowledge about the energy incorporated into damage growth. Therefore, the time-resolved optical output power traces can be considered. A typical curve, taken from device A_{12} is given in Fig. 5.18. The onset of COD is around $t_{COD} = 1320\,ns$. As long as the entire defect width is small against the emitter stripe width, it can be assumed, that the internal power in the laser cavity is almost constant. The energy missing in the output power after COD onset is supposed to be used for creating the damage[3]. In order to determine this energy W_{def}, the area between a hypothetical curve for the pulse without COD $[P_{hypo}(t)]$ and the actual measured one $[P_{real}(t)]$ has to be calculated. The time span for this integral is given by t_{COD} and the time (t_{end}) when the power drops to $P_{real}(t_{COD})/e^2 = 0.135 \cdot P_{real}(t_{COD})$, or when the pulse ends. The hypothetical curve for the COD free

[3] In principle, the amount of absorbed energy should be rather calculated from the internal optical power than from the external one. However, due to the low reflectivity of $\approx 3\%$ of the out-coupling facet, both values are very similar.

case is obtained by scaling the output power curve recorded during the last current step before COD to the same staring level. This approach is cross-checked with curves from devices of the same batch under similar conditions that experienced COD at higher currents. This distribution of I_{COD}, determined by small device inhomogeneities, is characterized by the histogram in Fig. 5.10 for batch A.

At this point one might ask, if the intra-cavity laser power does not decrease at the same moment and therefore the assumption that the energy W_{def} is re-distributed is simply wrong. In order to rule this possibility out, two experiments have been done:

First, the small amount of optical power transmitted through the high-reflective ($\approx 99\%$) rear facet of a device from batch A is used as monitor for the optical power in the cavity. In parallel, the power is measured which is emitted through the front facet. At the moment of approaching the COD threshold, a substantial power drop at the front facet (the COD occurred there) has been seen, while no decrease was measured at the (undamaged) rear facet. This means that the optical power in the cavity remains almost constant. The drop seen from the front facet is a result of the defect blocking the light path. In doing so, it can be assumed that this not-detected light energy is absorbed by the defect.

In a *second* experiment, several devices from batch F have been used. During the experiments it turned out that this device structure tend to rear facet COD. This is utilized as follows: The evolution of the lasing NF during the step test has been monitored by the streak camera. From the performed experiments including *ex-post* localization of the damage volume by SEM and EBIC, it is known that a defect at any position in the laser cavity influences the lasing NF. In this way, a sudden change of the lateral mode pattern indicates the COD onset at t_{COD}. In parallel the output power at the front facet (sum of lateral resolved lasing NF signal) was recorded as a measure of the intra-cavity optical power. The results show that no significant power drop at the front facet can be seen around the onset of COD. In some cases, the power showed a slight decrease, but in most cases it remains on approximately the same level. This has been found to remain true as long as the lateral defect extension keeps small compared to the emitter width.

Following this argumentation, it is valid to calculated the energy W_{def} as:

$$W_{\mathrm{def}} = \int_{t_{\mathrm{COD}}}^{t_{\mathrm{end}}} \left[P_{\mathrm{hypo}}(t) - P_{\mathrm{real}}(t) \right] \, \mathrm{d}t \quad . \tag{5.2.1}$$

The corresponding area is green-shaded in Fig. 5.18. This describes the process of a specific energy re-distribution. The laser light field collects energy via stimulated emission from the active material along the entire laser cavity and stores it in a small defect volume. In case of device A_{12}, the obtained value of this re-deposited energy is $W_{\mathrm{def}} = 155\,\mathrm{nJ}$.

At this point the question arises, if it is necessary to take the re-absorbed light energy (W_{heat}) into account which heats up the bulk and also the front facet region. In order to estimate W_{heat}, the drop in optical output power (without COD influence) during a single pulse can be considered. The value of W_{heat} is calculated by integrating the area between a constant curve set to the maximal power (P_{max}) obtained at the leading pulse edge at t_{max}, in case of Fig. 5.18 at 150 ns, and $P_{\mathrm{hypo}}(t)$:

$$W_{\mathrm{heat}} = \int_{t_{\mathrm{max}}}^{t_{\mathrm{end}}} \left[P_{\mathrm{max}} - P_{\mathrm{hypo}}(t) \right] \, \mathrm{d}t \quad . \tag{5.2.2}$$

The corresponding area is red-shaded in Fig. 5.18. The obtained energy is $W_{\mathrm{heat}} = 1337\,\mathrm{nJ}$. This value is ten times larger than the one for W_{def}, see also ratio between the shaded areas in Fig. 5.18.

However, the volumes where these energies are stored differ much more. The inset of Fig. 5.18 gives a schematic top view onto the device structure. The energy W_{heat} is absorbed in the entire emitter stripe with the volume V_{emitter} = length × width × thickness $= 1.4\,\mathrm{mm} \times 50\,\mu\mathrm{m} \times 1\,\mu\mathrm{m} = 7 \cdot 10^4\,\mu\mathrm{m}^3$ (a thickness of $1\,\mu$m is assumed for QW and waveguide). The defect volume (V_{def}) can be estimated from TEM cross sections prepared from this device (these data will be discussed in Sec. 5.2.3), times the width of the external damage visible at the facet surface. The result is $V_{\mathrm{def}} = 8.4\,\mu\mathrm{m}^3$.

Taking into account the different volumes, one can estimate the corresponding energy densities. The assumption of a homogenous distribution is a good approximation for the bulk, even if it is known that the temperature is slightly higher around the front facet, e.g., discussed by Menzel [143]. For the bulk heating this gives $19\,\mathrm{pJ}/\mu\mathrm{m}^3$ and an energy density of $18\,\mathrm{nJ}/\mu\mathrm{m}^3$ for the damage volume. The values differ by three orders of magnitude. This verifies the assumption that the contribution of W_{heat} can be neglected while dealing with the damage growth. Notice, that the contribution of W_{heat} is nevertheless important for reaching T_{crit}, cf. Sec. 2.2. The contribution of the bulk heating have been discussed in Sec. 4.2.3, in particular for the temperature at the facet, and will be further emphasized in Sec. 7.1.

To cross-check the made assumptions, the temperature rise (ΔT) in the material can be estimated. Caused by the short t_{PW} and the even shorter time between t_{COD} and t_{end} it is valid to neglect the heat transport in the device. This is in line with the studies done by Ziegler *et al.* [170, 171] and Kappeler *et al.* [127]. Therefore, the following simple expression can be used for the relation between an energy

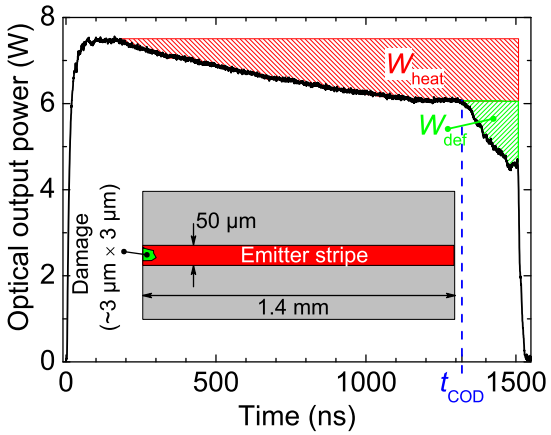

Figure 5.18: Temporal evolution of optical output power for device A_{12} during the pulse where COD occurs. The time t_{COD} is indicated. The green-shaded area represents the energy W_{def} incorporated in the defect growth. The red-shaded area gives an estimate for the energy W_{heat} of re-absorbed laser light leading to bulk temperature increase. The inset shows a top view onto the laser structure (x-z-plane). The emitter stripe is shown as red rectangle and its dimensions are given. The position of the damage pattern at the front facet is indicated as green area.

(W_{theo}) deposited in a specific volume and the resulting ΔT:

$$W_{\text{theo}} = c \cdot \rho \cdot V \cdot \Delta T \qquad \Rightarrow \qquad \Delta T = \frac{W_{\text{theo}}}{c \cdot \rho \cdot V} \quad , \tag{5.2.3}$$

with the specific heat $c = 0.372\,\text{J}/(\text{gK})$ and mass density $\rho = 4.774\,\text{g}/\text{cm}^3$ (values for $Al_{0.35}Ga_{0.65}As$, i.e., the waveguide material, taken from [172]). Putting in the values of W_{heat} for W_{theo} and V_{emitter} for the volume V in case of bulk heating gives $\Delta T \approx 11\,\text{K}$. This value is approximately the half of the temperature rise expected from the measurements of the spectral line shift of the emission presented in Sec. 4.2.2. This deviation is an effect of the averaging over the entire volume and of the assumption that only the missing energy in the output power contributes to the heating. Considering the deviation between applied electrical energy and extracted optical energy as heat energy deposited in the active region, one ends with a temperature rise of $\approx 20\,\text{K}$. Since these values are on the same order of magnitude, the made assumptions are valid. It demonstrates that the drop indicated by the red-shaded area in Fig. 5.18 can be neglected in calculations of energy introduced in the defect site. The bulk temperature rise and the temperature rise in the damage volume can be analyzed separately. A systematic investigation of W_{def} is presented in the following subsection.

Fast Energy Re-Distribution

In Sec. 4.1.1 and especially in Fig. 4.13 it is shown, that t_{COD} varies over two orders of magnitude depending on I. This means that the optical energy available for the thermal runaway also varies. An energy balance calculation is used in the following to verify that the COD is characterized by an initial local melting. This process is fed by thermal excess energy from local laser light absorption. If the basic concept keeps the same while I_{COD} (and therefore P_{COD} due to their relation via the L-I curve) varies over a wide range, the energy needed to create the damage volume should show a linear dependence on the available energy.

The available energy W_{def} is calculated following Eq. (5.2.1). The energy needed to create the damage is W_{theo} from Eq. (5.2.3). The COD data set from device batch A used in Fig. 4.13 is evaluated. In case of these devices, a high current was applied in a way that t_{COD} was reached close to the leading pulse edge. In this case, as demonstrated in Sec. 5.1.2, A_{def} (damage area at front facet) represents a good measure for the entire, especially internal, damage volume. The value of W_{def} has been calculated for every COD event from this sample set. Additionally, A_{def} was determined as shown in Fig. 5.8. Figure 5.19 shows an essentially linear correlation between these values. The meaning of the two outliers, indicated as open symbols, will be discussed later.

In order to calculate the values of W_{theo} following Eq. (5.2.3), the values for $Al_{0.35}Ga_{0.65}As$ are used again. Furthermore, the damage volume is calculated by multiplying the A_{def} values by a depth of $15\,\mu\text{m}$. This depth is verified by evaluating several cross sections of COD defects from device batch A. Nevertheless, due to the time and cost intensive device preparation, not all devices have been investigated this way. Therefore, this depth remains an approximation.

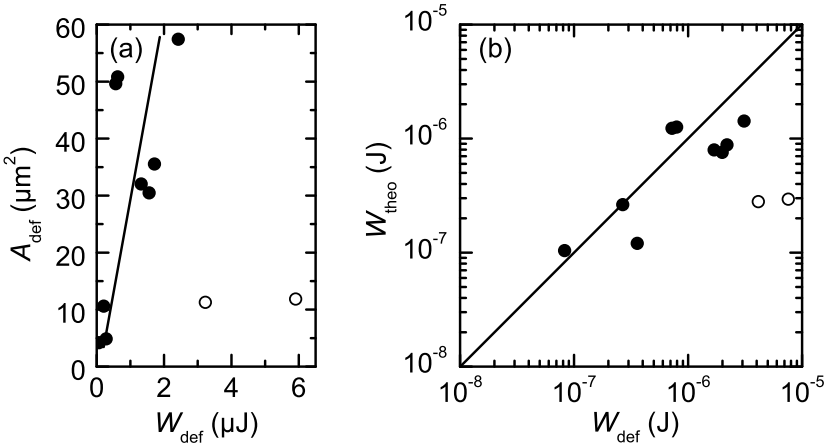

Figure 5.19: (a) Damage area at the front facet A_{def} versus the absorbed optical energy W_{def} calculated from the COD-related drop in the output power transients. (b) Calculated thermal energy W_{theo} required to heat the damaged device volume to the materials melting point as a function of the absorbed optical energy W_{def}. The solid lines in both sub-figures are guides to the eye. The open circles represent outliers which are discussed in the text.

Additionally, this follows the finding that for a high I_{COD} value the damage extension is more pronounced in lateral direction which allows us to use a constant depth. As value for ΔT, the difference between the melting temperature of $Al_{0.35}Ga_{0.65}As$ (1580°C) and the ambient temperature (23°C) is taken. Therefore W_{theo} represents the energy necessary to bring the damage volume to the materials melting point.

Figure 5.19(b) gives the W_{def} and W_{theo} values for all devices that experienced COD in Fig. 4.13 in a double-logarithmic plot. Notice, that the small amount of energy is neglected in this analysis that is needed to reach T_{crit}. A linear correlation with $W_{def} \approx W_{theo}$ is found for the majority of the devices [solid circles in Fig. 5.19(b)] covering nearly two orders of magnitude on the respective energy scale. This strongly supports the COD scenario outlined above, including temperatures around 1580°C, which is the melting point of $Al_{0.35}Ga_{0.65}As$, i.e., the waveguide material. Furthermore, it characterizes the COD as a mainly thermal effect. The two open circles in Figs. 5.19(a) and (b) which lie significantly away from the correlation line, represent devices with longer t_{PW} of 5 μs and 100 μs (compared to $t_{PW} = 1\,\mu$s) and experience COD in the microsecond time range. On this time scale, the heat transport from the damage volume into other parts of the device cannot be neglected anymore. It reduces the deposited excess energy W_{def}. Therefore, COD is induced with a fraction of W_{def} only. Thus, also these data points support the presented findings.

The correlation of the energy data verifies the assumed concept of a fast energy re-distribution from the entire active volume via the laser light field into a small damage volume. Furthermore, the heating of this volume to the materials' melting point is assured.

Temperature Estimation Based on Thermal Images

At this point, it is worthwhile to show how temperatures can be estimated from thermal images as in Figs. 4.2(j-l). Therefore, an experimental calibration is done. In order to connect the measured infrared radiant power and the temperature, a laser of the batch (in this case batch A) under investigation is heated up and stabilized at several temperatures in the range from 23°C to 200°C. Temperatures above this value have been extrapolated according to Planck's law, while taking into account the spectral responsivity of the thermocamera and the transmission properties of the optical elements. Details about such type of calibration and a discussion about effects leading to uncertainties are given by Ziegler [173]. The first step is to take into account that the heat source is much smaller than the area A_{pixel} imaged by a camera pixel. A feasible assumption for the size of the heat source is A_{def}. This leads to a simple geometric scaling of the experimentally determined thermal flash amplitude (F_{exp}), which is a function of the temperature transient T_{flash} of the damage region during the flash (t is the time):

$$F_{\mathrm{exp}}\left(T_{\mathrm{flash}},t\right) = F_{\mathrm{exp}}\left(T_{\mathrm{flash}},t,A_{\mathrm{def}}\right)\frac{A_{\mathrm{def}}}{A_{\mathrm{pixel}}} \quad . \tag{5.2.4}$$

Taking this into account, one gets a calibration curve connecting the measured thermal signal and the temperature, see Fig. 5.20(a).

The next step is to account for the temporal averaging of the measured heat flow during $t_{\mathrm{int,eff}} \approx 4\,\mu\mathrm{s}$. Within this integration time a temperature transient as schematically shown in Fig. 4.1 is assumed. The value of $T_{\mathrm{flash}}(t)$ first increases with the time constant τ_{drop} between 30 ns and 400 ns, as determined in Sec. 5.1.1. The damage volume reaches its maximal value (T_{max}) when most of the excess energy has been absorbed at t_{end}. Subsequently, the heated volume cools down to ambient temperature (T_0) with a material related time constant (τ_{cool}).

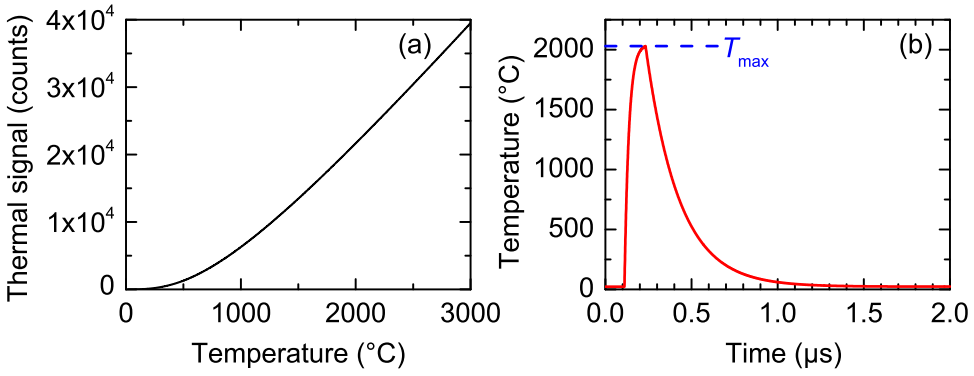

Figure 5.20: (a) Result of thermocamera calibration. One of the DLs from batch A is thermoelectrically stabilized to the calibration temperature. The resulting thermal signal is recorded. Notice, the thermal counts here are scaled already by taking into account the heat source size during COD. (b) A typical temperature transient determined following Eq. (5.2.5) from the thermal image shown in Fig. 4.2(l).

Therefore, the time-averaged flash amplitude is given by:

$$\begin{aligned} F_{\mathrm{exp}}\left(T_{\mathrm{flash}}\right) &= \int_{t_{\mathrm{COD}}}^{t_{\mathrm{end}}} F_{\mathrm{exp}}\left(T_{\mathrm{flash}}(t)\right)\,\mathrm{d}t + \int_{t_{\mathrm{end}}}^{t_{\mathrm{int,eff}}} F_{\mathrm{exp}}\left(T_{\mathrm{flash}}(t)\right)\,\mathrm{d}t \\ &= \int_{t_{\mathrm{COD}}}^{t_{\mathrm{end}}} F_{\mathrm{exp}}\left(\left[T_{\mathrm{max}}-T_0\right]\left[1-\exp\left(-\frac{t}{\tau_{\mathrm{drop}}}\right)\right]/a\right)\,\mathrm{d}t + \\ &+ \int_{t_{\mathrm{end}}}^{t_{\mathrm{int,eff}}} F_{\mathrm{exp}}\left(\left[T_{\mathrm{max}}-T_0\right]\exp\left(-\frac{t}{\tau_{\mathrm{cool}}}\right)\right)\,\mathrm{d}t \quad , \end{aligned} \tag{5.2.5}$$

with the normalization factor $a = 1-\exp(-\tau_{\mathrm{drop}}/\tau_{\mathrm{cool}})$ to keep the temperature curve continuous. The value of τ_{cool} is given by:

$$\tau_{\mathrm{cool}} = \rho \cdot V_{\mathrm{def}} \cdot c \cdot R_{\mathrm{th}} \quad , \tag{5.2.6}$$

with the absolute thermal resistance $R_{\mathrm{th}} = d/(k_{\mathrm{therm}} \cdot A_{\mathrm{surf}})$ of the bulk material of thickness d which surrounds V_{def} with surface area A_{surf}. The thermal conductivity $k_{\mathrm{therm}} = 0.55\,\mathrm{W\,cm^{-1}\,K^{-1}}$ and specific heat $c = 0.33\,\mathrm{J/(gK)}$ of GaAs are assumed. The main temperature gradient in heat transport is present over the thickness d. This value can be approximated from the thermal images (taken with the CEDIP thermocamera), e.g., shown in Figs. 4.2(j-l). Within $t_{\mathrm{int,eff}}$ the strongly heated area covers only two camera pixels, resulting in $d = 9.4\,\mu\mathrm{m}$. This yields to $\tau_{\mathrm{cool}} = (180 \pm 20)\,\mathrm{ns}$.

This model of the temperature dynamics, which is supported by experimental findings, allows for the re-construction of the temperature profile for the COD ignition site. The values of T_{max} can be determined with Eq. (5.2.5) from the F_{exp} values. This calculation is done for the samples of batch A that experienced COD in Fig. 4.13. An example for an temperature transient determined with the above mentioned equation is given in Fig. 5.20(b). There the thermal runaway starts at $t_{\mathrm{COD}} = 110\,\mathrm{ns}$. The result for the entire sample set is an averaged value of $T_{\mathrm{max}} = (1200 \pm 200)^{\circ}\mathrm{C}$. In case of the thermal flashes shown in Figs. 4.2(j-l), the values are $(1200 \pm 200)^{\circ}\mathrm{C}$ [sub-figure (j)], $(2000 \pm 200)^{\circ}\mathrm{C}$ (k), and $(2000 \pm 200)^{\circ}\mathrm{C}$ (l). The uncertainties of the values are a result of the assumptions that were made and the uncertainty of the measurement itself. Nevertheless, these temperatures are around or above the melting point of GaAs of 1240°C (substrate) and $Al_{0.35}Ga_{0.65}As$ of $\approx 1580^{\circ}\mathrm{C}$ (waveguide). This shows again, that the fast heating during the thermal runaway process is based on an energy re-distribution via the laser light field from the entire cavity into a small defect volume. Once started, this process shows a fast temperature dynamic governed by an avalanche-like feedback loop of local temperature rise and re-absorption. This is also verified by the statement of Nakwaski [137], who conclude from his modeling work that the exact value of T_{crit} is of minor importance for the thermal runaway. Furthermore, this indicates, that the step test at elevated current levels addresses the same defect mechanism as reported for cw tests. The only difference is, that the time needed to start the thermal runaway is significantly reduced, providing an improved experimental access to study COD.

Energy Balance Based on NF Data

The NF data shown in Sec. 5.1.2 allows an energy balance to be set up for the defect kinetics around thermal runaway. The idea is analogous to the calculation presented above, but in the following a different set of input data – time-resolved NF data and μPL maps – are used. Furthermore, this section is focused on the situation during COD re-ignition. As example, the following calculations will be done with the data obtained from device A_4, which is one of the device that have been opened after COD. This device experienced COD and its re-ignition during two identical subsequent current pulses ($I_{COD} = 10\,A$, $t_{PW} = 300\,ns$). Figures 5.4(a,b) and 5.5(a) give the lasing NFs during degradation and a μPL map of the internal defect structure after COD re-ignition, respectively. Furthermore, a discussion of the kinetics related to the NF gap is given in Sec. 5.1.2, data of device A_4 are given in Fig. 5.12.

The application of Eq. (5.2.1) to the power transients of device A_4 leads to values of $W_{def,COD} = 45\,nJ$ and $W_{def,reig} = 246\,nJ$ for the pulse with first COD occurrence and the following one, respectively.

For comparison, Eq. (5.2.3) is used to calculate the energy W_{theo} that would be needed for melting the volume V_{def}. The material parameters of GaAs ($c = 0.33\,J/(gK)$ and $\rho = 5.33\,g/cm^3$) and a temperature rise of $\Delta T = 1217\,K$ (representing the difference between room temperature and the melting point of GaAs) are used. The value for V_{def} is obtained by multiplying the damaged area (A_{dark}) visible as dark region in the μPL map, Fig. 5.5(a), with a thickness of $1\,\mu m$. This corresponds to the waveguide thickness and is confirmed by TEM measurements presented in Sec. 5.1.3 and heat dissipation studies in Sec. 5.2.4.

The value of the final defective area $A_{dark,final} = 139\,\mu m^2$ is taken from the μPL measurement. It consists of two parts: $A_{dark,COD}$ created during the initial COD pulse and $A_{dark,reig}$ added during the pulse where the process re-ignites. As discussed in Sec. 5.1.2, the width of the COD induced NF gap agrees well with the internal lateral defect extent and its growth is linear with time, indicated by the linear fits in Fig. 5.12(a). This allows estimating a value of $A_{dark,COD} = 23\,\mu m^2$ by a linear scaling of $A_{dark,final}$, while $A_{dark,reig} = A_{dark,final} - A_{dark,COD} = 116\,\mu m^2$. This gives energies of $W_{theo,COD} = 49\,nJ$ and $W_{theo,reig} = 248\,nJ$ required for melting the damaged volume detected by μPL mapping. They are in very good agreement with the corresponding W_{def} values ($W_{def,COD} = 45\,nJ$ and $W_{def,reig} = 246\,nJ$). This confirms, that the optical output power loss is fully accumulated in the defect growth. Note, that this is valid only as long as the width of the defect is small compared to the emitter width, so that the influence on the reduced laser feedback is negligible. The area $A_{dark,COD}$ is indicated as red-shaded region in Fig. 5.21, while $A_{dark,final}$ is surrounded by a yellow line. This gives a depth of $\approx 3\,\mu m$ along z for the defect pattern after the first COD event.

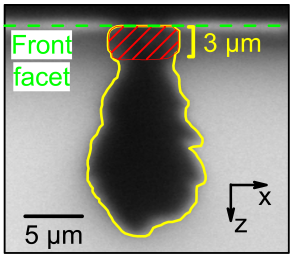

Figure 5.21: μPL of the QW plane of device A_4. The yellow line surrounds the damaged region after COD and COD re-ignition. The red-shaded area gives the damaged region after COD ignition, but before re-ignition. The position of the front facet is indicated.

Based on the NF data it is possible to estimate the energy that is necessary to re-ignite the process. From Fig. 5.12(a) follows a time interval of 100 ns after the leading edge of the pulse in which the NF gap of device A_4 (re-ignition data points) does not enlarge. As shown above, the defect volume absorbs the energy missing in the optical output power. This power loss amounts to ≈ 1 W in case of device A_4. Therefore an energy of ≈ 100 nJ has to be provided to re-start the defect growth. Compared to the value estimated above for initial COD ignition (≈ 50 nJ), this value is almost twice as high. Explanations for this difference are:

- The material heats up during regular laser operation, cf. measured bulk heating in Sec. 4.1.3. When COD occurs during a current pulse, a certain temperature profile has been reached. In the re-ignition case, the energy absorbing defect is already present at the leading pulse edge, but the entire structure is at room temperature. Now, this 'cold' material acts as heat sink with a short distance, i.e., a good thermal coupling, to the heat source. Therefore, this results in a short time constant for heat removal. A certain amount of energy has to be used to heat up the surrounding of the damage site again to restore the 'defect growth environment'.

- In addition to the primary damage detected by μPL, Fig. 5.5(a), a cloud of point defects is created around the COD site. This will be shown in Sec. 6.1.1. These defects absorb energy and heat up the region around the primary damage. The temperature, however, does not reach T_{crit}. Thus, this energy is lost in the energy balance that is made for the primary damage region.

- After an initial defect is created, a mode re-distribution occurs in the cavity. As a result, an increased NF intensity at still undamaged facet areas can be observed. This in turn results in a lower power density than expected at the initial defect.

With this data, it is also possible to calculate the minimal current (and via the L-I curve the optical power) that is necessary to re-ignite the process during a 300 ns long pulse. The result is $I_{\mathrm{COD}} = 2.8$ A. Therefore, the 1.6 A-*test pulse* used during the step test is not able to re-ignite COD and causes no further COD degradation. This is visible in Figs. 5.4(c,d), where the width of the NF gap remains constant.

The presented findings confirm our understanding of the energy transfer mechanisms involved in the process. This knowledge can be used for systematic preparation of early defect stages as will be demonstrated in the following section. Furthermore, it helps in understanding the third COD phase in which the extended damage pattern is created. Therefore, the presented concepts are the base of the defect growth model, that will be presented in Sec. 6.3.

5.2.3 Microscopic Defect Analysis

Origin of the 'White Line' and Interpretation of EDX Data

In the past, some authors [161–164, 166] have revealed a similar 'white line', as visible in Figs. 5.15 and 5.16, by TEM analysis of the defect pattern of COD. In contrast to the results presented here, they investigated devices emitting at 980 nm and used TEM lamellas cut perpendicular to the light emission direction in the *x*-*y*-plane (except for Sin *et al.* [163]). These reports focus on the diffusion of indium (from the In-rich QWs of these structures) during gradual degradation and COD, without directly claiming the cause of the 'white line', e.g., by In enrichment. However, the uniform small line thickness and

the high contrast of the 'white line' including sharp bends [see green arrows in Fig. 5.15(a)] make diffusion processes starting at the QW extremely unlikely. The lack of indium in the investigated 808 nm laser from batch A, eliminates this possible explanation completely.

The EDX analysis revealed a reduced Ga and increased Al and As content of the 'white line'. The situation is vice versa for the inner region [III in Figs. 5.15(c,d)]. This increased Al content let the line appear white in bright-field and black in dark-field contrast mode, Figs. 5.15(b) and (c), due to the lower atomic weight of Al. The gallium accumulation in region III, cf. Fig. 5.15(c), agrees well with earlier reports, e.g., by Snyder *et al.* [160], about Ga-enriched damage traces as result of COD.

This element re-distribution and the appearance of the defect region indicate a re-crystallization process that takes place after melting of the $Al_{0.35}Ga_{0.65}As$ waveguide. The most likely scenario is the following: The energy re-distributed during the thermal runaway, cf. Sec. 5.2.2, leads to temperatures high enough to melt $Al_{1-x}Ga_xAs$ of any composition. The necessary melt temperature can be obtained from the phase diagram of the Al-Ga-As system or simply from the pseudo-binary GaAs-AlAs part, Fig. 5.22, as reported by Foster *et al.* [174]. The system has no miscibility gap, therefore any composition is possible. The minimum temperature at which the material is liquid can be obtained from the liquidus. Assuming that a certain volume of the material gets molten during the thermal runaway, than the inverse process – the solidification – is of particular importance for forming the observed defect pattern. Initially the melt is expected to have the same composition as the surrounding solid material, namely $Al_{0.35}Ga_{0.65}As$. However, segregation effects cause the solidification process to result in material with inhomogeneous composition. These compositions can be calculated from the liquidus and solidus in the phase diagram, Fig. 5.22. They are expressed by the mole fraction ratio in the solid to the one in the melt. Al-rich solid solutions are in equilibrium with Ga-rich melts. These composition values can easily be estimated from the tie lines (e.g., horizontal dash yellow line in Fig. 5.22), which connect liquidus and solidus at one and the same temperature. Starting with the melt composition of $Al_{0.35}Ga_{0.65}As$, i.e., at $\approx 1580°C$, the first to freeze composition which is in equilibrium with this melt is roughly $Al_{0.83}Ga_{0.17}As$, see yellow arrows in Fig. 5.22. As a result of the solidification, the remaining melt becomes depleted in Al. While the cooling process continues, the liquidus temperature decreases due to its Al-depletion and consequently the composition of the solid solution, too.

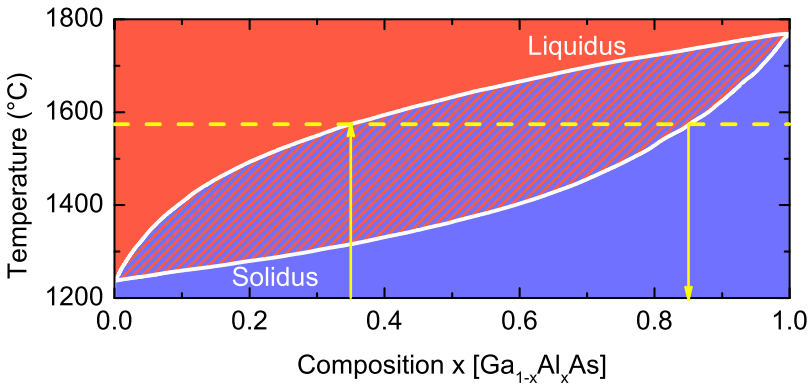

Figure 5.22: Pseudo-binary phase diagram for GaAs-AlAs. Above the liquidus curve, the material is completely liquid (red area), below the solidus curve, it is completely solid (blue area), while in between a mixed phase is present. The meaning of the yellow lines is explained in the text. Data taken from Foster *et al.* [174].

Assuming the solidification process to be core-directed, an Al-rich solid solution should be found at the border to the surrounding non-molten material. This is exactly what is visible in Figs. 5.15(a-c) and 5.16(c-f). As the solidification continues, the Al-content decreases continuously. It is worth to mention, that the described process is only valid for equilibrium conditions. Assuming equilibrium for the very first volume that solidifies, the conditions for the following crystallization might change substantially. An indication for that can be found in Fig. 5.15(a). After crystallization of some Al-rich material (forming the 'white line'), the solidification becomes morphological instable and dendrites can be observed, which grew due to constitutional supercooling. Dendrites are a clear hint for non-equilibrium growth conditions due to violations of interface stability limits, as discussed by Tiller [175]. Furthermore, they indicate a rapid thermocycle. After the solidification, diffusion processes are likely at these temperatures, but they do not change significantly the measured concentration profile.

Thus, re-crystallization can qualitatively explain the formation of the Al-rich 'white line', which therefore represents a kind of isothermal line visualizing the re-crystallization front. It is highly likely that the position where the 'white line' forms is indicative for the shape of the volume in which material has been molten during COD.

A question that arises from this is, if the material outside the volume surrounded by the 'white line' remains undamaged. In order to find an answer, the considerations from Sec. 5.2.2 are used. The energy incorporated into damage creation has been already determined ($W_{\mathrm{def}} = 155\,\mathrm{nJ}$, cf. Sec. 5.2.2). Now, the heated volume V_{def} can be assumed as the area inside the 'white line' [Fig. 5.15(a)] times the width of the external defect [Fig. 5.14(d)]. This yields to $V_{\mathrm{def}} = 2.4\,\mu\mathrm{m}^3$. With Eq. (5.2.3), this leads to $\Delta T = 3.6 \cdot 10^4\,\mathrm{K}$. This value is much too high to make sense, because the melting temperature for any composition in the GaAs-AlAs system is below 1800°C, cf. Fig. 5.22. Since the energy balance considerations in Sec. 5.2.2 confirms, that the value of W_{def} is correct, the assumption for V_{def} must be wrong. The 'white line' is not the border of the entire heated and damaged region. It will be shown by time-resolved thermography and investigations of point defects in Sec. 6.1.1, that the thermal energy is distributed over a larger volume and also creates defects there. In this way it is wrong to consider the area outside the 'white line' as undamaged. The 'white line' rather indicates the area of substantially damaged (re-solidified) material. A discussion about the heat dissipation in this area will be given in Sec. 5.2.4.

Position of Initial Defect Growth

Away from the front facet, the 'white line' follows the QW with almost fixed spacing which implies a constant temperature during defect growth within a single pulse. Moreover, the distances of the 'white line' on p- and n-side are the same from the location where the QW has been. This indicates that the QW is the origin of the defect. In vicinity of the front facet, however, the situation is different. Here, the obviously damaged region has a substantially larger extent in y-direction. Nevertheless, the 'white line' maintains its sharp shape. The specific line shape with the characteristic corners, marked by green arrows in Fig. 5.15(a), indicates the existence of separate initial points of COD on both sides of the QW. Their most likely position is next to the hollow spaces under the coating, indicated in Fig. 5.23(a) as the origin of the yellow arrows. There, the part of the damage structure at the facet from Fig. 5.15(a) is shown on an enlarged scale. One single starting point at the QW position could not explain the inhomogeneities of the temperature distribution expressed as corners of the 'white line'. Defect pattern showing these inhomogeneous structures were also reported for single-spatial-mode lasers during long

term degradation in 'kink free' operation. This means the emission mode pattern remains unchanged, e.g., no occurrence of higher order spatial modes. This rules out the possibility that the found damage pattern is an effect of higher order spatial modes occurring at elevated currents as used during the step test. A SEM image of the cross section of such a sample prepared by FIB is shown in Fig. 5.23(b), it was taken from Sin *et al.* [163]. Notice that the emission wavelength of this device is 980 nm in contrast to the 808 nm of batch A. Furthermore, it verifies again the use of the step test approach for COD analysis by producing similar defect pattern even on a nanoscopic scale.

Additional evidence for separate starting points is given by the positions of the hollow spaces under the coating that have been discovered by looking at the front facet before device preparation, e.g., Fig. 5.14(d). They are located next to the QW plane, but never direct on top of it. Thus, the most likely scenario is as follows: Fast nearly isotropic (in the *y*-*z*-plane) damage spread starts in the waveguide close to the front facet, indicated by the yellow arrows in Fig. 5.23(a). This extending defect than affects the QW, followed by further defect growth along the QW itself [orange arrow in Fig. 5.23(a)]. This is plausible, because the highest light field intensity is expected there. After defects make a part of the QW absorptive, it is highly likely that this is the location where the damage propagation process continues. This scenario can be further verified by looking at the facets of two 980 nm devices in Figs. 5.23(c) and (d). Whereas Fig. 5.23(c) shows a SEM image of the external defect part of device E_5 from batch E, sub-figure 5.23(d) is taken from Mallard *et al.* [165]. The red dashed lines give the positions of the QWs in both cases. It is obvious that the coating material is also locally affected above and below (in *y*-direction) the defect related material extrusion. Especially in case of Fig. 5.23(c), a thin layer at the top of the coating seems to be molten, forming two nearly equal kidney-shaped areas at both sides of the material extrusion. A similar area (size and shape) is affected in Fig. 5.23(d). Since these devices, Figs. 5.23(b-d), have another emission wavelength and degraded in cw operation, the above discussed scenario seems to be of general relevance and not restricted to a specific material system or operation condition.

Defect Growth at the Re-Ignition Site

In case of device A_4, two consecutive single current pulses have been applied. Performing the analysis as presented in Sec. 5.2.2, the depth of the damage pattern along *z* after the first COD pulse can be estimated to 3 μm, cf. Fig. 5.21. This corresponds to the position of the TEM cross section in Fig. 5.16(d). Exactly at the predicted position, a significant change of the defect pattern is found. There, the 'white line' shows for the one and only time a discontinuity. Obviously this is an overlap of two thermocycles, indicated by the overlap of the 'white lines'. Figures 5.16(e,f) show that the defect extension in *y*-direction rises up again to a value of $\approx$ 380 nm which was also present during the end of the first COD event.

By evaluating the thermal images recorded during subsequent pulses including COD re-ignitions, e.g., Fig. 5.8(k) and Ch. 6, no significant differences in the height of the received thermal signal can be found. This points to very similar temperatures. A constant temperature during the damage process explains also why constant defect growth velocities can be found, e.g., in Secs. 6.1.1 and 6.1.2 or by Jacob *et al.* [176].

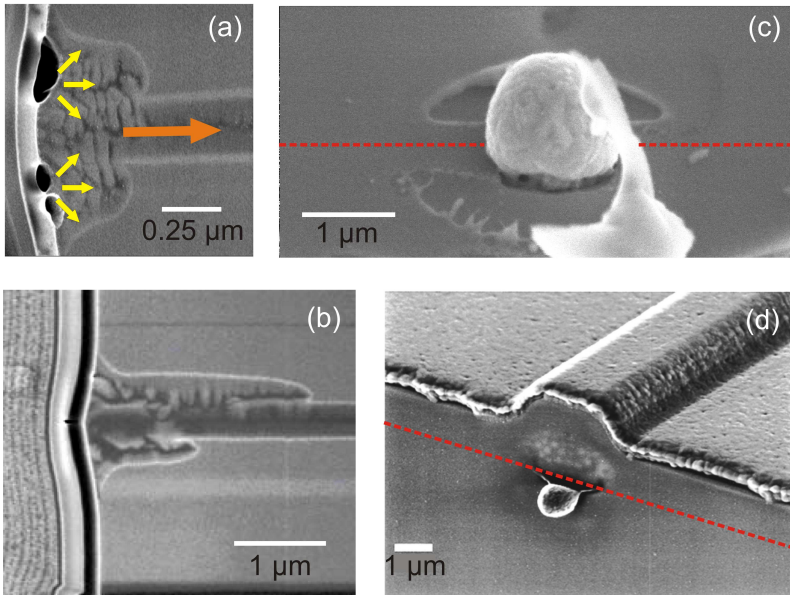

Figure 5.23: (a) The starting region of the defect shown in Fig. 5.15(a) from device A_{12}. The radial directed yellow arrows represents the assumed direction of initial defect growth. The orange arrow indicates the direction of further defect growth along the QW. (b) SEM image of a FIB cut cross section of a 980 nm-emitting device, taken from Ref. [163]. (c) SEM image of the external defect part of device E_5 from batch E (tilted $\approx 50°$). The position of the QW under the front facet coating is indicated by the dashed red line. The bright object between the material extrusion and the bottom of the image is a part of the coating that peel of during COD. (d) SEM image of the output facet of a 980 nm pump laser after COD failure, taken from Ref. [165]. The position of the QW under the front facet coating is indicated by the dashed red line.

Two different mechanisms for the start of defect growth can be identified:

- An explosion-like first COD ignition takes place at the laser facet, which has its origin rather at the waveguide than in the QW.

- A COD re-ignition occurs in the defect path around the QW. There is a local overlap of the end of the preceding defect growth and the beginning of the successive one. The width (in y-direction) of the damage is locally distorted, but retrieves its former extend within some microns. In sharp contrast to the first ignition, the 'white line' indicates here a rather smooth re-start.

This makes the first COD ignition a unique event. Its physical background and the one of the re-ignition in the subsequent pulse is different. Therefore, it is valid to separate the investigation of this first event and the creation of the extended defect pattern, as discussed in the next chapter.

5.2.4 Heat Dissipation

After having identified the extensions of the molten region and the temperature present during COD, it is worthwhile to discuss the heat dissipation from there. In order to keep the calculation simple, a one-dimensional situation is considered in one half space only (along y-axis). The process is assumed to be symmetrical to the other side, as indicated by a similar distance of the 'white line' at p- and n-side of the QW in Figs. 5.15(a) and 5.16(c-f). The initial situation at time zero is the following: The material properties of $Al_{0.3}Ga_{0.7}As$ are used (waveguide material). The heat source is located between zero and 200 nm, i.e., the separation of the 'white line' from the QW position. The temperature there is set to 1500 K which is $\approx 1230°C$ and therefore the lower limit for melting in the phase diagram, Fig. 5.22. The remaining material is set to ambient temperature (300 K). The heat equation is solved numerically with the solver package COMSOL 3.5. The distance is therefore discretized in 3 nm long sections. The spatial dependent temperature curve is recorded every 0.1 ns. With this starting configuration, two different scenarios are studied:

- The initial heat distribution develops in an isolated surrounding, e.g., no further heating of the source area takes place. With other words, the energy in the observed systems remains constant.
- The source area is heated in a way that its temperature remains constant at 1500 K. This simulates continuous energy entry, e.g., by re-absorbed laser light.

The results for the first case are shown in Fig. 5.24(a), while results for the second one are shown in Fig. 5.24(b). Notice, that only for the first nanosecond a curve is plotted every 0.1 ns. Thereafter, a curve is plotted just every 1 ns. This allows to distinguish between the different curves, because they are closer together for longer times.

Figures 5.24(c,d) show temporal cuts through the results of Figs. 5.24(a) and (b) at a distance of $0.5\,\mu$m. Only for times < 1 ns, the increase of both curves is quite similar. Thereafter, the deviation of both assumed cases becomes significant.

In the first mentioned case, the measurement point is just 300 nm separated from the initial high temperature region (1500 K at 0 ns); the maximal temperature reached in Fig. 5.24(c) is just 536 K ($\approx 240°C$ after 1 ns). Due to the fact that temperatures in this range are also present during the epitaxial growth, it can be assumed that no substantial damage is induced at this and larger distances from the heat source. Furthermore, a temperature below 240°C is reached in the middle (distance: 0 nm) of the initial heat source within ≈ 2.4 ns. This verifies the findings from the preceding section, that the 'white line' has been created by a rapid thermocycle.

The other extreme case – constant heat source, shown in Figs. 5.24(b,d) – leads to a fast temperature rise at the same distance from the heat source, see Fig. 5.24(d). The maximal temperature found in Fig. 5.24(c) is reached after 10 ns in a distance of $2.2\,\mu$m from the middle of the heat source, i.e., the QW position.

The real temperature distribution present in the device is in between these extreme cases. However, supported by the findings regarded to the 'white line' in the preceding section, a scenario as shown in Fig. 5.24(a) is more likely. It includes the rapid thermocycle and a defect volume thickness of $1\,\mu$m ($2 \times 0.5\,\mu$m, due to the assumed symmetric distribution in both half spaces) which is in line with the calculation presented in Sec. 5.2.2. In Ch. 6, the rapid cooling predicted in Figs. 5.24(a,c) is verified by time-resolved thermography.

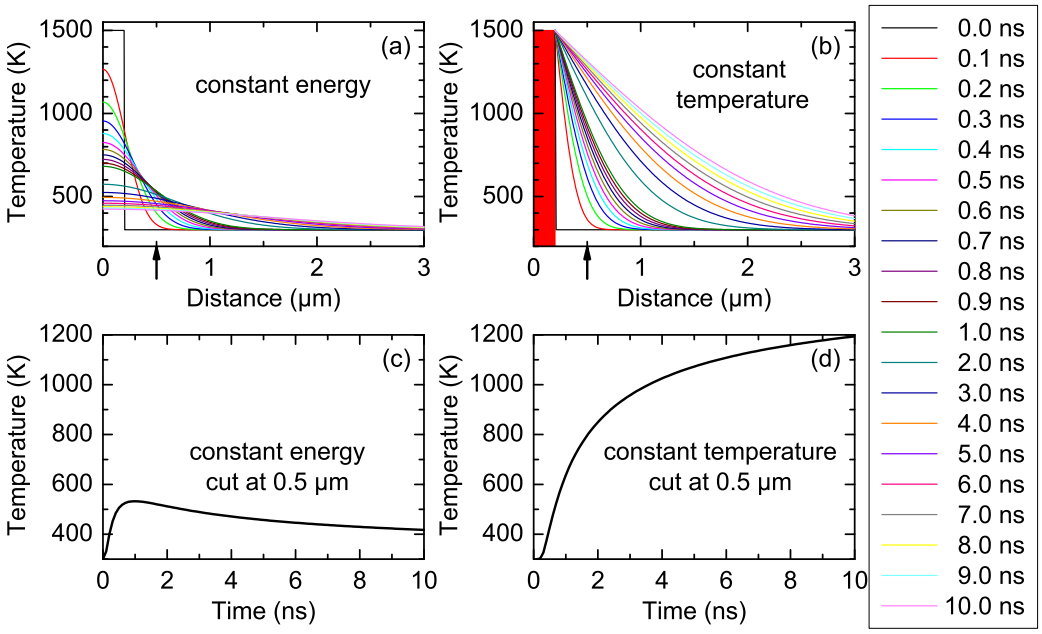

Figure 5.24: Results of 1D-heat modeling. The initial temperature distribution can be seen as '0.0 ns' data set in (a) and (b). (a) The initial temperature distribution is observed in an isolated environment, i.e., without additional energy entry. (b) The heat source (indicated as red rectangle between 0 and 200 nm) is kept on its initial temperature of 1500 K. (c) Cut through the results in (a); position is additionally indicated by the arrow in (a). (d) Cut through the results in (b); position is additionally indicated by the arrow in (b).

At a first glance, this result seems to be contradictory to the assumption made for Eq. (5.2.3), that the heat transport can be neglected. The following arguments, however, ensure that both match together. As shown by Kappeler *et al.* [127], the square root law, cf. Sec. 4.2.1, follows directly from the assumption of a negligible heat transport from the defect volume to the surrounding material. The parameter region, where Eq. (5.2.3) is used, is within the range of validity of the square root law, see Fig. 4.13. There, the square root law is consistent with the obtained data up to t_{COD} value of several hundred nanoseconds. For longer times the heat transport becomes important and reaches steady state in cw operation. The approximation made fails for longer times. This is visible in Fig. 5.19(b) as the outliers marked by open circles. There, the energy is in part removed from the defect region by heat transport and the considered energy balance does not hold anymore. Furthermore, the energy deposition at the defect front is so fast that the material cannot reach a thermal equilibrium. This is verified by the solidification with dendrites observed in TEM. The velocity of the isothermal line, i.e., the high-temperature front, in y-direction in the case shown in Fig. 5.24(a) drops to $\approx 10\,\mathrm{nm/ns}$ after $\approx 2\,\mathrm{ns}$. The heat source (defect front) moves with about the same velocity along z, as reported in Refs. [58, 126, 177], own measurements will be

discussed in Sec. 6.1. During this time the waveguide thickness is affected by degradation due to the heat. Therefore, this extension is used in Eq. (5.2.3). At the time when the heat transport would have to be considered, the volume used for calculation has been already passed by the defect front. The calculation itself addresses only the question how much energy is necessary to achieve the temperature for creating the primary damage. The heat spread model of this section addresses the heat dissipation after the defect front has passed a region and does not influence it anymore in case of Fig. 5.24(a). In contrast, the scenario shown in Fig. 5.24(b) gives a defect front without any motion. Therefore, the real heat distribution should be between these two extreme cases: A fast but not abrupt decrease of the heat source peak temperature. Nevertheless, the fast spread of thermal energy predicted here is relevant for the defect kinetics. In Sec. 6.1.1 it will be shown that the material affected directly by COD is surrounded by an extended area of point defects, caused by thermal energy.

5.2.5 Mechanisms Determining the Second Phase

The time constants determining the second phase kinetics are found to be related to the thermal resistances of the involved active region materials. If the waveguide surrounding the QW can extract the heat more efficient the defect growth slows down. This was verified by analyzing τ_{drop} which has been found to be indicative for the lateral defect growth. Furthermore, better heat extraction from the gain medium allows to reach higher P_{COD} values by delaying the situation when T_{crit} is reached. Additionally, a thermally induced reduction of the output power sets in later, too. Therefore, an optical induced energy transfer becomes less efficient. The COD threshold is a trade-off between the material and the optical power. The same holds for the further defect growth.

The initial starting points of COD have been identified to be most likely above and below the QW. This is an astonishing result, because one would expect the QW as gain medium to be subjected to higher power levels than the waveguide and cladding layers.

The temperature reached during COD was subject of extended speculations in the past, e.g., Refs. [58, 160]. Here, it has been shown, that a temperature of $\approx 1500^{\circ}\mathrm{C}$ is most likely to be present during defect growth. This is verified by the analysis of the re-crystallization front. Moreover, the step test approach allowed to make up energy balances for the COD, due to the knowledge about the energy necessary to create the defect. Additional evidence comes from the thermocamera images that could be evaluated with a model based on the experimental findings. A heat transfer model confirms that the creation of a point defect cloud around the heavily damaged area indeed requires these temperatures. The presence of high temperatures, even after a macroscopic defect site has been created, is verified by short-time thermography and the constant distance of the *white line* from the QW position, identified as an isothermal line.

6 Third Phase of COD – Defect Spread

After an initial damage site has been established in the thermal runaway phase, further defect growth is observed. This phase of defect spreading is analyzed in this chapter.

6.1 Experimental Results

A promising approach for an *in-situ* analysis is the combination of a step test scheme with a thermocamera based setup. The reasons are the high temperatures present during COD and the transparancy of GaAs for the thermal emission. Additionally, the temporal resolution is given by the time slicing as discussed in the preceding chapter and not by the rather long integration times of the thermocamera. First results have been already presented in Fig. 5.8(k). There, thermal measurements of the front facet show a motion of the thermal signal during COD re-ignitions in lateral direction. Such an one-dimensional projection is, however, insufficient to follow the motion of the defect front in the QW plane. In the following, strategies are presented to circumvent this lack of information [106, 178–180].

6.1.1 Defect Analysis Through the Top Contact

In order to trace the defect motion in two dimensions, a top window was implemented for selected DLs of batch A. This was done by partly removing the n-metallization on the substrate with a laser ablation system [178]. A rectangular window of $1.3\,\mathrm{mm} \times 0.3\,\mathrm{mm} \times 40\,\mu\mathrm{m}$ (length $\times$ width $\times$ depth) was applied. The active region is centered underneath this top-contact window. In order to prevent the facets from contamination during the ablation process, $30\,\mu\mathrm{m}$ and $70\,\mu\mathrm{m}$ wide strips of material were kept at the front and rear, respectively. A scheme of the modified device is given in Fig. 6.1(a), while Fig. 6.1(b) shows an image of it taken with an optical microscope looking from the top. To ensure that no damage was caused by the laser ablation, the cw L-I curves before and after implementing the top-contact window are compared, Fig. 6.1(c). The relative deviation of the both curves of 2.7% is within the reproducibility of such a measurement after about half a year. Therefore, the device properties are considered unchanged.

In-situ Measurements

The thermocamera was directed straight towards the top-contact window, observing additionally the front facet via a 45° tilted mirror. The sample was thermo-electrically stabilized to $(23.0 \pm 0.2)\,^{\circ}\mathrm{C}$. The step test started from $I_0 = 1.6\,\mathrm{A}$ and proceeded with $\Delta I = 0.5\,\mathrm{A}$ in $1\,\mu\mathrm{s}$ long pulses. The thermocamera integration window was $t_{\mathrm{int}} = 10\,\mu\mathrm{s}$, resulting in $t_{\mathrm{int,eff}} = 4.5\,\mu\mathrm{s}$. The 200 ns long test pulse was taken at 1.6 A. During each single pulse the current trace and the time-dependent laser output power were recorded additionally to the thermal image. The thermal image of the front facet was used to probe COD occurrence.

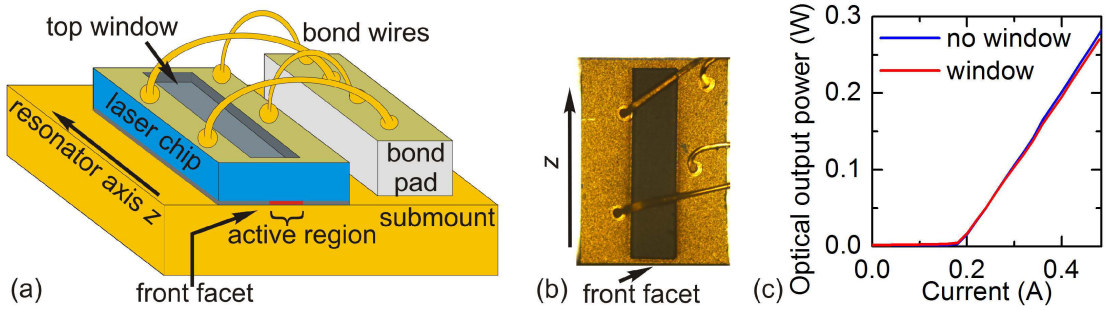

Figure 6.1: (a) Scheme of the DL with top-contact window. (b) Top view through a light microscope. (c) Comparison of the optical output power of the device before and after implementing the window into the top-contact.

The device, which data will be discussed in the following, experienced COD at $I_{\mathrm{COD}} = 10.5\,\mathrm{A}$ with $t_{\mathrm{COD}} = 134\,\mathrm{ns}$. After that 34 additional $1\,\mu\mathrm{s}$ long single pulses, each at 10.5 A were applied with constant $I = I_{\mathrm{COD}}$, i.e., $\approx 35\,\mu\mathrm{s}$ of operation. Eventually, all lasing has vanished. Figure 6.2 shows the evolution of the thermal flashes of Planck's radiation in the device observed through the top-contact window. Each sub-figure shows the result of a single current pulse applied to the device. The thermal background was subtracted. The image shows the geometry in grayscale and the thermal emission overlaid in color. While Fig. 6.2(a) shows the entire laser chip, the following smaller images (b)-(w) are restricted to the region of interest around the front facet, as indicated in (a). A region emitting an elevated thermal signal can be seen that starts at the front facet (bottom of the sub-figures) and moves along the resonator (z-axis) during the subsequent pulses. The signal itself is longish along z.

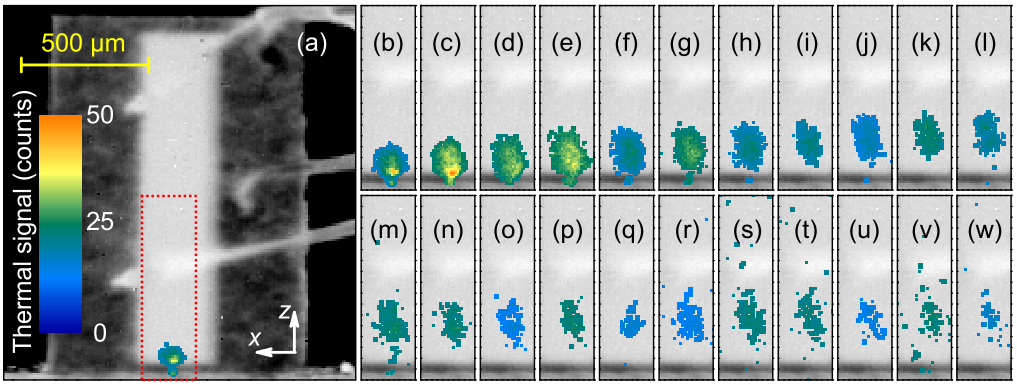

Figure 6.2: Time evolution of the area of thermal emission seen through the top window of the DL. Each sub-figure shows the result of a single current pulse applied to the device. (a-w) represents a series of consecutive experiments. (a) The geometry of the device is shown as grayscale image (emissivity contrast); the top-contact window appears as bright rectangle in the middle of the structure. The bright lines going to the right edge of the image are the bond wires. The red dotted rectangle gives the region shown in (b)-(w). (b)-(w) Time evolution of the thermal signal in the region around the front facet during successive $1\,\mu\mathrm{s}$ long single pulses, using the same color scheme and length scale as in (a).

From these data, the center of gravity of the thermal signal is taken, i.e., the *hot spot*. The propagation path of the hot spot along the emitter is shown in Fig. 6.3(a). The zero-value of z is at the front facet and x is the lateral position along the facet. The motion along x- and z-axes is obvious. In Fig. 6.3(b), the distance to the front facet is plotted versus the time. The single pulse duration of 1 μs defines the sampling rate. Therefore, velocities can be calculated from the recorded distances. Linear curve fits define different time ranges of almost constant mean velocities of the hot spot motion. In addition, the spatially integrated thermal signal is shown, i.e. the sum of counts of the pixels forming the thermal signal in Fig. 6.2. For later times both the mean velocity and the thermal signal strength decrease.

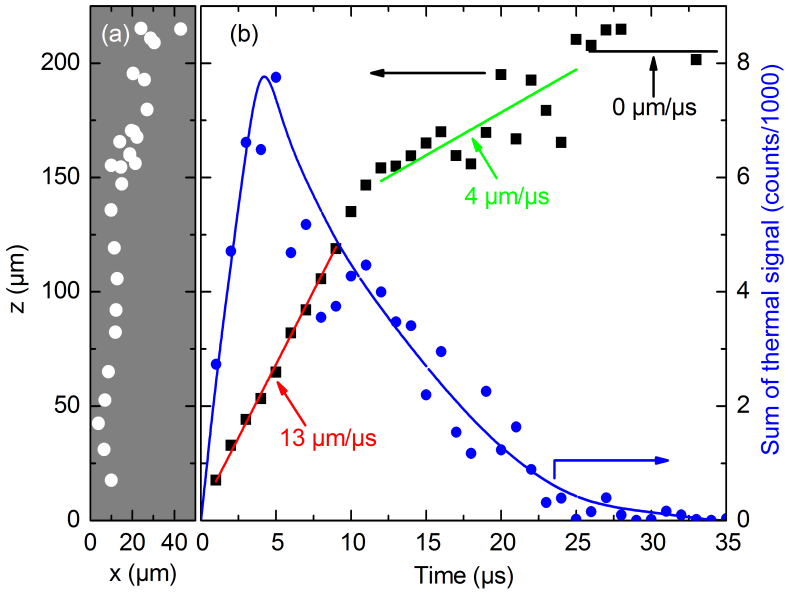

Figure 6.3: (a) Position of the hot spot in the emitter plane. The z-axis starts at the front facet. (b) Time evolution of distance z to front facet (left scale, black squares) and linear fits (red, green, and black lines) with their resulting velocities are shown. Blue symbols (right ordinate scale): spatially integrated intensity of thermal emission. The blue line is a guide to the eye.

Ex-post Measurements and Comparison with *In-situ* Data

Analysis of lasing and EL NFs of the device shows results analogous to those presented in Sec. 5.1.2. Furthermore, the surface extrusion found is typical for COD. A PC measurement through the top-contact window near the front facet gives information on the electronic structure of the damage site, Fig. 6.4(a). The PC spectrum was obtained with a spatial resolution, i.e., FWHM of the spot size, of about 100 μm. In absence of a bias voltage, the PC spectrum is dominated by contributions from the active region – QW and waveguide – where the potential gradients of the pn-junction are steepest. PC features observed in spectral regions energetically below the band gap, in case of bulk material, or the lowest quantum-confined transitions inside the QW are interpreted to be defect related [99]. Although their spectral shape may not exactly mirror the absorption cross section of a particular defect-related transition, it is highly likely that resonant defect excitation dominates. PC spectra taken as reference at undamaged areas, e.g., in the center of the top-contact window, show no defect-related signal.

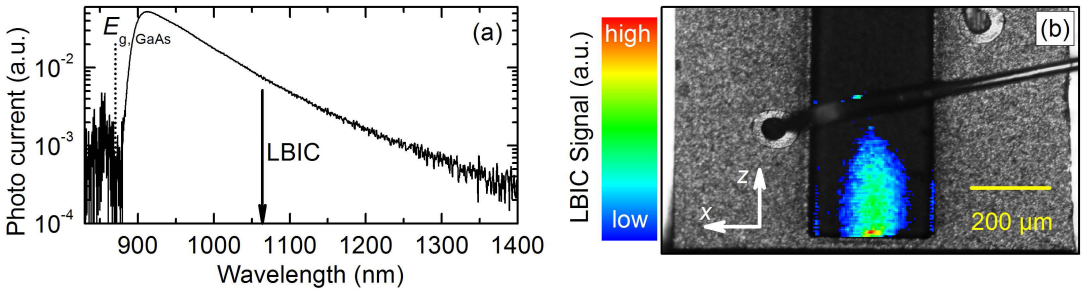

Figure 6.4: (a) Result of photocurrent measurement through the top-contact window. The band gap energy of GaAs on the high-energy side is marked by a dotted line. The wavelength used for the LBIC scan is indicated by the arrow. (b) Overlay of the LBIC data (color coded) on the optical microscope top view image (grayscale) of the DL.

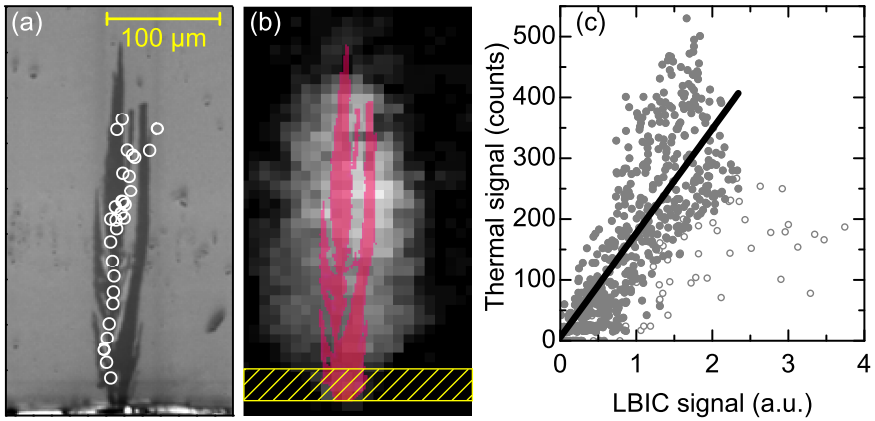

Figure 6.5: (a) Motion of the hot spot of thermal radiation (white open circles) overlaid to the CL map of the QW plane of the laser. (b) Sum of all thermal images [Figs. 6.2(a)-(w)] (grayscale) overlaid by a damage pattern found in CL measurements (reddish). The small stripe of top-contact material left to protect the facet while laser ablation is indicated by the yellow shaded area. (c) Comparison of the sum of thermal signals [as grayscale in (b)] and the LBIC signal [Fig. 6.4(b)] of each individual pixel. Open dots originate from the area close to the front facet; see yellow shaded area. The black line gives a linear fit to the full gray dots.

Based on the PC data, one gets information in which spectral region defect-related transitions are present. Using this knowledge, a 2-dimensional LBIC map was taken at $\lambda_c = 1064\,\text{nm}$. PC and LBIC measurements were done at ambient temperature. The result is shown in Fig. 6.4(b) as color-coded signal overlaid to a light-microscopic image (grayscale).

After *in-situ* measurements and non-destructive analysis have been finished, the devices were opened and prepared for CL imaging. By performing cross-checks with reference regions, it was ensured that only QW emission contributes to the CL images. In this way, the COD-related defects can be observed as regions of locally enhanced non-radiative recombination. The recorded CL defect map is shown in Fig. 6.5(a). Superimposing the hot-spot locations extracted from thermal images shown in Fig. 6.3(a) to the CL image shows excellent agreement of the data being evident from Fig. 6.5(a) (hot spot positions are represented by open white circles).

6.1.2 Simultaneous Analysis of Both Facets and Cavity

As discussed in Sec. 4.2.4 the devices from batches D and E tend to COD events with starting points at both facets. This favors a setup that monitors the two facets in parallel. Furthermore, it would be desirable to perform an analysis of the defect spread without any preparation. Devices from batches C, D, and E allow such an approach, since their p-up-packaging gives easy optical access to the emitter stripe by inspection from the side. The devices were investigated in a step test starting at $I_0 = 2\,\text{A}$ with $\Delta I = 1\,\text{A}$. The test pulse was performed with $I = 1.86\,\text{A}$ and a pulse width of $t_{\text{PW}} = 200\,\text{ns}$. Independent of the occurrence of COD, the step-wise current increase was proceeded up to the point where any laser emission from the device vanished. While the PD signal and the laser current are temporally resolved, the thermal image provides time-integrated information only with $t_{\text{int}} = 10\,\mu\text{s}$ and $t_{\text{int,eff}} = 4.5\,\mu\text{s}$. The samples were thermo-electrically stabilized to $T_{\text{hs}} = (23.0 \pm 0.2)^\circ\,\text{C}$.

A thermal image of the device in the corner mirror is shown in Fig. 6.6(a). An integration time of 1 ms was chosen for the background image showing the emissivity contrast on a grayscale. In the central part of the image, the 2 mm long laser cavity in side view is shown. The bond wires on top of the laser structure are clearly visible as thin dark-gray lines. In the left part of the image, the front facet is seen via the mirror. The entire diode chip in front view is inside the left inserted red box. The same holds for the rear facet on the right image side. The insets in Fig. 6.6(a) show typical thermal flashes related to the thermal runaway overlaid in yellow to orange colors to the separately recorded emissivity contrast image. The flashes of Planck's radiation are observed at front and rear facets as well as at the side of the active region. This allows the detection of the ignition site of the COD and additionally the tracing of the hot spot along the cavity.

The next step of data evaluation is focused on the side-view-data obtained by the thermocamera. Figure 6.7(a) shows the results of the propagation of the defect front along z. A sequence of 19 images was recorded for consecutive current pulses. Each frame displays two overlaid thermal images of the device (grayscale) and the thermal flash (colorscale). The flashes are blurred because the focus of the thermocamera has been fixed to the facets. The intensity fluctuations during the propagation along z are mainly caused by shadowing effects of the bond wires; see scheme on top of Fig. 6.7(a). Apart from that, the signal magnitude remains almost constant. The motion of the thermal signal can be traced by evaluating its center of mass, i.e., the hot spot. Figure 6.7(b) shows the propagation of the defect fronts in typical devices from three different batches. These batches differ in their active region material system and have been already discussed in Secs. 3.5 and 4.2.4. For both cases, front and rear facet as COD

starting point, almost the same amplitude of thermal flashes as well as an uniform propagation velocity of $30\,\mu\mathrm{m}/\,\mu\mathrm{s}$ are observed. Since there are matching thermal images from front, rear, and side available, the position of the hot spots within the laser stripe (x-z-plane) can be traced. They are overlaid to an EBIC image taken *ex-post*, see the red open circles in Fig. 6.7(c). The defect appears as dark shape in the active region, which is visible as vertical $\approx 100\,\mu\mathrm{m}$ wide stripe in the middle of the image. The two data sets – EBIC and hot spot locations – agree very well, especially regarding the defect extension in z direction.

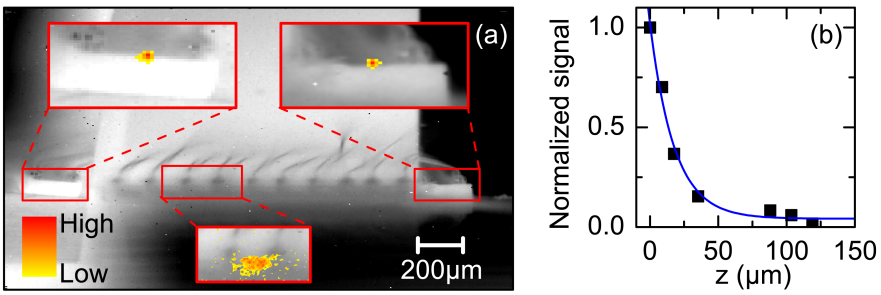

Figure 6.6: (a) Thermal image of the aligned setup. The emissivity contrast is given in grayscale. The central part of the image shows the side view on the DL, device D_1. The bond wires on top are clearly visible. At the left and right side the front and rear facet, respectively, can be seen via the mirrors. The insets show front (left) and rear facets (right) as well as a side view (bottom) on an enlarged scale. Thermal flashes as observed during the step test are overlaid in yellow to red color to the insets. Their respective amplitudes are normalized to a common level. (b) Spatial decay of the thermal flash amplitude along the laser axis z as observed from the front facet. $40\,\mu\mathrm{m}$ are found as lower limit for the depth of focus ($1/\mathrm{e}^2$-value).

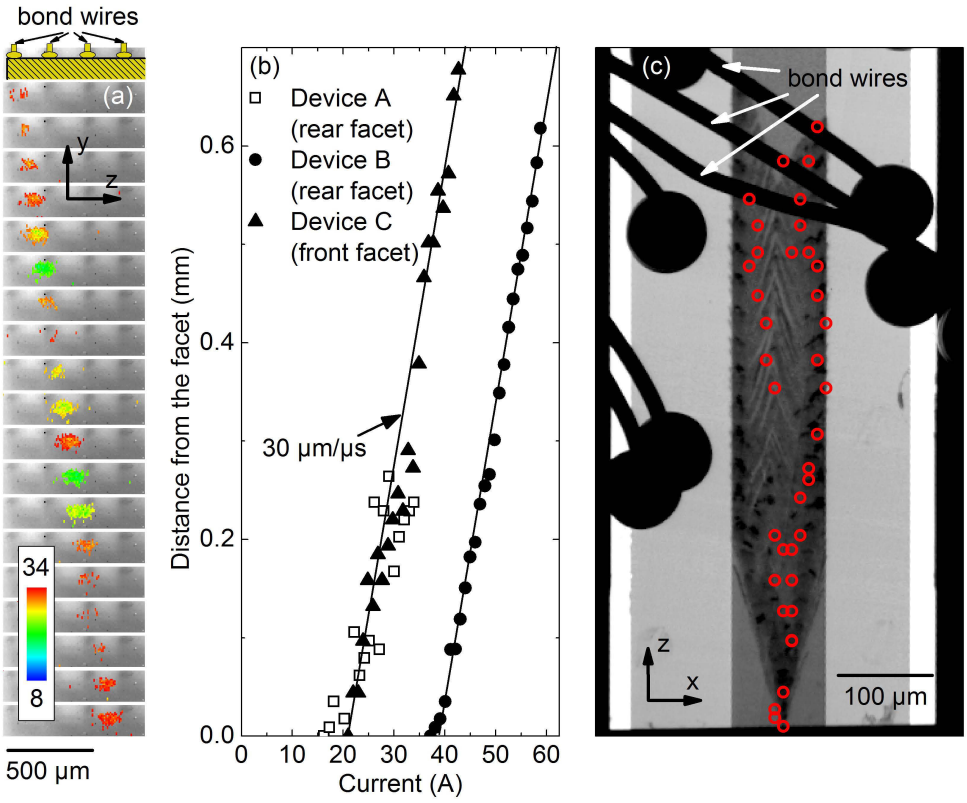

Figure 6.7: (a) Thermal images from device D_1 with overlaid thermal flashes tracing the propagation of the damage front along the laser axis z. The 19 images have been taken during 19 successive pulses each 1 μs in duration (starting from the top image). The device geometry is given by the emissivity contrast (grayscale) while the thermal signal, recorded during the single pulse excitation, is overlaid in colorscale. On top, a scheme depicts the structure including bond wiring. (b) Motion of the position (center of gravity) of the heated area versus current for three devices with different I_{COD} values. (c) Propagation of the spot of Planck's radiation (red open circles) within the emitter stripe (x-z-plane, front facet at the bottom) as reconstructed from the thermal images taken in parallel from the front facet and the side of the same device as in (a). These points are overlaid to an EBIC map of the QW plane of the device. The damage is visible as dark structure in the active laser stripe starting at the front facet (bottom).

6.2 Discussion of Third Phase Results

6.2.1 Data Obtained Through the Top-Contact Window

Hot Spot Kinetics

The propagation velocity of the hot spot during the first 10 μs is nearly constant at 13 μm/μs and drops in later pulses to nearly zero, cf. Fig. 6.3(b). The slowing down of damage propagation is directly observed in this experiment, while earlier studies give indirect information on this behavior only, e.g., Jacob *et al.* [176]. Such deceleration is expected to be caused by the ongoing loss of optical power during the increase of the extend of the damage in the active laser material. In order to verify this, the optical output energy per pulse is determined from temporal integration of the optical output power measured with the PD. The obtained data are plotted in Fig. 6.8 together with the sum of the thermal signal, as shown in Fig. 6.3(b). The discrepancy of the curves in the first 3 μs is a result of the fact that the top-contact window does not reach up to the front facet where COD starts. The remaining top-contact material there impedes the detection of a thermal signal. In contrast to that, the output power measurement is not affected and therefore gives higher values during the very first pulses. However, the shape of the decrease of both signals matches very well. The base lines (zero values) of both ordinates do not match. This indicates a situation where the material is heated by absorbed energy (ongoing degradation), but the resulting temperature is below the detection limit of the thermocamera. This will be discussed in detail later in this subsection.

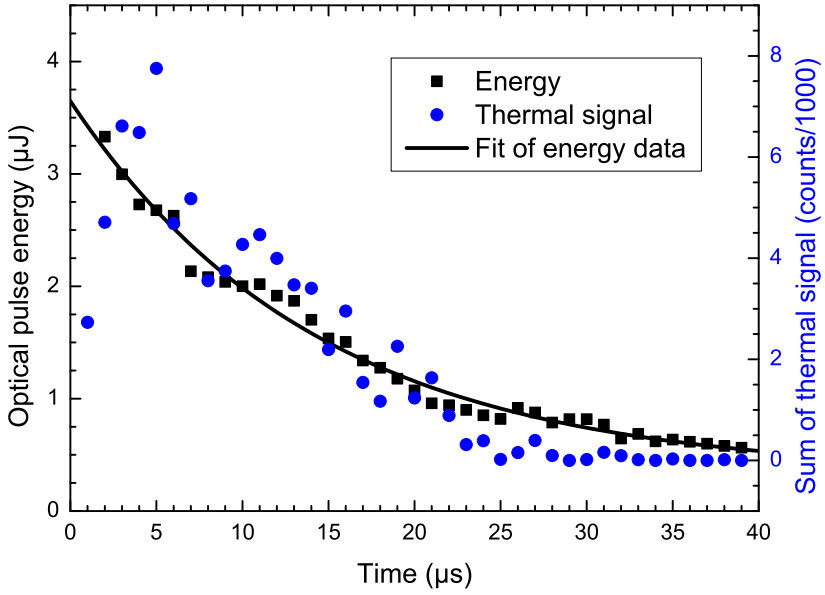

Figure 6.8: The black dots give the optical pulse energy as obtained by integrating the measured optical output power in the respective 1 μs pulse. The black line gives an exponential fit to the data. The temporal evolution of the sum of the thermal signal is shown by the blue dots, these data have also been shown in Fig. 6.3.

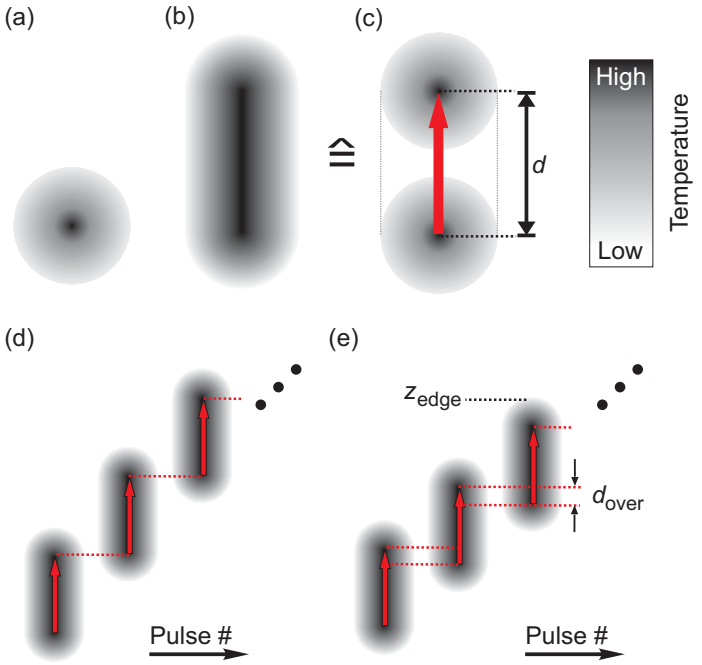

Figure 6.9: Scheme of velocity determination based on the geometric shape of the thermocamera signal. The strength of the thermal signal is represented in grayscale, an according scale-bar is given at the right side. (a) Thermal signal averaged over the integration time of the thermocamera from a heat source fixed at the center of the circle. (b) Time-averaged thermal signal from a heat source moving in upwards direction during integration time. (c) Demonstrates, how the obtained signal in (b) is formed by a hot spot moving during the integration time of the thermocamera (indicated by red arrow). The distance between the start and end position of the hot spot is labeled d. (d,e) A situation as shown in (d), the perfect match of hot spot motion paths in consecutive pulses, would need no correction. The situation found in experiment, cf. Fig. 6.2, reveals an overlap d_{over} of the paths (e). The determined value for the velocity has to be corrected for d_{over}. The position z_{edge}, indicated in (e), is of special interest for further evaluation.

The detected thermal signal is generated by absorbed laser light. This is confirmed by the deceleration of the defect propagation. It emphasizes that absorption of optical power is the essential driving mechanism behind the defect expansion.

The velocity can alternatively be determined by evaluating the shape of the time-integrated hot spot, see Figs. 6.2(a)-(w). A scheme illustrating the idea is given in Fig. 6.9.

A heat source without any motion would form a round spot Fig. 6.9(a). In contrast to that, the result of our measurements looks rather like the one shown in Fig. 6.9(b). This is the result of a linear motion of the hot spot, in the actual case along z away from the front facet, during the integration time of the thermocamera. As demonstrated in conjunction with Fig. 6.8, the light field is the energy source for the defect growth. Therefore, it is valid to use $t_{\text{PW}} = 1\,\mu\text{s}$ as the time in which the hot spot can move. In the

leftover of $t_{\mathrm{int,eff}} = 4.5\,\mu$s, the thermocamera simply records the blurring of the thermal signal due to heat transport in the material. Figure 6.9(c) shows the start and end position of the motion of a heat source as shown in (a) in order to produce a time-averaged signal as in (b). The red arrow indicates the motion of the heat source during the pulse. The relation between the motion to the recorded signal justifies the use of the distance d, as indicated in Fig. 6.9(c), as the way the heat source moved during $1\,\mu$s unaffected by heat dissipation after the pulse end.

By measuring the deviation d from the circular shape in the Figs. 6.2, velocities, i.e., $d/1\,\mu$s, can be obtained. In the case of a perfect circular shape, the result would be $d = 0$ and therefore the velocity zero.

In order to compare these data with those shown in Fig. 6.3, the velocity data from the deviation measurement have to be integrated. Additionally, they have to be corrected. This is a result of the situation depicted in Figs. 6.9(d,e). The distances d measured for each pulse cannot be simply added. The hot spot motion paths of consecutive pulses have a certain overlap, indicated as d_{over} in Fig. 6.9(e). For determination of this overlap during the pulses, the data in Fig. 6.2 have been analyzed again. The motion of the edge of the thermal signal z_{edge}, schematically shown in the inset of Fig. 6.10, has been evaluated. The result is given in Fig. 6.10. The difference between the z_{edge} values of consecutive $1\,\mu$s pulses Δz_{edge} is related to d_{over} by $d_{\mathrm{over}} = d - \Delta z_{\mathrm{edge}}$. This can be used to correct the z data by subtracting d_{over}.

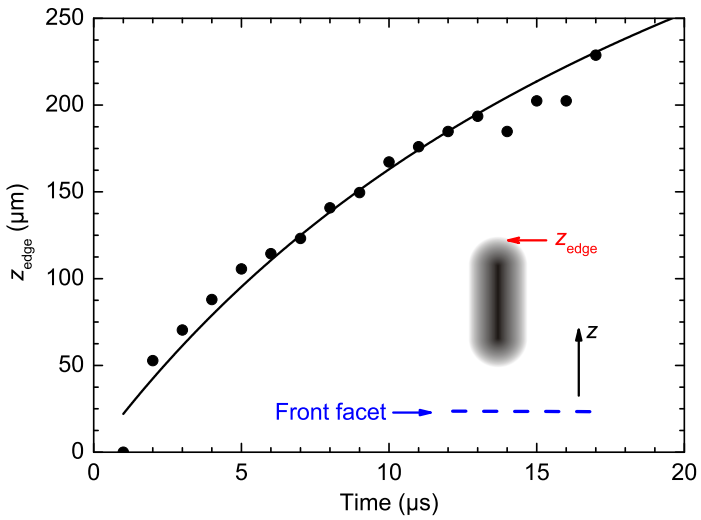

Figure 6.10: Evaluation of the position of the damage area edge z_{edge}. The inset indicates the position of z_{edge}. The relative position of the front facet is marked by the dashed line. Notice that the distance extracted for the first COD event, i.e. at $1\,\mu$s, is set to zero. The black line gives a hyperbolic fit to the data.

Figure 6.11 verifies a good agreement of both data sets. Notice, that the shown data are in the range of up to 12 μs. For times thereafter, the shape of the thermal signal becomes inhomogeneous and is therefore difficult to analyze with the shape deviation method. In this case, the determination of velocities by analyzing the motion of the center of gravity is more robust. However, both methods provide adequate information about the defect kinetics.

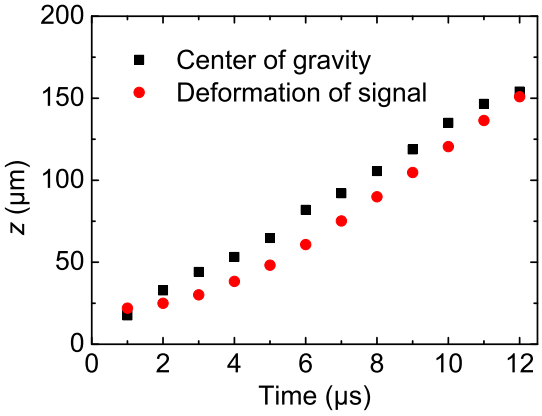

Figure 6.11: Comparison of the two data sets obtained for the distance z of the hot spot from the front facet. The black squares represent data taken from the center of gravity of the thermal signal. The red dots results from integration of the velocity data obtained by evaluation of the deformation of the thermal signal. Additionally, this data set is corrected for d_{over}, cf. Fig. 6.9.

Temperature Estimation

With the data obtained above, it is possible to make up an energy balance, following the idea already presented in Sec. 5.2.2. Therefore three aspects have to be considered:

- The available energy,
- The volume that absorbs this energy,
- The heat dissipation.

The discussion starts with the *first* aspect. As demonstrated in Sec. 5.2.2, it is valid to take the difference in the output power between consecutive pulses as the energy stored in the damage. The internal power is slightly higher, because of the remaining $\approx 3\%$ reflectivity of the anti-reflection front facet coating. A deviation of the results, however, originating from this is much smaller than the error made by estimations, so no correction for this was implemented. The evolution of the optical output power is shown in Fig. 6.8. It can be assumed that the lateral defect evolution is slow. Therefore, the obtainable laser light energy is almost constant during a pulse. In order to determine the values for the following calculation, the fitted curve shown in Fig. 6.8 is used. The energy re-absorbed per 1 μs long pulse is given in Fig. 6.12.

The *second* aspect, the volume in which this energy is stored during each pulse, is addressed in the following. The shape of this volume, representing the heat source in the subsequent discussion, is assumed to be rectangular, within the QW and waveguide plane. There, the laser light field is present which is the energy source of the process. Its extension in z direction is the difference between the distances shown in Fig. 6.10 for two consecutive pulses. This is valid as long as the damage growth is considered to take place during a pulse. A height of $1\,\mu$m is used which corresponds to the waveguide thickness and which is verified by calculations presented in Sec. 5.2.2. The width of $20\,\mu$m is taken from the images of the opened device, see Fig. 6.5(a). The evolution of this volume in time is given in Fig. 6.12.

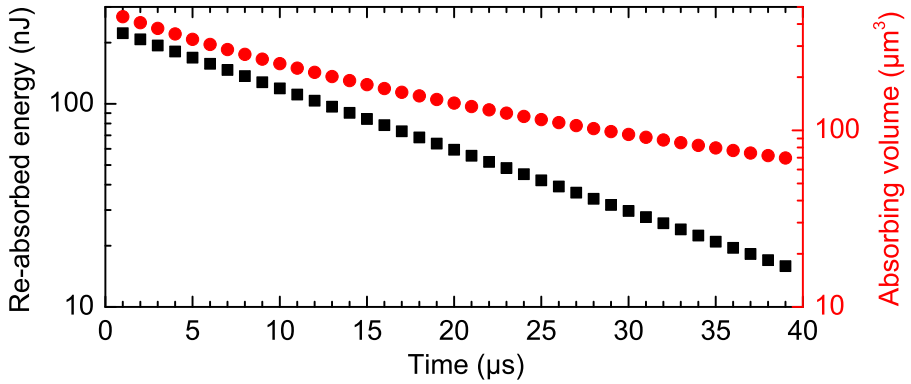

Figure 6.12: Re-absorbed laser light energy (black rectangles) and absorbing volume (red dots). The data points are obtained using the fit curves in Figs. 6.8 and 6.10.

Due to the short times considered here, the heat transport during the laser light pulse is neglected and Eq. (5.2.3) is used again:

$$W_{\text{theo}} = c \cdot \rho \cdot V_{\text{def}} \cdot \Delta T \qquad \Rightarrow \qquad \Delta T = \frac{W_{\text{theo}}}{c \cdot \rho \cdot V_{\text{def}}} \quad , \tag{6.2.1}$$

with the specific heat $c = 0.33\,\text{J}/(\text{gK})$ and mass density $\rho = 5.33\,\text{g}/\text{cm}^3$ for GaAs. For W_{theo} and V_{def}, the values for the energy and volume from Fig. 6.12 are taken, respectively. The result is the average temperature rise $\Delta\overline{T}$ of the absorbing volume. By adding the heat sink temperature of 23°C, one gets the average temperature $\overline{T}$, see Fig. 6.13.

The *third* aspect, considerations about the heat dissipation, will lead to a calculation of the maximal temperature T_{max} that was achieved during the degradation process. Therefore, the temperature profile must be known. In this situation, the thermocamera data help. Figure 6.14(a) shows, e.g., the cut along the z-axis through the middle of the thermal signal presented in Fig. 6.2(d). The temperature profile on the side where laser light is absorbed, i.e., the side facing the inner cavity, is crucial. A linear decrease can be found there, indicated by the dashed line.

In the following calculation, the linear temperature profile is assumed to be of spherical symmetry, because the heat transport can be assumed as isotropic. Furthermore, the thermocamera integration time is longer than the pulse. This means, the heat transport comes into play when analyzing the thermal signal, in contrast to the considerations about energy absorption above.

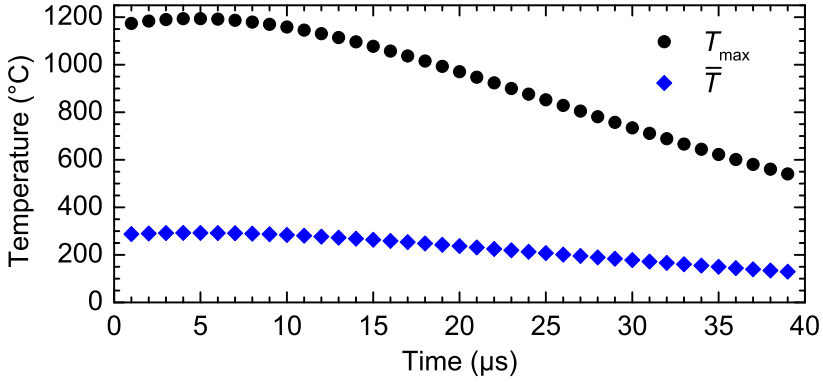

Figure 6.13: Evolution of the estimated average temperature $\overline{T}$ (blue rectangles) in the absorption volume and maximal temperature T_{max} (black dots) at the location of the hot spot.

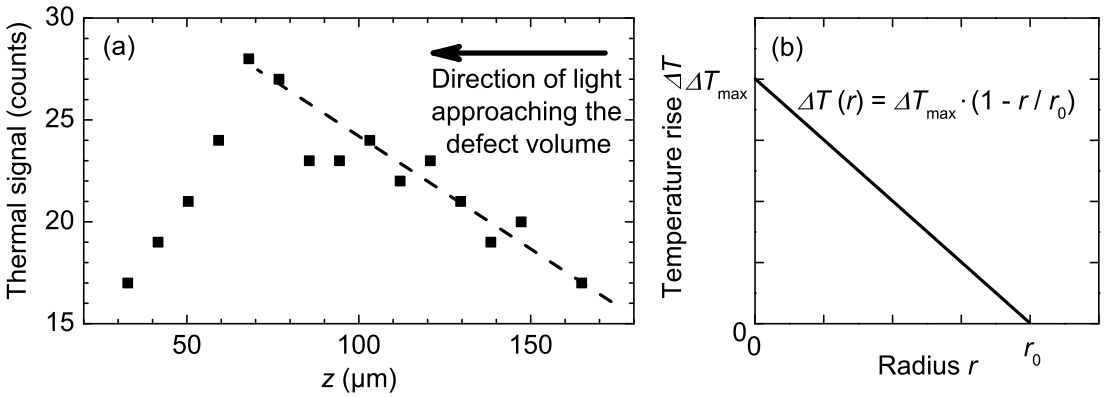

Figure 6.14: (a) Cut through the thermal image in Fig. 6.2(d). The direction of the light from the inner-cavity towards the front facet is indicated. The dashed line indicates a linear temperature profile at this side of the damaged area. (b) The radial temperature distribution as used for the estimation of the maximal temperature.

As a result of the spherical volume, the linear temperature profile only depends on the radius r, where $r = 0$ is at the center associated with the highest temperature rise ΔT_{max} with respect to the heat sink temperature. This profile is shown in Fig. 6.14(b). The functional dependence of the temperature rise is:

$$\Delta T\,(r) = \Delta T_{max} \cdot \left(1 - \frac{r}{r_0}\right) \quad . \tag{6.2.2}$$

The radius of the considered sphere is r_0. At this distance, the temperature reaches the heat sink temperature.

In order to determine $\Delta T_{\max}$ the following integral for the average temperature $\Delta\overline{T}$ in the spherical volume V_{Sphere} has to be solved:

$$\begin{aligned}\Delta\overline{T} &= \frac{\int\limits_{V_{\text{Sphere}}} \Delta T\,(r)\,\mathrm{d}V_{\text{Sphere}}}{V_{\text{Sphere}}} \\ &= \frac{\overbrace{\int\limits_0^{2\pi}\mathrm{d}\varphi \int\limits_0^{\pi}\sin\theta\;\mathrm{d}\theta}^{=4\pi}\int\limits_0^{r_0}\Delta T_{\max}\cdot\left(1-\frac{r}{r_0}\right)\,r^2\,\mathrm{d}r}{V_{\text{Sphere}}} \\ &= \frac{\frac{\pi}{3}\,r_0^3\cdot\Delta T_{\max}}{\frac{4}{3}\pi\,r_0^3} \\ &= \frac{\Delta T_{\max}}{4}\end{aligned} \tag{6.2.3}$$

This gives the relation between the maximal and the average temperature rise:

$$\Delta T_{\max} = 4\cdot\Delta\overline{T} \tag{6.2.4}$$

The values for $T_{\max} = \Delta T_{\max} + 23°\text{C}$ are given in Fig. 6.13. During the first $12\,\mu$s, i.e. the first 12 single pulses, $T_{\max}$ has a nearly constant value of $(1200 \pm 400)°\text{C}$ which is on the order of the melting temperature of pure GaAs at 1240°C and the $Al_{0.35}Ga_{0.65}As$ waveguide at 1580°C. The error arising from the made assumptions is given by the detection limit of the thermocamera of $400°\text{C} - 500°\text{C}$ at the used experimental conditions. Details will be given in the following section. This temperature confirms the statement given in Sec. 5.2.3, where TEM images have been analyzed, that the core region of the defect volume melts and re-solidifies. Furthermore, the constant temperature during the first pulses can be seen in the thermal images taken trough the top window, Fig. 6.2. There the colorscale, indicating the magnitude of the thermal signal, does not change significantly in the beginning. The temperature keeps constant due to the parallel reduction of the re-absorbed energy and the absorbing volume, that is visible in Fig. 6.12 for the first $\approx 12\,\mu$s. When the volume decrease slows down ($> 12\,\mu$s, Fig. 6.12) the estimated temperature decreases, cf. Fig. 6.13. The presence of temperatures on the order of the materials melting point after microseconds rules out considerations about a Ga-rich defect front propagating at substantially lower temperatures, as suggested by Snyder *et al.* [160].

The Detection Limit of the Thermocamera

As one can see, the thermal signal reaches the noise level after $\approx 40\,\mu$s, Fig. 6.3(b), while light energy is still re-absorbed and heats up the material. The hot spot temperature there is $\approx 500°\text{C}$. This temperature represents a detection limit for the case of a heat source that is heated up during $1\,\mu$s and detected with the microscope-objective of the thermocamera with $t_{\text{int,eff}} = 4.5\,\mu$s. In order to verify this estimation, a NETD of 20 K for this configuration, cf. Tab. 3.1, can be used. Moreover, the geometric dimension of the heat source has to be considered. While a pixel of the thermocamera images a square of $8.8\,\mu\text{m} \times 8.8\,\mu\text{m}$, the area of the heat source is $3.5\,\mu\text{m} \times 3.5\,\mu\text{m}$. This can be estimated by the z-shift of the 35th pulse

(Fig. 6.10), i.e., the one where the thermal signal vanishes [cf. Fig. 6.3(b)]. Scaling the NETD value with the area ratio (camera pixel area / heat source area), results in a detection limit of $\approx 400°C$. This is on the same order of magnitude as the value obtained by the above estimation. Eventually, this leads to the statement, that any COD-related thermal signal recorded under similar conditions indicates a temperature of at least $400°C - 500°C$.

Ex-post Data

There is an excellent agreement visible in Fig. 6.5(a) of the region of non-radiative recombination identified by CL and the hot spot positions obtained during the step test. This indicates that the dark band regions in the CL maps are indeed the source of the significant local heating monitored by the thermocamera. Furthermore, the accumulated sum of the thermal events, as shown in Figs. 6.2(a-w), reproduces the area covered by the dark lines of the CL map well, Fig. 6.5(b). There the sum of the thermal signal is represented in grayscale, while the defect pattern found by CL is shown as reddish area. The yellow shaded area indicates the remaining part of the n-contact close to the front facet. In this region the thermal signal gets partly blocked.

The damage pattern found by CL is more localized than the thermal signal due to the heat transfer during $t_{\mathrm{int,eff}} = 4.5\,\mu$s of the thermocamera. The clearly increased LBIC signal, Fig. 6.4(b), close to the facet compared to the middle of the laser cavity illustrates the elevated defect density there. Similar to the thermal signal in Fig. 6.2, it is also spread over an area significantly wider than the emitter stripe. This indicates the defects detected by LBIC to be thermally induced. The correlation of the shapes of thermal and LBIC signals is demonstrated in Fig. 6.5(c), showing the result of a pixel-by-pixel analysis. Therefore the pixel-grid of the LBIC measurement is adapted to the coarse grid of the thermocamera; both are aligned by the clear visible edges of the top-contact window. The backgrounds of both signals have been subtracted. For each pixel the amplitudes of thermal signal and LBIC signal are plotted against each other. The linear dependence in Fig. 6.5(c) points to a similar spatial extension and distribution of signal heights of the two data sets. A clear deviation is only visible for locations very close to the facet, where the LBIC signal is remarkably higher [open circles in Fig. 6.5(c)]. This can be assigned to shadowing effects of the thermocamera signal by the remaining part of the top-contact materialization. The LBIC map has a higher spatial resolution than the thermal image. Therefore, the detected thermal signal close to that blocking region is lowered by averaging. In contrast the higher LBIC resolution reduces averaging effects for that signal.

The damage detected by CL is of different nature compared to the defects found by LBIC. While CL is sensitive to regions in the QW where spontaneous emission is significantly reduced or completely terminated by the destruction of the QW, LBIC detects defect levels in the electronic structure even in areas where stimulated emission is still present. This indicates the following two different degradation processes:

- A thermally activated spread of small damage sites occurs, e.g., point defects, over an extended area of $\approx 60\,\mu$m around the damage found by CL, Fig. 6.5(a). These defects may potentially act as trigger for further degradation processes particularly if the intensity of the light field in this region is still high.

- A spatially more localized degradation of the material directly involved and substantially damaged within a thermal runaway process, as assumed in the literature [176, 181], leads to a destroyed QW-region.

Both mechanisms are related to temperature, but the second one by a threshold condition. It occurs only once at a specific location, while the first one is always present at elevated temperatures. In this way, the point defects can act as starting points for the second and all further thermal runaways, which create new point defects by pronounced local heating. In contrast, the reason for the initial thermal runaway, starting this chain of events, is harder to identify. However, it will start at the weakest point of the structure at the facet or inside the cavity, as discussed on the basis of high resolution microscopy in Sec. 5.2.3. The idea of tracing the damage back to its origin and identifying the COD ignition site will be addressed in Sec. 6.3. In comparison with CL images of devices with reduced damage duration, i.e., less than the 35 pulses applied in the case shown here, it becomes evident, that the internal damage structure is created step-by-step during the series of successive single pulses. A comparison with literature dealing with CL characterization of cw COD damage, e.g., Chin *et al.* [41], confirms the damage pattern found, see Fig. 6.5(a), to correspond to the ones observed in cw tests. This is important, because it demonstrates that the step test addresses the same degradation mode as present during cw operation.

6.2.2 Data Obtained From Both Facets and Cavity

Depth of Focus of the Thermocamera System

The thermal emission as result of the runaway process is quite localized, see middle-inset in Fig. 6.6(a). Therefore it is highly likely that it indicates the position of the damage front moving along the cavity, following the energy source of the degradation process – the laser light field. Evaluating the recorded data allows to determine the depth of focus of the thermocamera in case of the structure and material system typical for DLs. To get this information, the strength of the thermal signal seen from the front facet is plotted over the distance of the signal source from this facet. These z-values are the positions of the hot spots seen in the side view of the cavity. The camera was focused to the front facet plane. Furthermore, the thermal images recorded from the side ensure that the signal magnitude itself keeps constant. The absorption of the thermal light in the semiconductor structure can be neglected. Since, the free carrier absorption of GaAs is below $10\,\mathrm{cm}^{-1}$ [172], it will only affect the signal significantly in the millimeter range. Therefore, the reduction of the thermal flash amplitude seen from the front is the effect of the signal source leaving the focal plane. The result of this analysis is shown in Fig. 6.6(b). A lower limit of $40\,\mu\mathrm{m}$ is estimated for the depth of focus; the criterion is the $\left(1/\mathrm{e}^2\right)$-drop of the signal.

Kinetics in Different Material Systems

The physical background resulting in either front or rear facet COD of devices which are nearly similar in their electrical and optical specifications, has been discussed in Sec. 4.2.4. However, the subsequent propagation of the defect front in terms of thermal flash magnitude (with respect to size and temperature of the heated area) and propagation velocity, while creating the secondary damage, is quite similar. This leads to the following picture: Once macroscopic primary damage is created, it serves as main origin for any further heating and subsequent propagation of the defect front by closing the external feedback loop, cf. Sec. 2.2. Although QW and waveguide design affect P_{COD}, see Sec. 4.2.4, the subsequent propagation of the defect front is almost independent of these parameters. The $30\,\mu\mathrm{m}/\,\mathrm{pulse} = 30\ \mu\mathrm{m}/\,\mu\mathrm{s}$ propagation velocity of the defect front along the laser axis matches well the data by Jacob *et al.* [176]. No slowing down of the propagation in later pulses was observed in this particular experiment. This is a re-

sult of the maintained step-wise current increase. The thermal signal almost maintains its magnitude, see Fig. 6.7(a). This indicates a constant temperature during the propagation of the defect front. It verifies the results based on TEM cross sections, presented in Sec. 5.1.3, also indicating a constant value. The measured uniform defect propagation velocities are complementary to the results of Sec. 5.1.2. There it has been shown that the geometric spread of the damage depends on small differences only for a short time, i.e., $< 100\,\mathrm{ns}$, after COD ignition. The situation changes for longer times: The influence of small inhomogeneities vanishes and the defect propagation velocities reach a material specific value. In this way, the velocities allow rather comparing structures, while the fast dynamics are sensitive to inhomogeneities and weak points as result of device processing.

The observations of the propagating hot spots of Planck's radiation along the z-axis clearly prove that the front facet and the areas already passed by the damage front return quickly to substantially lowered temperatures. Finally these measurements show, that it is possible to trace the motion of the damage front inside the emitter stripe in a standard device, i.e., without any windowed contacts or device modification.

6.3 Modeling

A fully developed COD manifests itself as an extended damage pattern in the QW plane. Figure 6.15 includes examples of EBIC maps taken from devices of batches C,D, and E.

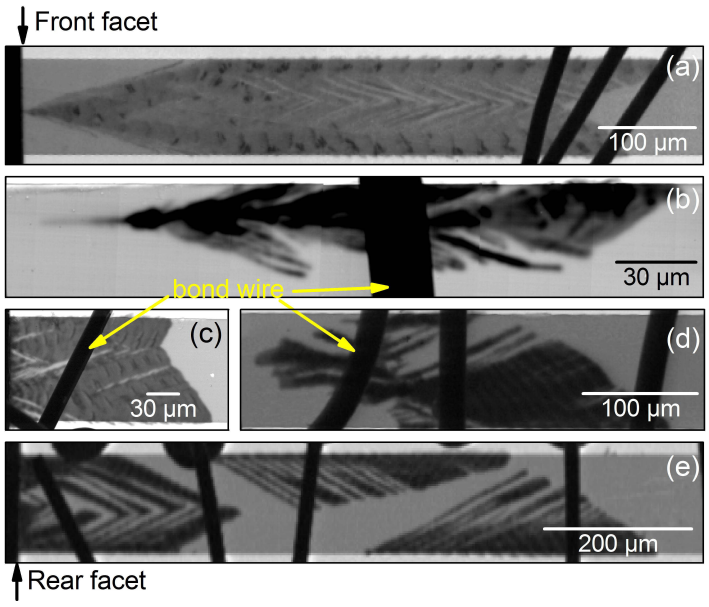

Figure 6.15: Defect pattern at different DLs detected by EBIC: (a) Observed in a region close to the front facet (device D_1). (b) Being located inside the cavity ($\approx 400\,\mu$m form the front facet; device D_2). (c) Located at the rear facet (device C_1). (d) Starting inside the cavity ($\approx 550\,\mu$m from the front facet; device E_4). (e) located at the rear facet (device E_5). The appearance of bond wires in the foreground is indicated at some examples.

In case of Fig. 6.15(a), a COD starting from the front facet is shown, verified by thermography, cf. Fig. 6.7(c). Figure 6.15(b) gives an example of a COD starting inside the cavity $\approx 400\,\mu$m from the front facet of the 2 mm long emitter stripe. In Fig. 6.15(c), a rear facet COD is shown. Two rather complex defect pattern are given in Figs. 6.15(d) and (e) for the cases of internal and rear facet COD, respectively. The last two examples are not easy to understand in terms of causality, i.e., the temporal sequence of damage path formation is not obvious. For example, one could assume that the defect growth in Fig. 6.15(e) started at the peak of the defect pattern $\approx 250\,\mu$m from the rear facet and propagated than towards it. As will be shown later, *in-situ* thermography proves this wrong. This points to the need of a deeper understanding of the dynamics of the third COD phase.

Various other authors, e.g., Refs. [134, 141, 182], have modeled the light field dynamics in the past. Further authors [183–186] have modeled the thermal distribution in the device. Modeling incorporating both aspects in detail has just been done up to the point of thermal runaway [48, 143, 151]. Taking into account the complexity of the problem, Romo *et al.* [151] use a finite element solver to deal with the coupled three dimensional differential equations. However, the additional incorporation of a permanently changing device geometry due to the damage growth in such a model would require extremely long calculation times.

The model of the 3rd COD phase presented in the following is reduced to the following basic principles:

- *Unidirectional energy entry* into the existing damage site by the laser light field as energy source for the growth process, cf. Sec. 2.2,
- *Isotropic thermal energy and defect spread*, as measured by LBIC in Sec. 6.1.1, and
- *Shadowing effects* as seen from side-view thermography in Sec. 6.1.2.

The unidirectional character of the energy entry is a valid assumption as long as the model region is close to a facet. As discussed in the previous chapters, a COD starting there is the most likely scenario. Shadowing describes the situation when an absorbing site blocks the direct light path between the two cavity mirrors.

6.3.1 Introduction of the Model

An iterative phenomenological 2-dimensional macroscopic model has been developed [178–180]. The third dimension (growth direction) is essential for the heat transport and is included in the model as a parameter. The QW plane is discretized as a 2-dimensional matrix consisting of quadratic grid cells, being initially empty. The only energy source for the damage process is the laser light field. The model is based on two energy transfer mechanisms:

- Energy from the laser field, that is *directed* along z is absorbed in a cell, depending on the amount of damage stored there. Absorbed energy further increases the damage level.
- After reaching a critical damage limit (*CD*), an *isotropic* energy transfer to the surrounding cells is assumed. This simulates the thermal runaway effect and an energy re-distribution via thermal transport.

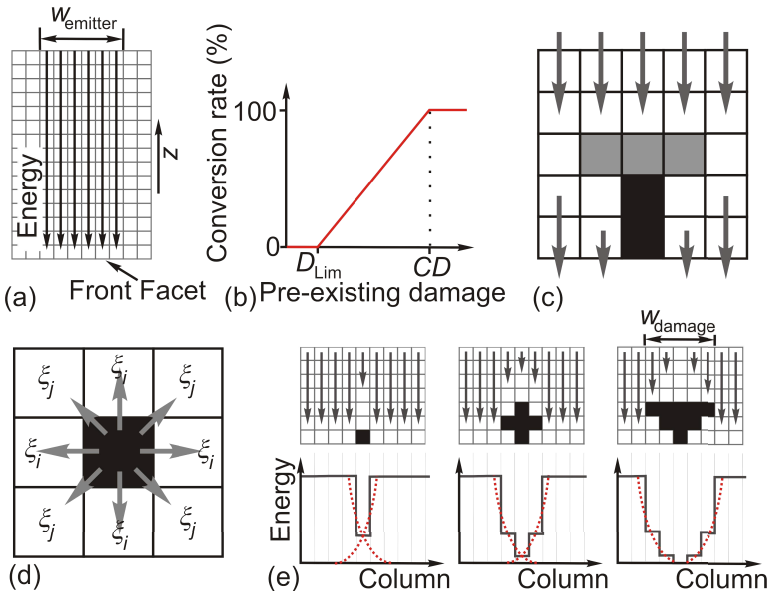

Figure 6.16: The defect growth model. (a) Scheme of the grid. The light energy entry is indicated by arrows. (b) Functional dependency of the absorbed energy to damage conversion rate on pre-existing damage level in the cell. (c) Scheme of the absorption process (full black cells have exceeded *CD* level, while the gray cells are damaged at a level between D_{Lim} and *CD*). (d) Isotropic energy dissipation from a cell that exceeded *CD* level to neighbor cells (diagonal transfer is scaled accordingly). (e) The length of the arrows quantifies the different energies available in the different columns as caused by the presence of defects (upper panel). Lower panel shows the exponential lateral energy distribution (red dotted line) starting from both edges of the damage (representing the reduced optical feedback due to defect sites in the cavity).

While modeling the energy flow, optical and thermal energies are treated as equivalent. Absorbed energy is equivalent to an increase of the damage level.

One iteration step includes calculations as described in the following: The resulting grid after an iteration is the starting grid for the next iteration. The energy, representing the laser light field, is directed along z and points from the inner cavity towards the facet, see Fig. 6.16. The laser light field collects energy from the entire cavity length by stimulated emission and transfers it to a particular defect volume, e.g., at a facet or another absorbing site in the cavity. In this way, a substantial amount of energy can be redistributed in a short time to a small volume, which is nothing but a description of the thermal runaway itself. The number of columns with energy flow is n_{emitter}. Altogether they represent the emitter stripe with a width of w_{emitter}.

The total available energy $E_{\max}$ per iteration is:

$$E_{\max} = [E_{\max,0} \cdot (1-P)] \cdot \left(1 - \frac{w_{\text{damage}}}{w_{\text{emitter}}}\right) + \underbrace{P \cdot E_{\max,0}}_{E_{\text{Low}}} \quad , \tag{6.3.1}$$

where $E_{\max,0}$ is the energy available in absence of any damage and w_{damage} is the overall lateral width of the internal defect structure [see Fig. 6.16(e)]. In this way, the fraction $w_{\text{damaged}}/w_{\text{emitter}}$ introduces a linear scaling depending on the fraction of undamaged laser cavity, i.e., regions of undamaged material on a straight line between the two mirrors. P is the percentage of the light energy that results from amplification of spontaneous emission. This accounts for the high single loop-gain in a semiconductor laser. As a result, there is still a certain light intensity remaining, even if the light cannot reach the facet in the particular column. This remaining energy is E_{Low}. An experimental indication for the presence of this effect has been given in Sec. 5.1.4.

In case of an undamaged device, each emitter column receives the same amount of energy $E_{\max}/n_{\text{emitter}}$, see Fig. 6.16(a). If energy is deposited in a cell, its damage level increases. This damage level determines the absorption in the cell in the next iteration, leading to further defect accumulation. The energy-to-damage-conversion follows a function as shown in Fig. 6.16(b). Below a certain cell damage level, denoted D_{Lim}, the cell is non-absorbing, in this case a potential heating of the cell is compensated by the heat sink and causes no damage. Above D_{Lim}, the conversion rate of absorbed energy to cell damage is linear representing defect accumulation, e.g. by temperature enhanced defect motion and generation. This goes on up to the level called *CD*, where the cell has reached a complete damaged state. Afterwards, this cell completely absorbs and converts all entering energy. The light not absorbed by a cell passes it and can be absorbed by another one or, if reaching the facet, leaves the laser, Fig. 6.16(c). A consequence of this concept is that damage growth is only possible, if a pre-existing damage at D_{Lim} level or higher is present. However, this is no real limitation to the model, since this situation is given after the thermal runaway in phase two took place.

If a cell exceeds the *CD* level, an isotropic energy transfer of a percentile ξ of the absorbed energy to the eight surrounding neighbor cells takes place (where ξ is the sum over all ξ_{i} and ξ_{j} plus one ξ_{i} for the initial cell). This simulates the fast temperature rise and its consequences during the thermal runaway. The energy along the diagonal direction is scaled accordingly to account for the quadratic shape of the cells; see Fig. 6.16(d). This isotropic transfer simulates a spread of damage by thermal energy which is independent of the directionality of the laser light field.

If a region in the grid exceeds the D_{Lim} level, the energy $E_{\text{column,x}}$ available in this column is reduced. It decreases exponentially with lateral distance x_{edge} from the edges of the absorbing region:

$$E_{\text{column,x}} = \frac{E_{\max}}{n_{\text{emitter}}} \cdot \exp\left(-\frac{x_{\text{edge}}}{\tau_{\text{d}}}\right) \quad , \tag{6.3.2}$$

where the parameter τ_{d} is a characteristic decay length. This decrease of the laser field at the edges of the damage, see Fig. 6.16(e), takes into account reduced feedback, diffraction effects, and changes in the mode pattern in presence of defects. In each iteration step, $E_{\text{column,x}}$ is calculated before the absorption is simulated. By setting different defect distributions in the starting grid, different scenarios can be modeled.

6.3.2 Influence of the Model Parameters

Having set up a model as the one described above, it is essential to examine the influence of the input parameters. After extensive modeling it became clear that they can be separated into two groups: Parameters having only negligible influence on the result, and parameters with high importance for the result. The ones of minor importance are the D_{Lim} level, as long as $D_{\mathrm{Lim}} \ll CD$, and $E_{\mathrm{max},0}$, as long as the ratio $E_{\mathrm{max},0}/CD$ remains constant. The *principle* parameters are, the *CD* level, P, ξ, and τ_{d}. The effects of the latter ones are investigated in the following.

The influence of these four parameters of major importance on the shape of the damage is shown in Fig. 6.17. There, a grid with 701×701 cells is used, $1\,\mu$m equals 10 cells, the emitter stripe is $50\,\mu$m in width, $E_{\mathrm{max},0} = 10$ energy units, $D_{\mathrm{Lim}} = 0.1$ energy unit, and the configuration is refreshed 1500 times (number of iterations). A single starting point (damage level $> CD$) is set at the facet which is located at the bottom of each sub-figure. The first column, Fig. 6.17(a-c), shows the influence of the *CD* level, by varying *CD* (10, 20, and 40 energy units), while the other parameters are kept constant at $\xi = 85\%$, $P = 5\%$, and $\tau_{\mathrm{d}} = 1.25$. The other parameters are investigated the same way: ξ in Figs. 6.17(d-f) ($CD = 10$ energy units, $\tau_{\mathrm{d}} = 1.25$ cells, $P = 5\%$), τ_{d} in Figs. 6.17(g-i) ($CD = 10$ energy units, $\xi = 85\%$, $P = 5\%$), and P in Figs. 6.17(j-l) ($CD = 10$ energy units, $\xi = 85\%$, $\tau_{\mathrm{d}} = 1.25$ cells). Many parameter combinations have been tested to evaluate the obviously existing crosstalk between the parameters, the shown configurations are found to be the ones showing the main influence of each parameter.

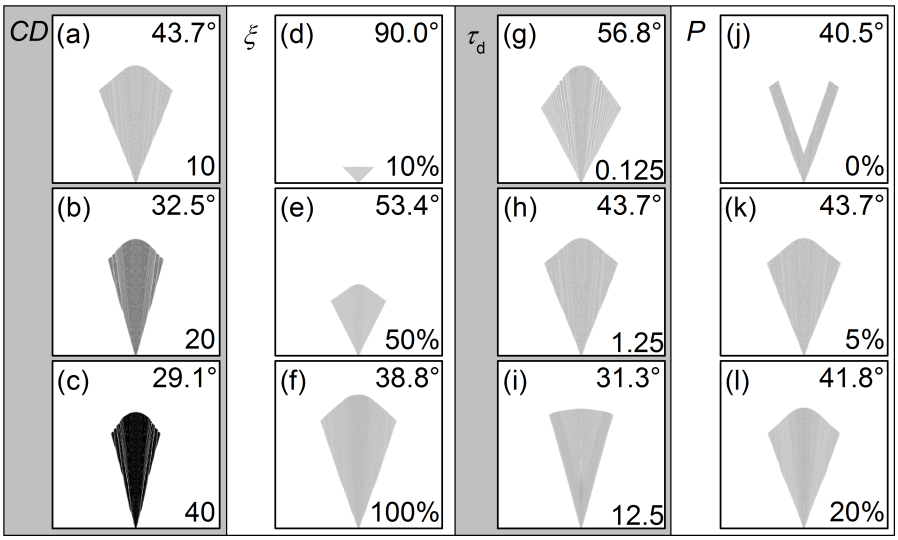

Figure 6.17: Influence of the principle modeling parameters *CD* level, ξ, τ_{d}, and P ($E_{\mathrm{Low}} = P \cdot E_{\mathrm{max},0}$). The shown images represent an area of $70\,\mu\mathrm{m} \times 70\,\mu\mathrm{m}$ each. For each modeling run, one COD starting point is set, always in the middle of the emitter stripe at the facet (bottom). The grayscale is the same for all sub-figures. The value of the modified parameter is given in the right lower corner of each sub-figure. The opening angle α_{spread} of the wedge-like defect structure is given in the right upper corner of each sub-figure. The other used parameters are specified in the text. Note, that (a,h,k) are similar as a kind of reference. The values for *CD* are given in energy units and the ones for τ_{d} in cells.

The *CD* level affects mainly the grayscale of the damage pattern Figs. 6.17(a-c). In contrast to that, the opening angles α_{spread} of the wedge-like defect structure, as given in Fig. 6.17, are determined rather by ξ. The shape of the damage front, Figs. 6.17(d-l), is determined by ξ, τ_{d}, and $E_{\text{Low}} = P \cdot E_{\text{max,0}}$.

Nevertheless, as mentioned above, these parameters are not independent from each other, which makes it difficult to assign them to real physical quantities. However, the *CD* value can be seen as the *COD resistance* of the material. This stands for the amount of energy and preexisting defects in a certain volume of the material, which are necessary to start the thermal runaway process.

The parameter ξ represents the ability of the material and its surrounding (waveguide and cladding layers) to transfer thermal energy. In particular, the connection between ξ and the specific thermal resistance R_λ will be discussed in the following Sec. 6.3.3.

The parameter τ_{d} summarizes the mechanisms of diffraction effects and mode redistribution in the cavity. Its influence on the shape of the defect pattern, in cases where only one COD starting point is present, is rather small, Fig. 6.17. In extended defect networks with multiple ignition points, the influence of τ_{d} on the final shape is elevated, as verified by extensive modeling.

The maximal achievable energy $E_{\text{max,0}}$ can be simply related to the optical output power of the laser before COD starts.

The energy E_{Low} is directly related to the amplified spontaneous emission in the DL cavity. It is the light power achievable without feedback due to a blocked light path towards the mirror by damaged material, i.e., *shadowing*. The influence of E_{Low} is quite small if $w_{\text{damage}} \ll w_{\text{emitter}}$, when $P \ll 1$ which is the case for DLs. A limitation of the model is that the energy transfer is limited to the neighboring cells. This distance underestimates the real range of influenced cells by thermal energy. In the shown simulation, this isotropic energy transfer happens on a length scale of $1\,\text{cell} = 100\,\text{nm}$, while the data presented in Sec. 6.1.1 indicate point defect creation with a radius of $\approx 60\,\mu\text{m}$. However, the simplification to a 1 cell radius is necessary to keep the calculation time in a reasonable range. This weakness of the model is balanced by $E_{\text{Low}} > 0$ so that V-like shapes as in Fig. 6.17(j) are suppressed. Furthermore, $P = 0$ would mean, that the damage growth process would be stopped if the full width of the cavity is shaded somewhere. This is not consistent with the experiment – defect growth goes on in this case, e.g., verified by *in-situ* thermography measurements as shown in Fig. 6.7.

The possible shapes obtainable for a given set of starting points are not extremely different as long as the combination of parameters and their values are realistic. Especially, they have to respect the energy conservation law by distributing not more energy via thermal transport as absorbed from the electromagnetic energy of the light field. This stability of the defect pattern arising from a given set of initially damaged cells allows to estimate the position and extension of the COD starting points from the final defect pattern with remarkable accuracy, cf. Sec. 6.3.3.

In the literature, the defect pattern are alternatively explained by geometric effects [41]. There, the authors discuss the possibility of stable modes arising from reflection not only at the cavity mirrors but additionally at the lateral edges of the emitter stripes. These multiple internal reflections lead to an optical beam approaching the facets not perpendicular but under a certain angle. This angle is then identified as reason for the extending width of the damage pattern along the cavity. The occurrence of these hypothetical modes, however, is related to a sharp index step at the lateral emitter edges of $\Delta n > 0.1$ for BA DLs which is an unrealistic high value, e.g., compared to $\Delta n \approx 1 \cdot 10^{-3}$ typically used for ridge waveguides and found to be thermally induced in BA DLs (see Sec. 4.2.3). Moreover, this approach cannot explain a lot of obvious effects. Among them are the branching of the defect structure and regions

of undamaged material enclosed by defects. In the model discussed here, the defect shapes and the mentioned effects are results of the three basic mechanisms – unidirection energy entry, isotropic thermal distribution, and shadowing effects. Especially the shadowing of the laser field makes the development of complex defect pattern possible. Its occurrence has been verified by the measurements of the hot spot motion presented in Sec. 6.1.2. There a heating was found *only* at the part of the damage region facing the impinging laser light. This means, that the light, as energy source of the process, was not able to pass this edge region between damaged and undamaged material and is completely absorbed there – exactly what *shadowing* means.

6.3.3 Application of the Model

In this section, the practical relevance of the above presented model is demonstrated [178–180]. In a first part, using static results of the model, the connection between material system and experimentally found damage pattern is explained with the help of results obtained by varying the model parameters, see Sec. 6.3.2. Furthermore, the origin of the branching, observed usually in COD defect pattern of real DLs, is discussed. A second part, related to the defect kinetics, shows the ability of the model to uncover weak-points of a device architecture by modeling the kinetics of defect growth.

Static Case

In the following, the physical reasons are discussed for two major experimental findings:

- Different spreading angles α_{spread} of the defect structure, Fig. 6.18, for different material systems, Tab. 6.1, and
- branching of the defect pattern, see Fig. 6.19(a).

As shown in the previous section in Fig. 6.17, the spreading angle of the defect α_{spread} is mainly influenced by ξ. A higher ξ-value results in a larger α_{spread}. The isotropic defect spread is likely a thermo-mechanical mechanism that is more pronounced if the heat conduction in the material is poor. The term *thermo-mechanical* refers to two findings described earlier: (i) The spread of point defects

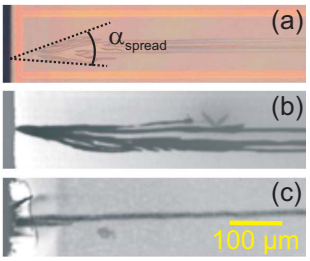

Figure 6.18: Experimentally determined damage pattern: (a) PL map of a 650 nm emitting device [187], (b) CL map of an 808 nm laser, (c) CL map of a 980 nm device. The front facets are at the left side. The opening angle α_{spread} of the defect pattern is indicated in (a). The given scale bar in (c) is valid for all sub-figures.

Figure	Wavelength (nm)	Material	R_λ (K·cm/W)	α_{spread}
6.18(a)	650	InGaAlP	13	24°
6.18(b)	808	$Al_{0.3}Ga_{0.7}As$	8	18°
6.18(c)	980	$Al_{0.085}Ga_{0.915}As$	4.5	$< 6°$

Table 6.1: Material properties of the waveguide and measured angles. R_λ values are taken from [172].

that is initiated by the high temperatures during COD, as seen in the comparison of LBIC data and thermal images in Sec. 6.1.1. This is initiated by the local thermal expansion of the region of heated semiconductor material. (ii) The conversion of the former mono-crystalline structure to a poly-crystalline one, shown by TEM measurements in Sec. 5.1.3. The damaged material requires an extended volume and induces strain in the surrounding material. The impact of both effects is elevated if the heat is more confined which is a synonym for a higher R_λ value. In case of the model, this means, the temperature in the neighbor cells is increased, leading to more efficient damage creation there. Exactly this mechanism is addressed by an increasing ξ-value. To close the line of arguments: An increasing ξ-value represents also an increasing R_λ. It is obvious that the material on both sides of the thin QW, namely the waveguide, accounts for the major part of the heat dissipation. Regarding to this argument, one has to take the material parameters of the waveguide material into account, while studying this effect.

Figure 6.18 shows examples for DLs that experienced COD. For comparison, representative samples of structures lasing at 650 nm (taken from [187]), 808 nm, and 980 nm are given. The respective waveguide materials and R_λ-values are given in Tab. 6.1. The measured values of the angle reflect the predicted behavior – larger values of α_{spread} are found in systems with larger R_λ. The angles are distinctive for each material system and therefore R_λ value. This can also be seen in Fig. 6.19(a). There α_{spread} has nearly the same value, indicated by the green lines, after each branching point. Such a behavior rules out possible connections to the following quantities, due to the fact that they are non-constant:

- The available energy from the laser light field, because this is consecutively reduced during the damage growth (this value is connected to the model parameters: CD and E_{Low})
- The mode redistribution and diffraction which changes in presence of damage (model parameter τ_{d})
- Geometric considerations, as suggested in [41] by Chin *et al.*, because the geometry of the remaining lasing material changes and branching points and already expressed branches can run side-by-side without an influence on α_{spread}

This again verifies the connection between α_{spread} and the thermal material properties established by the model.

Another issue addressed by the model is the branching of the defect pattern, e.g., see experimental data in Fig. 6.19(a). This effect can be seen especially if there are small inhomogeneities in the starting grid used for the model calculation. An example for modeling is given in Fig. 6.19(b). The used parameters are: $CD = 10$ energy units, $\xi = 20\%$, $\tau_{\text{d}} = 1.25$ cells, $P = 0\%$, $E_{\text{max},0} = 10$ energy units, a grid size of 701 cells $\times$ 701 cells, 10 cells/μm, emitter width 50 μm, and $D_{\text{Lim}} = 0.1$ energy units. The points of preset-damage are marked by red dots. This represents the situation of non-uniformity as present in

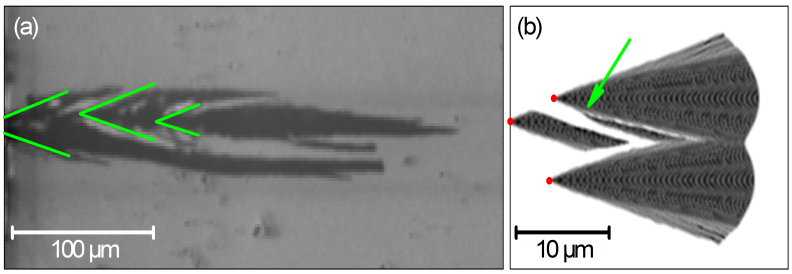

Figure 6.19: Branching effects measured (a) and simulated for a case with three different starting points (b). The front facet is at the left side. (a) The angles of the damage pattern at branching points are indicated by green lines. (b) The positions of pre-damaged sites in the simulation grid are marked by red dots, the location of a branching is marked by the green arrow.

practical devices. Even if these points do not show a sufficient level of absorption at the beginning, they can be further impaired during defect growth. An example of such a mechanism is the large distance spread of point defects as shown in Sec. 6.1.1. Eventually this brings them to a point where they act as additional starting points for damage growth. From the model, it is obvious that a small deviation from the isotropic energy re-distribution around a cell that exceeds *CD* level can cause a split in the damage pattern by creating a preferred direction for further damage growth. An enhanced branching behavior of the defect pattern indicates the presence of an elevated number of inhomogeneities in the material. Additionally, this is verified by the experimental finding in Sec. 5.1.2, where the re-distribution of the lateral modes after COD is discussed.

Moreover, the shadowing of areas by already damaged and therefore high-absorbing cells also causes the geometric stability of the created branches. It keeps them separately running side-by-side along the resonator axis. This effect is shown experimentally in Fig. 6.19(a) and modeled in Fig. 6.19(b). The obtained result shows the possibility to model even complex defect structures by setting starting and pre-damaged points in the initial simulation grid. This means, if a defect structure could be simulated well, the necessary starting points indicate weak-points of the real device structure.

Dynamic Case

Ex-post investigations of COD damage structures typically lack of pieces of information, namely details about the sequence of events during defect formation. A solution for this problem is presented in Secs. 6.1.1 and 6.1.2, the *in-situ* tracing of the damage front by micro-thermography. It has been shown, that this approach is suitable for reconstructing the internal defect pattern, even without device opening. Furthermore, the applied step test scheme allows to reconstruct the defect kinetics from thermal images due to the used time slicing. In the following, the discussion will be focused on a defect structure observed at device E_5 from batch E. This particular device has been chosen because of its rather complex defect pattern [see Fig. 6.20(b)], representing a benchmark for the model. The question will be addressed, if it is possible to re-construct the defect kinetics based on the final damage pattern by application of the model.

After the first COD event took place at $I_{COD} \approx 5\,A$, additional 42 pulses, each $t_{PW} = 1\,\mu s$ long and sequentially stepped up by $\Delta I = 1\,A$ were applied to it. This results in an overall time available to

damage growth of $\approx 43\,\mu$s. The laser is mounted p-side up, i.e. with the substrate side to the heat sink. Figure 6.20(a) shows a SEM top view image of the DL chip. The two rows of bond wires are clearly visible; the emitter stripe is located in between them. This image shows that the surface of the chip on top of the active region has absolutely no features which might influence the EBIC image taken through it. Figure 6.20(b) gives the results from the EBIC mapping. The emitter stripe can be seen clearly as dark gray rectangle. The areas next to the emitter stripe are light gray. It might be surprising that the structure beside the emitter stripe appears in a lighter color. However, here the distance from the top surface to the pn-junction is reduced with respect to the emitter stripe due to the etch step leading to an increased EBIC current. Inside the active device part, the defect pattern appears as black structure as a result of a reduced EBIC signal. The defect sites act as recombination centers and reduce in this way the steady-state non-equilibrium carrier concentration. Therefore, the creation of an EBIC signal (= current) in the potential gradient of the pn-junction is reduced. The defect network discussed here is located at the rear facet. The question whether COD starts at the front, rear or both facets depends strongly on the material system and the coating technology. For the used structure this is discussed in Sec. 4.2.4 (the actual device belongs to batch E).

Using the thermocamera in a corner mirror setup a step test approach gives a thermal image ($t_{\mathrm{int,eff}} \approx 4\,\mu$s) during each single pulse. In this way, the defect growth is monitored with $1\,\mu$s ($= t_{\mathrm{PW}}$) time resolution from two directions in parallel, similar to the experiments presented in Sec. 6.1.2. The hot spots extracted from these images are given as colored squares in Fig. 6.20(b). The ones in the bottom line come from side view observation, while the ones at the left side are detected from the rear facet (via the tilted mirror). Different colors point to different regions, in terms of a temporal delay in their appearance, of increased temperature. All the hot spots taken during the 43 pulses are summarized along these two axis. A two-dimensional reconstruction of the damage path, as in Fig. 6.7(c), is not possible with this data set. This is caused by the presence of multiple ignition points which does not allow an unambiguous assignment of x- and z-coordinates for each defect front.

The same color scheme as in Fig. 6.20(b) is used in Figs. 6.20(c) and (d), where the temporal evolution of the hot spots along the particular direction of observation is shown. Figure 6.20(c) contains the temporal evolution of the thermal signal seen from the side, i.e., in z-direction. In case of the signal obtained at the rear facet, Fig. 6.20(d), a first COD site occurs at $x \approx 80\,\mu$m. This is followed by a zig-zag motion of the signal with a slight tendency to the middle of the active region ($x = 50\,\mu$m) at the end. A second COD site occurs at $\approx 20\,\mu$m with a temporal delay of around $10\,\mu$s. This one also shows a motion towards the emitter center. Figure 6.20(d) shows that after $\approx 28\,\mu$s the entire width of the emitter stripe is affected by COD, also indicated by the colored squares on the left side of Fig. 6.20(b). The on-going of the defect growth after that verifies the use of $E_{\mathrm{Low}} > 0$ in the model for the third phase.

The comparison of the thermal *in-situ* signal, Figs. 6.20(c,d), and the defect pattern mapped by EBIC, shown in Fig. 6.20(b), gives remarkable agreement and provides the temporal sequence of pattern creation. Both the depth, with respect to the resonator axis, and the structure of the internal damage pattern are well reproduced by the measured hot spots, while taking into account the observation volume of the thermocamera. This volume is determined by the depth of focus of the thermocamera, cf. Sec. 6.1.2. This shows, that the *in-situ* thermography gives sufficient information to determine the structure of the internal damage and additionally its kinetics. The latter is of importance, in particular if the defect propagation direction is not intuitive: In Fig. 6.20(b), without information on the kinetics, one could have

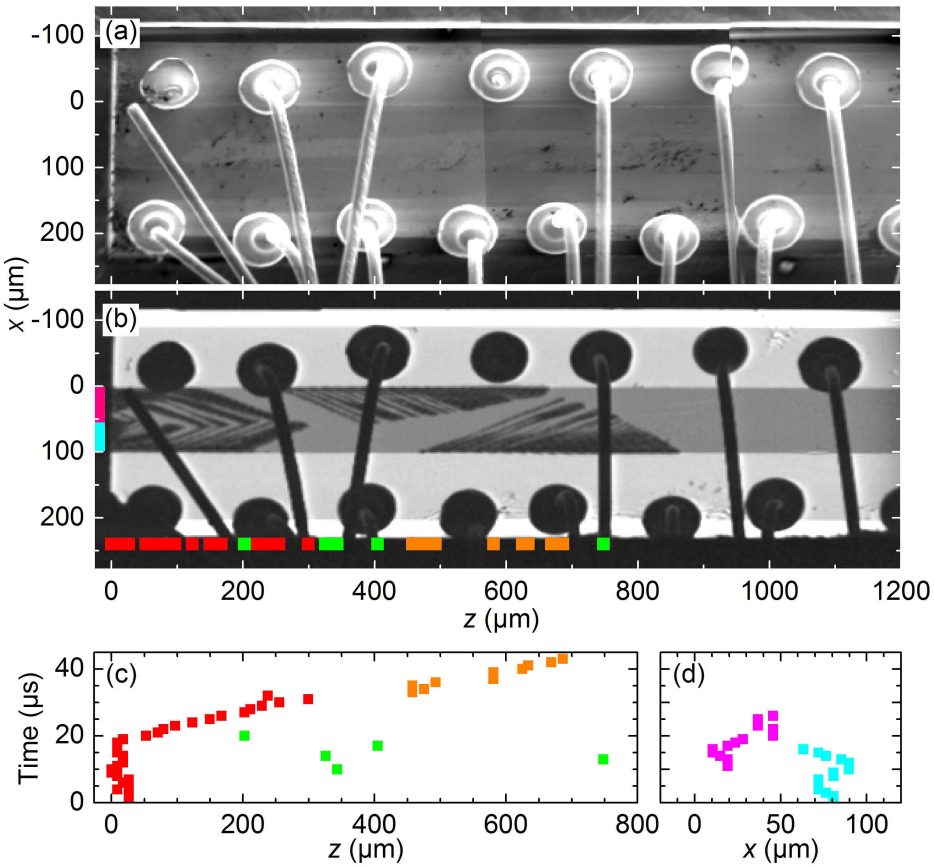

Figure 6.20: (a) SEM image of the top contact (p-side) of the DL. (b) EBIC map of the same image section. The rear facet is on the left side. The colored rectangles indicate the positions of the centers of gravity (*hot spots*) of the thermal signals, summarized for all consecutive pulses seen from the rear facet in case of magenta and cyan and in the side view for red, orange, and green. (c,d) Temporal evolution of the hot spot motion; the same color scheme is used as in (b).

assumed that the defect located between $0 \leq x \leq 300\,\mu$m has started at the single point in the cavity at $x \approx 300\,\mu$m and propagated up to the rear facet, i.e. from the right to the left. However, the thermography data in Figs. 6.20(c,d) prove the opposite, the starting point location at the facet.

As demonstrated, a thermography setup is able to provide the needed information about the sequence of events to separate between initial points of a defect structure and collateral damage. In the mentioned case, the facet is identified as the weak-point, that demands improvement. However, this setup is rather complex and therefore not applicable in all situations. In order to solve this problem, the model provides the possibility to reconstruct the defect creation sequence on base of the *ex-post* found damage pattern.

As discussed in the preceding section for the static case, it is possible to reconstruct a real defect pattern by appropriate setting of pre-damaged cells as starting points in the simulation grid. In this section, additionally, the defect dynamics is modeled, by assigning a certain number of iterations of the

model to a time interval. In order to model the damage visible in Fig. 6.20(b), 1 μs must be identified with 20594 iterations. The optical energy available in the model $E_{\mathrm{max},0}$ equals 10 energy units per μm, which corresponds to $\approx 150\,\mathrm{mW}/\mu\mathrm{m}$ optical power density for the device under investigation. The value for E_{Low} is set to 1 energy unit per μm. Other input parameters for the model are chosen, also in accordance with Sec. 6.3.2, to be: $\xi = 85\%$, 10 pixels in the grid represent 1 μm in the QW-plane, a cell is completely transparent up to a D_{Lim} level of 10% of the CD value, which is set to $CD = 10$ energy units. The simulation result is shown in Fig. 6.21. The locations of the initial damaged cells are indicated by green rectangles in Fig. 6.21, the cells themself are much smaller and not visible in the graph. The time delays between the appearance of these starting points in the simulation grid are given in the figure caption.

While Figs. 6.21(a-c) give the simulated damage for different times after the COD starts, Fig. 6.21(d) shows a comparison between the final damage detected by EBIC and the final model result. The shape of the damage is reproduced very well. The remaining small differences can be assigned to the simple nature of the model and not taking small material inhomogeneities into account which are always present

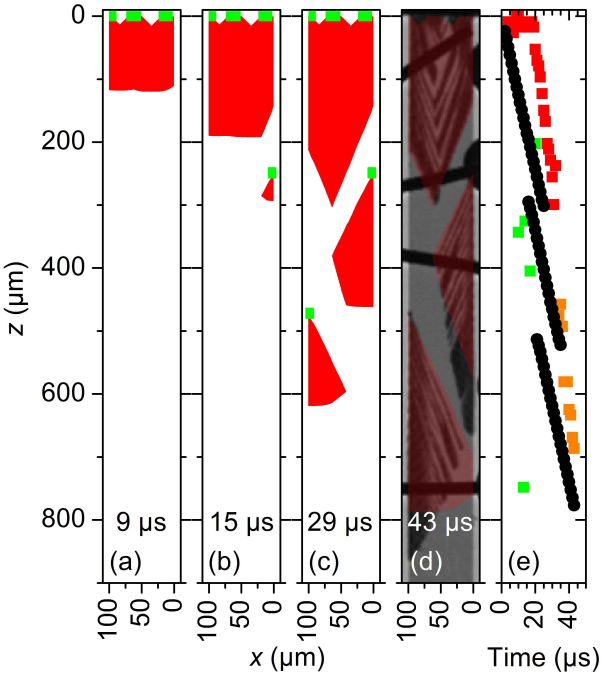

Figure 6.21: (a-d) Simulation results of the defect pattern for different times after COD ignition (a: 9 μs; b: 15 μs; c: 29 μs; d: 43 μs, as indicated). Points of initial defects are marked by green rectangles in (a-c). The damages at zero length, i.e., the rear facet, have zero time delay, while the ones at $z \approx 250\,\mu$m and $z \approx 470\,\mu$m appear after 14 μs and 22 μs, respectively. Subfigure (d) shows an overlay of the simulation results for the complete degradation time (red, semi-transparent) with the EBIC map (grayscale) of the real damage after the same time. (e) Comparison of the measured thermocamera signal [same color scheme as in Fig. 6.20(b)] with simulated one (black dots).

in real DLs and can change the defect spread, as discussed in conjunction with the branching effect in Sec. 6.3.3. However, it is proven by varying the parameters in a wide range, cf. Sec. 6.3.2, that the chosen parameter set has a rather small influence on the result, as long as they are in a realistic range for the particular device. The major difference between the obtained simulation results comes from the positions of the pre-damaged cells and the moment when their influence becomes effective. This strong dependence of the result on the starting points is what enables the model to reconstruct the initial points with just the completely expressed damage pattern as input.

In-situ defect maps from the model have been taken, as shown in Figs. 6.21(a-d) every 1 μs, i.e. every 20594 iterations. This corresponds to the length of each single current pulse and makes it possible to get a simulated thermal signal of the growing damage pattern. It is the damage that is added to the defect pattern during 1 μs in the range of the depth of focus of the thermocamera, under the assumption that the defect spread is governed by thermal energy transfer. The result of this analysis can now be compared with the real thermal *in-situ* measurements, as shown in Fig. 6.21(e).

The modeled data reproduce the existence of three moving hot spots, indicated by the three different colors of the measured data, very well. The main deviation between the two data sets can be found close to the facet ($z = 0$). Here the real defect formation is slower than the simulated one. This indicates a rather lateral defect spread along the facet during the first $\approx 20\,\mu$s which can be also seen as zig-zag motion in Fig. 6.20(d). The existing differences between the simulation and measured data could be reduced by adjusting the pre-set level of damage in the initial cells and by using a slightly non-linear conversion curve between absorbed energy and damage, cf. Fig. 6.16(b). This would result in a more complex model while giving the same main results, as proofed by testing modifications of the model. However, the good agreement of the two data sets justifies the use of the model in dynamic reconstructions.

The modeling confirms that the complex damage structure seen in Fig. 6.20(b) is simply the result of shadowing the unidirectional energy flow by a damage located further away from the facet. The starting points used in the model represent the bottlenecks of the device structure under investigation. As one can see in Fig. 6.21(a), damage sites at the rear facet, covering a significant part of the active region, model the defect evolution reasonably well. This means, the degradation took place at the rear facet at an early stage. The large extend of the pre-damage along the facet indicates a problem with the facet quality, otherwise the starting site would be very localized, as at the facet in Fig. 6.15(a). Furthermore, two more damage starting points which are delayed with respect to the ones near the facet [actual times are 14 μs at $\approx 250\,\mu$m corresponding to $I = 18$ A and 22 μs at $\approx 470\,\mu$m at $I = 26$ A, see Fig. 6.21(c)] have to be incorporated. These are located at the edge of the emitter stripe and are most likely related to the etch step. The delayed occurrence of these starting points indicates an activation of them by the large distant point defect spread experimentally found and discussed in Sec. 6.1.1. However, the incorporation of both sides of the waveguide at the etch steps indicates a weak-point in the device architecture there. This is not only of importance if a COD event takes place next to them and thermally activates the damage process, it is highly likely that the strain induced by the etch step also reduces the long term reliability by accumulating defects and eventually leading to device failure.

This is an example showing the possibility of reconstructing the real damage and its kinetics with the presented model. The uncovering of weak-points of a device architecture, which are also of importance under cw operation conditions, has been demonstrated. In this way, the combination of the step test approach and the used reconstruction model provides a kind of accelerated life test for DLs. The analysis presented here is also successfully applied to other samples where the same set of data is available and gives always results comparable to the ones shown above.

6.3.4 Evaluation of the Model

In conclusion, the modeling results and their agreement with the measured data verifies that the three basic ideas:

- Unidirectional energy entry by the laser light field,
- Isotropic thermal energy re-distribution, and
- Shadowing of the laser light

represent the main aspects of the damage expansion in the third phase of COD. The minor influence of parameter changes on the modeled defect pattern demonstrates the robustness of these ideas. The intention was to keep the model as simple as possible. The limitation of its applicability to regions close to facets is of cause a drawback. Figure 6.15(d) shows a case of a damage inside the cavity. The ignition point here cannot be resolved by the simple model with unidirectional energy entry. The model has to be extended taking into account the laser light field coming form both sides. However, the case of internal COD is rather rare. Considering the basic ideas of the model including an additional energy entry from the opposite side, makes it highly likely that the starting point in this case is in between the position of the left and middle bond wire.

Moreover, it has been shown that these three ideas are sufficient to explain complex damage pattern, including branching effects and the stability of the branches running side-by-side through the material. Although the model parameters are not one-by-one linked to physical quantities, the processes described are real. Thus a physical description of the sequences of events and disclosure of mechanisms is achieved.

6.4 Mechanisms Determining the Third Phase

The use of thermography allowed an *in-situ* defect tracing without any device modification. The accuracy of the trace obtained is verified by *ex-post* mapping of the damage pattern.

A constant magnitude of the thermal signal has been detected during defect propagation along the cavity axis. This result has been verified by measurements through the top-contact window. This indicates an almost constant temperature during defect evolution. The temperature present during COD has been determined in this and preceding chapters with different methods:

1. A temperature of (1200 ± 400)°C comes from the analysis of the *motion* of the thermal signal obtained through a top-contact window.
2. A value of (1200 ± 200)°C was estimated from a fit of an assumed temperature transient to the *magnitude* of the thermal signal, cf. Sec. 5.2.2.
3. *Energy balance calculations* lead to temperatures of ≈ 1500°C considering the energy introduced into the defect volume, cf. Sec. 5.2.2.
4. The *TEM data* and there crystallographic interpretation point to temperatures around 1580°C.

All analysis reveal similar temperatures around the QW and waveguide material's melting points present during the entire process. Tracing of the hot spot reveals that the region passed by the damage front returns quickly to a substantially lower temperature, i.e., below the detection limit of the thermocamera of 400°C in this experimental configuration. This is consistent with the calculations of heat dissipation in an one-dimensional model in Sec. 5.2.4. There, the heat spread is estimated to take place on the order of tenth of nanoseconds.

The heat spread causes the creation of point defects around the fully damaged region detected by CL. This defect generation was detected by LBIC measurements. Secondary COD ignition sites can be created by these point defects. These defects make the material in general susceptible to further degradation.

The developed model verifies that the defect growth in the third phase is dominated by three basic ideas – unidirectional energy entry, isotropic thermal energy and defect spread, and shadowing effects. This concept has been proved to be stable against slight variations of the used parameters. The main factors that influence the final COD defect pattern are found to be the positions of the COD ignition sites and the thermal resistance of the material system. This allows to reconstruct the damage evolution starting from the final defect pattern. The analysis of device structures with this method verifies that the COD ignition sites are indeed regions where a higher temperature during regular operation is likely.

The comparison of the step-wise created damage pattern with comparable ones from cw analysis indicates that the high-current single-pulse step test addresses the same degradation regime as present in cw. This holds even on a microscopic scale, as stated in the preceding chapter. A further argument is that the process is thermally activated in both cases, as shown by the Arrhenius analysis in Ch. 4. This proves the step test to be an appropriate tool to artificially slow down the fast COD kinetics by stopping the defect growth at the pulse end, while accelerating t_{COD} at the same time.

An evaluation of the DL material quality, the device processing, and the facet passivation is possible by analyzing the location and extend of the initial defect points. If the branching of the defect structure is well expressed it indicates an elevated level of inhomogeneities in the active region which is an indication for a reduced material quality. COD ignition points at locations related to device processing indicate defects introduced there, e.g., by strain induced by etch steps. Furthermore, the step test allows to evaluate the quality of the facet coatings. Analysis of defect pattern at front facets reveals the following: In case of one small COD defect visible at the facet and a following defect growth inside the cavity, the COD process started when a particular region of the facet cannot sustain the optical load anymore. In the following the lateral modes redistribute, but the remaining front facet material is not affect by the in part higher optical load. In contrast, if multiple ignition points are located at the facet, it indicates that the optical load in the pulse was able to exceed a critical value at multiple positions at a time. One of these two scenarios is found typically in damaged devices. By comparing the particular COD thresholds with those obtained for devices produced using other facet technologies, it is possible to decide if the facet passivation is of high quality or not. If I_{COD} is high and only a single COD site is present, a good passivation is applied, the inhomogeneity leading to COD is not significant. If the same happens at low I_{COD} values, there is a problem with localized inhomogeneities introduced during facet coating. Having multiple ignition points at low I_{COD} values indicates a general problem with the coating technology. Multiple starting points at high I_{COD} would point to a very homogeneous facet coating.

7 Investigation of Special Structures

In this chapter, a number of case studies at special device structures is presented. The results are analyzed and discussed based on the data presented in chapters 4-6.

7.1 Laser Bars

Arrays of DLs are used for high-power applications. Especially in cases where single emitters are not able to deliver enough optical output power, e.g., pumping of solid-state lasers. Therefore, several emitters are combined on a single chip. This means, BA lasers are placed next to each other on a single wafer piece without optical coupling of their waveguides. Due to the standard chip width of one centimeter, this arrays are called *cm-bars*.

An optical coupling would form a system of interacting non-linear oscillators. Therefore, light-induced coupling is blocked by etch-grooves through the active layer avoiding light-field interaction between the active regions of the stripes. Nevertheless, on a longer time scale in the range of milliseconds to one second, thermal interaction between the individual emitters takes place. The thermal profile along the lateral direction of such a bar depends strongly on the used mounting technology as discussed in [188]. In the following, the COD mechanisms were investigated with batch H representing standard devices mounted p-side down with In-solder on a conduction-cooled copper sub-mount.

7.1.1 Experimental Results

In order to detect the COD, the thermocamera was used to monitor the front facet of the device [108, 189]. In contrast to the single emitters, another current source was employed to provide the high current necessary to drive a cm-bar: PicoLAS LDP-V200-20 (current rise time 1 μs and 4 μs at 40 A and 150 A, respectively). The *standard* thermocamera objective allowed for inspection of all 19 emitters in parallel. The value of t_{int} has been chosen in each experiment to cover the entire laser pulse width. An example of a detected COD event is given in Fig. 7.1(a). The thermal event is overlaid to an emissivity contrast image. Flashes of Planck's radiation clearly indicate failures of the first and seventh emitter (counted from the left side of the chip) of bar H_1 at $I = 129.4\,\mathrm{A}$ and $t_{\mathrm{PW}} = 100\,\mu\mathrm{s}$. A following inspection of the front facet by means of optical microscopy revealed a defect there, too. In all experiments, a one-to-one agreement has been found of the position of facet defects and the thermal flashes.

While working with a system of laser emitters, the question may arise how to determine the COD threshold value. The following strategy is applied: A step test was performed. The used parameters are $I_0 = 40\,\mathrm{A}$ and $\Delta I = 4\,\mathrm{A}$. During every current step, the thermal image was analyzed to detect COD events. Additionally, a cut at the emitter plane is extracted from the particular thermal image. In order to summarize the evolution of the thermal signal at the front facet, they are combined to a contour plot as shown in Fig. 7.1(b) for device H_1 or in Fig. 7.1(c) for device H_2. These plots give an overview of the currents at which Flashes of Planck's radiation occur. Moreover, the involved emitter can be identified.

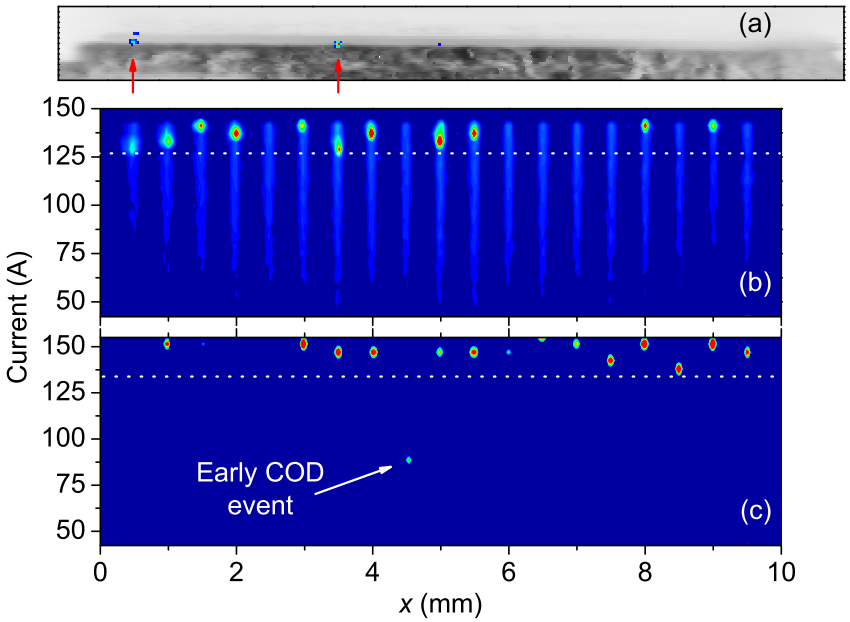

Figure 7.1: (a) Thermal image of laser bar H_1. The pulse parameters are: $t_{PW} = 100\,\mu s$ and $I = 129.4\,A$. The red arrows indicate the positions of flashes of Planck's radiation overlaid in colorscale to the gray background image. (b,c) Evolution of the thermal emission signatures of bars H_1(b) and H_2(c) while the current pulse amplitude increases. The t_{PW} values are $100\,\mu s$ and $30\,\mu s$ for bar H_1 and H_2, respectively. The COD thresholds are marked by dotted horizontal lines.

The vertical stripes appearing in Fig. 7.1(b) at the emitter positions are a result of the long integration time ($t_{int} = 100\,\mu s$, in sub-figure (c) only $30\,\mu s$). It enables the detection of the regular device heating. The COD, however, produced a distinct spike clearly distinguishable from this signal. In Fig. 7.1(c), an early COD event, indicated by the peak in the thermal signal (see white arrow), can be seen well separated from the currents at which the majority of the emitters experience COD. A reasonable explanation for this is a pre-damage of the emitter, which has not been recognized during the visual inspection before the tests. The 'true' COD thresholds of the bars for the given operation conditions (especially t_{PW}) are indicated by the dashed lines in Figs. 7.1(b,c). They represent the currents where the onset of COD is most likely for the structure at the given pulse length. This means, the distribution of all I_{COD} values of the single emitters of the device is taken, the outliers are removed, and then the lowest value gives the I_{COD} value of the laser bar.

7.1.2 Discussion of the Results Obtained with Laser Bars

The results of all tests are summarized in Fig. 7.2(a), giving the I_{COD}-values as a function of t_{PW}. Obviously, there is a systematic decrease of I_{COD} towards longer t_{PW}. The time range below milliseconds is too short to allow any lateral thermal crosstalk. Therefore, the emitters can be regarded as individual emitters, especially under the assumption of a homogeneous current distribution to the individual emitters of the bar. However, even for longer times, when thermal cross-talk is likely, the decreasing tendency holds. A stationary temperature profile is expected after $\approx 1\,s$ according to Puchert *et al.* [190] and Ziegler *et al.* [170].

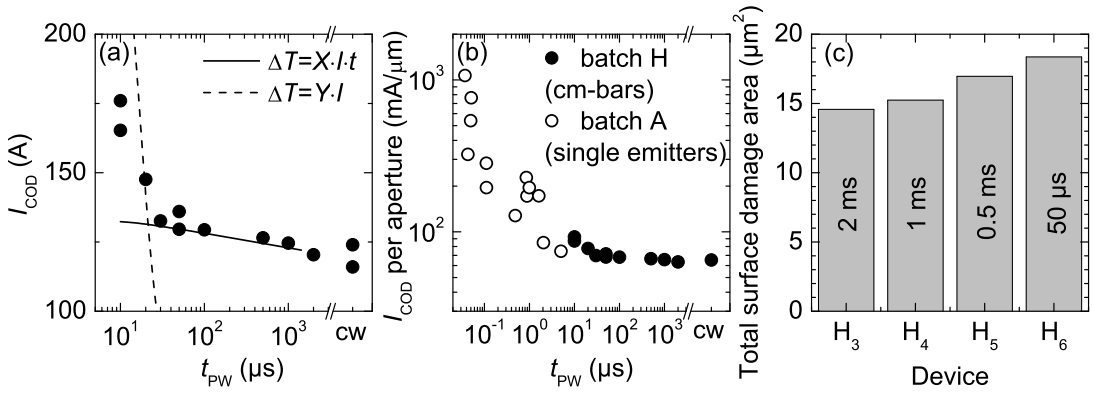

Figure 7.2: (a) Summary of COD thresholds I_{COD} in dependence of t_{PW} as obtained by step tests with cm-bars from batch H. The lines represents two models that are discussed in the text, including the scaling factors X and Y. (b) The same data as shown in (a) complemented by reference data obtained by analyzing single emitters of batch A. In order to account for different emitter stripe widths, the data sets are normalized to the emitter widths. (c) Total damage area as measured from micrographs for four cm-bars degraded at the indicated t_{PW}.

At this point it is worthwhile to reconsider the discussion about T_{crit} in Sec. 4.2.3. As discussed there, T_{facet} consists of two contributions $[T_{\mathrm{facet}}(t) = T_{\mathrm{bulk}}(t) + \Delta T_{\mathrm{facet}}(t)]$ that can lead to the situation where $T_{\mathrm{crit}} = T_{\mathrm{facet}}(t_{\mathrm{COD}})$ and the thermal runaway starts. While $T_{\mathrm{bulk}}(t)$ is qualitatively known for this bar-structure from modeling and experiments, e.g., done by Ziegler *et al.* [170], there is a lack of detailed knowledge about $\Delta T_{\mathrm{facet}}(t)$. $\Delta T_{\mathrm{facet}}$ is created by the absorption of laser power P_{opt}, therefore two types of *ansatz* can be made to describe the extreme cases [108]:

- The accumulated heat governs the facet heating ($\Delta T_{\mathrm{facet}}(t) \propto P_{\mathrm{opt}} \cdot t$).
- Power entry and heat removal create a steady-state equilibrium ($\Delta T_{\mathrm{facet}}(t) \propto P_{\mathrm{opt}}$).

At injection currents far above the laser threshold P_{opt} can be replaced by the current I. Therefore, this gives two scenarios for I_{COD} (where $T_{\mathrm{crit}} = T_{\mathrm{facet}}$ and $I = I_{\mathrm{COD}}$):

$$I_{\mathrm{COD}} \propto (T_{\mathrm{crit}} - T_{\mathrm{bulk}}(t)) \qquad \text{or} \qquad I_{\mathrm{COD}} \propto \frac{(T_{\mathrm{crit}} - T_{\mathrm{bulk}}(t))}{t} \quad ; \tag{7.1.1}$$

$T_{\mathrm{crit}} = 140°\mathrm{C}$, cf. Sec. 2.2, and numerical values for $T_{\mathrm{bulk}}(t)$ determined by Ziegler *et al.* [170] are used. The change of the bulk contribution during the current pulse is found to be small compared to T_{crit}. The two resulting curves are shown in Fig. 7.2(a). The terms X and Y are proportionality factors, chosen to facilitate a comparison with the data points. The experimental results are clearly between these two cases. For small times, the facet accumulates heat [model indicated by the dashed line in Fig. 7.2(a)]. For longer t, the heat loss via the surrounding material comes into play, leading towards an equilibrium

state (full line). Moreover, the kinetics of $T_{\text{facet}}(t)$ is four to six orders of magnitude faster than that of $T_{\text{bulk}}(t)$. This is caused by the different volumes where energy is stored. While the facet temperature is determined by a region of $\approx 1\,\mu$m behind the facet, $T_{\text{bulk}}(t)$ is determined by the entire chip and heat sink, representing a much larger volume. Therefore, the energy density differs significantly. It results in a longer time constant for temperature changes for the bulk material.

Another finding in this context is, that the COD threshold remains almost constant between 2 ms and the cw case. In contrast, earlier work on transient thermal properties of laser bars by Puchert *et al.* [190] and Ziegler *et al.* [170] revealed that there is still a substantial increase of T_{bulk} in this time range. They concluded that this is mainly an effect of thermalization of the volume material of the laser chip and the heat spreader itself. By measuring the active region temperature via the spectral shift of the emission of the bars under investigation, a temperature increase was found of about 40 K between $t_{\text{PW}} = 2$ ms and cw operation. At the same time, a decrease of the optical output power from ≈ 150 W to ≈ 120 W was detected. Obviously these two effects almost compensate each other. Thus, the emission power reduction of ≈ 30 W corresponds to an increase of T_{facet} of ≈ 40 K. This behavior becomes also clear within the concept of T_{crit}. While the increase of T_{bulk} increases T_{facet}, the emission power reduction decreases its value by the reduced re-absorption heating, i.e., a decrease of ΔT_{facet} at the same time.

This interplay of the temperature contributions also explains the dependence of the size of the front facet damage pattern on t_{PW}, see Fig. 7.2(c). In contrast to what one might expect, the pulses with longer t_{PW} and therefore higher total power entry create a smaller front facet damage. However, for shorter pulses the emission power is higher at COD threshold. The defect pattern directly at the facet is created within nanoseconds, hence its spatial extension is governed by the actual optical facet load. As shorter the pulses are as higher the optical load is when reaching COD threshold, leading to an increased front facet defect. This reflects exactly the mechanism behind the thermal runaway process, the fast transition of a small volume from an almost transparent state to a highly absorbing one for the laser wavelength. This includes a fast energy redistribution quantified by the emission power present at this moment. The energy provided to the defect side thereafter leads to the growth of the defect pattern in the interior only and does not affect the front facet defect pattern.

Due to the limitations set by the pulse generator, it was not possible to access values for t_{PW} below $10\,\mu$s. As discussed for this pulse width range, the emitters of the bar can be treated as independent. Therefore, it is straightforward to complement the graph with the data obtained for the single BA lasers from batch A, cf. Fig. 4.13. Although these single emitters do not stem from exactly the same epi-structure, their electro-optical parameters almost match. In order to account for the different emitter widths, the currents for both batches are normalized to the emitter width. Figure 7.2(b) shows a summary of both data sets. Obviously the single emitters continue the trend observed at the bars. This underlines the above statement about the importance of ΔT_{facet} for short times. Furthermore, it verifies the treatment of the emitters of the cm-bar as individual lasers in the case of short t_{PW}. The thermal crosstalk for longer t_{PW} and cw operation can be expected to influence mainly the long-term-aging of the devices due to the presence of temperature gradients which results in strain gradients. This enables the formation and propagation of various defect species, e.g., dislocations, in the semiconductor.

7.2 Single-Spatial-Mode Ridge Waveguide Diode Lasers

Up to now the COD has been discussed by observing its kinetics in BA DLs. In this section, the COD behavior of single-spatial-mode ridge waveguide lasers will be addressed. This is done in order to proof the universality of the uncovered physical mechanisms [191].

7.2.1 Experimental Results

Lasers from batch J were used for this study. This batch of 26 individual devices is sub-divided into three groups of devices, named a,b, and c. They differ by their front facet coating technologies.

The lateral emitter stripe width of these lasers is reduced in a way that during regular cw operation only the fundamental spatial mode can propagate. This remains not true for very high pump-powers. The physical mechanisms resulting in multi lateral modes will be discussed later. However, the investigation of a device with a strongly confined lateral mode allows to analyze the later COD site *on route* to COD.

Analysis of cw Operation

During cw operation, the front facet surface temperatures have been measured by micro-Raman spectroscopy. Figure 7.3 shows the front facet temperatures versus operation current by giving the averaged value of measurements at 5 devices per sub-batch, i.e., a, b, and c. During the successive cw current increase, the devices typically fail by front facet COD accompanied by a local melting of the facet coating. A typical image of the externally visible defect taken with the optical microscope is given as inset of Fig. 7.3. The I_{COD} values are indicated by arrows in Fig. 7.3. The facet temperatures measured just before COD are around 180°C and differ not significantly among the sub-batches.

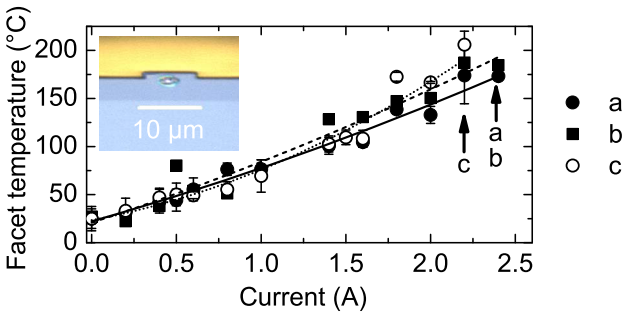

Figure 7.3: Facet temperatures (symbols) in dependence on cw operation current for sub-batches a-c of device batch J. The arrows indicate the COD thresholds. The lines give second order polynomial fits to the data as guides to the eye. The inset gives the external damage of device J_{b1} from batch J_b created by a COD during cw operation, as detected through an optical microscope.

Analysis of Pulsed High-Power Operation

After the quantification of the cw COD behavior of the device, the high-power pulsed operation regime is addressed in the following. A step test was made with $t_{PW} = 150\,\text{ns}$, $\Delta I = 1\,\text{A}$, and $I_0 = 1.6\,\text{A}$. A test pulse was used to monitor device health. Since the COD behavior and operation parameters of the three sub-batches under investigation do not differ notably, the presentation of results of pulsed devices will be restricted to batch J_a. The step test is done at two heat sink temperatures, $T_{hs} = 25°\text{C}$ and $85°\text{C}$, representing the range of realistic application conditions. The probed parameters of the devices in this operation regime are:

- The lasing NF, recorded with the streak camera to determine its spatio-temporal evolution,
- The time-resolved monitoring of near-infrared and laser emission in parallel, which is complemented by an integral measurement of the thermal emission of the device.

In the following, these two approaches will be discussed in detail.

Spatio-Temporal Nearfield Kinetics: From the data recorded during the step test, one gets a L-I curve for the pulsed operation regime. Figure 7.4 gives typical results for the maximal power achieved during the 150 ns long single pulses. Device J_{a1} reaches about 20 W at $T_{hs} = 25°\text{C}$ before it goes into thermal roll-over[1] without any notable degradation at this point and beyond. Device J_{a2} reaches a maximal optical output power of up to 30 W at $T_{hs} = 85°\text{C}$.

Information about the optical output power represents an important emission property. Another key parameter is the beam quality, single-spatial mode lasing maintains excellent beam quality and brightness. The spatio-temporal NF evolution is directly monitored with the streak camera.

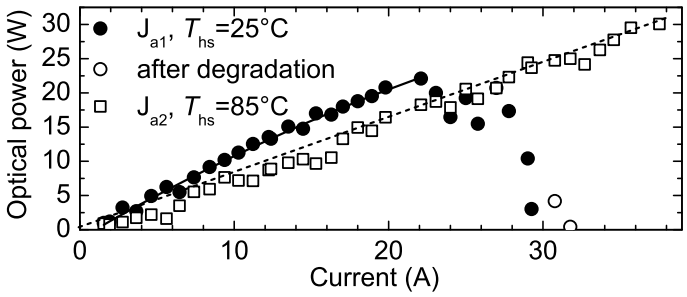

Figure 7.4: Pulsed L-I curves for two devices at different heat sink temperatures ($t_{PW} = 150\,\text{ns}$). The power represents the peak value during the pulse. The points labeled 'after degradation' represents values recorded while device J_{a1} experiences irreversible degradation.

[1] This means, that the optical output power reversibly decreases while the pump current is increased.

Figure 7.5 shows selected data. At $I = 12.4\,\mathrm{A}$ a power of 13.8 W (cf. Fig. 7.4), i.e., $> 18\times$ of the specified power for reliable cw operation, in single-spatial-mode is available during the entire $t_{\mathrm{PW}} = 150\,\mathrm{ns}$; Fig. 7.5(a,b). The presence of single-mode operation is proved by the Gaussian shape of the lateral mode profile. The lines in Fig. 7.5(b) represent fits to Gaussians while open circles give the experimental data. For further increased operation currents, there is a tendency towards the presence of two to three lateral modes, as shown in Figs. 7.5(c,d). For $I = 22.5\,\mathrm{A}$, single-spatial-mode operation is available only during the first 50 ns of the pulse. The optical output power during this time reaches 20 W, cf. Fig. 7.4.

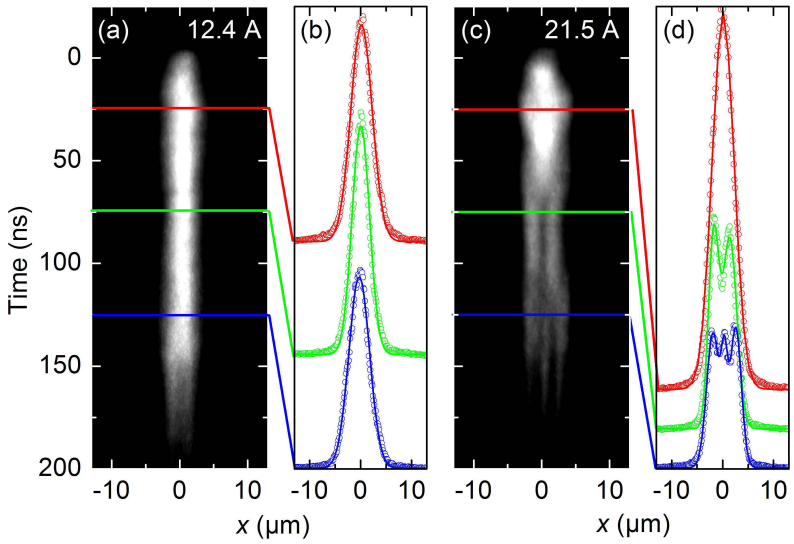

Figure 7.5: Streak camera images (a,c) of device J_{a1} taken at $T_{\mathrm{hs}} = 25^{\circ}\mathrm{C}$. (b,d) Cuts through them (open circles) are taken at the marked delay times. Full lines in (b) and (d) represent Gaussian and multi-Gaussian fits, respectively.

The transition from single- to multi-spatial-mode operation is quantified in Fig. 7.6. The 'single-mode time' is the time, where the lateral mode profile changes from one Gaussian to two. Temporarily a top hat profile appears at this point, e.g., at $\approx 60\,\mathrm{ns}$ between red and green curve in Fig. 7.5(d), which are taken 25 ns and 75 ns after leading pulse edge, respectively. Considering the data in Fig. 7.6(a) and the L-I curves in Fig. 7.4, the energy can be determined, which is available during single-spatial-mode operation. The result is given in Fig. 7.6(b). A 'single-mode energy' of up to $2\,\mu\mathrm{J}$ is obtained in true single-spatial-mode operation at $T_{\mathrm{hs}} = 25^{\circ}\mathrm{C}$ and $I = 13.6\,\mathrm{A}$, while $4.5\,\mu\mathrm{J}$ are reached in operation with three lateral modes ($T_{\mathrm{hs}} = 85^{\circ}\mathrm{C}$, $I = 39.3\,\mathrm{A}$), see Fig. 7.4. In the discussion of Fig. 7.4, it was already mentioned, that device J_{a1} experienced a reversible roll-over at $I \approx 20\,\mathrm{A}$. However, at $I \approx 30\,\mathrm{A}$, this device irreversibly failed at a fairly low emission power level (open circles in Fig. 7.4). The device failure has been detected by analyzing the evolution of the test pulse pattern taken at $I_0 = 1.6\,\mathrm{A}$ after each pulse. The test pulse taken after the pulse with $I = 29.3\,\mathrm{A}$, shown in Fig. 7.6(c), still looks similar to the one taken at I_0 at the beginning of the step test. In contrast the one taken after $I = 30.7\,\mathrm{A}$, see Fig. 7.6(d), shows a loss of optical power and the presence of five lateral modes. A careful inspection of the device revealed no external degradation signature.

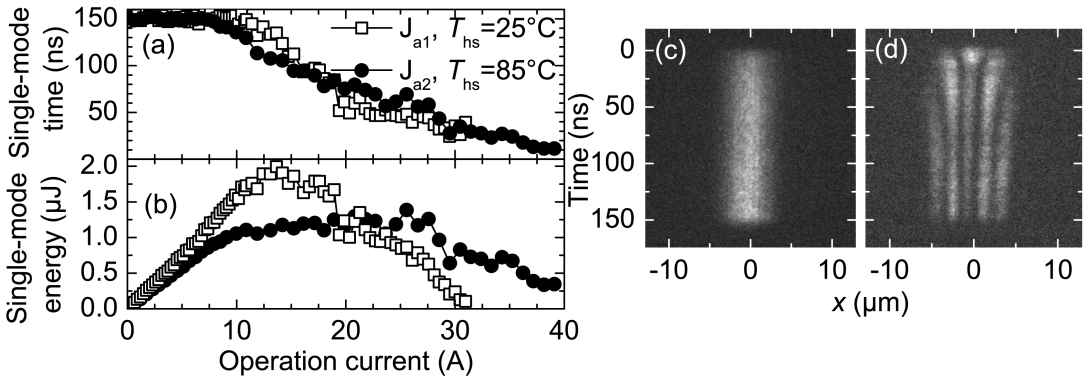

Figure 7.6: (a) Time during which single-spatial-mode operation is maintained ('single-mode time') during the 150 ns long current pulses. 'Kink-free' cw operation until 1.8 A indicates the value for cw. (b) Energy emitted in true single-spatial-mode operation ('single-mode energy') during the 150 ns long pulses. (c,d) Streak camera images of the lasing NF during test pulses with $I_0 = 1.6$ A of device J_{a1} ($T_{hs} = 25°C$). They have been taken after $I = 29.3$ A (c) and $I = 30.7$ A (d) high current pulses.

Laser- and Infrared-Emission-Kinetics: There is a deviation between the location of COD between cw and pulsed operation for the devices under investigation. In the cw regime, a front facet damage occurs, whereas in pulsed mode the defect location is inside the cavity, detected via the NF change. This calls for an additional study of the underlying mechanisms. Therefore, a setup as shown in Fig. 3.1 is used. During a step test, the emission power transient from the front facet is monitored by the PD and additionally the infrared emission by the NIR detector. For several devices, the pulse lengths have been changed between 50 ns and 9 μs. T_{hs} was kept at $(25.0 \pm 0.2)°C$.

It turned out, that provocation and detection of a sudden degradation become possible only when switching to long pulses, i.e., 9 μs which is 60× longer as used in preceding experiments. Figure 7.7 shows data from device J_{a3}, obtained at $I = 8.2$ A (a,c) and $I = 8.7$ A (b). The initial degradation event took place after 7.8 μs at $I = 8.2$ A, indicated by the red arrow in Fig. 7.7(c). The sudden drop of the laser output power, detected as PD-signal, is accompanied by a thermal signature deep inside the laser cavity at ≈ 1.2 mm behind the front facet. This area is marked in red in Fig. 7.7(a). In the subsequent $I = 8.7$ A pulse, two more extended thermal signatures are observed, see Fig. 7.7(b). They are shifted compared to the initial one. The emission power detected by PD and NIR detectors dropped down to 10% and 5% of their averaged value during the first COD pulse during this second one, respectively.

The PD- and NIR-traces reveal additional details about the processes taking place in the interior of the device during the microsecond pulses, Fig. 7.7(c). The fluctuations are true variations of the output power and no noise. Both signals are not independent, they change between an correlated and an anti-correlated state.

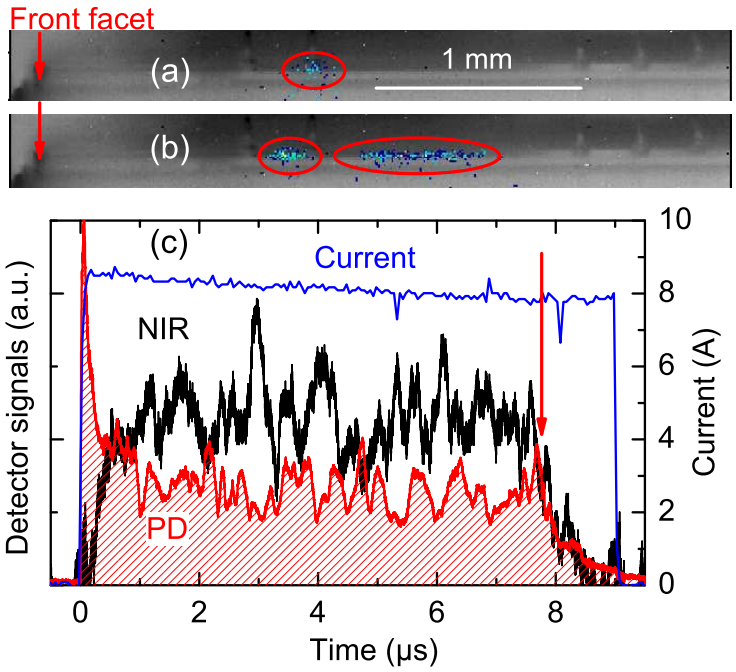

Figure 7.7: (a,b) Thermal images of device J_{a3} composed of an emissivity contrast image ($t_{int} = 1\,ms$, given in grayscale) and the emission during the single pulse ($t_{int} = 10\,\mu s$, colorscale). Images taken during high-power current pulses with $I = 8.2\,A$ (a) and $I = 8.7\,A$ (b) of $9\,\mu s$ duration. The red highlighted regions point to elevated thermal signals. (c) Transient data giving the current (blue, right ordinate) and the evolution of laser emission (PD signal, left ordinate) and NIR-signal (left ordinate) during the same pulse as investigated in (a). The arrow indicates the ignition of COD.

7.2.2 Discussion of the Ridge Waveguide Laser Dynamics

Facet Temperature

The external defect pattern of all devices degraded by facet-related COD look similar, see e.g., inset of Fig. 7.3. Therefore, the same high temperature can be assumed to be reached at the facet during COD. Furthermore, the temperature increase between 180°C and the high COD temperature (≈ 1500°C is likely, cf. Sec. 6.4) takes place fast compared to the 100 s of micro-Raman measuring time. This makes the temperature analysis of the thermal runaway by micro-Raman spectroscopy impossible. However, a long-term stable device operation with facet temperatures around 180°C has been confirmed by these measurements. In the literature [47, 54, 59, 67, 153, 154], critical temperatures in the range of $T_{crit} = 120°C - 160°C$ are quoted as distinctive for the COD ignition. This shows on the one hand, that the devices of batch J can withstand high facet temperatures. Moreover, the wide spread of the T_{crit} values in the literature indicates the dependence on the used technology (passivation, protection, coating).

Analysis of High-Power Operation

There are two main physical mechanisms for the occurrence of higher order modes in ridge waveguide structures, if the width of the ridge is on the order of the emission wavelength. These mechanisms are discussed by Ziegler *et al.* [192]:

- The fundamental and first higher spatial mode interact at intermediate pumping currents ($\approx 5 - 11 \times I_{\mathrm{th}}$).
- Anti-guiding due to an asymmetric charge-carrier profile occurs at high pumping currents ($> 11 \times I_{\mathrm{th}}$).

The first mentioned mechanism causes a switching of a high intensity peak between the lateral left- and right side of the cavity with a switching frequency of several GHz. This frequency is proportional to the pump-current. In order to explain this experimental result, the authors [192] solve the equations for the electric field and the carrier concentration in dependence of the lateral position in parallel. Lateral coupling is achieved by diffraction of the optical field and charge-carrier diffusion. The optical gain depends on the charge-carrier concentration and the mirror losses are introduced by a damping constant. An eigenmode analysis of the electric field is applied for comparison of the numerical results with the experimental data. It turned out that it is sufficient to consider the fundamental and first excited mode. However, the overtone of these two frequencies is 20 times faster than the experimental value. This is explained by the interaction between different longitudinal mode families resulting in a kind of phase-locking mediated by the non-linear susceptibility of the semiconductor material.

For higher pump currents, another mechanism is identified as dominant. The maximum of the emitted light intensity moves lateral between left and right side of the stripe. This is explained by the accumulation of charge-carriers. It increases the optical gain, but leads also to a repulsion of the optical field by a local decrease of the refractive index as shown by Ziegler *et al.* [192]. A small offset of the optical mode from a perfect symmetrical position is enough to increase the carrier concentration at the opposite site. This creates a positive feedback loop pushing the optical mode to the edge of the waveguide. Than the high carrier concentration which have been build up close to the middle is depleted by emitting a strong light pulse in a symmetrical mode. Thereafter the process repeats.

An additional factor for a change of the spatial mode pattern of the devices from batch J is their tapered stripe structure, i.e., the lateral waveguide width changes continuously from 3 μm at the rear facet to 8 μm at the front. This is done in order to combine single mode operation and high optical output powers, i.e., an increase of the brightness of the device. This emitter stripe structure allows the existence of higher order modes which will occur due to the above mentioned reasons (mode interaction and anti-guiding). Additionally, temperature caused changes of the refractive index have to be considered.

However, in the experiments done with device batch J a time-resolution was used for NF monitoring that does not allow to resolve this fast switching. That is why a motion of the optical mode between left and right side of the cavity cannot be seen. The applied time-averaging causes the detection of two or more lateral modes side-by-side if one of the mentioned operation regimes is reached (or a combination of them).

The appearance of the multi-mode structure at low emission powers in Fig. 7.6(d) indicates a change of the cavity probably caused by damage. This leads to a re-ordering of the internal mode structure depending on size and position of the defect, as demonstrated in Ref. [193] in case of BA DLs.

The emission power detected by PD and NIR detectors was already quite low during the degradation of device J_{a3} in a long pulse, see Fig. 7.7. Therefore, it can be concluded, that the device degraded caused by a thermal overload within the waveguide. Since the hotspot location is moving along the laser axis from one pulse to the next, cf. highlighted areas in Figs. 7.7(a,b), the growth of a defect network as discussed in Sec. 6.3 is highly likely. This takes place inside the cavity without affecting the facets and is clearly revealed by CL mapping.

The PD- and NIR-traces reveal additional details about the processes taking place in the interior of the device during the microsecond pulses, Fig. 7.7(c). When considering the PD-signal [red curve in Fig. 7.7(c)], it should be noticed that the fluctuations are true variations of the output power and no noise. The 'single-mode time' in dependence on the operation current has been investigated in detail for shorter pulses, cf. Fig. 7.6. This data show clearly that on the microsecond time scale definitly multi-spatial mode operation takes place. Therefore, it is clear that the observed emission power fluctuation is a result of spatial mode hopping in the waveguide that is still not fully thermalized on this time scale. The recorded NIR-signal represents a kind of 'defect photoluminescence' created in the substrate, which is excited by laser emission that is transferred from the waveguide into its vicinity including the substrate. This has been reported by Ziegler *et al.* [96] for cw operation. The experimental setup allows additionally the time-dependent analysis of this signal. An increase of the NIR signal is caused, e.g., if multiple spatial modes do not fit into the waveguide that is designed for single-spatial-mode operation. Thus, the NIR-signal is a rough indicator for the fraction of laser power remaining in the device, but leaving the waveguide. Therefore, the PD- and NIR-signals are predominantly anti-correlated, but not always, since the laser light is also the only source for exciting the 'defect photoluminescence'. The amplitude fluctuation of the PD signal amounts to $> 30\%$ of the average amplitude (averaged between $1\,\mu$s and $7\,\mu$s), which is about 2.5 W. Thus there is a heat source near the waveguide in this operation regime, resulting from the redistribution of more than 700 mW on a sub-microsecond time scale in an uncontrolled way. This causes a local heating and eventually leads to device degradation. Additionally, the position where the thermal runaway takes place is found to be located most likely in the waveguide and cladding material, cf. TEM investigations in Sec. 5.2.3. This means that there could be an additional step that has to be incorporated into the feedback loops: If a certain temperature is reached, the laser light field becomes deflected in a way that also the waveguide and cladding regions are heated locally. The material forming these layers cannot withstand such a high optical load as the QW itself and the thermal runaway starts. The high temperatures achieved above and below the QW eventually impairs it. The QW is from that time on the location where the further damage takes place, because the highest light field intensity is present and additionally an absorbing region (the already destroyed QW).

Furthermore, this reveals the limits of applicability of pulsed operation. It works well in single-spatial-mode operation with short pulses. In this case, a transition to multi lateral modes protects the device from COD by redistributing power to a larger volume and going into thermal rollover. On a time scale of several microseconds the device becomes thermally unstable. Therefore, the advantages of a power enhancement by two orders of magnitude and the COD-self-protection are obtained by short pulse operation only.

7.2.3 Comparison to BA Diode Lasers

A major advantage of using ridge waveguide structures for COD analysis is the limited front facet area. In contrast to BA lasers, the position of a later COD-related external defect can be clearly predicted. This enables measurements of the facet temperature evolution there. Furthermore, a detection method giving a spatial resolved image of the front facet, e.g., use of the thermocamera, is not needed. It can be replaced by a fast point-detector, because the location of the signal-origin is known.

As pointed out in Ch. 6, the light field is the main energy source of the defect growth process. In case of device J_{a3}, the initial starting point is inside the cavity, cf. Fig. 7.7(a), $\approx 1.2\,\mathrm{mm}$ behind the front facet. If the degradation observed here relies on the same mechanisms as identified in Sec. 6.3, the direction and extension of defect growth should reflect the energy entry from the respective direction. The structure under investigation here is a single-mode ridge waveguide laser, that is why one can assume that only two directions are of importance: Energy coming from the rear facet and energy coming from the front facet towards the defect. This is confirmed by the fact that the position at which the thermal signature during the first pulse was recorded is in-between the areas detected in the subsequent pulse, see Figs. 7.7(a) and (b). Taking into account the shadowing effect discussed in Sec. 6.3, the situation becomes clear: In the pulse depicted in Fig. 7.7(a), the initial defect site is created dividing the laser cavity into two parts: One between front facet and damage site and one between rear facet and damage site. In the subsequent pulse, the damage growth is re-ignited. Even if the destroyed cavity not allows lasing, the amplified spontaneous emission provides enough energy, as demonstrated by short-time thermography in Sec. 5.1.4. In order to verify this, the ratio of the defect extension on both sides of the initial defect site can be compared with the ratios of the remaining cavity fractions on these sides. The quotient of the right defect pattern length [marked area on the right side in Fig. 7.7(b)] and the left one (left marked area) yields ≈ 2.5. The quotient of the length of the cavity right from the defect site (2.7 mm) and on the left side of it (1.2 mm) is 2.25. Both ratios show a remarkable agreement. The remaining deviation arises mainly from not taking into account the tapered waveguide and the facet coatings with different reflectivities. Nevertheless, this shows that the basic concepts identified for the defect extension are also valid in case of ridge waveguide lasers.

A further feature of dealing with these ridge waveguide structures is that the time evolution of a confined mode can be investigated. This allows for monitoring the lasing and NIR-signals coming from a single optical mode. The observed deflection of the optical mode towards the substrate is a possible reason for the found defect pattern in TEM analysis in Sec. 5.1.3. There, the most likely place of COD ignition was found not to be the QW itself, but the waveguide and cladding region. Furthermore, this region have also been identified as potential trigger for degradation in experiments addressing device degradation during operation under external feedback [194].

The presence of the mechanisms leading to COD, identified for BA lasers, have been verified to be present in ridge waveguide structures. The step test, however, was not able to provoke a front facet COD as the cw test. This is caused by the change to spatial-multi-mode emission of the ridge waveguide lasers. In BA laser, in contrast, multi-mode emission is an intrinsic device property and no switching of the fundamental emission characteristics influences the COD-ignition. Furthermore, a fast uncontrolled deflection of the optical mode towards the cladding and substrate layers can be seen. It is highly likely that this mechanism also affects the temperature profile in a BA laser.

7.3 Quantum Dot Devices

It is frequently claimed, e.g., in [110], that devices with quantum dots (QD) as active material could withstand COD better than QW devices. This is explained by following arguments:

- The lower v_{surf}, as demonstrated by Moore *et al.* [195], they found a value which is one order of magnitude smaller than for QW devices,
- The reduced filamentation as shown by Smowton *et al.*[196] and Ribbat *et al.* [197], which is explained by a reduced in-plane carrier diffusion and the lower α-factor[2],
- A lower in-plain diffusion constant that reduces the motion of charge carriers towards the surface,
- A lower absorption at the facet, caused by the fact, that the presence of a QD exactly at the facet is rare, in contrast to the QW where an entire potentially absorbing layer is present.

A description of the way these parameters influence the COD threshold in case of QW devices is given in particular in Secs. 4.2.4 (surface recombination) and 4.2.2 (lasing NF). However, a direct comparison between QW and QD devices is difficult. It is not possible to find comparable devices where only the QW is replaced by a QD layer. Furthermore, QD structures are mostly produced on a research level and therefore not available in batches of homogeneous quality. This excludes experimental approaches that rely on extracting data from several COD failures while varying a single parameter only.

Nevertheless, it is also possible to obtain results with a few devices that allow a comparison to the defect kinetics of QW devices. In the used setup the thermocamera was directed onto the top-contact of the device while a fast PD detected the laser emission from the front facet. A QD DL from batch K (device K_1) was studied. These devices are mounted p-side down and have a $110\,\mu$m wide (x-direction) window in the n-side metallization, which was implemented during device processing. The window is centered on top of the active stripe region. An emissivity contrast image taken by the thermocamera representing the geometry ($t_{\text{int}} = 1\,$ms) of the mounted sample is shown in Fig. 7.8. There, the entire laser chip is indicated by a green rectangle. The light gray stripe inside is the n-side window, the dark areas represent the remaining top contact metallization. The positions of the bond wires are indicated by the yellow lines. The front facet is at the top. In case of this device, the discrimination between front and rear facet is not necessary, because both facets are as-cleaved, i.e., uncoated.

The device's degradation behavior was analyzed in a step test. The used parameters are $t_{\text{PW}} = 1\,\mu$s and $\Delta I = 0.3\,$A. Thermocamera images (emissivity contrast: grayscale; thermal signal: colorscale) are shown in Fig. 7.8(b-g). They show the region indicated by a dashed rectangle in (a) on an enlarged scale. These thermal images are recorded during successive pulses of the step test. In order to provide a better visibility of the results, different color bars for the thermal signal in sub-figures 7.8(b-d) and (e-g) are used. The first catastrophic failure occurred at $I = 10.4\,$A. The associated thermal image is shown in Fig. 7.8(b). Additionally, this event is accompanied by a drop of the output power, see Fig. 7.9(a).

[2]The α-factor or line width enhancement factor was introduced by Henry [198] to explain the linewidth broadening in semiconductor DLs. The argumentation why this broadening happens is as follows: The real part of the refractive index (n) varies with the carrier density. Phase and intensity changes in the laser field are introduced by spontaneous emission. While the laser comes back to its steady-state intensity, changes of the imaginary part of the refractive index (Δk) are provoked. This leads to changes of n (Δn), causing additional phase fluctuations and line broadening. The linewidth enhancement can be determined by the factor $(1+\alpha^2)$ with $\alpha = \Delta n/\Delta k$.

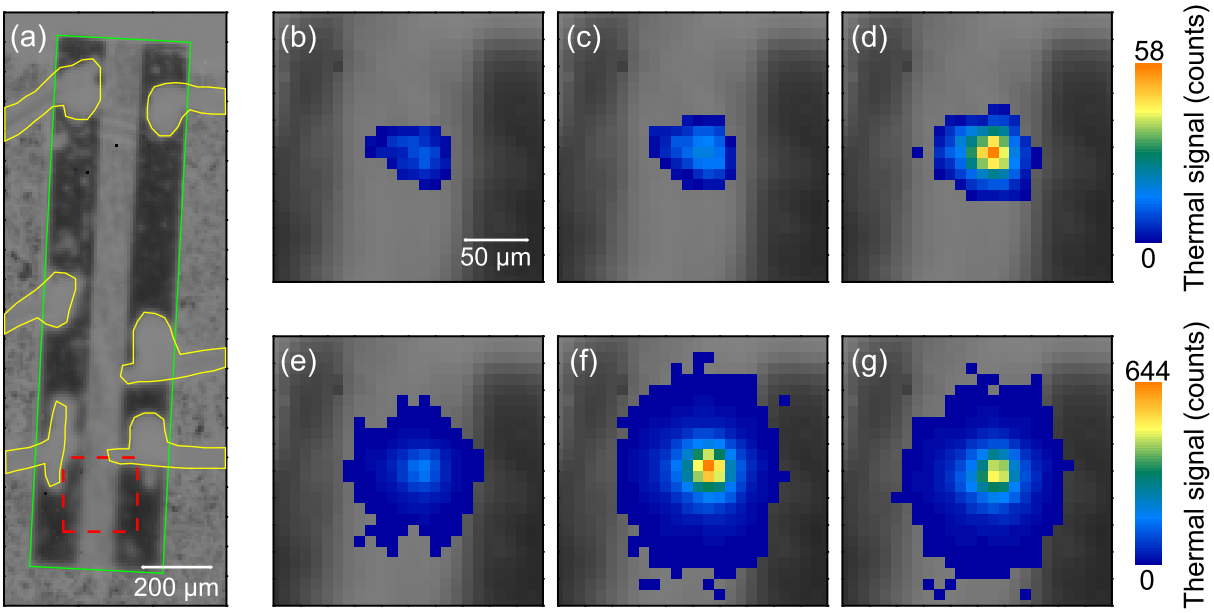

Figure 7.8: Thermography applied to device K_1 (QD DL). (a) Geometry of the DL seen in emissivity contrast. The chip is surrounded by the green line. The bond wires are indicated by yellow lines. The red dashed rectangle indicates the position of images (b-g). (b-g) Thermal images taken during successive pulses of a step test (from 10.4 A (b) to 11.9 A (g) with $\Delta I = 0.3$ A). In order to enhance the contrast, two different color bars are used, one for (b-d) and another for (e-g). They are given right next to the images of the respective line.

Figures 7.8(c-g) show the evolution of the thermal signal at the same site as (b) for the subsequent pulses in the step test, i.e., 10.7 A (c), 11.0 A (d), 11.3 A (e), 11.6 A (f), and 11.9 A (g). The signal magnitude increase monotonously up to the 11.6 A-pulse [Fig. 7.8(f)]. The center of gravity of the thermal signal remains at the same location during the catastrophic failure.

While the resulting thermal signature of the QW laser in Fig. 6.2 is rather longish along z, here its shape is circular. Following the discussion in Sec. 6.2.1, this implies that the heat source does not move. Moreover, Figs. 7.8(b-g) show no motion of the center of gravity of the signal. The heat remains symmetrical distributed around its center, which is therefore supposed to be the initial defect site. In the pulses shown in Figs. 7.8(f) and (g), the signal in lateral direction is in part blocked by the remaining metallization (visible as dark gray areas in the background). This is why a slight deviation from the circular shape can be seen at the signal edge. Taking into account that both facets are equal, the laser light intensity approaching from the front facet (top to bottom in Fig. 7.8) should be much higher, because the defect location is much closer to the rear facet, see Fig. 6.2. Under the assumption that the defect is a COD as discussed in the preceding chapters, it should be fed with energy from the light field. Therefore, the defect expansion should show a motion in the direction of highest light incidence. But this cannot be seen here. That is why the observed defect is most likely not caused by light re-absorption. In that sense, it is not a COD as observed in QW devices where the light field has been identified as energy source of the process (cf. especially Secs. 5.2.2, 6.1.1, and 6.3.3).

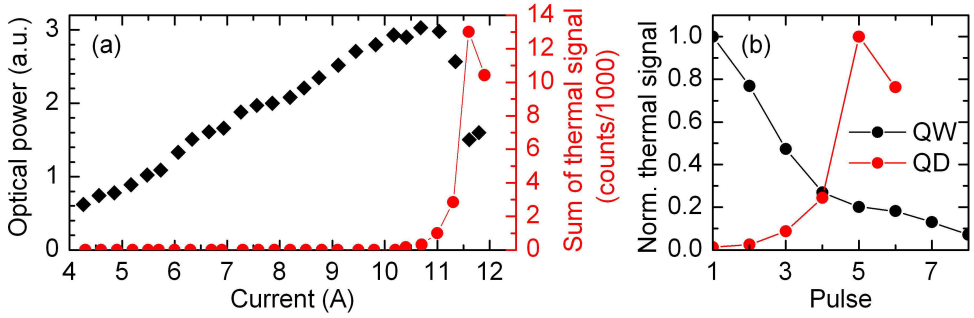

Figure 7.9: (a) Evolution of the optical output power of device K_1 (measured by PD) in dependence on the current applied during a single pulse of the step test. The respective sum of the thermal signal (added from all camera pixels, background noise subtracted) is also given. (b) Comparison between the evolution of the thermal signal-amplitude in subsequent single pulse experiments after COD ignition (set to pulse 1). The QD data are from device K_1 and the QW data are from device D_1. The data are normalized to the maximal amplitude.

Another feature that is different compared to the COD events detected in QW lasers is the build up of the thermal signal. Figure 7.9(b) gives a comparison between the evolution of the amplitude of the thermal signal after COD ignition (pulse 1 in the graph) in the QD device K_1 and the QW device D_1. The data of device D_1 are taken from the front facet view and are corrected for the distance of the signal from the focal plane of the thermocamera. The amplitudes are normalized to the respective maximal values. While for QW lasers the thermal signal amplitude rises fast (first or second pulse gives the maximal value), it needs a couple of pulses to reach the maximum in case of QD DLs, see Fig. 7.9(b). This indicates the presence of different degradation mechanisms. The signal in QW device is highest at the beginning of degradation, because the light intensity is at the highest level. This gives further evidence that the main energy source for the degradation observed at QD DLs is not the laser light field.

Nevertheless, the observed damage mechanism is accompanied by a sudden output power drop and high temperatures on the order of several hundred degree Celsius. For an accurate temperature determination, the present knowledge about this mechanisms is not sufficient, e.g., in order to estimate the size of the heat source.

In summary, the technique of defect recognition by thermography through a top contact window is applied successfully to detect a defect site. The growth process creates a quasi-random[3] distribution of the QDs in the plane and also a distribution of QD sizes. Therefore, the existence of weak points, as a result of extreme values in this size and distance distributions, is much more likely than in QW devices. The challenge for QD device improvement is to avoid, even single, extreme deviations from the mean QD size and distance. As shown in case of the QW devices, a single microscopic defect is sufficient to impair the entire DL. The observed degradation in QD DLs is not a classical COD, because the main energy source of the degradation is not the laser light field.

[3] In fact, the position of a single dot is random, but the distances between them underlay a certain distribution governed by the parameters during Stranski-Krastanow growth mode, e.g., discussed by Baskaran and Smereka [199].

8 Conclusions

The main findings of this study are:

- The step test approach as a special kind of accelerated aging addresses the same COD degradation mechanisms as found in cw tests. It is an appropriate tool to reduce the first phase of COD to the nanosecond time scale. Therefore, it allows to systematically provoke the COD and makes a time-resolved study of the process possible for the first time on this time scale.
- The applied thermographic techniques makes the *in-situ* tracing of the defect growth possible, even if the device is not prepared, e.g., by windows in the contacts.
- This *in-situ* tracing allowed to monitor the propagation of the high temperature defect front directly. Propagation velocities up to $200\,\mu\mathrm{m}/\,\mu\mathrm{s}$ have been observed. The connection of the value found at a specific device to the available light power have been shown.
- The laser light field is verified to be the main energy source for the COD.
- It was shown that the temperature of the defect front during the entire process keeps on a constant level of about $1200^{\circ}\mathrm{C} - 1500^{\circ}\mathrm{C}$. For this purpose, various approaches have been used: The motion of the heat source observed through a top-contact window of the device, the magnitude of the flash of Planck's radiation, energy balance calculations, and TEM images and their crystallographic interpretation.
- Short-time thermography, TEM analysis, and *in-situ* defect tracing verified that the amplified spontaneous emission is sufficient for further damage growth when lasing is terminated.
- The tracing of the defect front, heat flow modeling, and crystallographic analysis show that the material passed by the defect front returns to substantially lower temperatures within nanoseconds.
- Due to the high temperatures present at the defect front and the heat flow, a point defect cloud is generated around the primary defect. These defects potentially trigger secondary COD starting points.
- A model for the defect spread in the third COD phase is presented. It verifies that this phase is dominated by three basic mechanisms – unidirectional energy entry via the light field, isotropic thermal energy and defect spread after re-absorption, and shadowing of the light field by existing damage.
- A certain temperature difference has to be reached between the future COD ignition site and the remaining active material to ignite the thermal runaway. The locations of these initial points have determining influence on the later fully developed defect pattern. This strong connection allows the presented defect spread model to reconstruct the kinetics of the defect front *ex-post*.

- The analysis of the defect spread in the second and third phase identifies the thermal resistance of the material as major parameter determining its dynamics.
- Based on the presented experimental approaches and the strategies for data analysis, it becomes possible to evaluate the material quality, influence of device processing on its reliability, and the quality of the facet passivation. The main input data for such an analysis are the size and position of the initial defect points, the branching behavior of the internal defect structure, and the distribution of the COD threshold values of the individual device from a batch.
- Experimental indications were found that the ignition of COD does not take place at the QW itself, but in the waveguide and cladding region above and below the QW. This is a surprising result, since the QW as the gain medium is expected to be exposed to the highest optical load.

The results indicate that the starting points of COD, which are located in waveguide or cladding, are triggered by a distortion of the light field caused by an elevated QW temperature. This directs it away from the QW towards the surrounding layers that cannot withstand the increase optical load. In order to verify this, additional experiments are necessary focusing on the early defect stages. The tools to prepare these degradation stages are developed in the present work.

Moreover, a future study should contain a systematic investigation of the degradation during applied external optical feedback. It is likely that the same mechanism, light that is coupled into a region above or below the QW, favors this mechanism and lowers the COD threshold. This aspect is relevant for all today's laser systems where the DL light beam is partly reflected by beam-combining or -shaping optics.

List of Abbreviations and Symbols

Abbreviation

μPL	micro-photoluminescence
BA	broad area
CCD	charged coupled device
CL	plane view cathodoluminescence
COD	catastrophic optical damage
cw	continuous wave
DL	diode laser
EBIC	electron beam-induced current
EDX	energy dispersive X-ray
EL	electroluminescence
FIB	focused ion beam
FWHM	full width at half maximum
L-I curve	optical output power plotted over applied current
L-I-V curve	optical output power and voltage drop plotted over applied current
LBIC	laser beam-induced current
MCT	mercury cadmium telluride
ND	neutral-density filter
Nd:YAG	neodymium-doped yttrium aluminum garnet
NETD	noise equivalent temperature difference
NF	lasing near-field
NIR	near-infrared
PC	photocurrent
PD	photo-diode
QCL	quantum cascade laser
QD	quantum dot
QW	quantum well
SEM	scanning electron microscopy
TEM	transmission electron microscopy
TTL	transistor-transistor logic

Symbol

α_{spread}	spreading angle of the defect pattern

$\Delta\overline{T}$ ..... average temperature rise in defect region
ΔI ..... current step in step test approach
ΔT ..... temperature rise
$\Delta T_{\mathrm{facet}}$ ..... additional temperature increase of facet near region with respect to the active region bulk
ΔT_{max} ..... maximal temperature rise achieved during the COD
Δz_{edge} ..... difference of z_{edge} values for two consecutive pulses
η_{d} ..... slope efficiency
$\hbar$ ..... reduced Planck constant
λ_{c} ..... emission wavelength
$\overline{T}$ ..... average temperature in defect region
τ ..... effective carrier lifetime
τ_{cool} ..... time constant for cooling down of the damage volume after energy feeding stops
τ_{drop} ..... characteristic 1/e output power decay time during COD
τ_{d} ..... characteristic decay length in defect growth model
τ_{p} ..... characteristic intensity decay time at the COD site
ρ_{c} ..... density of states
ρ ..... mass density
ξ ..... percentile of transferred energy in the defect growth model
A_{dark} ..... area of damage pattern in the QW plane
A_{def} ..... area of the external, i.e, at the facet, defect pattern
A_{nr} ..... Shockley-Read-Hall coefficient
A_{pixel} ..... area imaged by a pixel of the thermocamera
c ..... specific heat
C_{Auger} ..... Auger coefficient
CD ..... critical damage limit in the defect growth model
d ..... distance passed by the heat source during a single pulse
D_{Lim} ..... damage level up to which no absorption occurs in the defect growth model
d_{over} ..... overlap of damage paths of consecutive pulses
$E_{\mathrm{g,GaAs}}$ ..... band gap energy of GaAs
$E_{\mathrm{max,0}}$ ..... energy available in absence of any damage in defect growth model
E_{max} ..... total available energy per iteration in defect growth model
$E_{\mathrm{column,x}}$ ..... energy per column in defect growth model
E_{Low} ..... minimal amount of energy in one column in the defect growth model
F_{exp} ..... experimentally determined thermal flash amplitude
h ..... Planck's constant
I ..... current through the diode laser
I_0 ..... starting current in step test approach
I_{COD} ..... COD threshold current
I_{th} ..... threshold current
k ..... imaginary part of the refractive index
k_{therm} ..... thermal conductivity

N	carrier concentration
n	real part of the refractive index
n_{emitter}	number of columns in the defect growth model
P	percentage of the light energy that results of amplification of spontaneous emission in defect growth model
P_{COD}	COD threshold optical output power
$P_{\text{hypo}}(t)$	hypothetical optical output power transient for a pulse without COD
P_{max}	maximal optical output power
$P_{\text{real}}(t)$	measured optical output power transient
R	total recombination rate
r	radial distance in the spherical linear temperature profile
r_0	radius of the sphere
R_λ	specific thermal resistance
R_{sp}	radiative recombination coefficient
R_{th}	absolute thermal resistance
t	time
T_0	ambient temperature
T_{bulk}	bulk temperature, i.e., the active material in the cavity
T_{crit}	critical temperature for starting COD
t_{end}	time after optical output power drops, due to COD, to the $1/e^2$ value or the pulse end
T_{facet}	temperature of the laser facet
T_{flash}	temperature transient of the damage region
T_{hs}	heat sink temperature
$t_{\text{int,eff}}$	effective image integration time
t_{int}	image integration time
T_{max}	maximal temperature achieved during the COD
t_{max}	time at which the maximal optical output power in a pulse is reached
t_{PW}	pulse width
V_{def}	spatial volume of the defect
V_{emitter}	volume of the emitter stripe
V_{Sphere}	spherical volume
v_{surf}	surface recombination velocity
W_{def}	energy incorporated into damage creation, determined from power traces
w_{emitter}	width of the emitter stripe
W_{heat}	re-absorbed light energy which heats up the bulk material
W_{theo}	amount of energy deposited in the volume, following the made assumptions
w_{damage}	overall lateral width of the COD defect pattern
x_{edge}	lateral distance from edge of absorbing region in defect growth model
z_{edge}	edge of the thermal signal in z-direction

Publications

Publications Related to this Thesis

1. M. Ziegler, M. Hempel, H. E. Larsen, J. W. Tomm, P. E. Andersen, S. Clausen, S. N. Elliott, and T. Elsaesser. Physical limits of semiconductor laser operation: A time-resolved analysis of catastrophic optical damage. *Applied Physics Letters*, 97(2): 021110, 2010.

2. M. Hempel, M. Ziegler, J. W. Tomm, T. Elsaesser, N. Michel, and M. Krakowski. Time-resolved analysis of catastrophic optical damage in 975 nm emitting diode lasers. *Applied Physics Letters*, 96(25): 251105, 2010.

3. M. Hempel, J. W. Tomm, M. Ziegler, T. Elsaesser, N. Michel, and M. Krakowski. Catastrophic optical damage at front and rear facets of diode lasers. *Applied Physics Letters*, 97(23): 231101, 2010.

4. M. Hempel, F. La Mattina, J. W. Tomm, U. Zeimer, R. Broennimann, and T. Elsaesser. Defect evolution during catastrophic optical damage of diode lasers. *Semiconductor Science and Technology*, 26(7): 075020, 2011.

5. M. Hempel, J. W. Tomm, M. Baeumler, H. Konstanzer, J. Mukherjee, and T. Elsaesser. Near-field dynamics of broad area diode laser at very high pump levels. *AIP Advances*, 1(4): 042148, 2011.

6. M. Hempel, J. W. Tomm, P. Hennig, and T. Elsaesser. Emission properties of diode laser bars during pulsed high-power operation. *Semiconductor Science and Technology*, 26(9): 092001, 2011.

7. J. W. Tomm, M. Ziegler, M. Hempel, and T. Elsaesser. Mechanisms and fast kinetics of the catastrophic optical damage (COD) in GaAs-based diode lasers. *Laser & Photonics Reviews*, 5(3): 422-441, 2011.

8. S. N. Elliott, M. Hempel, U. Zeimer, P. M. Smowton, and J. W. Tomm. Catastrophic optical bulk damage in InP 7xx emitting quantum dot diode lasers. *Semiconductor Science and Technology*, 27(10): 102001, 2012.

9. M. Hempel, J. W. Tomm, M. Baeumler, H. Konstanzer, J. Mukherjee, and T. Elsaesser. Near-field evolution in strongly pumped broad area diode lasers. *SPIE Proceedings*, 8277: 82771H, 2012.

10. M. Olecki, J. W. Tomm, M. Hempel, P. Hennig, and T. Elsaesser. Emission properties of diode laser bars during pulsed high-power operation. *SPIE Proceedings*, 8241: 824107, 2012.

11. M. Hempel, J. W. Tomm, M. Baeumler, H. Konstanzer, J. Mukherjee, and T. Elsaesser. Near-field characteristics of broad area diode lasers during catastrophic optical damage failure. *SPIE Proc.*, 8432: 84320O, 2012.

12. M. Hempel, J. W. Tomm, U. Zeimer, and T. Elsaesser. Defect propagation in broad-area diode lasers. *Materials Science Forum*, 725: 101-104, 2012

13. J. W. Tomm, M. Hempel, and T. Elsaesser. Kinetics of defect propagation during catastrophic optical damage (COD) in broad-area diode lasers. *Materials Science Forum*, 725: 105-108, 2012

14. M. Hempel, M. Ziegler, S. Schwirzke-Schaaf, J. W. Tomm, D. Jankowski, and D. Schröder. Spectroscopic analysis of packaging concepts for high-power diode laser bars. *Applied Physics A: Materials Science & Processing*, 107(2): 371-377, 2012.

15. J. W. Tomm, M. Hempel, M. Krakowski, and T. Elsaesser. Mechanisms and kinetics of the catastrophic optical damage (COD) of high-power semiconductor lasers. *IEEE Photonics Society Summer Topical Meetings Series 2012*, 51-52, 2012.

16. M. Hempel, J. W. Tomm, V. Hortelano, N. Michel, J. Jimenéz, M. Krakowski, and T. Elsaesser. Time-resolved reconstruction of defect creation sequences in diode lasers. *Laser & Photonics Reviews*, 6(6): L15-L19, 2012.

17. M. Hempel, J. W. Tomm, T. Elsaesser, and M. Bettiati. High single-spatial-mode pulsed power from 980 nm emitting diode lasers. *Applied Physics Letters*, 101(19): 191105, 2012.

18. M. Hempel, M. Chi, P. M. Petersen, U. Zeimer, and J. W. Tomm. How does external feedback cause AlGaAs-based diode lasers to degrade? *Applied Physics Letters*, 102(2): 023502, 2013.

19. M. Hempel, J. W. Tomm, F. La Mattina, I. Ratschinski, M. Schade, I. Shorubalko, M. Stiefel, H. S. Leipner, F. M. Kießling, and T. Elsaesser. Microscopic Origins of Catastrophic Optical Damage in Diode Lasers. *IEEE Journal of Selected Topics in Quantum Electronics*, in print.

20. M. Hempel, M. Chi, P. M. Petersen, U. Zeimer, M. Weyers, and J. W. Tomm. The impact of external optical feedback on the degradation behavior of high-power diode lasers. *SPIE Proceedings*, 8605: in print, 2013.

21. S. N. Elliott, M. Hempel, S. Shutts, U. Zeimer, P. M. Smowton, and J. W. Tomm. Comparison of catastrophic optical damage in InP/(Al)GaInP quantum dot and quantum well diode lasers. *SPIE Proceedings*, 8640: in print, 2013.

22. J. W. Tomm, M. Hempel, F. La Mattina, F. M. Kießling, and T. Elsaesser. Analysis of bulk and facet failures in AlGaAs-based high-power diode lasers. *SPIE Proceedings*, 8640: in print, 2013.

Other Publications

1. I. Bayrakli, M. Wienold, M. Hempel, M. Klinkmueller, M. Semtsiv, and W. T. Masselink. Grating-coupled external-cavity short-wavelength ($\lambda \approx 3.9\,\mu$m) InGaAs/InAlAs/AlAs quantum-cascade lasers. *Optical and Quantum Electronics*, 41(14-15): 1019-1025, 2009.

Conference Contributions

Contributions presented by myself are indicated by *.

1. J. W. Tomm, M. Hempel, and T. Elsaesser. COD monitoring of diode lasers. *High Power Diode Lasers and Systems Conference (HPD)*, Telford, 2010.

2. * M. Hempel, J. W. Tomm, and T. Elsaesser. Monitoring the infrared thermal signature of catastrophic optical damage in diode lasers. *40th Freiburg Infrared Colloquium*, Freiburg, 2011.

3. * M. Hempel, J. W. Tomm, M. Ziegler, T. Elsaesser, N. Michel, and M. Krakowski. Catastrophic optical damage at front and rear facets of 975 nm emitting diode lasers. *Conference on Lasers and Electro-Optics (CLEO)*, Baltimore, 2011.

4. * M. Hempel, J. W. Tomm, and T. Elsaesser. Sequence of events during the catastrophic optical damage in broad-area lasers. *Conference on Lasers and Electro-Optics (CLEO)*, Baltimore, 2011.

5. * M. Hempel, J. W. Tomm, U. Zeimer, and T. Elsaesser. Defect propagation in broad-area diode lasers. *14th International Conference on Defects - Recognition, Imaging and Physics in Semiconductors (DRIP XIV)*, Myazaki, 2011.

6. J. W. Tomm, M. Hempel, and T. Elsaesser. Kinetics of defect propagation during catastrophic optical damage (COD) in broad-area diode lasers. *14th International Conference on Defects - Recognition, Imagin and Physics in Semiconductors (DRIP XIV)*, Myazaki, 2011.

7. * M. Hempel, J. W. Tomm, M. Baeumler, H. Konstanzer, J. Mukherjee, and T. Elsasser. Near-field evolution in strongly pumped broad area diode lasers. *Novel In-Plane Semiconductor Lasers XI, Photonics West – OPTO*, San Francisco, 2012.

8. M. Olecki, J. W. Tomm, M. Hempel, P. Hennig, and T. Elsaesser. Emission properties of diode laser bars during pulsed high-power operation. *High-Power Diode Laser Technology and Applications X, Photonics West – LASE*, San Francisco, 2012.

9. * M. Hempel, J. W. Tomm, M. Baeumler, H. Konstanzer, J. Mukherjee, and T. Elsaesser. Near-field characteristics of broad area diode lasers during catastrophic optical damage failure. *Semiconductor Lasers and Laser Dynamics V, Photonics Europe*, Brussels, 2012.

10. J. W. Tomm, M. Hempel, and T. Elsaesser. Fast kinetics of the catastrophic optical damage (COD) in broad-area diode lasers. *International Symposium on Reliability of Optoelectronics For Space*, Cagliari, 2012.

11. J. W. Tomm, M. Hempel, M. Krakowski, and T. Elsaesser. Mechanisms and kinetics of the catastrophic optical damage (COD) of high-power semiconductor lasers. *IEEE Photonics Society Summer Topical Meetings*, Seattle, 2012.

12. J. W. Tomm, M. Hempel, and T. Elsaesser. The limits of high-power diode lasers in terms of reliability. *7th International Conference on Photonics and Applications*, Hanoi, 2012.

13. ⋆ M. Hempel, M. Chi, P. M. Petersen, U. Zeimer, M. Weyers, and J. W. Tomm. The impact of external optical feedback on the degradation behavior of high-power diode lasers. *High-Power Diode Laser Technology and Applications XI, Photonics West – LASE*, San Francisco, 2013.

14. S. N. Elliott, M. Hempel, S. Shutts, U. Zeimer, P. M. Smowton, and J. W. Tomm. Comparison of catastrophic optical damage in InP/(Al)GaInP quantum dot and quantum well diode lasers. *Novel In-Plane Semiconductor Lasers XII, Photonics West – OPTO*, San Francisco, 2013.

15. J. W. Tomm, M. Hempel, F. La Mattina, F. M. Kießling, and T. Elsaesser. Analysis of bulk and facet failures in AlGaAs-based high-power diode lasers. *Novel In-Plane Semiconductor Lasers XII, Photonics West – OPTO*, San Francisco, 2013.

Awards

1. *Young Researcher Poster Award* at the DRIP-XIV, Miyazaki, Japan, 2011.

2. The article *Defect evolution during catastrophic optical damage of diode lasers* by Martin Hempel, Fabio La Mattina, Jens W. Tomm, Ute Zeimer, Rolf Broennimann, and Thomas Elsaesser has been selected by the editors of *Semiconductor Science and Technology* for inclusion in the '2011 Highlights' collection.

Bibliography

[1] A. Knigge, G. Erbert, J. Jonsson, W. Pittroff, R. Staske, B. Sumpf, M. Weyers, and G. Tränkle. Passively cooled 940 nm laser bars with 73% wall-plug efficiency at 70 W and 25°C. *Electronics Letters*, 41(5):250–251, 2005.

[2] P. Crump, M. Grimshaw, Wang Jun, Dong Weimin, Zhang Shiguo, S. Das, J. Farmer, M. DeVito, L. S. Meng, and J. K. Brasseur. 85% power conversion efficiency 975-nm broad area diode lasers at -50°C, 76% at 10°C. In *Conference on Lasers and Electro-Optics, 2006 and 2006 Quantum Electronics and Laser Science Conference. CLEO/QELS 2006.*, pages 1–2, 2006.

[3] R. L. Byer. Diode laser-pumped solid-state lasers. *Science*, 239(4841):742–747, 1988.

[4] O. Ueda. On degradation studies of III-V compound semiconductor optical devices over three decades: Focusing on gradual degradation. *Japanese Journal of Applied Physics*, 49(9):090001, 2010.

[5] H. Wenzel, P. Crump, A. Pietrzak, X. Wang, G. Erbert, and G. Tränkle. Theoretical and experimental investigations of the limits to the maximum output power of laser diodes. *New Journal of Physics*, 12:085007 1–11, 2010.

[6] M. J. Myers, J. D. Myers, B. Guo, C. Yang, and C. R. Hardy. Practical internal combustion engine laser spark plug development. *Proceedings of SPIE*, 6662:66620E, 2007.

[7] R. Feeler, J. Junghans, and E. Stephens. Low-cost diode arrays for the life project. *Proceedings of SPIE*, 7916:791608, 2011.

[8] R. N. Hall, R. O. Carlson, T. J. Soltys, G. E. Fenner, and J. D. Kingsley. Coherent light emission from GaAs junctions. *Physical Review Letters*, 9(9):366–369, 1962.

[9] M. I. Nathan, W. P. Dumke, G. Burns, F. H. Dill, and G. Lasher. Stimulated emission of radiation from GaAs p-n junctions. *Applied Physics Letters*, 1(3):62–64, 1962.

[10] N. Holonyak and S. F. Bevacqua. Coherent (visible) light emission from $Ga(As_{1-x}P_x)$ junctions. *Applied Physics Letters*, 1(4):82–83, 1962.

[11] T. M. Quist, R. H. Rediker, R. J. Keyes, W. E. Krag, B. Lax, A. L. McWhorter, and H. J. Zeigler. Semiconductor maser of GaAs. *Applied Physics Letters*, 1(4):91–92, 1962.

[12] J. J. Coleman. The development of the semiconductor laser diode after the first demonstration in 1962. *Semiconductor Science and Technology*, 27(9):090207, 2012.

[13] H. Kroemer. A proposed class of heterojunction injection lasers. *Proceedings of the IEEE*, 51 (12):1782–1783, 1963.

[14] Z. I. Alferov, V. M. Andreev, E. L. Portnoi, and M. K. Turkan. AlAs-GaAs heterojunction injection laser with a low room-temperature threshold. *Fizika i Tekhnika Poluprovodnikov*, 3:1328–1332, 1969.

[15] I. Hayashi, M. B. Panish, P. W. Foy, and S. Sumski. Junction lasers which operate continuously at room temperature. *Applied Physics Letters*, 17(3):109–111, 1970.

[16] S. M. Sze and K. K. Ng. *Physics of semiconductor devices*. Wiley-Interscience, Hoboken, N.J., 3rd edition, 2007.

[17] M. B. Panish, H. C. Casey, S. Sumski, and P. W. Foy. Reduction of threshold current-density in GaAs-$Al_xGa_{1-x}As$ heterostructure lasers by separate optical and carrier confinement. *Applied Physics Letters*, 22(11):590–591, 1973.

[18] R. Dingle, W. Wiegmann, and C. H. Henry. Quantum states of confined carriers in very thin $Al_xGa_{1-x}As$-GaAs-$Al_xGa_{1-x}As$ heterostructures. *Physical Review Letters*, 33(14):827–830, 1974.

[19] J. C. Dyment. Hermite-gaussian mode patterns in gaas junction lasers. *Applied Physics Letters*, 10(3):84–86, 1967.

[20] B. R. Bennett, R. A. Soref, and J. A. Delalamo. Carrier-induced change in refractive-index of InP, GaAs, and InGaAsP. *IEEE Journal of Quantum Electronics*, 26(1):113–122, 1990.

[21] J. J. Coleman, N. Holonyak, M. J. Ludowise, P. D. Wright, R. Chin, W. O. Groves, and D. L. Keune. Pulsed room-temperature operation of $In_{1-x}Ga_xP_{1-z}As_z$ double heterojunction lasers at high-energy (6470 Å, 1.916 eV). *Applied Physics Letters*, 29(3):167–169, 1976.

[22] M. Ikeda, Y. Mori, H. Sato, K. Kaneko, and N. Watanabe. Room-temperature continuous-wave operation of an AlGaInP double heterostructure laser grown by atmospheric-pressure metalorganic chemical vapor-deposition. *Applied Physics Letters*, 47(10):1027–1028, 1985.

[23] E. Yablonovitch and E. O. Kane. Reduction of lasing threshold current-density by the lowering of valence band effective mass. *Journal of Lightwave Technology*, 4(5):504–506, 1986.

[24] A. R. Adams. Band-structure engineering for low-threshold high-efficiency semiconductor-lasers. *Electronics Letters*, 22(5):249–250, 1986.

[25] J. W. Matthews and A. E. Blakeslee. Defects in epitaxial multilayers .1. misfit dislocations. *Journal of Crystal Growth*, 27:118–125, 1974.

[26] K. J. Beernink, P. K. York, J. J. Coleman, R. G. Waters, J. Kim, and C. M. Wayman. Characterization of InGaAs-GaAs strained-layer lasers with quantum wells near the critical thickness. *Applied Physics Letters*, 55(21):2167–2169, 1989.

[27] S. Nakamura, M. Senoh, and T. Mukai. High-power InGaN/GaN double-heterostructure violet light-emitting-diodes. *Applied Physics Letters*, 62(19):2390–2392, 1993.

[28] P. J. A. Thijs and T. van Dongen. High quantum efficiency, high power, modulation doped GaInAs strained-layer quantum well laser diodes emitting at 1.5 μm. *Electronics Letters*, 25(25):1735–1737, 1989.

[29] Y. Arakawa, H. Sakaki, M. Nishioka, H. Okamoto, and N. Miura. Spontaneous emission characteristics of quantum well lasers in strong magnetic-fields - an approach to quantum-well-box light-source. *Japanese Journal of Applied Physics Part 2-Letters*, 22(12):L804–L806, 1983.

[30] J. Faist, F. Capasso, D. L. Sivco, C. Sirtori, A. L. Hutchinson, and A. Y. Cho. Quantum cascade laser. *Science*, 264(5158):553–556, 1994.

[31] J. W. Tomm and J. Jiménez, editors. *Quantum-Well Laser Array Packaging*. Mcgraw-Hill Nanoscience and Technology Series. McGraw-Hill, New York, 2007.

[32] P. Y. Yu and M. Cardona. *Fundamentals of semiconductors: physics and materials properties*. Springer, 2001.

[33] B. E. A. Saleh and M. C. Teich. *Fundamentals of photonics*. Wiley Interscience, 2007.

[34] M. Hempel. Funktionale Schichten und optische Beschichtungen für MIR-Quantenkaskaden-Laser. Diplomarbeit, Humboldt-Universität zu Berlin, 2009.

[35] J. Singh. *Electronic and optoelectronic properties of semiconductor structures*. Cambridge University Press, 2003.

[36] H. Haug and S. W. Koch. *Quantum theory of the optical and electronic properties of semiconductors*. World Scientific, 4th edition, 2004.

[37] P. S. Zory. *Quantum well lasers*. Academic Press, 1993.

[38] L. A. Coldren, S. W. Corzine, and Milan Mashanovitch. *Diode lasers and photonic integrated circuits*. Wiley, 2012.

[39] P. Unger. *High-power diode lasers: Fundamentals, technology, applications*, page 46 pp. Springer, 2000.

[40] J. Jiménez. Laser diode reliability: crystal defects and degradation modes. *Comptes Rendus Physique*, 4(6):663–673, 2003.

[41] A. K. Chin, R. K. Bertaska, M. A. Jaspan, A. M. Flusberg, S. D. Swartz, M. T. Knapczyk, R. Petr, I. Smilanski, and J. H. Jacob. A comprehensive model of catastrophic optical-damage in broad-area laser diodes. In *High-Power Diode Laser Technology and Applications VII*, volume 7198, page 71981A. SPIE, 2009.

[42] M. Bou Sanayeh. *Catastrophic Optical Damage in High-Power AlGaInP Diode Lasers*. PhD thesis, Universität Duisburg-Essen, 2008.

[43] D. P. Cooper, C. H. Gooch, and R. J. Sherwell. Internal self-damage of Gallium Arsenide lasers. *IEEE Journal of Quantum Electronics*, QE 2(8):329–330, 1966.

[44] H. Kressel and H. Mierop. Catastrophic degradation in GaAs injection lasers. *Journal of Applied Physics*, 38(13):5419–5421, 1967.

[45] P. G. Eliseev. Degradation of injection lasers. *Journal of Luminescence*, 7:338–356, 1973.

[46] C. H. Henry, P. M. Petroff, R. A. Logan, and F. R. Merritt. Catastrophic damage of $Al_xGa_{1-x}As$ double-heterostructure laser material. *Journal of Applied Physics*, 50(5):3721–3732, 1979.

[47] W. C. Tang, H. J. Rosen, P. Vettiger, and D. J. Webb. Raman microprobe study of the time development of AlGaAs single quantum well laser facet temperature on route to catastrophic breakdown. *Applied Physics Letters*, 58(6):557, 1991.

[48] W. Nakwaski. Thermal analysis of the catastrophic mirror damage in laser-diodes. *Journal of Applied Physics*, 57(7):2424–2430, 1985.

[49] G. Chen and C. L. Tien. Facet heating of quantum-well lasers. *Journal of Applied Physics*, 74(4): 2167–2174, 1993.

[50] R. Schatz and C. G. Bethea. Steady-state model for the facet heating leading to thermal runaway in semiconductor lasers. *Journal of Applied Physics*, 76(4):2509–2521, 1994.

[51] T. Shibutani, M. Kume, K. Hamada, H. Shimizu, K. Itoh, G. Kano, and I. Teramoto. A novel high-power laser structure with current-blocked regions near cavity facets. *IEEE Journal of Quantum Electronics*, 23(6):760–764, 1987.

[52] T. Kamejima and H. Yonezu. Catastrophic optical damage generation mechanism in (AlGa)As DH lasers. *Japanese Journal of Applied Physics*, 19:425–429, 1980.

[53] M. Ziegler, V. Talalaev, J. W. Tomm, T. Elsaesser, P. Ressel, B. Sumpf, and G. Erbert. Surface recombination and facet heating in high-power diode lasers. *Applied Physics Letters*, 92(20): 203506, 2008.

[54] W. C. Tang, H. J. Rosen, P. Vettiger, and D. J. Webb. Evidence for current-density-induced heating of AlGaAs single-quantum-well laser facets. *Applied Physics Letters*, 59(9):1005, 1991.

[55] J. S. Yoo, H. H. Lee, and P. Zory. Temperature rise at mirror facet of cw semiconductor lasers. *IEEE Journal of Quantum Electronics*, 28(3):635–639, 1992.

[56] M. Ziegler, J. W. Tomm, D. Reeber, T. Elsaesser, U. Zeimer, H. E. Larsen, P. M. Petersen, and P. E. Andersen. Catastrophic optical mirror damage in diode lasers monitored during single-pulse operation. *Applied Physics Letters*, 94(19):191101, 2009.

[57] M. Fukuda. *Reliability and Degradation of Semiconductor Lasers and LEDs*. Artech House Publishers, 1991.

[58] J. W. Tomm, M. Ziegler, M. Hempel, and T. Elsaesser. Mechanisms and fast kinetics of the catastrophic optical damage (COD) in GaAs-based diode lasers. *Laser & Photonics Reviews*, 5 (3):422–441, 2011.

[59] W. C. Tang, H. J. Rosen, P. Vettiger, and D. J. Webb. Comparison of the facet heating behavior between AlGaAs single quantum-well lasers and double-heterojunction lasers. *Applied Physics Letters*, 60(9):1043, 1992.

[60] F. A. Houle, D. L. Neiman, W. C. Tang, and H. J. Rosen. Chemical changes accompanying facet degradation of AlGaAs quantum well lasers. *Journal of Applied Physics*, 72(9):3884–3896, 1992.

[61] A. Chavan, R. Radionova, G. W. Charache, R. J. Menna, H. Schluter, and J. L. Hostetler. Comparison of facet temperature and degradation of unpumped and passivated facets of Al-free 940-nm lasers using photoluminescence. *IEEE Journal of Quantum Electronics*, 41(5):630–635, 2005.

[62] J. Hashimoto, I. Yoshida, M. Murata, and T. Katsuyama. Aging time dependence of catastrophic optical damage (COD) failure of a 0.98-μm GaInAs-GaInP strained quantum-well laser. *IEEE Journal of Quantum Electronics*, 33(1):66–70, 1997.

[63] T. Fukushima, A. Furuya, Y. Kito, H. Sudo, M. Sugano, and T. Tanahashi. Catastrophic optical damage of AlGaInP visible laser diodes under high-power operation. *Electronics and Communications in Japan (Part II: Electronics)*, 78(7):11–19, 1995.

[64] H. A. Macleod. *Thin-film optical filters*. Series in optics and optoelectronics. CRC Press/Taylor & Francis, Boca Raton, FL, 4th edition, 2010.

[65] A. Moser, E.-E. Latta, and D. J. Webb. Thermodynamics approach to catastrophic optical mirror damage of AlGaAs single quantum well lasers. *Applied Physics Letters*, 55(12):1152–1154, 1989.

[66] A. Moser. Thermodynamics of facet damage in cleaved AlGaAs lasers. *Applied Physics Letters*, 59(5):522–524, 1991.

[67] A. Moser and E. E. Latta. Arrhenius parameters for the rate process leading to catastrophic damage of AlGaAs-GaAs laser facets. *Journal of Applied Physics*, 71(10):4848–4853, 1992.

[68] A. Oosenbrug and E. E. Latta. High-power operational stability of 980 nm pump lasers for EDFA applications. In *7th Annual Meeting of the IEEE Lasers-and-Electro-Optics-Society – Proceedings*, volume 2, pages 37–38, 1994.

[69] L. W. Tu, E. F. Schubert, M. Hong, and G. J. Zydzik. In-vacuum cleaving and coating of semiconductor laser facets using thin silicon and a dielectric. *Journal of Applied Physics*, 80(11): 6448–6451, 1996.

[70] H. Ichikawa, C. Fukuda, K. Hamada, and T. Nakabayashi. Facet passivation of GaInAsP/InP edge-emitting laser diode by aluminum ultrathin layer insertion. *Japanese Journal of Applied Physics*, 47(10):7890–7895, 2008.

[71] H. Horie, H. Ohta, and T. Fujimori. Reliability improvement of 980-nm laser diodes with a new facet passivation process. *IEEE Journal of Selected Topics in Quantum Electronics*, 5(3):832–838, 1999.

[72] R. W. Lambert, T. Ayling, A. F. Hendry, J. M. Carson, D. A. Barrow, S. McHendry, C. J. Scott, A. McKee, and W. Meredith. Facet-passivation processes for the improvement of Al-containing semiconductor laser diodes. *Journal of Lightwave Technology*, 24(2):956–961, 2006.

[73] G. Beister, J. Maege, D. Gutsche, G. Erbert, J. Sebastian, K. Vogel, M. Weyers, J. Würfl, and O. P. Daga. Simple method for examining sulphur passivation of facets in InGaAs-AlGaAs ($\lambda = 0.98\,\mu$m) laser diodes. *Applied Physics Letters*, 68(18):2467–2468, 1996.

[74] S. Kamiyama, Y. Mori, Y. Takahashi, and K. Ohnaka. Improvement of catastrophic optical damage level of AlGaInP visible laser diodes by sulfur treatment. *Applied Physics Letters*, 58(23):2595–2597, 1991.

[75] G. Beister, J. Maege, J. Sebastian, G. Erbert, L. Weixelbaum, M. Weyers, J. Würfl, and O. P. Daga. Stability of sulfur-passivated facets of InGaAs-AlGaAs laser diodes. *IEEE Photonics Technology Letters*, 8(9):1124–1126, 1996.

[76] P. Ressel, G. Erbert, U. Zeimer, K. Häusler, G. Beister, B. Sumpf, A. Klehr, and G. Tränkle. Novel passivation process for the mirror facets of Al-free active-region high-power semiconductor diode lasers. *IEEE Photonics Technology Letters*, 17(5):962–964, 2005.

[77] D. R. Miftakhutdinov, I. V. Akimova, A. P. Bogatov, T. I. Gushchik, A. E. Drakin, N. V. D'Yachkov, V. V. Popovichev, and A. P. Nekrasov. Radiation parameters of ridge lasers at high pump currents. *Quantum Electronics*, 38(11):993–1000, 2008.

[78] F. R. Gfeller, P. Buchmann, P. W. Epperlein, H. P. Meier, and J. P. Reithmaier. High-power single-mode AlGaAs lasers with bent-waveguide nonabsorbing etched mirrors. *Journal of Applied Physics*, 72(6):2131–2135, 1992.

[79] B. Corbett, P. Lambkin, J. O'Callaghan, S. Deubert, W. Kaiser, J. P. Reithmaier, and A. Forchel. Modal analysis of large spot size, low output beam divergence quantum-dot lasers. *IEEE Photonics Technology Letters*, 19(9-12):916–918, 2007.

[80] D. Botez. Design considerations and analytical approximations for high continuous-wave power, broad-waveguide diode lasers. *Applied Physics Letters*, 74(21):3102–3104, 1999.

[81] I. B. Petrescu-Prahova, P. Modak, E. Goutain, D. Silan, D. Bambrick, J. Riordan, T. Moritz, S. D. McDougall, B. Qiu, and J. H. Marsh. High d/Γ values in diode laser structures for very high power. *Proceedings of SPIE*, 7198:71981I, 2009.

[82] P. G. Eliseev. Optical strength of semiconductor laser materials. *Progress in Quantum Electronics*, 20(1):1–82, 1996.

[83] M. Maiorov, D. Damm, I. Trofimov, V. Zeidel, and R. Sellers. Reliability assessment of GaAs- and InP-based diode lasers for high-energy single-pulse operation. *Proceedings of SPIE*, 7434: 743404, 2009.

[84] F. U. Herrmann, S. Beeck, G. Abstreiter, C. Hanke, C. Hoyler, and L. Korte. Reduction of mirror temperature in GaAs/AlGaAs quantum-well laser-diodes with segmented contacts. *Applied Physics Letters*, 58(10):1007–1009, 1991.

[85] H. Horie, Y. Yamamoto, N. Arai, and H. Ohta. Thermal rollover characteristics up to 150°C of buried-stripe type 980-nm laser diodes with a current injection window delineated by a SiN_x layer. *IEEE Photonics Technology Letters*, 12(1):13–15, 2000.

[86] F. Rinner, J. Rogg, M. T. Kelemen, M. Mikulla, G. Weimann, J. W. Tomm, E. Thamm, and R. Poprawe. Facet temperature reduction by a current blocking layer at the front facets of high-power InGaAs/AlGaAs lasers. *Journal of Applied Physics*, 93(3):1848–1850, 2003.

[87] J. Hashimoto, T. Katsuyama, I. Yoshida, M. Murata, and H. Hayashi. Stable single mode operation of 0.98 μm GaInAs/GaInAsP/GaInP buried ridge stripe laser with AlGaInP current blocking layer. *Electronics Letters*, 30(14):1146–1147, 1994.

[88] H. O. Yonezu, M. Ueno, T. Kamejima, and I. Hayashi. An AlGaAs window structure laser. *IEEE Journal of Quantum Electronics*, 15(8):775–781, 1979.

[89] C. L. Walker, A. C. Bryce, and J. H. Marsh. Improved catastrophic optical damage level from laser with nonabsorbing mirrors. *IEEE Photonics Technology Letters*, 14(10):1394–1396, 2002.

[90] H. Taniguchi, H. Ishii, R. Minato, Y. Ohki, T. Namegaya, and A. Kasukawa. 25-W 915-nm lasers with window structure fabricated by impurity-free vacancy disordering (IFVD). *IEEE Journal of Selected Topics in Quantum Electronics*, 13(5):1176–1179, 2007.

[91] P. G. Piva, S. Fafard, M. Dion, M. Buchanan, S. Charbonneau, R. D. Goldberg, and I. V. Mitchell. Reduction of InGaAs/GaAs laser facet temperatures by band gap shifted extended cavities. *Applied Physics Letters*, 70(13):1662–1664, 1997.

[92] P. G. Piva, R. D. Goldberg, I. V. Mitchell, S. Fafard, M. Dion, M. Buchanan, S. Charbonneau, G. Hillier, and C. Miner. Reduced 980 nm laser facet absorption by band gap shifted extended cavities. *Journal of Vacuum Science & Technology B*, 16(4):1790–1793, 1998.

[93] H. C. Ko, M. W. Cho, J. H. Chang, and M. Yang. A new structure of 780 nm AlGaAs/GaAs high power laser diode with non-absorbing mirrors. *Applied Physics A - Materials Science & Processing*, 68(4):467–470, 1999.

[94] J. Ungar, N. Barchaim, and I. Ury. High-power GaAlAs window lasers. *Electronics Letters*, 22 (5):279–280, 1986.

[95] R. L. Thornton, D. F. Welch, R. D. Burnham, T. L. Paoli, and P. S. Cross. High power (2.1 W) 10-stripe AlGaAs laser arrays with Si disordered facet windows. *Applied Physics Letters*, 49(23): 1572–1574, 1986.

[96] M. Ziegler, R. Pomraenke, M. Felger, J. W. Tomm, P. Vasa, C. Lienau, M. B. Sanayeh, A. Gomez-Iglesias, M. Reufer, F. Bugge, and G. Erbert. Infrared emission from the substrate of GaAs-based semiconductor lasers. *Applied Physics Letters*, 93(4):041101, 2008.

[97] R. Giri, S. Schwirzke-Schaaf, and J. W. Tomm. Extrinsic contributions to photocurrents from quantum-wells. *Journal of Applied Physics*, 108(1):013103, 2010.

[98] T. Q. Tien, A. Gerhardt, S. Schwirzke-Schaaf, J. W. Tomm, M. Pommies, M. Avella, J. Jiménez, M. Oudart, and J. Nagle. Screening of high-power diode laser bars by optical scanning. *Applied Physics Letters*, 87(21):211110, 2005.

[99] C. Ropers, T. Q. Tien, C. Lienau, J. W. Tomm, P. Brick, N. Linder, B. Mayer, M. Muller, S. Tautz, and W. Schmid. Observation of deep level defects within the waveguide of red-emitting high-power diode lasers. *Applied Physics Letters*, 88(13):133513, 2006.

[100] P. W. Epperlein, P. Buchmann, and A. Jakubowicz. Lattice disorder, facet heating and catastrophic optical mirror damage of AlGaAs quantum well lasers. *Applied Physics Letters*, 62(5):455–457, 1993.

[101] D. Drouin, A. R. Couture, D. Joly, X. Tastet, V. Aimez, and R. Gauvin. CASINO V2.42 – a fast and easy-to-use modeling tool for scanning electron microscopy and microanalysis users. *Scanning*, 29(3):92–101, 2007.

[102] M. Baeumler, J. L. Weyher, S. Müller, W. Jantz, R. Stibal, G. Herrmann, J. Luft, K. Sporrer, and W. Spath. Investigation of degraded laser diodes by chemical preparation and luminescence microscopy. In *7th International Conference on Defect Recognition and Image Processing in Semiconductors (DRIP-VII)*, volume 160, pages 467–470. Institute of Physics Conference Series, 1998.

[103] R. Wirth. Focused ion beam (FIB) combined with SEM and TEM: Advanced analytical tools for studies of chemical composition, microstructure and crystal structure in geomaterials on a nanometre scale. *Chemical Geology*, 261(3-4):217–229, 2009.

[104] R. Ramachandra, B. Griffin, and D. Joy. A model of secondary electron imaging in the helium ion scanning microscope. *Ultramicroscopy*, 109(6):748–757, 2009.

[105] B. C. Qiu, O. Kowalski, S. D. McDougall, X. F. Liu, and J. H. Marsh. High reliability, high power arrays of 808 nm single mode diode lasers employing various quantum well structures. In *Novel In-Plane Semiconductor Lasers VII*, volume 6909, page 69090S. SPIE, 2008.

[106] M. Hempel, J. W. Tomm, M. Ziegler, T. Elsaesser, N. Michel, and M. Krakowski. Catastrophic optical damage at front and rear facets of diode lasers. *Applied Physics Letters*, 97(23):231101, 2010.

[107] M. Bou Sanayeh, P. Brick, W. Schmid, B. Mayer, M. Müller, M. Reufer, K. Streubel, J. W. Tomm, and G. Bacher. Temperature-power dependence of catastrophic optical damage in AlGaInP laser diodes. *Applied Physics Letters*, 91(4):041115, 2007.

[108] M. Hempel, J. W. Tomm, P. Hennig, and T. Elsaesser. Emission properties of diode laser bars during pulsed high-power operation. *Semiconductor Science and Technology*, 26(9):092001 (1–4), 2011.

[109] M.A. Bettiati, C. Starck, F. Laruelle, V. Cargemel, P. Pagnod, P. Garabedian, D. Keller, G. Ughetto, J-C. Bertreux, L. Raymond, G. Gelly, and R-M. Capella. Very high power operation of 980 nm single-mode InGaAs/AlGaAs pump lasers. *Proceedings of SPIE*, 6104:61040F, 2006.

[110] S. N. Elliott, M. Hempel, U. Zeimer, P. Smowton, and J. W. Tomm. Catastrophic optical bulk damage in InP 7xx emitting quantum dot diode lasers. *Semiconductor Science and Technology*, 27(10):102001, 2012.

[111] X. Z. Wang, P. Crump, H. Wenzel, A. Liero, T. Hoffmann, A. Pietrzak, C. M. Schultz, A. Klehr, A. Ginolas, S. Einfeldt, F. Bugge, G. Erbert, and G. Tränkle. Root-cause analysis of peak power saturation in pulse-pumped 1100 nm broad area single emitter diode lasers. *IEEE Journal of Quantum Electronics*, 46(5):658–665, 2010.

[112] A. Pietrzak, P. Crump, H. Wenzel, R. Staske, G. Erbert, and G. Tränkle. 55 W peak power from 1100 nm wavelength 60 μm broad-area laser diodes enabled by reduced carrier accumulation in the waveguide. *Semiconductor Science and Technology*, 24(3):035020 (1–5), 2009.

[113] S. O. Slipchenko, Z. N. Sokolova, N. A. Pikhtin, K. S. Borschev, D. A. Vinokurov, and I. S. Tarasov. Finite time of carrier energy relaxation as a cause of optical-power limitation in semiconductor lasers. *Semiconductors*, 40(8):990–995, 2006.

[114] F. Rinner, J. Rogg, P. Friedmann, M. Mikulla, G. Weimann, and R. Poprawe. Longitudinal carrier density measurement of high power broad area laser diodes. *Applied Physics Letters*, 80(1):19–21, 2002.

[115] P. Crump, S. Böldicke, C.M. Schultz, H. Ekhteraei, H. Wenzel, and G. Erbert. Experimental and theoretical analysis of the dominant lateral waveguiding mechanism in 975 nm high power broad area diode lasers. *Semiconductor Science and Technology*, 27(4):045001, 2012.

[116] M. Ziegler, M. Hempel, H. E. Larsen, J. W. Tomm, P. E. Andersen, S. Clausen, S. N. Elliott, and T. Elsaesser. Physical limits of semiconductor laser operation: A time-resolved analysis of catastrophic optical damage. *Applied Physics Letters*, 97(2):021110, 2010.

[117] M. Hempel, J. W. Tomm, and T. Elsaesser. Sequence of events during the catastrophic optical damage in broad-area lasers. In *Conference on Lasers and Electro-Optics (CLEO)*, pages 1–2. SPIE, 2011.

[118] M. Hempel, J. W. Tomm, M. Baeumler, H. Konstanzer, J. Mukherjee, and T. Elsaesser. Near-field dynamics of broad area diode laser at very high pump levels. *AIP Advances*, 1(4):042148 1–6, 2011.

[119] M. Hempel, J. W. Tomm, M. Baeumler, H. Konstanzer, J. Mukherjee, and T. Elsasser. Near-field evolution in strongly pumped broad area diode lasers. In A. Belyanin Alexey and M. Smowton Peter, editors, *Novel In-Plane Semiconductor Lasers XI*, volume 8277, page 82771H. SPIE, 2012.

[120] M. Hempel, J. W. Tomm, M. Baeumler, H. Konstanzer, J. Mukherjee, and T. Elsaesser. Near-field characteristics of broad area diode lasers during catastrophic optical damage failure. In Panajotov

Krassimir, Sciamanna Marc, Valle Angel, and Michalzik Rainer, editors, *Semiconductor Lasers and Laser Dynamics V*, volume 8432, page 84320O. SPIE, 2012.

[121] P. B. Allen and M. Cardona. Temperature dependence of the direct gap of Si and Ge. *Physical Review B*, 27(8):4760–4769, 1983.

[122] S. A. Lourenço, M. A. T. da Silva, I. F. L. Dias, J. L. Duarte, and J. C. Harmand. Effects of temperature on transition energies of GaAsSbN/GaAs single quantum wells. *Journal of Physics-Condensed Matter*, 23(32):325801, 2011.

[123] A. Olkhovets, R.-C. Hsu, A. Lipovskii, and F. W. Wise. Size-dependent temperature variation of the energy gap in lead-salt quantum dots. *Physical Review Letters*, 81(16):3539–3542, 1998.

[124] J. Liu and L. H. Liu. First-principles study of temperature-dependent optical properties of semiconductors from ultraviolet to infrared regions. *Journal of Applied Physics*, 111(8):083508, 2012.

[125] M. Hempel, J. W. Tomm, M. Ziegler, T. Elsaesser, N. Michel, and M. Krakowski. Catastrophic optical damage at front and rear facets of 975 nm emitting diode lasers. In *Conference on Lasers and Electro-Optics (CLEO)*, pages 1–2. SPIE, 2011.

[126] S. N. Elliott, P. M. Smowton, M. Ziegler, J. W. Tomm, and U. Zeimer. Time resolved studies of catastrophic optical mirror damage in red-emitting laser diodes. *Journal of Applied Physics*, 107 (12):123116, 2010.

[127] F. Kappeler, K. Mettler, and K. H. Zschauer. Pulsed-power performance and stability of 880 nm GaAlAs/GaAs oxide-stripe lasers. *IEE Proceedings-I Communications Speech and Vision*, 129 (6):256–261, 1982.

[128] H. S. Carslaw and J. C. Jaeger. *Conduction of heat in solids*. Clarendon Press ; Oxford University Press, 1986.

[129] K. J. Laidler. *The world of physical chemistry*. Oxford University Press, 1993.

[130] F. R. Nash. Mode guidance parallel to junction plane of double-heterostructure GaAs lasers. *Journal of Applied Physics*, 44(10):4696–4707, 1973.

[131] J. R. Andrews. Variable focusing due to refractive-index gradients in a diode-array traveling-wave amplifier. *Journal of Applied Physics*, 64(4):2134–2137, 1988.

[132] A. I. Bawamia, B. Eppich, K. Paschke, H. Wenzel, F. Schnieder, G. Erbert, and G. Tränkle. Experimental determination of the thermal lens parameters in a broad area semiconductor laser amplifier. *Applied Physics B-Lasers and Optics*, 97(1):95–101, 2009.

[133] R. J. Lang, A. G. Larsson, and J. G. Cody. Lateral-modes of broad area semiconductor-lasers - theory and experiment. *IEEE Journal of Quantum Electronics*, 27(3):312–320, 1991.

[134] I. Fischer, O. Hess, W. Elsasser, and E. Gobel. Complex spatio-temporal dynamics in the near-field of a broad-area semiconductor laser. *Europhysics Letters*, 35(8):579–584, 1996.

[135] H. Adachihara, O. Hess, E. Abraham, P. Ru, and J. V. Moloney. Spatiotemporal chaos in broad-area semiconductor laser. *Journal of the Optical Society of America B*, 10(4):658–665, 1993.

[136] F. Gity, V. Ahmadi, and M. Noshiravani. Numerical analysis of void-induced thermal effects on GaAs/$Al_xGa_{1-x}As$ high power single-quantum-well laser diodes. *Solid-State Electronics*, 50 (11-12):1767–1773, 2006.

[137] W. Nakwaski. Thermal model of the catastrophic degradation of high-power stripe-geometry GaAs/(AlGa)As double-heterostructure diode lasers. *Journal of Applied Physics*, 67(4):1659–1668, 1990.

[138] K. Kopitzki. *Einführung in die Festkörperphysik*. B.G. Teubner, 1986.

[139] D. E. Aspnes, S. M. Kelso, R. A. Logan, and R. Bhat. Optical properties of $Al_xGa_{1-x}As$. *Journal of Applied Physics*, 60(2):754–767, 1986.

[140] M. C. Amann and B. Stegmuller. Calculation of the effective refractive-index step for the metal-cladded-ridge-waveguide laser. *Applied Optics*, 20(8):1483–1486, 1981.

[141] J. Mukherjee and J. G. McInerney. Spatial mode dynamics in wide-aperture quantum-dot lasers. *Physical Review A*, 79(5):053813, 2009.

[142] G. R. Hadley, J. P. Hohimer, and A. Owyoung. Comprehensive modeling of diode arrays and broad-area devices with applications to lateral index tailoring. *IEEE Journal of Quantum Electronics*, 24(11):2138–2152, 1988.

[143] U. Menzel. Self-consistent calculation of facet heating in asymmetrically coated edge emitting diode lasers. *Semiconductor Science and Technology*, 13(3):265–276, 1998.

[144] D. R. Miftakhutdinov, A. P. Bogatov, and A. E. Drakin. Catastrophic optical degradation of the output facet of high-power single-transverse-mode diode lasers. 1. Physical model. *Quantum Electronics*, 40(7):583–588, 2010.

[145] D. R. Miftakhutdinov, A. P. Bogatov, and A. E. Drakin. Catastrophic optical degradation of the output facet of high-power single-transverse-mode diode lasers. 2. Calculation of the spatial temperature distribution and threshold of the catastrophic optical degradation. *Quantum Electronics*, 40(7):589–595, 2010.

[146] J. S. Yoo, M. S. Oh, H. S. Park, S. T. Jung, G. T. Park, and K. Y. Park. Studies on the low local temperature rise in the mirror facet of a high-power InGaAsP/GaAs laser. *Japanese Journal of Applied Physics Part 2-Letters*, 31(12A):L1686–L1688, 1992.

[147] I. B. Petrescu-Prahova, P. Modak, E. Goutain, D. Bambrick, D. Silan, J. Riordan, T. Moritz, and J. H. Marsh. 253 $mW/\mu m$ maximum power density from 9xx nm epitaxial laser structures with d/Γ greater than 1 μm. In *2008 IEEE 21st International Semiconductor Laser Conference*, pages 135–136, 2008.

[148] E. Yablonovitch, R. Bhat, C. E. Zah, T. J. Gmitter, and M. A. Koza. Nearly ideal InP/$In_{0.53}Ga_{0.47}As$ heterojunction regrowth on chemically prepared $In_{0.53}Ga_{0.47}As$ surfaces. *Applied Physics Letters*, 60(3):371–373, 1992.

[149] S. J. Pearton, F. Ren, W. S. Hobson, C. R. Abernathy, and U. K. Chakrabarti. Comparision od surface recombination velocities in InGaP and AlGaAs mesa diodes. *Journal of Vacuum Science & Technology B*, 12(1):142–146, 1994.

[150] J. K. Wade, L. J. Mawst, D. Botez, M. Jansen, F. Fang, and R. F. Nabiev. High continuous wave power, 0.8 μm-band, Al-free active-region diode lasers. *Applied Physics Letters*, 70(2):149–151, 1997.

[151] G. Romo, T. Smy, D. Walkey, and B. Reid. Modeling facet heating in ridge lasers. *Microelectronics Reliability*, 43(1):99–110, 2003.

[152] S. Ghosh, P. Bhattacharya, E. Stoner, J. Singh, H. Jiang, S. Nuttinck, and J. Laskar. Temperature-dependent measurement of Auger recombination in self-organized $In_{0.4}Ga_{0.6}As$/GaAs quantum dots. *Applied Physics Letters*, 79(6):722–724, 2001.

[153] P. W. Epperlein and O. J. F. Martin. Reflectance modulation studies on laser diode mirrors. *Institute of Physics Conference Series*, 120:353, 1992.

[154] J. W. Tomm, M. Ziegler, V. Talalaev, C. Matthiesen, T. Elsaesser, M. Bou Sanayeh, P. Brick, and M. Reufer. New approaches towards the understanding of the catastrophic optical damage process in in-plane diode lasers. *Proceedings of SPIE*, 7230:72300V, 2009.

[155] M. Hempel, M. Ziegler, J. W. Tomm, T. Elsaesser, N. Michel, and M. Krakowski. Time-resolved analysis of catastrophic optical damage in 975 nm emitting diode lasers. *Applied Physics Letters*, 96(25):251105, 2010.

[156] J. W. Tomm, M. Hempel, M. Krakowski, and T. Elsaesser. Mechanisms and kinetics of the Catastrophic Optical Damage (COD) of high-power semiconductor lasers. In *IEEE Photonics Society Summer Topical Meeting Series 2012*, pages 51–52, 2012.

[157] S. Mahajan, H. Temkin, and R. A. Logan. Formation of optically induced catastrophic degradation lines in InGaAsP epilayers. *Applied Physics Letters*, 44(1):119–121, 1984.

[158] S. N. G. Chu, S. Nakahara, M. E. Twigg, L. A. Koszi, E. J. Flynn, A. K. Chin, B. P. Segner, and W. D. Johnston. Defect mechanisms in degradation of 1.3-μm wavelength channeled-substrate buried heterostructure lasers. *Journal of Applied Physics*, 63(3):611–623, 1988.

[159] O. Ueda, K. Wakao, S. Komiya, A. Yamaguchi, S. Isozumi, and I. Umebu. Catastrophic degradation of InGaAsP/InGaP double-heterostructure lasers grown on (001) GaAs substrates by liquid-phase epitaxy. *Journal of Applied Physics*, 58(11):3996–4002, 1985.

[160] C. W. Snyder, J. W. Lee, R. Hull, and R. A. Logan. Catastrophic degradation lines at the facet of InGaAsP/InP lasers investigated by transmission electron microscopy. *Applied Physics Letters*, 67(4):488–490, 1995.

[161] I. Rechenberg, A. Höpner, J. Maege, A. Klein, G. Beister, and M. Weyers. Heating and damage of InGaAs/GaAs/AlGaAs laser facets. *Institute of Physics Conference Series Microscopy of Semiconducting Materials 1995*, 146:587–590, 1995.

[162] I. Rechenberg, U. Richter, A. Klein, W. Höppner, J. Maege, and G. Beister. Early stage of facet degradation in 980 nm pump laser diodes. In J. Donecker and I. Rechenberg, editors, *Defect Recognition and Image Processing in Semiconductors 1997*, volume 160, pages 479–482, 1998.

[163] Y. Sin, N. Presser, B. Foran, M. Mason, and S. C. Moss. Investigation of catastrophic optical mirror damage in high power single-mode InGaAs-AlGaAs strained quantum well lasers with focused ion beam and HR-TEM techniques. In *Conference on Lasers and Electro-Optics (CLEO)*, 2007.

[164] Y. Sin, N. Presser, B. Foran, N. Ives, and S. C. Moss. Catastrophic facet and bulk degradation in high power multi-mode InGaAs strained quantum well single emitters. *Proceedings of SPIE*, 7198:719818, 2009.

[165] R. E. Mallard, R. Clayton, D. Mayer, and L. Hobbs. Failure analysis of high power GaAs-based lasers using electron beam induced current analysis and transmission electron microscopy. *J. Vac. Sci. Technol.*, 16(2):825, 1998.

[166] S. N. G. Chu, N. Chand, W. B. Joyce, P. Parayanthal, and D. P. Wilt. Generic degradation mechanism for 980 nm $In_xGa_{1-x}As$/GaAs strained quantum-well lasers. *Applied Physics Letters*, 78 (21):3166–3168, 2001.

[167] M. Hempel, J. W. Tomm, F. La Mattina, I. Ratschinski, M. Schade, I. Shorubalko, M. Stiefel, H. S. Leipner, F. M. Kießling, and T. Elsaesser. Microscopic origins of catastrophic optical damage in diode lasers. *IEEE Journal of Selected Topics in Quantum Electronics*, 2013. in print.

[168] H. Fujii, Y. Ueno, and K. Endo. Effect of thermal resistivity on the catastrophic optical damage power density of AlGaInP laser diodes. *Applied Physics Letters*, 62(17):2114–2115, 1993.

[169] W. Nakwaski. Three-dimensional time-dependent thermal model of catastrophic mirror damage in stripe-geometry double-heterostructure GaAs/(AlGa)As diode lasers. *Optical and Quantum Electronics*, 21(4):331–334, 1989.

[170] M. Ziegler, F. Weik, J. W. Tomm, T. Elsaesser, W. Nakwaski, R. P. Sarzala, D. Lorenzen, J. Meusel, and A. Kozlowska. Transient thermal properties of high-power diode laser bars. *Applied Physics Letters*, 89(26):263506, 2006.

[171] M. Ziegler, J. W. Tomm, T. Elsaesser, G. Erbert, F. Bugge, W. Nakwaski, and R. P. Sarzala. Visualization of heat flows in high-power diode lasers by lock-in thermography. *Applied Physics Letters*, 92(10):103513, 2008.

[172] M. Levinshtein, S. Rumyantsev, and M. Shur. *Handbook Series on Semiconductor Parameters*, volume 2: Ternary and Quaternary III-V Compounds. World Scientific, Singapore New Jersey London HongKong, 1999.

[173] M. Ziegler. *Thermography of semiconductor lasers - from thermal emission of semiconductors towards a novel analytical tool for optoelectronic devices*. PhD thesis, Humboldt-Universität zu Berlin, 2009.

[174] L. M. Foster, J. E. Scardefield, and J. F. Woods. Thermodynamic analysis of the III-V alloy semiconductor phase diagrams. *Journal of the Electrochemical Society*, 119(6):765–766, 1972.

[175] W. A. Tiller. Theoretical analysis of requirements for crystal growth from solution. *Journal of Crystal Growth*, 2(2):69–79, 1968.

[176] J. H. Jacob, R. Petr, M. A. Jaspan, S. D. Swartz, M. T. Knapczyk, and A. M. Flusberg. Fault protection of broad-area laser diodes. *Proceedings of SPIE*, 7198:719815, 2009.

[177] E. C. Madhavamenon, P. M. Petroff, and R. G. Waters. Degradation kinetics of GaAs quantum well lasers. *Applied Physics Letters*, 54(26):2683–2685, 1989.

[178] M. Hempel, F. La Mattina, J. W. Tomm, U. Zeimer, R. Broennimann, and T. Elsaesser. Defect evolution during catastrophic optical damage of diode lasers. *Semiconductor Science and Technology*, 26(7):075020, 2011.

[179] M. Hempel, J. W. Tomm, U. Zeimer, and T. Elsaesser. Defect propagation in broad-area diode lasers. *Materials Science Forum*, 725:101–104, 2012.

[180] M. Hempel, J. W. Tomm, V. Hortelano, N. Michel, J. Jim, M. Krakowski, and T. Elsaesser. Time-resolved reconstruction of defect creation sequences in diode lasers. *Laser & Photonics Reviews*, 6(6):L15–L19, 2012.

[181] M. Bou Sanayeh, A. Jaeger, W. Schmid, S. Tautz, P. Brick, K. Streubel, and G. Bacher. Investigation of dark line defects induced by catastrophic optical damage in broad-area AlGaInP laser diodes. *Applied Physics Letters*, 89(10):101111, 2006.

[182] J. Houlihan, J. R. O'Callaghan, V. Voignier, G. Huyet, J. G. McInerney, and B. Corbett. Experimental observation of traveling waves in the transverse section of a laser. *Optics Letters*, 26(20): 1556–1558, 2001.

[183] J. Mukherjee, M. Ziegler, J. LeClech, J. W. Tomm, B. Corbett, J. G. McInerney, J. P. Reithmaier, S. Deubert, and A. Forchel. Bulk temperature mapping of broad area quantum dot lasers: modeling and micro-thermographic analysis. *Proceedings of SPIE*, 7230:72300W–1–72300W–7, 2009.

[184] W. Nakwaski. Heat-sinking process in light-emitting-diodes. *Optica Applicata*, 14(3):385–397, 1984.

[185] W. Nakwaski. Spreading thermal-resistance of the heat-sink of a light-emitting diode. *Solid-State Electronics*, 27(8-9):823–824, 1984.

[186] W. Nakwaski and A. M. Kontkiewicz. Heat-spreading in light-emitting burrus-type diodes. *Optica Applicata*, 15(1):22–37, 1985.

[187] M. Bou Sanayeh, P. Brick, W. Schmid, B. Mayer, M. Muller, M. Reufer, K. Streubel, M. Ziegler, J. W. Tomm, and G. Bacher. The physics of catastrophic optical damage in high-power AlGaInP laser diodes. *Proceedings of SPIE*, 6997(Semiconductor Lasers and Laser Dynamics III):699703–1–699703–12, 2008.

[188] M. Hempel, M. Ziegler, S. Schwirzke-Schaaf, J. W. Tomm, D. Jankowski, and D. Schröder. Spectroscopic analysis of packaging concepts for high-power diode laser bars. *Applied Physics A: Materials Science & Processing*, 107(2):371–377, 2012.

[189] M. Olecki, J. W. Tomm, M. Hempel, P. Hennig, and T. Elsaesser. Emission properties of diode laser bars during pulsed high-power operation. In S. Zediker Mark, editor, *High-Power Diode Laser Technology and Applications X*, volume 8241, page 824107. SPIE, 2012.

[190] R. Puchert, A. Barwolff, M. Voss, U. Menzel, J. W. Tomm, and J. Luft. Transient thermal behavior of high power diode laser arrays. *Components and Packaging Technologies, IEEE Transactions on*, 23(1):95–100, 2000.

[191] M. Hempel, J. W. Tomm, M. Bettiati, and T. Elsaesser. High single-spatial-mode pulsed power from 980 nm emitting lasers. *Applied Physics Letters*, 101(19):191105–1–5, 2012.

[192] M. O. Ziegler, M. Münkel, T. Burkhard, G. Jennemann, I. Fischer, and W. Elsässer. Spatiotemporal emission dynamics of ridge waveguide laser diodes: picosecond pulsing and switching. *Journal of the Optical Society of America B*, 16(11):2015–2022, 1999.

[193] A. Klehr, G. Beister, G. Erbert, A. Klein, J. Maege, I. Rechenberg, J. Sebastian, H. Wenzel, and G. Tränkle. Defect recognition via longitudinal mode analysis of high power fundamental mode and broad area edge emitting laser diodes. *Journal of Applied Physics*, 90(1):43–47, 2001.

[194] M. Hempel, M. Chi, P. M. Petersen, U. Zeimer, and J. W. Tomm. How does external feedback cause AlGaAs-based diode lasers to degrade? *Applied Physics Letters*, 102(2):023502, 2013.

[195] S. A. Moore, L. O'Faolain, M. A. Cataluna, M. B. Flynn, M. V. Kotlyar, and T. F. Krauss. Reduced surface sidewall recombination and diffusion in quantum-dot lasers. *IEEE Photonics Technology Letters*, 18(17-20):1861–1863, 2006.

[196] P. M. Smowton, E. J. Pearce, H. C. Schneider, W. W. Chow, and M. Hopkinson. Filamentation and linewidth enhancement factor in ingaas quantum dot lasers. *Applied Physics Letters*, 81(17): 3251–3253, 2002.

[197] C. Ribbat, R. L. Sellin, I. Kaiander, F. Hopfer, N. N. Ledentsov, D. Bimberg, A. R. Kovsh, V. M. Ustinov, A. E. Zhukov, and M. V. Maximov. Complete suppression of filamentation and superior beam quality in quantum-dot lasers. *Applied Physics Letters*, 82(6):952–954, 2003.

[198] C. Henry. Theory of the linewidth of semiconductor lasers. *Quantum Electronics, IEEE Journal of*, 18(2):259–264, 1982.

[199] A. Baskaran and P. Smereka. Mechanisms of Stranski-Krastanov growth. *Journal of Applied Physics*, 111(4):044321, 2012.

Danksagung

Ich möchte mich hiermit bei all denen bedanken, die mich im Rahmen dieser Arbeit unterstützt haben.

Ein besonderer Dank gilt dabei Herrn Prof. Dr. Elsässer, der mir die Beschäftigung mit diesem Forschungsthema ermöglicht hat und für die zahlreichen zielführenden Diskussionen zu dieser Arbeit und den gemeinsamen Publikationen.

Den Gutachtern und Mitgliedern der Prüfungskommission möchte ich dafür danken, dass sie sich die Zeit genommen haben, sich mit meiner Arbeit zu beschäftigen.

Für die umfassende Betreuung in der Arbeitsgruppe, möchte ich meinen allerherzlichsten Dank an Dr. Jens W. Tomm aussprechen. Seine Unterstützung umfasste nicht nur die wissenschaftliche Betreuung durch tägliche Diskussionen, sondern auch die Einbeziehung in Projekt-, Konferenz- und Publikationstätigkeiten.

Ein Dank gilt Dr. Mathias Ziegler für die Zusammenarbeit mit ihm am MBI. Weiterhin bedanke ich mich bei unseren Technikerinnen Sandy Schwirzke-Schaaf, Monika Tischer, Marina Friedrich und den Auszubildenden in unserem Projekt für die freundliche und kompetente Unterstützung bei der Laborarbeit, ebenso bei allen weiteren Mitarbeitern des MBI mit denen ich während meiner Dissertation zusammenarbeiten durfte.

Darüber hinaus danke ich Dr. Ute Zeimer und ihren Kollegen vom Ferdinand-Braun-Institut, Dr. Fabio La Mattina, Dr. Rolf Brönnimann und den weiteren Mitarbeitern der EMPA in Dübendorf, Dr. Martina Bäumler und Kollegen vom IAF Freiburg, Prof. Dr. Juan Jiménez und Vanesa Hortelano von der Universidad de Valladolid, Dr. Jayanta Mukherjee, Dr. Frank M. Kießling vom IKZ Berlin, PD Dr. Hartmut S. Leipner vom Interdisziplinären Zentrum für Materialwissenschaften der Martin-Luther-Universität Halle-Wittenberg und seinem Team, Prof. Dr. Peter M. Smowton und Dr. Stella Elliott und ihren Kollegen von der Cardiff University, Prof. Dr. Peter E. Andersen und seinen Mitarbeitern von der DTU in Dänemark, Dr. Heiko Kissel und DILAS, Prof. Dr. Michel Krakowski und seinen Mitarbeitern von Alcatel-Thales III-V Lab, Dr. Mauro Bettiati und 3S Photonics, OSRAM Opto Semiconductors und JENOPTIK für die Zusammenarbeit.

Besonders dankbar bin ich meiner Familie, insbesondere meiner Frau, und meinen Freunden, die mir in der Zeit meiner Promotion den nötigen Rückhalt gegeben haben.

Selbständigkeitserklärung

Ich erkläre, dass ich die vorliegende Arbeit selbständig und nur unter Verwendung der angegebenen Literatur und Hilfsmittel angefertigt habe.

Berlin, den 30.04.2013 Martin Hempel